Event Localization In Bulk Scintillator Crystals Using Optical Coded Apertures

A Dissertation Presented for the

Doctor of Philosophy

Degree

The University of Tennessee, Knoxville

Joshua Brian Braverman

May 2015

ACKNOWLEDGEMENTS

First and foremost, I would like to thank my advisor, Dr. Klaus Ziock, for his infinite patience and guidance from my first day of research to my last working for him. He had an open door for my questions and spent countless hours teaching me not just what was required to complete the project, but necessary skills and lessons that allowed me to grow as a researcher, critical thinker, and scientist. I also thank him for continuing to demand a high quality of work, especially near the end of my research. Even when I struggled to believe I could overcome challenges that arose in the project he continued to be patient and kept the goal of me having a successful graduate experience in mind.

I also thank Dr. Donny Hornback and Dr. Jason Newby at Oak Ridge National Lab (ORNL) for all of the help throughout my research. Both of them spent many hours making sure I was taught the essential fundamentals and tools that I needed to learn, especially in my first two years of research. I also thank them for the advice in navigating my way through many other aspects of graduate school unrelated to the experiment itself.

Thanks to Curtis Fitzgerald at ORNL who was instrumental in designing and building any hardware we needed, no matter how complicated things became on along the way.

Also, many thanks to Dr. Paul Hausladen at ORNL, for the numerous discussions when particularly difficult challenges arose in the experiment.

I especially thank my friend Robert Van Wesep, who I met on the first day of graduate school and owe a huge amount of gratitude for frequently giving his support and perspective throughout the last few years, and occasionally giving his mathematics expertise to double check a problem.

Thank you also to my friend Adam Kadet, who was never too busy to plan a visit for a break.

Finally, thanks to my family; my mom Linda, stepdad Rick, dad Doug, and aunt and uncle Marc and Michelle for providing endless support throughout graduate school. Especially thank you to my mom, who unconditionally supported me through every step along the way.

ABSTRACT

Scintillation-based radiation detectors provide an effective method to detect radioactive materials. In medical physics, astrophysics, and national security oftentimes it is optimal to have the ability to localize a radioactive interaction in a scintillator to as small a region as possible within the crystal. Current methods rely on the ability to centroid a light spot as read onto a phototransducer (commonly a photomultiplier tube), and due to the typical width of the light spot when it reaches the phototransducer, the resolution is generally limited to several millimeters. One method to achieve a finer resolution is to use a segmented crystal that allows the position of the event to be localized to the scale of the segmentation. However, this lessens the ability to collect all of the available scintillation light, thereby sacrificing energy resolution.

To avoid a segmented crystal and attempt to improve on the spatial resolution, this dissertation explores a detector that uses a shadow-mask pattern between the crystal and the phototransducer. This method uses principles of coded-aperture imaging to localize an event to approximately a 1-cubic-millimeter voxel in three dimensions inside a large crystal. This work explores all aspects of the concept including current state-of-the-art event localization capabilities, possible applications, design parameters, simulation studies, and experimental implementations of the concept with the results from two prototype systems.

TABLE OF CONTENTS

CHAPTER 1. INTRODUCTION 1

CHAPTER 2. BACKGROUND 8

2.1. INTRODUCTION 8

2.1.A. ANGER CAMERAS 8

2.2. CODED APERTURES 9

2.2.A. PINHOLE APERTURES 9

2.2.B. CODED-APERTURE OVERVIEW 10

2.3. RECONSTRUCTION METHODS 12

2.3.A. CROSS CORRELATION 14

2.3.B. PHOTON TAGGING 15

2.3.C. ITERATIVE METHODS 15

2.4. MASK PATTERNS 16

2.4.A. CYCLIC DIFFERENCE SETS 17

2.4.B. ONE-DIMENSIONAL URA PATTERNS 18

2.4.C. TWO-DIMENSIONAL URA PATTERNS 19

2.4.D. ONE-DIMENSIONAL MURA PATTERNS 20

2.4.E. TWO-DIMENSIONAL MURA PATTERNS 21

2.4.F. GEOMETRIC MASK PATTERNS 22

2.4.G. BIQUADRATIC AND DILUTE URAS 22

2.5. SIGNAL-TO-NOISE RATIO OF CODED APERTURES 22

2.5.A. CODED-APERTURE SYSTEM GEOMETRIES 28

2.6. CODED-APERTURE FIELD OF VIEW 29

2.7. CODED-APERTURE RESOLUTION 34

2.7.A. CODED APERTURES IN THE NEAR FIELD 35

2.8. CODED-APERTURE APPLICATIONS 36

2.8.A. CODED APERTURES IN MEDICAL PHYSICS 37

2.8.B. CODED APERTURES IN ASTROPHYSICS 38

2.8.C. CODED APERTURES IN NATIONAL SECURITY 38

2.9. COMPTON CAMERAS 39

2.9.A. COMPTON CAMERA THEORY 39
2.9.B. COMPTON CAMERA OVERVIEW 47
2.10. EVENT LOCALIZATION IN BULK SCINTILLATORS 51
2.10.A. CENTROIDING METHOD IMPROVEMENTS 51
2.10.B. SEGMENTED CRYSTALS 52
2.11. POSITRON EMISSION TOMOGRAPHY OVERVIEW 54
2.11.A. DEPTH OF INTERACTION AND HORIZONTAL SPATIAL RESOLUTION IN PET IMAGING 56
CHAPTER 3. THEORETICAL OVERVIEW 59
3.1. CRYSTAL COMPTON CAMERA THEORETICAL OVERVIEW 59
3.1.A. ADVANTAGES OF NEW METHOD 60
3.2. OVERALL SYSTEM DESIGN 61
3.3. EVENT PROCESSING AND IMAGE RECONSTRUCTION 63
3.3.A. COARSE LATERAL LOCALIZATION 64
3.3.B. DEPTH DETERMINATION 65
3.3.C. LATERAL POSITION DETERMINATION 68
3.4. METHODS USED IN EVENT PROCESSING 68
3.4.A. REPEATING CYCLES 68
3.4.B. INDEX OF REFRACTION DEPTH CORRECTION 69
CHAPTER 4. EXPERIMENTAL OVERVIEW 72
4.1. SYSTEM PARAMETERS AND SIMULATIONS 72
4.2. SCINTILLATOR SELECTION 72
4.2.A. INTRODUCTION 72
4.2.B. MECHANISMS FOR LIGHT GENERATION 73
4.2.C. EFFICIENCY 74
4.2.D. LIGHT GUIDE MATERIAL 77
4.3. PHOTOTRANSDUCER REVIEW 80
4.3.A. SILICON PHOTOMULTIPLIERS 80
4.3.B. CHARGE-COUPLED DEVICES 81
4.3.C. ELECTRON MULTIPLYING CHARGE-COUPLED DEVICES 83
4.3.D. PHOTOMULTIPLIER TUBES 83

4.3.E. MULTIANODE PHOTOMULTIPLIER TUBES 87
4.4. PHOTOTRANSDUCER SELECTION 88
4.4.A. SINGLE PHOTON RESPONSE 88
4.5. SIMULATIONS 93
4.5.A. OPTICAL GEOMETRY SELECTION 95
4.5.B. TWO-DIMENSIONAL SYSTEM OPTICAL GEOMETRY 95
4.6. TWO-DIMENSIONAL SIMULATION RESULTS 98
4.7. THREE-DIMENSIONAL SIMULATION RESULTS 111
4.7.A. DEPTH RESOLUTION 125
4.7.B. LATERAL DIMENSION RESOLUTION 125
4.7.C. MULTIPLE MASK CYCLES 128
CHAPTER 5. EXPERIMENTAL DESIGN 133
5.1. TWO-DIMENSIONAL SYSTEM 133
5.1.A. ELECTRONICS OVERVIEW 133
5.1.A.i. STRÜCK WAVEFORM DIGITIZERS 135
5.1.A.ii. SIGNAL AND WAVEFORM ANALYSIS 137
5.1.B. TWO-DIMENSIONAL SYSTEM HARDWARE 140
5.1.C. ENERGY SPECTRUM CALIBRATIONS 145
5.1.D. MAGNIFICATION DIFFERENCE VERIFICATION 147
5.1.E. EVENT PROCESSING 151
5.1.F. GAIN CORRECTIONS 152
5.1.G CENTER LOCATION ADJUSTMENT 153
5.2. THREE-DIMENSIONAL SYSTEM 153
5.2.A. ELECTRONICS 154
5.2.A.i. DATA ACQUISITION SYSTEM 155
5.2.A.ii. FRONT-END READOUT MODULE 155
5.2.A.iii. DIGITIZER 157
5.2.A.iv. TRIGGER MODULE 158
5.2.A.v. ELECTRONICS NOISE 159
5.2.A.vi. DATA ACQUISITION SYSTEM SOFTWARE 162
5.2.B. HARDWARE 162

5.2.C. DATA COLLECTION AND SYSTEM PERFORMANCE 166
5.2.C.i. ENERGY CALIBRATIONS 166
5.2.C.ii. PATTERN VISIBILITY CHECK 168
5.2.C.iii. GAIN MAPPING 169
5.2.D. MASK AND MASK ALIGNMENT 170
5.2.E. IMAGING SOFTWARE 173
CHAPTER 6. FINAL RESULTS 175
6.1. TWO-DIMENSIONAL SYSTEM 175
6.1.A. SINGLE EVENT RECONSTRUCTION 175
6.1.B. EVENT FILTERING 177
6.1.C. TWO-DIMENSIONAL FINAL RESULTS 181
6.1.D. TWO-DIMENSIONAL COMPARISONS TO SIMULATIONS 185
6.2. THREE-DIMENSIONAL SYSTEM 187
6.2.A. SINGLE EVENT RESULTS 187
6.2.B. OUTER CYCLES IMPROVEMENTS 188
6.2.C. GAIN CORRECTIONS 190
6.2.D. SINGLE EVENT DEPTH RECONSTRUCTION 191
6.2.E. LATERAL POSITION DETERMINATION 191
6.2.F. THREE-DIMENSIONAL SYSTEM THICK-CRYSTAL EMULATION FINAL RESULTS 195
6.2.G. ENERGY RESOLUTION 204
6.2.H. COMPARISON TO SIMULATIONS 205
6.2.I. ^{133}BARIUM RESULTS 207
6.2.J. THICK CRYSTAL RESULTS 215
CHAPTER 7. CONCLUSION 218
BIBLIOGRAPHY 222
APPENDICES 231
APPENDIX 1. FLUX DENSITY EXPRESSION DERIVATION 232
APPENDIX 2. FILTERING ALGORITHMS 238
APPENDIX 3. ANGLED BEAM SETUP 239

VITA 242

LIST OF TABLES

Table 1. Parameters and intervals of materials used in scintillator crystal selection study 75
Table 2. The parameters used in the Monte Carlo simulations for optical geometry of the system. 93
Table 3. The upper light guide thickness and flux density of the light spot for each geometry... 96
Table 4. The ranks of the mask patterns, feature sizes, focal lengths and upper light guide thicknesses for each system considered for the full three-dimensional system..... 112
Table 5. The depth of the launched events and depth resolution at each depth in the simulated system 125
Table 6. The lateral resolution for each depth in the simulated system..... 128
Table 7. The final depth and lateral results for the experimental two-dimensional system. 183
Table 8. The percentage of events found within the correct peak for each depth for the experimental two-dimensional system..... 183
Table 9. The final depth results of the experimental three-dimensional system 196
Table 10. The final lateral results for the experimental three-dimensional system 202
Table 11. The lower energy gamma-ray results for the experimental three-dimensional system 208

LIST OF FIGURES

Figure 1. The attenuation length of gamma-rays in the earth's atmosphere as a function of energy 4
Figure 2. An Anger camera design with a collimator between the source to be imaged and scintillator 9
Figure 3. A schematic of a pinhole aperture and the relationship between the aperture size and image 10
Figure 4. The original coded-aperture concept 11
Figure 5. A visual diagram of a cross-correlation operation 13
Figure 6. A rank 19 x 19 coded-aperture pattern and its autocorrelation function 20
Figure 7. A one-dimensional typical reconstructed point source against the background 23
Figure 8. Two possible coded-aperture mask and detector geometries 28
Figure 9. A detector geometry that uses the repeating nature of larger a mask pattern 29
Figure 10. The magnification of a coded-aperture feature 30
Figure 11. An object magnified through a simple pinhole camera 31
Figure 12. The field of view of an object a distance from a mask plane 33
Figure 13. A center base pattern and two half-cycle patterns repeated around the center 33
Figure 14. The ratio of the opening angles at the object and reconstructed image arc length can be used to calculate the image pixel size 35
Figure 15. A diagram of a photon interacting with a stationary charged particle via Compton scattering 40
Figure 16. A diagram of a Compton camera 43
Figure 17. A diagram of the Compton camera telescope, COMPTEL 49
Figure 18. The effective area versus incident gamma-ray energy for the Nuclear Compton Telescope and COMPTEL 50
Figure 19. An diagram of segmented crystals with coupled photomultiplier tubes. 53
Figure 20. A diagram of segmented scintillator crystal with collimation holes 54
Figure 21 A diagram of a positron emission tomography imager 55
Figure 22. Various setups of scintillator crystals and methods used to localize event interactions 57
Figure 23.A diagram of the optical coded-aperture concept 59

Figure 24. A diagram of two events at different depths in the system 62
Figure 25. A diagram how to find the centroid of a light distribution and a simulated detector response with an optical coded-aperture pattern between the crystal and the phototransducer 64
Figure 26. The bin boundaries for rebinning and imaging in the system 66
Figure 27. Some sample reconstructed events (simulated data) using the optical coded-aperture system 67
Figure 28. The projected base mask cycle repeating onto the phototransducer plane..... 69
Figure 29. A diagram of how light in a scintillator crystal spreads as it encounters the crystal to light guide boundary 70
Figure 30. The relationship between an event's location in a thick crystal and the apparent location in a low index light guide..... 70
Figure 31. A greyscale map of the parameters described in Table 1..... 75
Figure 32. Total useable sequence efficiencies versus energy of the gamma-ray for several scintillator crystals 76
Figure 33. The measured percent transmission versus wavelength for a 2 mm thick cell of the high index optical coupling material..... 78
Figure 34. The detector pattern with an ideal 0.8 mm pixel phototransducer array for 40k launched photons from a single point 20 mm from the bottom of the crystal 79
Figure 35. Diagram of operation of a charge-coupled device. 82
Figure 36. A diagram of a photomultiplier tube 85
Figure 37. A multianode photomultiplier tube schematic 87
Figure 38. The quantum efficiency and gain map of a typical Hamamatsu 9500 89
Figure 39. An apparatus to measure the response of the Hamamatsu 9500 photomultiplier tube. 90
Figure 40. Three classes of waveforms were observed in the Hamamatsu 9500 output signals.. 91
Figure 41. Histograms of the responses of a Hamamtsu 9500 pixel with and without a 50% neutral density filter above the entrance window 92
Figure 42. Diagrams of the simulated system used to choose an optical geometry 94
Figure 43. A lateral view of optical photons launched over the shadow mask pattern. 95

Figure 44. The full width half maximum of the light spot versus the upper light guide thickness for an event at the bottom of a scintillator crystal. 97
Figure 45. Heat maps of detector responses for various geometries including without a mask pattern and events at several depths with a mask pattern 100
Figure 46. Reconstructed one-dimensional images for a single event at several depths through the depth range..... 103
Figure 47. The maximum peak heights of each reconstructed image plotted for a single event for a range of depths from the mask pattern. 104
Figure 48. Histograms of the mean for each fitting method (Gaussian fit and flux density expression) for events where the detector sees 400 photons launched from a single point.105
Figure 49. The imaged and absolute lateral position found with the coded-aperture imaging method using the mean and Gaussian fit approach to obtain the coarse localization.. 107
Figure 50. The found depth for 1000 events emulated at various depths in a scintillator crystal. 109
Figure 51. The lateral position reconstructed location for 1000, 200-photon events. 110
Figure 52. Detector responses for various detector geometries and numbers of photons per event for locations in a 30 mm thick crystal with the optical geometry of a rank 19 mask, 1.3 mm feature sizes, 2.2 cm focal length and 1.0 cm upper light guide. 113
Figure 53. The heat map for 200k photons with an ideal anode pixel array, with the data collapsed in each lateral direction..... 114
Figure 54. The collapsed data with a Gaussian fit.. 115
Figure 55. Collapsed data in both lateral directions for 400 photons with a real detector array. 116
Figure 56. The histograms of the coarse lateral position found for 250 400-photon events 20 mm from the bottom of a thick scintillator crystal, with a real detector array..... 117
Figure 57. Reconstructed images for a 200k-photon event. 120
Figure 58. The maximum peak height from the individual images in Figure 57 plotted against the depth each image was reconstructed for. 121
Figure 59. The heat maps and reconstructed events for a variou number of photons per event. 124
Figure 60. The depth reconstruction for 250, 400-photon events at various depths throughout a bulk crystal..... 127

Figure 61. The lateral results for events at 1 mm, 10 mm, 20 mm and 30 mm into the scintillator crystals. 129
Figure 62. The reconstructed images at correct depths with and without outer mask cycles..... 132
Figure 63. Two configurations for the photomultiplier tube readout in the two-dimensional system. 134
Figure 64. The photomultiplier tube readout boards used in the two-dimensional experiment . 135
Figure 65. A 16-channel waveform digitizer and the VME-to-USB controller 136
Figure 66. The recorded waveforms for 16 channels in a 3200-nanosecond integration window. 138
Figure 67. The entire recorded waveform for a single anode strip with the digitizer set on low impedance. 139
Figure 68. A schematic of the concept used to determine event location in a thick crystal. 141
Figure 69. Each individual plane in the system that the hardware is designed to hold with the required alignment labeled in the figure. 142
Figure 70. The optical stack consisting of the focal length plane, the photomask and upper light guide..... 143
Figure 71. The hardware of the two-dimensional system..... 144
Figure 72. A one-dimensional binary mask pattern with alternating 2 mm transparent and opaque elements 145
Figure 73. The energy spectra with and without the 50% binary mask pattern using a 2-mm-thick NaI(Tl) crystal..... 146
Figure 74. Images of the magnification test setup 148
Figure 75. A one-dimensional binary magnified pattern for a single 356-keV gamma-ray interaction 148
Figure 76. Sample event from the second readout configuration used to demonstrate the ability to detect pattern magnification differences..... 149
Figure 77. Many aggregated events with the two-dimensional readout board. The upper right pixel is empty as it was used for the last-dynode data of the photomultiplier tube. 150
Figure 78. Single events from the same data set as the aggregate events shown in Figure 77... 151
Figure 79. The anode response for many events in a thin crystal 22 mm from the photomultiplier tube plane..... 153

Figure 80. The anode map of both the original system design and the one used experimentally 154
Figure 81. The connectors on the back side of the photomultiplier tube readout module and a side view of the module..... 156
Figure 82. The Hamamatsu 9500 anode mapping and the corresponding multiplexed signal groups..... 157
Figure 83. A data acquisition system digitizer card..... 158
Figure 84. A histogram of the root mean square values of each active anode in the entire system using a forced trigger 160
Figure 85. A heat map of each anode's root mean squre value for 3800 forced trigger events.. 161
Figure 86. A schematic of the entire enclosed hardware system. 163
Figure 87. The photomultiplier tube array optically coupled to the 17 mm quartz plate and mounted in the hardware assembly.. 164
Figure 88. The system used to mount the Hamamtsu 9500s to a uniform height..... 165
Figure 89. Crystal schematics for the 2 mm and 20 mm crystals used for energy calibrations . 167
Figure 90. The energy spectrums for a ^{57}Cobalt and a ^{133}Barium sources 167
Figure 91. The detector response of the system with a thin crystal and 2-mm binary mask pattern 168
Figure 92. The LED array used for gain mapping the system..... 169
Figure 93. A single Hamamtsu 9500 signal taken with the diffusing glass planes and LED illuminator centered over the photomultiplier tube and moved 4 cm from the center 170
Figure 94. A simple schematic of the alignment hardware 171
Figure 95. Images of the entire system at several stages in assembly 172
Figure 96. Single event reconstructions at three depths into the thick crystal emulation range. 176
Figure 97. The peak pixel values versus the reconstructed distances for each depth reconstruction 177
Figure 98. The depth results for 1000 events at the upper-most depth with 14.7 mm of additional upper light guide 178
Figure 99. The raw detector patterns for a single event from each of the low (closest to the mask plane, largest magnified mask features) and high (farthest from the mask plane, smallest magnified mask features) data sets 179

Figure 100. The number of times the raw detector data crosses 40% of the maximum bin value for the low and high data sets. 180
Figure 101. The results with and without the coarse depth localization crossover counting method..... 181
Figure 102. The final depth results for four data sets collected. 182
Figure 103. The coarse lateral event localization using a weighted mean of the raw detector data for the bottom data set (pink on the depth results) and top data set (green on the depth results) in Figure 102. 184
Figure 104. The lateral dimension event localization after the coded-aperture imaging..... 185
Figure 105. The simulation depth results (red squares) plotted with the experimental depth results (blue triangles) of the two-dimensional system 186
Figure 106. The simulation lateral results (red squares) plotted with the experimental depth results (blue triangles) of the two-dimensional system..... 187
Figure 107. A diagram of the outer cycles used in the event reconstructions in Figure 108..... 188
Figure 108. A single event in the 662-keV peak with 10 mm of additional upper light guide .. 189
Figure 109. The heat maps and corresponding single-event image reconstructions with and without a gain mapping..... 190
Figure 110. Reconstructed images over the depth range of the thick crystal emulation 192
Figure 111. The heat map for the single event with the collapsed detector data in both lateral dimensions 193
Figure 112. The single event data collapsed in constant lateral dimensions, with each collapsed to larger bin sizes to improve the coarse event localization 194
Figure 113. Five data sets with varying layers of additional quartz upper light guide..... 195
Figure 114. The range above the possible location of the 30 mm thick crystal 197
Figure 115. The lateral results for each data set 201
Figure 116. The absolute lateral reconstruction for two data sets with the collimated source moved 2 cm..... 203
Figure 117. The energy spectrum for the ^{137}Cs source 204
Figure 118. The lateral dimension results for the 3-D system compared to simulations..... 206
Figure 119. Simulation results versus experimental results for the both lateral and depth results 207

Figure 120. The ^{133}Ba depth results 208
Figure 121. A single event (experimental data) reconstructed over the depth range 209
Figure 122. 400, 400-photon events at two depths (5 mm and 20 mm) with varying gain changes to two photomultiplier tubes that surround the center photomultiplier tube in the three-dimensional experimental array. 210
Figure 123. 400, 650-photon events at two depths (5 mm and 20 mm) with varying gain changes to two photomultiplier tubes that surround the center photomultiplier tube in the three-dimensional experimental array 211
Figure 124. Single events reconstructed with and without gain variations in the simulated system 214
Figure 125. Thick crystal event reconstruction results for the depth versus both lateral dimensions 216
Figure 126. The simulation results (400-keV simulated events) with an ideal PMT array with 3 mm pixels and the array used in the experiment..... 217
Figure 127. A light spot and the flux through the a surface a distance from the original point . 233
Figure 128. A horizontal view of the face of the phototransducer 233
Figure 129. A light ray and the associated angles as the light undergoes an index change 234
Figure 130. A fraction of the incident ray is reflected due to the index of refraction change. ... 235
Figure 131. A comparison of the flux density expression to simulation data..... 237
Figure 132. The depth found for 400-photoelectron simulation events for 5 mm and 20 mm into the crystal using the maximum root mean square method. 238
Figure 133. A schematic of the angled beam approach 239
Figure 134. The upper image shows the position of the collimated vertical beam with the corresponding spectra in the bottom image 241

CHAPTER 1. INTRODUCTION

Controlling the movement and procurement of radioactive materials is of great interest to many domestic and international communities. Particularly with respect to national nuclear security interests, Uranium and Plutonium are isotopes of concern. The International Agency of Atomic Energy defines significant quantities of Plutonium, highly enriched Uranium-235 and natural or low enriched Uranium-235 to be 9 kg, 25 kg, and 75 kg, respectively [1] [2]. If these materials were acquired with the goal of making a nuclear weapon, the level of technological expertise needed is low [2]. These realizations provide motivation to locate, detect, and monitor nuclear sources of interest [3] [4] [5].

Nuclear materials of interest to national security applications typically emit gamma-ray radiation between 10 keV and 3 MeV. Specifically, Uranium-235 has a spectral line (i.e. a large percentage of photons emitted at a certain energy) at 186 keV, and Plutonium-239 has prominent lines at 375 keV and 414 keV. Depending on the material, gamma-rays interact with matter primarily via photoelectric absorption at energies lower than several hundred keV, Compton scattering from several hundred keV to a few MeV, and pair production above that. A scintillator crystal paired with a phototransducer (PT) is the standard method of detecting radiation today. The fundamental way this method works is that when radiation enters a luminescent material, the energy of the photons is absorbed and reemitted in the form of scintillation light. This is discussed in detail in Chapter 4. Different materials absorb different types of radiation and can emit light in various wavelengths and with a wide range of decay times, ranging from a few nanoseconds to hours. To detect the emitted light the scintillators are paired to a PT, which converts light into a useable electronic signal. This is done using a photocathode that emits electrons via the photoelectric effect. The emitted electron signal can then be amplified or directed via an electric field to give information on the amount of light emitted. In a commonly used scintillator such as Sodium Iodide (NaI), photoelectric absorption dominates below 0.25 MeV, Compton scattering dominates between 0.25 MeV and 7 MeV, and pair production above that. In a photoelectric absorption interaction the incoming X-ray or gamma-ray transfers its energy to an orbital electron in an atom [6]. A gamma-ray with sufficient energy interacts with the atom and a photoelectron is ejected from one of the bound shells. The energy of the ejected photoelectron is given by the difference between the incoming photon energy and the binding energy of the photoelectron in its original shell in the atom. As the typical binding energy of

inner shell bound electrons in atoms is on the order of tens of keVs, for an interacting photon of several hundred keV or higher the ejected photoelectron will carry most of the original photon energy. Compton scattering is when a photon undergoes an elastic collision with an electron. The transfer of energy results in a wavelength shift between the incoming and outgoing photon and an increase in kinetic energy of the charged particle [6]. Pair production is when a photon interacts with a nucleus and an elementary particle and its associated antiparticle are created from the interaction. Generally, pair production occurs in higher energy radiation interactions. Due to the inverse quantum numbers of the particle and antiparticle, the creation of the particle conserves all quantities including energy and momentum.

Instances of detecting radiation first occurred in the 17th century when the first descriptions of thermo luminescence were recorded [7]. In the late 19th century, X-ray pictures were invented and the field greatly expanded as the usefulness of radiation detection grew with initial applications in medicine and imaging the human body. In 1895, while studying vacuum tubes, Wilhelm Röntgen observed a fluorescent effect on a cardboard screen painted with barium platinocyanide due to cathode rays emitted from the an electron beam striking the target and emitting X-rays. This was the first detection of electromagnetic radiation in the X-ray energy range [7]. One year later in 1896, Becquerel discovered radioactivity by experimenting with Uranium compounds. He discovered that when placing a photographic plate on a radioactive compound he could see the positions of the Uranium on the developed photograph [7]. This marked the birth of the modern field of radiation detection methods.

Throughout the 20th century other means of detection were developed. In particular, in the early 20th century, after radioactivity had been discovered, Rutherford and Geiger developed a method to count individual radioactive particles [7]. The method used a fluorescent screen to observe scattered alpha particles. The luminescence of a material that they observed occurs when incident radiation interacts via one of the processes mentioned above. This discovery resulted in an instrument that could measure the strength of a radioactive source by counting the number of flashes on the screen; this was the foundation for the modern Geiger counter. Radiation detection continued to develop into essentially three methods: photography, scintillation and ionization detection [7]. Photographic emulsions continued to be developed and eventually led to the development of films that can be used to record radiation signals and image objects, such as in X-ray imaging in medical physics.

A detailed explanation of the processes and characteristics of scintillators are discussed in Section 4.2. The basic principle is that by measuring the output light of a scintillation event, properties of the radiation emitter such as radioactivity (decays per second) and energy can be measured as well. The light is measured using a PT, and a wide array of instruments exists to make the most of the scintillation light. Instruments such as light guides [6] that collect light as efficiently as possible have been developed to trap and guide light from a scintillator to a PT.

Additionally, the ionization of materials by radiation is a useful method of measurement. Ionization occurs in a material when an incident charged particle interacts with atoms in the material causing them to lose an electron. The free electrons can then be moved under the influence of an externally applied electric field. The net freed electrons (i.e. current) can be measured and the energy lost by the ionizing radiation can be deduced.

These methods, along with the development of electronics to instrument these techniques, such as photomultipliers and advances in circuit development, have led to advanced radiation detectors. Traditionally, unless a more advanced technique is used, these techniques effectively measure energy of the radiation but do not give directional information from which the radiation originated.

When addressing a physical situation with a single nuclear source among background terrestrial radiation, it is often useful to locate the source of the radiation. Gamma-ray imaging has been applied to this problem in recent years. One method that has been successfully applied to a range of problems is called Compton imaging [8] [9] [10]. Compton imaging works by making use of gamma-ray Compton scattering events followed by photoelectric absorption interactions, and originally consisted of two planes of detector material oriented perpendicular to the incoming radiation [10]. Gamma-rays from the source are scattered in the first plane and subsequently interact via photoelectric absorption in the second plane. The incident gamma-ray energy is determined by summing the measured energies of the scattered electron and the recoiled gamma-ray. Knowing these, and applying conservation of energy and momentum, a cone of possible angles of the incident gamma-ray can be calculated (Section 2.9.A). By detecting several events and overlaying multiple cones, the original location of the gamma-rays and, in turn, the nuclear source can be located.

For this project in particular, standoff detection of nuclear sources of interest to national security is the motivation of the project. As seen in Figure 1, due to the attenuation length of

gamma-rays emitted by sources of interest in the atmosphere, it is generally not possible to detect sources at distances greater than 100 meters [11].

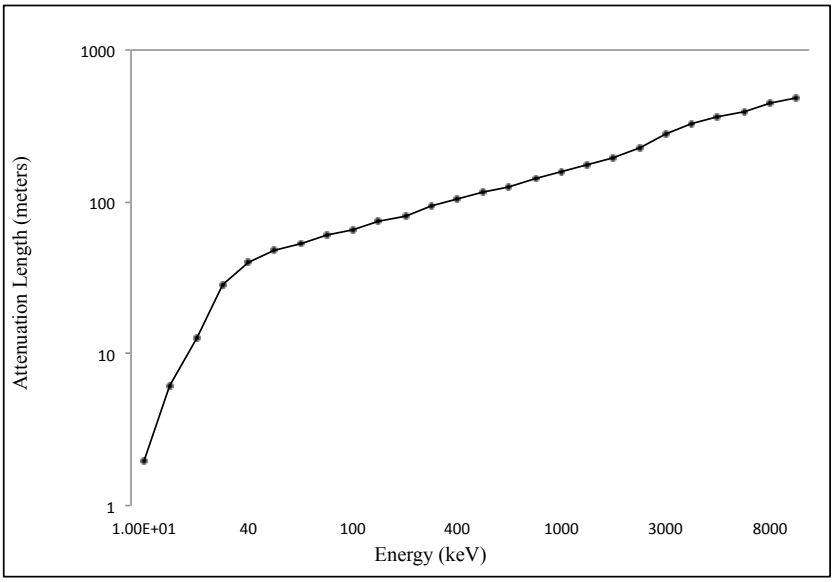

Figure 1 [11]. The 1/e attenuation length of gamma-rays in the earth's atmosphere as a function of energy. The sources of concern (Uranium and Plutonium) have lines at 186 keV, and 375 keV and 414 keV, respectively. The figure shows that gamma-rays with energies of 400 keV have a range of ~ 100 meters in the atmosphere.

There are two issues in detecting a source in the real world with large fluctuating backgrounds. A 1-milliCurie Uranium-235 source if frequently used as a target threshold got material detection and equates to only 119 milligrams of material; this is well under the significant quantity stated above. The typical background [12] is about 1 count per square cm per minute per keV. In order to detect a source above the background at a significant level (using a ~5 sigma level), based on the solid angle of a detector at 100 m from a source a detector area on the order of 1 m^2 is needed [12] [13]. While a detector size of about 1 m^2 is needed to detect enough counts from the source, it was also found [12] that increasing the detector further does not increase the range that a source can be detected. The second issue in detecting a source is that as a detector moves through a fluctuating background it can be difficult to differentiate between

a true source and a section of the detected scene that emits a higher background than the neighboring area. Compton imaging addresses this issue; by only including point sources in the search, all cones outside of the intersecting point can be characterized as background. This allows for a spatial cut in the events that correspond to pixels in the real-world reconstruction of the recorded scene.

Several Compton cameras have been built and instrumented for astrophysical imaging. While effective in imaging far field sources, specifically in gamma-ray astronomy, the effective area of these detectors relative to their overall size have so far been extremely limited, resulting in volumetrically inefficient detectors that must be built on large scales to detect sources at large distances (gamma-rays are not attenuated through space with no atmosphere) [9]. The effective area is defined as the how large the area of a detector would be that detected all incoming incident radiation if a constant flux of gamma-rays were normally incident onto the detector. This takes into consideration the area, the thickness of each plane to account for the percentage of gamma-rays that pass through without interacting, the quantum efficiency (QE) and other factors. This project seeks to provide the ability to use a single bulk volume scintillator as opposed to two discrete detector planes; up to this point only ionization based detectors with a large percentage of effective area relative to overall size have been developed. These are more expensive than scintillators and are described in detail in Section 2.9.B.

If it were possible to distinguish between two events (Compton scatter followed by photoelectric absorption) in a single volume to within a small voxel of the larger volume, a full-volume detector with a high percentage of effective volume could be built. For efficient Compton imaging, approximately 1 mm^3 event localization inside the bulk volume is needed. This is because the uncertainty in each interaction location contributes to the overall angular uncertainty in Compton imaging (see Chapter 2). While semiconductor detectors would be ideal due to their small voxel size, the cost is restrictive as they are about \$1000/cm^3 [13]. Other materials with small voxel sizes such as plastic and liquid scintillators are capable of instrumenting large volumes but due to handling difficulties and poor energy resolution their uses are also limited [14]. Inorganic crystal scintillators coupled to photomultiplier tubes are much more cost effective. A commonly used scintillator crystal such as Thallium doped Sodium Iodide (NaI(Tl)) costs ~\$3/cm^3 [13]. However, event localization in systems with the readout at the sides of a bulk crystal is poor. The most straightforward method of using the centroid of the

light spot to localize the event fails to effectively locate at this resolution for several centimeter thick crystals [15] [16] [17]. In an alternate approach the scintillator crystal is segmented into small voxels. While this eliminates the need to localize the event by finding the centroid or other means, segmenting the crystal results in a significant loss of energy resolution, increases costs, and only provides a two-dimensional solution without complicated readout approaches [18]. Advances in medical physics, astrophysics, and nuclear security technology have improved event localization in bulk scintillators through other means. While effective, none of these methods have been able to achieve the target goal of 1 mm^3 event localization in all three dimensions in an un-segmented crystal that is several centimeters thick and tens of centimeter wide; the work in this dissertation attempts to fill this need. The current state of event localization capabilities in bulk scintillators is discussed in detail in Chapter 2.

To make a system with the ability to locate a radiation event to within a small voxel within a larger un-segmented bulk scintillator crystal, a coded-aperture mask [19] is used. The system is made up of a bulk scintillator crystal on the order of 1 cm thick and tens of cm on each side with light guide below the crystal, an optical coded-aperture mask pattern, another layer of light guide and a PT. Diagrams of the system are shown in Chapter 3. A radiation interaction occurs in the bulk crystal and scintillation light projects the optical shadow pattern onto the PT. For events farther away from the pattern, the pattern is projected to a smaller size than for events closer to the pattern. This allows for a varying signal at the PT plane that is dependent on the depth of interaction of the event and, in turn, a method of determining the depth of the interaction in the crystal. In addition to the magnified pattern size carrying spatial information, the projection of the aperture pattern also carries lateral position information. These concepts are illustrated and derived in detail in Chapters 2 and 3.

Originally developed for far-field gamma-ray imaging, this work utilizes the method in the extreme near-field for optical photons. Through standard coded-aperture-reconstruction techniques and reconstructing over the range of all possible depth locations, an event can be located in all three dimensions. To detect the projected shadow pattern, the signal is read out with multianode position-sensitive photomultiplier tubes (MAPMT). As discussed in Sections 4.3 and 4.4, these were chosen due to their small pixel size and relatively low cost per unit area.

This work concentrates on the design, proof of principle, production and analysis of a bulk scintillator detector that uses a coded-aperture shadow mask pattern to locate the events in the

crystal. Overall, the system provides a novel method of locating an event to a small voxel in a bulk scintillator crystal and, in turn, is an enabling technology for the next iteration of the project, which would be to use the improved event localization capabilities to build a full-volume Compton camera. While the work of this dissertation does not contain any Compton camera results, as this specific application drives all of the required parameters of the event localization method (voxel size, size of instrumented crystal, etc.) the Compton camera portion of the project will still be discussed in detail. This novel method of event localization in bulk scintillators has immediate uses in nuclear security and potential uses in medical physics and astrophysics.

It should be stressed that while the overall goal and funding behind the project is to image nuclear sources using Compton imaging, locating an event to a small voxel in a crystal using a coded aperture is a novel method and the true focus of this dissertation. The technique represents a significant advance in detector physics technology in general and could significantly contribute to several other fields of research and technology. The work has proceeded in stages. An initial simulation study [13] was conducted prior to the work presented here and is briefly summarized in Chapter 4. Building on those, a physical one-dimensional prototype was developed, built, and analyzed in late 2012 and 2013. The final two-dimensional system was developed and built starting in late 2013 and through 2014. Both systems will be discussed in this dissertation.

In addition to the state of current event localization capabilities in bulk scintillator crystals, Chapter 2 gives background on the Compton camera as well as coded-aperture imaging. Chapter 3 discusses the theory of the technique under development. In Chapter 4, the experimental design including simulations, optical geometry, scintillator, and photo transducer selection are discussed. In Chapter 5, the physical setups including data acquisition systems and electronics of both the one and two-dimensional systems are discussed. In Chapter 6, the specifics of the imaging processes for each system, capabilities and results of each are discussed. Chapter 7 summarizes the results in the larger context of the field, and gives suggestions to improve future iterations of the work in this dissertation.

CHAPTER 2. BACKGROUND

2.1. INTRODUCTION

This section will present a background on gamma-ray imagers that have been used in the fields of astrophysics, nuclear security technology, and medical physics. Anger cameras were the first gamma-ray imagers, and will be presented first. Coded-aperture imagers soon followed and were a monumental advancement in gamma-ray imaging. While the use for this dissertation project of coded-aperture technology is different than has been used historically, the concepts are the same and the differences for this project will be addressed. Soon after coded-aperture imaging was developed, Compton cameras were developed, initially for gamma-ray astronomy; they were later used in medical imaging. Finally, positron emission tomography (PET) imagers will be discussed, as several advancements in the field are relevant to event localization in bulk scintillators.

2.1.A. ANGER CAMERAS

The first gamma-ray imagers were called scintillation cameras or Anger cameras [20]. Developed by Hal Anger in the 1950s and 1960s, these detectors were used for medical imaging. They consisted of a lead housing shielding a scintillator crystal coupled to several photomultiplier tubes (PMTs). The entrance to the scintillator crystal was a small pinhole aperture that allowed gamma-rays to enter and interact in the crystal. The event position was found by comparing the ratios of the PMT signals, which were output via a resistor divider network. The electronics read out the signal from the divider network and formed three signals that defined the event location in the scintillator in two dimensions. The event locations in the scintillator crystal created an image of sources in the field of view as the pinhole aperture limited the possible directions from which the gamma-rays reached the camera. The sources imaged were typically radioisotopes administered to medical patients. The imaging occurred at close range (< 1 m) to the cameras.

Since the development of the original Anger camera many advances in event localization capabilities have been made. Several changes to the aperture system have been responsible for improving the systems. Specifically, improvements in the spatial resolution of position-sensitive detectors have led to improvements in the image resolution of the Anger camera systems. Instead of a single aperture, many cameras now use a set of pinhole collimators as seen in Figure 2 [21].

This greatly increases the amount of radiation seen by the detector as opposed to a single pinhole collimator. After Anger cameras were developed, coded apertures were one of the next major imaging capabilities invented.

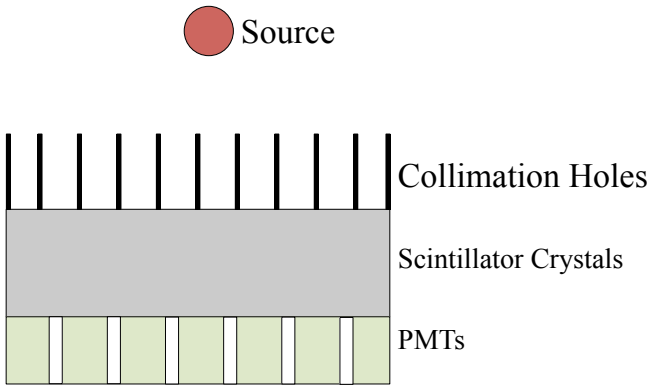

Figure 2. An Anger camera design with a collimator between the source to be imaged and scintillator. The amount of light seen by each PMT determines which section of the crystal the event occurs in. Advancements in PMTs have also impacted the ability to find the centroid of a distribution; they are discussed in Chapter 4.

2.2. CODED APERTURES

Coded apertures were originally designed for imaging with high-energy photons where focusing optics do not exist, and for application in the extreme far field such as in X-ray and gamma-ray astronomy. The original coded aperture was a simple pinhole camera expanded to a large number of randomly placed pinhole apertures [22]. Since then much advancement has been made with respect to mask patterns and reconstruction methods. This section will give an overview of the history and methods concerning coded-aperture technology.

2.2.A. PINHOLE APERTURES

The motivation behind using an aperture to image radiation-emitting sources comes from the fact that if a position-sensitive detector is used to try to image a source directly, no image can be obtained; any signal registered at the detector could have come from any part of the source [23].

If a pinhole aperture is used between the object and the detector, each recorded event can be traced back along a straight line to the source. This creates an inverted image of the object on the detector. For an ideal pinhole with an infinitesimally small area, the resolution is perfect but as no signal is able to pass through, the flux is zero [23]. As the pinhole area increases more photons are transmitted but the resolution degrades since multiple object locations are linked to each detector location. This results in a blurring of the object and thus a decreasing resolution as seen in Figure 3. Because of this, small aperture holes are preferred since they maintain good resolution. However, this means a fundamental compromise between flux and resolution is inherent in pinhole cameras.

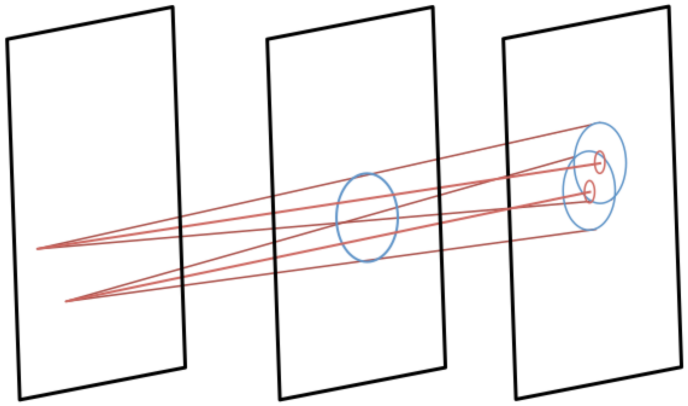

Figure 3. Adapted from [23]. As the aperture area is increased, objects close together become unresolvable.Thus, the resolution of the imager decreases with increasing aperture size.

2.2.B. CODED-APERTURE OVERVIEW

In 1968 R.H. Dicke developed a method based on pinhole aperture imaging to image gamma-ray sources with the goal of satisfying two conditions: the imaging system had high angular resolution, and the signal-to-noise ratio (SNR) was high enough to use it to image X-ray and gamma-ray sources that are typically weak relative to the background [22]. He was able to do this by using a mask between the source and the detector that contained many randomly placed aperture pinholes.

For a shadow mask pattern containing N pinholes, the detector contains N (overlapping) projections of the pattern. Relative to a single pinhole camera, using multiple pinholes can improve the SNR by approximately up to $\sqrt{N}$ [19].

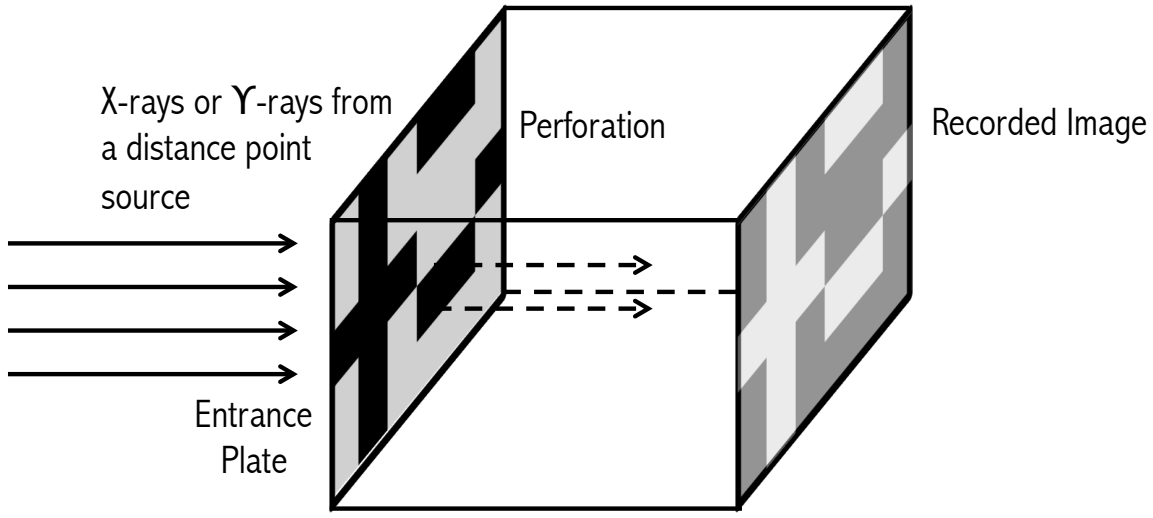

Figure 4. Adapted from [19]. Dicke's original design: the gamma-rays are incident on multiple aperture holes with each projecting an image onto a detector. The image is then decoded using statistical methods to obtain the image of the original object.

A basic coded-aperture system consists of a shadow mask that is located between a radiation-emitting source and a position-sensitive detector that records the projected image of the mask pattern. In the most common design the mask is larger than the detector. Depending on the location of the source relative to the mask, a different portion of the mask is projected onto the detector.

The coded-aperture imaging method works through the following: the radiation is incident on the shadow mask pattern and projects the pattern onto the detector where the projected pattern is recorded. Once the picture is recorded, the response is decoded using one of several available methods and a reconstructed image is obtained.

There are two goals when choosing a mask pattern: the autocorrelation function of the pattern (cross correlation with itself) should be a delta function, and the SNR of a point source among background radiation should be optimized [24]. A historical and technical review of shadow mask patterns will be presented after reconstruction methods are discussed.

In addition to imaging the source in the plane parallel to the mask pattern, the distance to a source can also obtained from the projected size of the pattern on the detector. It should be noted that this refers to locating the source as opposed to imaging a scene. This is most easily seen for a point source. For such a source at large distances (far-field or infinite approximation) from the mask pattern, the size of the projected shadow is uniform on the detector and independent of distance from the mask. When the source is closer, the size of the projected mask pattern depends on the distance; because of this the coded-aperture pattern contains information on the source-to-mask distance.

2.3. RECONSTRUCTION METHODS

There are several methods to reconstruct an image of a source from a function describing the shadow-mask pattern and the pattern recorded by the detector. For an object $\boldsymbol{S}$, an aperture function $\boldsymbol{A}$, consisting of a 1 for an open element and 0 for a closed element, the signal the detector sees, $\boldsymbol{D}$, is

$$\boldsymbol{S} * \boldsymbol{A} = \boldsymbol{D}$$

Eq. 1

where $*$ is the cross-correlation operator. It should be noted that $\boldsymbol{S}$, $\boldsymbol{A}$, and $\boldsymbol{D}$ are matrices. This operation can be described as a sliding dot product. It is essentially a measure of the similarity of two functions as one is moved along the other stationary function as shown in Figure 5. From the recorded pattern the goal of the reconstruction procedure is to obtain a reconstructed object $\widehat{\boldsymbol{S}}$ where $\boldsymbol{S} = \widehat{\boldsymbol{S}}$. If $\boldsymbol{S}$ is assumed to be a point source, then it would be represented by a delta function δ and equation Eq. 1 would become

$$\delta * \boldsymbol{A} = \boldsymbol{D} = \boldsymbol{A}$$

Eq. 2

This states that a point source is recorded onto the detector as a projection of the mask pattern [23].

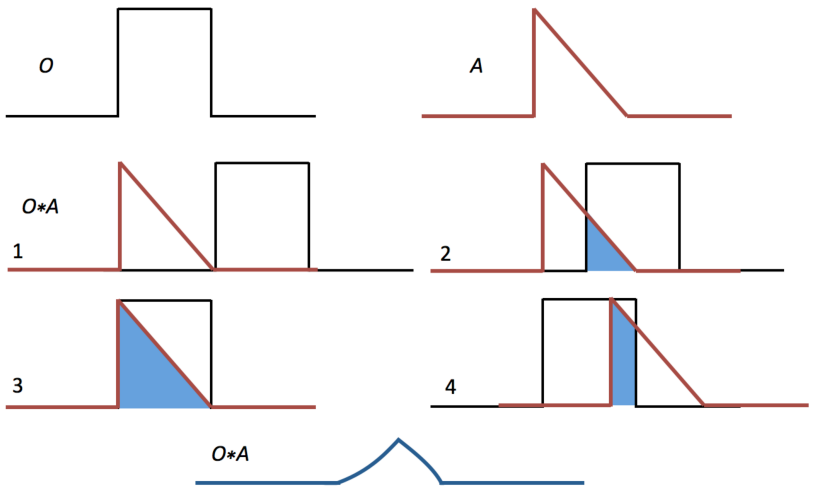

Figure 5. Adapted from [25]. For the cross correlation of O and A, the result is given by the blue value and final function by the blue line. The process follows steps 1, 2, 3, and 4 as shown above.

However, in a real system there will also be a noise term that contributes to ***D,*** and $\widehat{\boldsymbol{S}}$ will only be an approximation to ***S***. Deconvolution was an early reconstruction method. It found $\widehat{\boldsymbol{S}}$ by multiplying ***D*** by a deconvolution matrix based on Fourier transforms of ***D*** and ***A*** (*F(**D**)* and *F(**A**)*) with

$$\hat{S} = RF^{-1}\left[\frac{F(\boldsymbol{D})}{F(\boldsymbol{A})}\right] = S + RF^{-1}\left[\frac{F(\boldsymbol{B})}{F(\boldsymbol{A})}\right] \textit{[19]}$$

Eq. 3

where *R* is the reflection operator and ***B*** is any background noise captured in the detector. However, if *F(**A**)* has small terms, the reconstructed background will dominate the actual object. Fenimore and Canon determined that a significant number of the Fourier transforms of random

arrays possess at least one term, which is zero [19]. In general, binary arrays with large dimensions often possess small or zero terms in their Fourier transforms. Therefore the deconvolution reconstruction method is not a good method of image reconstruction.

If it is possible to construct a pattern and a chosen post-processing decoding pattern, $\boldsymbol{G}$, such that

$$\boldsymbol{A} * \boldsymbol{G} = \delta,$$

Eq. 4

then from Eq. 1, to find the reconstructed object

$$\widehat{\boldsymbol{S}} = \boldsymbol{D} * \boldsymbol{G} = R\boldsymbol{S} * (\boldsymbol{A} * \boldsymbol{G}) + \boldsymbol{B} * \boldsymbol{G}$$

Eq. 5.

If $\boldsymbol{A} * \boldsymbol{G} = \delta$ then $\widehat{\boldsymbol{S}} = \boldsymbol{D} * \boldsymbol{G} = \boldsymbol{S} + \boldsymbol{B} * \boldsymbol{G}$ and the reconstructed object is perfectly imaged apart from a background noise term. The cross-correlation method is the method this project will use, although additional methods are also presented in Section 2.3. Mask patterns that have been developed with the goal of $\boldsymbol{A} * \boldsymbol{G} = \delta$ will also be discussed in Section 2.4.

2.3.A. CROSS CORRELATION

Fenimore and Canon introduced the cross-correlation reconstruction method in 1978 [19]. This method follows directly from the discussion above. They developed mask patterns with the goal of satisfying Eq. 4. They used patterns called Uniformly Redundant Array (URA) mask patterns. They consist of a base-size mask pattern with the entire aperture made up of repeated cycles of the base pattern. For now, assuming such a mask pattern can be constructed, the reconstructed object is found by Eq. 5. The cross-correlation of two functions in discrete form is given by

$$(f * g)[n] = \sum_{m=-\infty}^{\infty} f[m]\, g[n+m]$$

Eq. 6

As one realistically deals with pixelated (discrete) PT, mask pattern, and reconstructed object arrays, from Eq. 6 the reconstructed object is given by

$$\widehat{\boldsymbol{S}} = \sum_{m} D_m G_{i+m}$$

Eq. 7

in the one-dimensional case. In the two-dimensional case, the reconstructed object is found by

$$\hat{S}(i,j) = \sum_{k} \sum_{l} D_{k,l} G_{k+i,l+j}$$

Eq. 8

where $\widehat{\boldsymbol{S}}$ is the constructed image, $\boldsymbol{D}$ is the recorded detector response, and $\boldsymbol{G}$ is the post-processing array. This is simply a sum over the detector through every base pattern size cycle of the mask post-processing array pattern. Again, this is explained more in a description of URAs in Section 2.4.

2.3.B. PHOTON TAGGING

Fenimore later developed a method using URA patterns that relied on tagging individual photons tracked through the mask pattern towards the source location [26]. This method assumes a detector that could record the position of a detected photon, the energy deposited and time of the occurrence. For a given window of time, recorded and decoded images are obtained. This method takes the recorded response and back projects each recorded photon through the known mask pattern, adding it to the source location if it encounters an open element [24]. If the number of detected photons is small relative to the number of mask elements in the entire coded-aperture mask, this is computationally faster than a cross correlation [24].

2.3.C. ITERATIVE METHODS

Iterative methods, such as maximum likelihood estimation method (MLEM) exist and have been successfully used [27] [28]. In the 1970s, the maximum entropy method was applied to X-ray astronomy. These methods work by solving for the $\hat{S}(i,j)$ distribution through statistical

approaches. One of the earliest methods developed by Frieden in 1972 [27] uses the fact that given a detector distribution, when reconstructing the source plane, the most likely result obeys a principle of maximum likelihood. This method defines constraints to the noise and object terms; they are that the number of objects is known through a measure of the total signal in the image and would require some calibrations, and that the image consists of spiked object signals defined by a given point spread function plus noise terms. Then, with the given constraints, a set of equations can be solved for the most likely source distributions. While effective, this is computationally intensive as opposed to deterministic methods. Additionally, errors cannot be propagated using this type of reconstruction method. For this dissertation in particular, due to the nature of it being a novel technique, a deterministic method was desired due to its reliability and simplicity.

2.4. MASK PATTERNS

There are two goals in designing coded-aperture shadow-mask patterns. The first is that the autocorrelation function (cross correlation of a function with itself) should result in a delta function. The second is that the SNR of the source to background should be optimized [24]. One early attempt at using several pinhole apertures was reported in 1973 by Wouters, Simon and Hirschberg [29]. They found that for an array of pinholes placed in a regular pattern with each pinhole an equal distance from its neighbors, the reconstructed [26] image shows artifacts because the autocorrelation function of the pattern is not peaked in only one location [29]. These artifacts occur as ghosts of the object in the reconstructed image resulting in a decoded image that has ambiguously positioned reconstructed objects [29]. To avoid these artifacts, an array is desired such that $\boldsymbol{A} * \boldsymbol{G}$ is a delta function. Non-redundant arrays (NRA) have the property that the autocorrelation of the mask pattern results in a central spike with non-zero side lobes out to a distance L, and zero beyond that distance [19]. For an NRA the separations between a single pinhole and every other in the pattern are a different distance out to L (the maximum separation). As this results in a single peak in the autocorrelation of the pattern and thus no inherent noise, it also makes generating patterns difficult as the pattern can only have a limited number of holes [19]. Additionally, since the side lobes are not equal to a constant value everywhere, this results in noise in the reconstructed object that would otherwise not exist if the side lobes were either constant everywhere or zero. Thus, an NRA pattern is not an ideal pattern without any further

modification due to the non-equal side lobe characteristics.

2.4.A. CYCLIC DIFFERENCE SETS

A sequence called a cyclic difference set is a one-dimensional set of integers that satisfies the autocorrelation condition (Eq. 4) [24]. Because of this, these sets form ideal coded-aperture mask patterns. The sets are defined as a set *D* with *k* positive numbers $\{a_1, a_2, \dots, a_k\}$ each less than a value *n*, where all differences in the set modulo *n*[1]

$$(a_i - a_j) mod\ n \text{ for } i \neq j$$

Eq. 9

are different values with the set having *z* of these values [30]. The number *n* is the modulus of the set *D* and *s* is the size of the set. An example of a cyclic difference set is *{0, 1, 2, 4}* with *n = 7, k = 4,* and *z = 2.* This set can be represented by a binary sequence by assigning a *1* in the binary set if that integer is included in *D* and a *0* if it is not; i.e. *1110100.* The autocorrelation of this set is given by

$$c_l = \sum_{i=0}^{n-1} a_i a_{(i+l) mod\ n}$$

Eq. 10

$$c_l = k, \text{ if } l\ mod\ n = 0$$

Eq. 11

$$c_l = z = \frac{k(k-1)}{n-1}, \text{ if } l\ mod\ n \neq 0$$

Eq. 12

For a cyclic difference set these values results in a single peak and a flat background; i.e., the autocorrelation is a delta function. Among cyclic difference sets several variations exist. From

[1] $a \equiv b(mod\ n)$ means $a - b$ is an interger multiple of *n*.

the autocorrelation function it can be seen that the largest difference between k and z will maximize the SNR. One subset of the cyclic difference sets is called Singer sets [24]. These sets generally have much smaller fractions of open (*1*) elements to closed (*0*) elements. This makes them undesirable for coded-aperture imaging as the source is generally weak so a mask with near 50% open elements is desired to maximize the detected signal. Another cyclic difference set subset are called Hadamard difference sets [24]. Hadamard sets have the feature that $k = (n - 1)/2$, meaning they contain close to half open elements. For these sets, D, where $t = z + 1$, the maximum difference between k and z is when $n = 4t - 1$ and $k = 2t - 1$ [31]. There are three types of Hadamard difference sets: quadratic residue sets, twin prime sets, and pseudo-noise sets [30]. Quadratic residue sets are when n is a prime number. Twin prime sets have $n = p(p+2)$ where p and $p + 2$ are prime. Pseudo-noise sets have $n = 2^m - 1$ where $m > 1$ and is an integer. Some sets belong to multiple classifications.

Most notably, Calabro and Wolf have done work to create two-dimensional arrays of dimensions r by s based on cyclic difference sets [32]. These sets are characterized according to the value of $|r - s|$. Different values of $|r - s|$ result in different features of the sets; for $|r - s| = 0$, the autocorrelation function of the set is not a delta function and the pattern is square; these sets are quadratic residue arrays [33]. For $|r - s| = 2$ the pattern is no longer square but the autocorrelation function is a delta function. This is called a twin-prime array. Note that cyclic difference sets are defined as one-dimensional sequences, so while in the 1-D case the quadratic residue sets are a subset of cyclic difference sets, the 2-D case is not. This language is differentiated by the 1-D case being called a quadratic residue set and the 2-D case being called a quadratic residue array. These two sets are the basis of modern coded-aperture patterns and this work will focus on these cases.

2.4.B. ONE-DIMENSIONAL URA PATTERNS

The one-dimensional construction of URA patterns uses the pseudo-noise sets, which are subsets of Hadamard sets [19] [32] [34]. For these sequences the autocorrelation function of the set is a delta function, making the post-processing array simple to construct directly from the mask pattern $A(i)$. For an integer $m=1, 2, 3, ...$ the mask length is given by

$$L = 4m + 3$$

Eq. 13

The mask pattern is constructed with

$$A(i) = 0, \text{ if } i = 0.$$
$$A(i) = 1, \text{ if there exists an integer } 0 < x < i \text{ such that } x^2 = i \ (mod\ L).$$
$$A(i) = 0, \text{ otherwise.}$$

Only if $A_0 = 1$ is a URA pattern generated; thus, the URA patterns only exist for certain values of *m* [34]. The decoding array is given by *G(i)* where

$$G(i,j) = 1, \text{ for } A = 1.$$
$$G(i,j) = -1, \text{ for } A = 0.$$

Because the autocorrelation function of the pseudo-noise sets is a delta function [33], $\boldsymbol{A} * \boldsymbol{G} = \delta$ is satisfied. To make a larger pattern, the base pattern can be repeated to as many cycles as desired (each of length *L*). In URA patterns the number of elements between open elements in the pattern occur only once per base pattern [19]. As these patterns are based on Hadamard sets they are about 50% open, making them useful for coded-aperture imaging.

2.4.C. TWO-DIMENSIONAL URA PATTERNS

Fenimore and Canon used the factorization of the pseudo-noise sets into two-dimensional arrays to make patterns of size *r* by *s* where $|r - s| = 2$ [33]. The mask pattern *A(i,j)* is given by

$$A(i,j) = 0, \text{ if } i = 0,$$
$$A(i,j) = 0, \text{ if } j = 0,\ i \neq 0,$$
$$A(i,j) = 1, \text{ if } C_r(i)C_s(j) = 1,$$
$$A(i,j) = 0, \text{ otherwise.}$$

where

$$C_r(i) = 1, \text{ if there exists an integer } 0 < x < r \text{ such that } x^2 = i(mod\ r), and$$
$$C_s(i) = 1, \text{ if there exists an integer } 0 < x < s \text{ such that } x^2 = i(mod\ s).$$

The post-processing array $\boldsymbol{G}$ is defined as

$$G(i,j) = 1, \text{ for } A = 1, and$$
$$G(i,j) = -1, \text{ for } A = 0.$$

This satisfies the desired condition of $\boldsymbol{A} * \boldsymbol{G}$ being a delta function with no sidelobes [19]. An example of a URA (rank 19) and a pictorial delta function are shown in Figure 6.

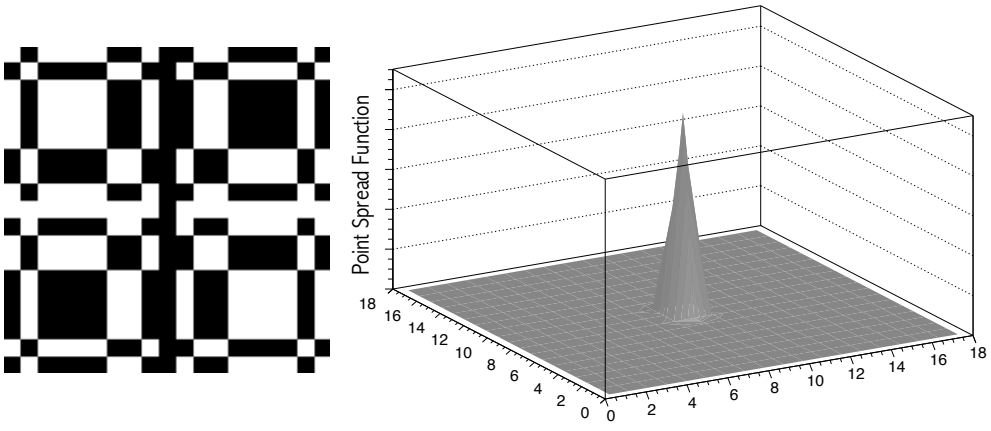

Figure 6. A 19 x 19 coded-aperture URA pattern and its autocorrelation function.

2.4.D. ONE-DIMENSIONAL MURA PATTERNS

While URA patterns use pseudo-noise sets to create the mask array, Fenimore and Canon developed another type of array using another subset of cyclic difference sets; quadratic residue sets. While the autocorrelation function of these patterns is not itself a delta function, a modified post-processing array can be used that results in the desired $\boldsymbol{A} * \boldsymbol{G} = \delta$ property [34]. For a mask pattern length L that is a prime number, a modified uniformly redundant array (MURA) pattern can be generated in lengths

$$L = 4m + 1,\ m = 1, 2, 3, \ldots.$$

Eq. 14

To construct this pattern the same method is used as in the one-dimensional URA patterns. If $L = 4m + 3$ and $A_0 = 1$ it is a URA; otherwise it is a MURA [32]. However, the decoding function is changed to

$$G(i) = 1, \text{ if } i = 0;$$
$$G(i) = 1, \text{ if } A(i) = 1,\ i \neq 0;$$
$$\text{and } G(i) = -1, \text{ if } A(i) = 0,\ i \neq 0.$$

Eq. 15

This adjustment to the post-processing array results in the required delta function property. Fenimore and Canon computed these binary patterns for several lengths; the first few are length 5, 13, 17, 29, and 37 [34].

2.4.E. TWO-DIMENSIONAL MURA PATTERNS

The one-dimensional quadratic residue sets can be expanded to produce quadratic residue arrays [33]. For these arrays of dimensions r by s, $|r - s| = 0$. The MURA patterns are constructed in the same way as the two-dimensional URA patterns but they are square patterns. Fenimore and Canon used post-processing arrays slightly different than for the URA patterns to give $\boldsymbol{A} * \boldsymbol{G} = \delta$. *G(i,j)* is now found by

$$G(i,j) = 1, \text{ if } i + j = 0;$$
$$G(i,j) = 1, \text{ if } A(i,j) = 1,\ i + j \neq 0; \text{and}$$
$$G(i,j) = -1, \text{ if } A(i,j) = 0,\ i + j \neq 0.$$

Eq. 16

These patterns, with the adjusted decoding function, have ideal imaging properties like the URA patterns.

2.4.F. GEOMETRIC MASK PATTERNS

In 1983 geometric coded-aperture mask patterns were introduced [35]. These masks are based on regular geometric patterns and are easier to construct than a URA pattern of similar element size. However, unlike URA patterns, they are generally less than 50% open and do not possess the autocorrelation property.

2.4.G. BIQUADRATIC AND DILUTE URAS

One class of mask patterns was developed to benefit from features of both URAs and NRAs [36]. URA patterns have a peak-to-side lobe ratio as defined by the autocorrelation function of about 2:1 and MURAs of about 4:1 [36]. NRA patterns have better peak-to-side lobe ratio outside of a distance L, where L is the maximum distance between any opening and another in the pattern. Dilute URAs were developed to possess good peak-to-side lobe ratio but have side lobes that are flat everywhere but the peak. These patterns are based on Barker codes [37]. The arrays have autocorrelation peaks equal to the number of open areas N and side lobe values of unity. Thus, large peak-to-side lobe ratio can be achieved for patterns with large N. While effective in maximizing the peak signal in the autocorrelation function, the known patterns have much lower ratios of open to closed elements as the length of the pattern is increased. The length of the known patterns is given by $N(N-1)+1$ [36]. This makes these patterns impractical for an optical coded-aperture application with very little light.

2.5. SIGNAL-TO-NOISE RATIO OF CODED APERTURES

Fenimore and Canon derived the SNR of both URA and MURA patterns [34] [38]. They concluded that the SNR of the coded-aperture system is dependent only on the post-processing array $\boldsymbol{G}$ and not which of the two types of aperture pattern is used [38]. Thus, the derivation of the SNR for both patterns is the same. Traditionally, the SNR of a system is defined as the ratio of the power of the signal to the power of the background noise. The SNR of a coded-aperture system is the ratio of the height of the source peak to a selected noise term [38]. The most basic definition would be the variance in the reconstructed peak height intensity. As seen in Figure 7 the integrated signal of the reconstructed peak is very large relative to the fluctuation in the peak height. Thus, the SNR will be defined on a point-by-point basis and will be given by the ratio of the strength of the reconstructed object at the location of the source over the standard deviation

of the reconstructed object at that point [34]. The SNR is then given by

$$SNR(i,j) = \frac{E(S_{i,j})}{\sigma(\hat{\boldsymbol{s}})} \text{ [38]}$$

Eq. 17

where $E(S_{i,j})$ is the expected value of the *i,j* point in the reconstructed object. This is given by $E\left(S_{i,j}\right) = NS_{i,j}$ where *N* is a normalizing factor.

In the following discussion the indices *i,j* indicate the reconstructed image coordinates near the reconstructed source peak, *k,l* indicate any other arbitrary point in the entire reconstructed image plane, and *u,v* indicate the detector array. Additionally, an upper index denotes an array function instead of a specific element of an array. Fenimore's derivation uses the cyclic nature of the pattern, so an offset of *r* by *s* is a cyclic permutation of the original pattern [38].

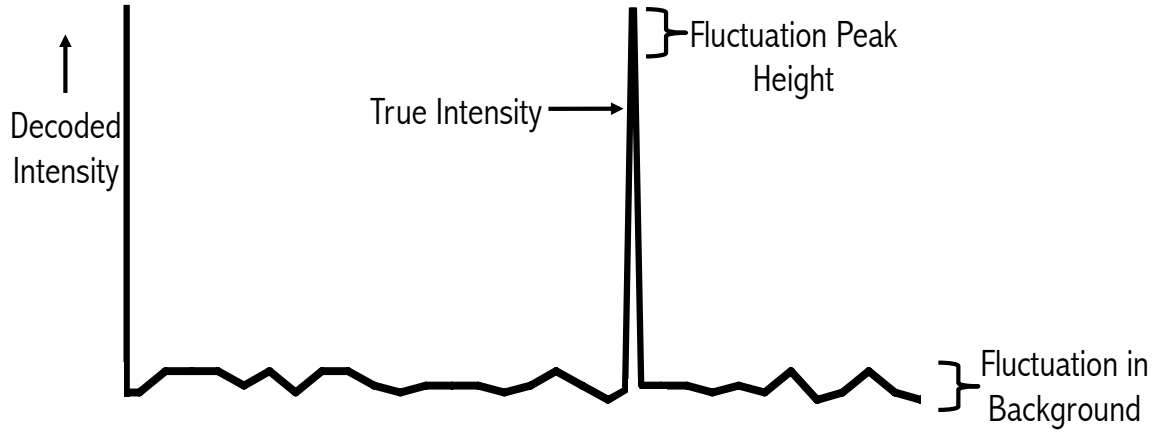

Figure 7. Adapted from [38]. A one-dimensional typical reconstructed point source against the background.

First the standard deviation of the reconstructed object needs to be derived. The total variance

is given by

$$\sigma(\hat{S}_{i,j}) = \sqrt{var(S_{i,j}, \hat{S}_{i,j}) + \sum_{kl} var(S_{k,l}, \hat{S}_{i,j}) + var(\boldsymbol{B}, \hat{S}_{i,j})}$$ [38].

Eq. 18

The first term is the variance in the determination of $\hat{S}_{i,j}$. The second term is the variance of the reconstructed source due to all other sources within the field of view and the final term is the variance due to the background $\boldsymbol{B}$ [38].

To calculate the first term, the contribution of the $S_{i,j}$ element to $\hat{S}_{i,j}$ must be found. The recorded picture from an element of the source $S_{i,j}$ is given by the source modulated with the mask pattern, or $S_{i,j}A_{i,j}$. The contribution from $S_{i,j}$ to $\hat{S}_{i,j}$ is given by the elements of the decoder pattern that align with the recorded detector elements, or

$$(S_{i,j}\hat{S}_{i,j}) = \sum_{u}\sum_{v} P_{u,v}^{i,j}\ G_{u,v}^{i,j}$$

Eq. 19

This is a weighted sum of the elements in the detector array [38]. As the system follows Poisson statistics, the expected value is given by the expected value of the detector array times the sum of the weighting coefficients ($\boldsymbol{G}$), so

$$E(S_{i,j}\hat{S}_{i,j}) = S_{i,j}\sum_{u}\sum_{v} A_{u,v}^{i,j}\ G_{u,v}^{i,j}$$

Eq. 20

The second term is given by the variance from all other sources in the field of view (the entire detector response). The entire field of view is given by the indices *k* and *l*. Fenimore then uses the definition of the height of the sidelobes in a URA pattern to show that

$$\sum_{k,l} var(S_{k,l}, \hat{S}_{i,j}) = [D * G^2]_{i,j} = [(S * A) * G^2]_{i,j}$$ [34] [38].

Eq. 21

This term indicates that sources other than $S_{i,j}$ contribute to the variance of the reconstructed source [34].

The final term is given by the background with the weighting function, and again Fenimore uses the value of the height of the sidelobes of a URA pattern to find that

$$var\left(\boldsymbol{B}, \hat{S}_{i,j}\right) = (B * G^2)_{i,j}$$ [34].

Eq. 22

The first term's contribution to $\sigma\left(\hat{S}_{i,j}\right)$ is only dependent on the source itself. The second term adds contributions from other sources for which the detector records mask projections [34]. As each term is weighted by the square of $\boldsymbol{G}$, to ensure that the source contributes uniformly to the noise regardless of position, Fenimore and Gottesman concluded it is the best choice to have all values of $(G_{ij})^2$ be equal to make sure each source uniformly contributes to the noise. Thus, $\boldsymbol{G}$ is either 1 or -1.This is true for both URA and MURA patterns as defined above.

To understand the SNR result further, the peak intensity is normalized to the number of open elements in the aperture

$$N = \sum_{i,j} A_{i,j}$$

Eq. 23

The cross correlation of $\boldsymbol{A}$ with $\boldsymbol{G}$ becomes

$$\boldsymbol{A} * \boldsymbol{G} = N\delta$$

Eq. 24

The reconstructed image becomes

$$\hat{S}_{i,j} = NS_{i,j} + (B * G)_{i,j}$$

Eq. 25

The first term under the radical in the denominator of the SNR (Eq. 18) simplifies using N and the fact that each term of $\boldsymbol{A}$ is aligned with $\boldsymbol{G}$. Then, $E(S_{i,j}\hat{S}_{i,j}) = NS_{i,j}$ and using Poisson statistics

$$var\left(S_{i,j}, \hat{S}_{i,j}\right) = NS_{i,j}.$$

Eq. 26

Because $\boldsymbol{G}$ is unimodular and all $(G_{i,j})^2$ are equal, Eq. 21 can be reduced to

$$\sum_{k,l} var(S_{k,l}, \hat{S}_{i,j}) = N \sum_{k,l} S_{k,l} \text{ [34]}.$$

Eq. 27

The final term can be simplified using the fact that for URA and MURA patterns $\boldsymbol{G}$ is unimodular [34]

$$var\left(\boldsymbol{B}, \hat{S}_{i,j}\right) = \sum_{u,v} B_{u,v}$$

Eq. 28

This term is the sum of the background over the whole detector. The SNR now can be written as

$$SNR_{i,j} = \frac{NS_{i,j}}{\sqrt{NS_{i,j} + N \sum_{k,l} S_{k,l} + \sum_{u,v} B_{u,v}}} \text{ [34]}.$$

Eq. 29

This expression applies to both URA and MURA patterns. The only assumption made is that all values of $(G_{ij})^2$ are the same value. In the case of URA and MURA patterns used $(G_{ij})^2 = 1$. The expression can be explained conceptually by further examining each term. The numerator is the number of reconstructed counts emitted by the i,j element of the source. $N \sum_{k,l} S_{k,l}$ is the total number of counts reconstructed of all sources not located at i,j recorded by the detector, and

$\sum_{m,n} B_{m,n}$ is the total background recorded [34]. Thus, the two latter denominator terms are the total number of recorded counts in the detector. The SNR can then be written as

$$SNR_{i,j} = \frac{net\ source\ counts}{\sqrt{net\ source\ counts + total\ detector\ counts\ not\ at\ i,j}}$$ [34].

Eq. 30

It should be noted that the counts from the source at *i,j* are not being counted twice. This provides a simple and useful expression to calculate the SNR of the reconstructed image.

In addition to this derivation, another expression was derived in 2014 [39] for the uncertainty on a single image pixel. An image pixel value $I_{i,j}$ is given by the standard cross-correlation reconstruction

$$I_n = \sum_i G_{n,i} D_i.$$

Eq. 31

From standard error propagation, the uncertainty on an image element is given by

$$\sigma_{I_n}^2 = \sum_i \left(\frac{\partial I_n}{\partial G_i}\right)^2 \sigma_{G_i}^2 + \sum_i \left(\frac{\partial I_n}{\partial D_i}\right)^2 \sigma_{D_i}^2$$

Eq. 32

The first term is zero because each term in *G* is a constant. For the second term, each partial derivative is equal to $G_{n,i} = \pm 1$ [39] for a given image pixel. The errors for each detector pixel are given by Poisson statistics, so since $\sigma_{D_i} = \sqrt{D_i}$, then $\sum_i \sigma_{D_i}^2 = N_{total}$, where N_{total} is the total number of counts in the detector from a source and background [39]. The uncertainty on a single pixel is then

$$\sigma_{I_n}^2 = N_{total}$$ [39].

Eq. 33.

2.5.A. CODED-APERTURE SYSTEM GEOMETRIES

There are several possible coded-aperture geometries that can be chosen for a coded-aperture detector system. The most fundamental requirement for an imaging system's geometry is that the detector for each event captures a full cycle of the shadow pattern. The most basic arrangement is a detector that is the size of one full mask cycle. In the far-field case a source at infinity projects a mask pattern that is the same size as the mask pattern. In the near field case the projected mask pattern is always larger than the physical mask pattern so the detector needs to be large enough to record the full projected mask pattern. Other than this difference, the two cases are similar and the discussion will be introduced for the case of a source at infinity. Note that for both figures in Figure 8, the source is indeed at infinity; a shift laterally is what causes the lateral shift of the recorded pattern.

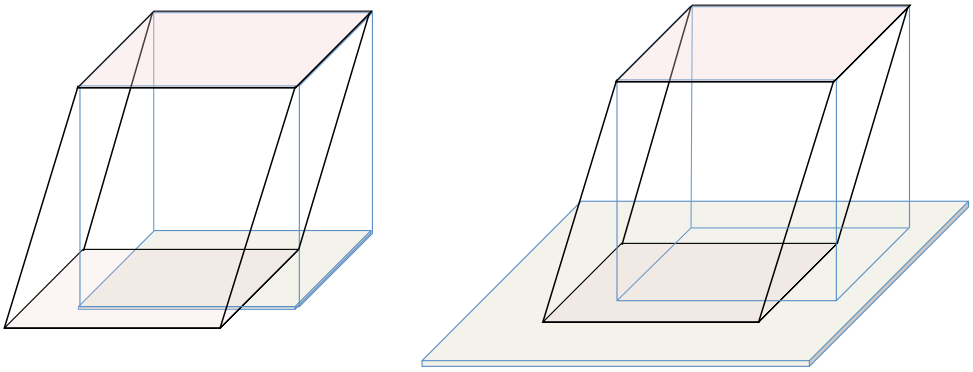

Figure 8. Adapted from [23]. (Left) In this geometry the detector (gray) is the same size as the mask pattern (red). When the projected pattern (red at the bottom green detector plane) is not aligned with the detector, a full cycle cannot be captured. (Right) The detector is larger than the magnified pattern. This geometry ensures a full cycle is captured even when the source does not project a pattern centered on the center of the detector.

A third option of detector geometry is to use a mask pattern consisting of repeating base

pattern cycles paired with a large detector area (Figure 9). This ensures a full mask pattern base cycle is always projected on the detector for a wider field of view making reconstructing an image possible for a much larger range of object locations. However, the reconstruction will include multiple repetitions of the source image. Hence, with this configuration the object must be coarsely localized to the correct mask cycle to ensure it is not reconstructed within the wrong cycle, in turn finding the absolute position shifted by the physical size of one projected cycle. Again, this setup is for a source at infinity. The wider field of view allows for a wider lateral view of the source field.

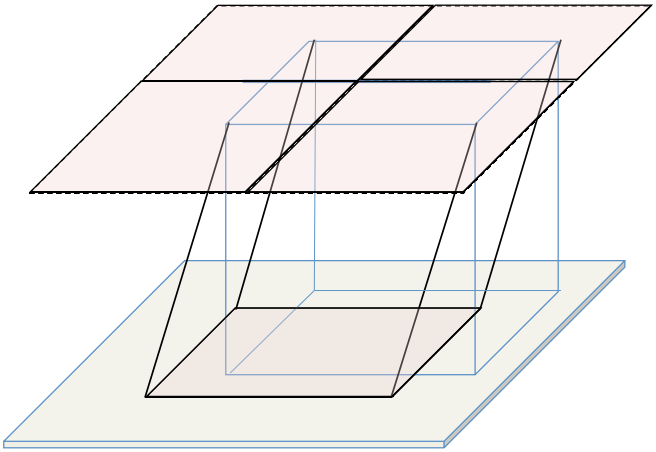

Figure 9. Adapted from [23]. The dashed outline is the large repeated mask cycle with each smaller square containing a base pattern. The detector needs to only capture one full cycle to reconstruct an image as shown in Figure 8 (left). Each red square represents one cycle of the pattern; thus, a full cycle is always captured which gives enough information for image reconstruction.

2.6. CODED-APERTURE FIELD OF VIEW (FOV)

In the system geometry shown in Figure 8 (left) only a source located at the center of the mask pattern at infinity would be able to be imaged [23]. This is because an object slightly off center would project part of the mask pattern outside of the detector area. Thus the FOV is limited to

one point. In the second arrangement the larger detector area allows for a wider FOV. This is also true of the arrangement shown in Figure 9.

In the near field the FOV is different than for a source at infinity because the size of the magnified pattern on the detector varies with the distance from the object to the mask pattern, as seen in Figure 10.

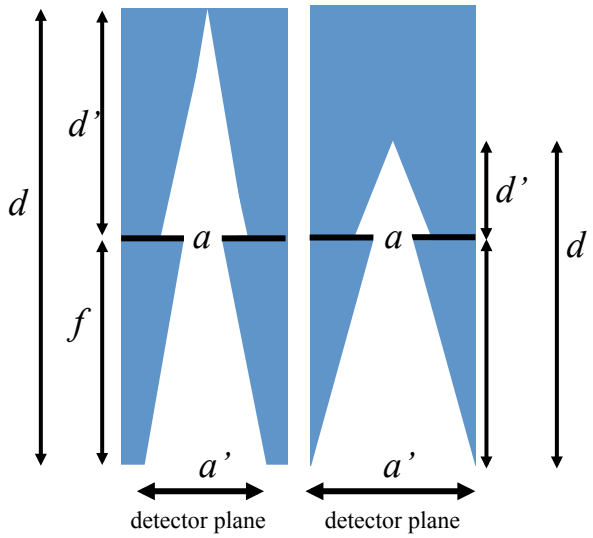

Figure 10. For an event in the near field at a distance d from the detector and d' from a mask feature opening, the magnified feature size of the mask feature on the detector is a'. An event farther away from the mask opening will project a smaller magnified feature size onto the detector at a fixed f (focal length).

First, as seen in Figure 10, defining the magnification of the mask pattern onto the detector to be

$$m \equiv \frac{a'}{a} = \frac{d}{d-f} = 1 + \frac{f}{d'}$$

Eq. 34

where *d* is the distance from the detector to object, *d'* is the distance from mask to object, *f* is the distance from the detector to the mask plane, *a* is the size of a mask pattern element and *a'* is the projected (or magnified) size of a mask element on the detector.

In order to calculate the *FOV*, concepts from a simple pinhole camera are needed. As seen in Figure 11, for an object a distance *d'* from a pinhole aperture and an image plane *f* from the pinhole, the size of the projected object with a height h_i is given by

$$m_{object} \equiv \frac{h_i}{h_o} = \frac{f}{d'} .$$

Eq. 35

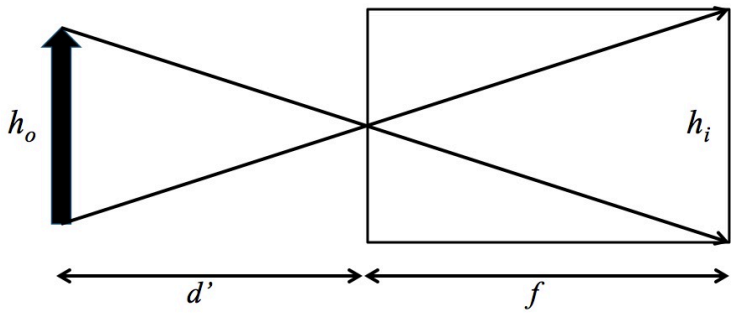

Figure 11. An object magnified through a simple pinhole camera. The ratio of the size of the projected object to the object is found using the distances between the object and pinhole aperture, d', and distance from the aperture to image plane, f.

Using the distances to express the object magnification to the mask magnification

$$m = m_{object} + 1 .$$

Eq. 36

In the configuration shown in Figure 12, defining the length of a mask on each side (for a square pattern) d_{mask} and the detector length on a side as d_{det} the projected mask pattern has a size of

$$md_{mask}$$ [23].

Eq. 37

Thus in the arrangement in Figure 8 (right), the size of the projected object (assumed to be a point source) subtracted from the full detector length is

$$d_{det} - md_{mask}$$

Eq. 38

and on each side is

$$(d_{det} - md_{mask})/_2$$ [23].

Eq. 39

The *FOV* can be found from the diagram in Figure 12 (adapted from [23]). The *FOV* is given by

$$\frac{FOV}{2} = \frac{(\frac{d_{det} - md_{mask}}{2})}{f} \cdot d'$$

Eq. 40

Substituting Eq. 34 we arrive at

$$FOV = \frac{d_{det} - md_{mask}}{m-1}$$ [23].

Eq. 41

As seen in the above equation, for a detector where the magnified mask pattern is equal to the size of the detector, the field of view is limited to a point source at the center of the mask pattern.

Thus, other geometries such as repeated mask cycles are more desirable.

Figure 13 shows the *FOV* for a repeated mask pattern with a base pattern in the center and half a base pattern on each side. The *FOV* is a range where a full projected base cycle is captured by the detector pattern.

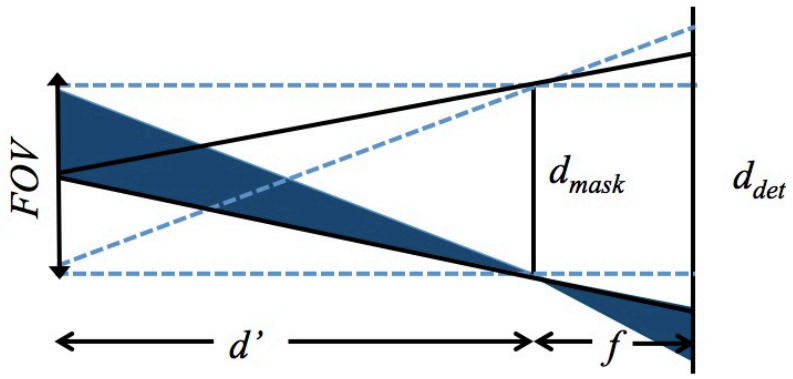

Figure 12. The field of view of an object a distance d' from the mask plane.

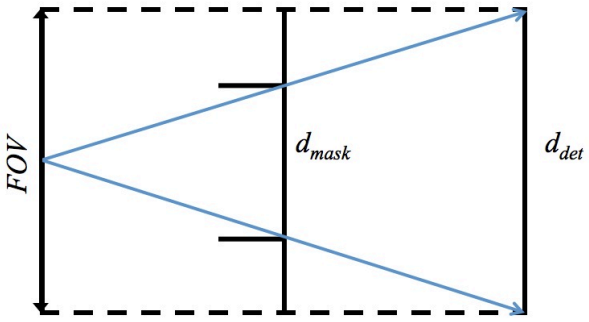

Figure 13. Adapted from [23]. A center base pattern and two half-cycle patterns repeated around the center.

Every point in the *FOV* magnifies a full mask cycle onto the detector. This *FOV* is given by

$$FOV = \frac{d_{det}}{m-1}$$ [23].

Eq. 42

This FOV is larger than the non-repeating pattern. The repeated pattern geometry is thus more desirable to maximize the FOV of the detector.

2.7. CODED-APERTURE RESOLUTION

The resolution of a coded-aperture system depends on the coded-aperture individual element sizes, the detector-to-mask distance, and the detector-to-source distance (i.e. detector to object). The reconstructed resolution in the x and y directions, e.g. parallel to the mask pattern plane, can be found using the arc length formula for a segment of a circle as seen in Figure 14. From the arc length formula, the size of the mask element at the mask plane as seen from the detector plane as a function of the focal length and opening angle for a single mask element *a* is

$$a = f\theta$$

Eq. 43

and

$$\delta x = d(\theta) = d\left(\frac{a}{f}\right).$$

Eq. 44

In practice *a* and δx are flat and not curved as in the case of an arc length calculation, but the distances *f* and *d* are much greater than *a* and δx, so the approximation may be used. Optimizing the image pixel size is an important design consideration for the overall system.

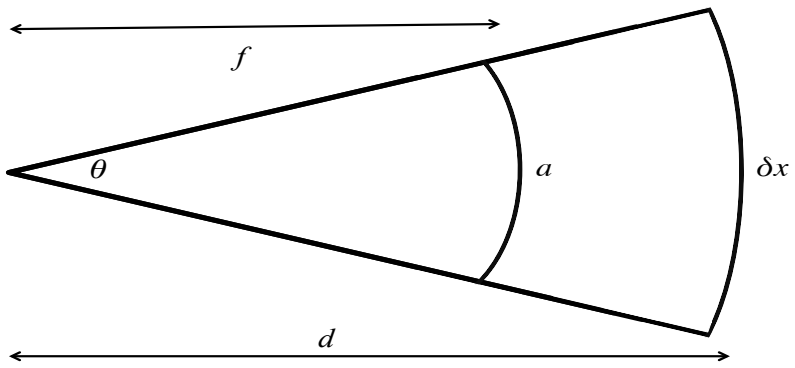

Figure 14. The ratio of the opening angles at the object and reconstructed image arc length can be used to calculate the image pixel size. Because of the size of the mask elements relative to the size of the system the small angle approximation can be used.

2.7.A. CODED APERTURES IN THE NEAR FIELD

As coded-aperture technology and its applications have been primarily developed for the far field, little work has been done to investigate the extreme near field effects that apply to the work in this dissertation. Accorsi [40] investigated near field artifacts of gamma-ray coded-aperture imaging that arose from two causes. First, for a thick object only a single plane is constructed in focus so the other planes of the object contribute to a blurring of the overall image. Second, for gamma-rays incident on the mask pattern at non normal angles Accorsi found that artifacts exist depending on where in the field of view the object was located. Accorsi investigated the first issue experimentally and in simulations, and found that the depth resolution was about one order of magnitude worse than the lateral dimension. However, this result does not arise from an analytical evaluation and was not found to be valid in the work presented here as will be shown in the results in Chapter 6.

For the second case, the changing field of view results in artifacts due to a shift in the mask

pattern as it is projected onto the detector. This problem does not pertain to the work in this dissertation; the mask pattern chosen is many more than two repetitions of a base cycle and the imaging always begins around the approximate center of the event using a coarse event localization technique that is discussed in Sections 3.3.A., 4.6, and 4.7. However, to address the problem for his work, Accorsi developed a mask and anti-mask imaging technique to lessen the effects of these artifacts. It should be noted that while the most dominant near-field artifacts were found from centering in the FOV, another less dominant artifact was found to be due to the self-collimation of the mask transmission rate of the gamma-rays. Again, as the work in this dissertation deals with opaque mask patterns for visible light this does not apply.

Accorsi notes that the $\boldsymbol{A}$ and $\boldsymbol{G}$ matrices (defined above in this chapter) have the same ideal correlation properties as the negatives of the matrices, $1\text{-}\boldsymbol{A}$ and $\boldsymbol{G}$. Thus, when an image is reconstructed using these negatives the reconstructed object does not change sign. However, the first and second order artifacts he mentions (due to the FOV and mask transmission) only depend on $\boldsymbol{G}$, so when using the anti-mask imaging method "the artifacts change sign while the image does not" [40]. Taking both images and adding the two cancels the observed artifacts and helps to create a cleaner reconstructed object.

While the artifacts observed by Accorsi do not apply, the near-field case does, however, produce other complications for this work. For a light spot incident on a mask pattern, the size of the light spot relative to the base cycle size of the mask pattern impacts the imaging. Additionally, the indices of refraction for the materials used in the physical system have effects on the imaging. These effects are discussed in detail in Section 3.4.B.

2.8. CODED-APERTURE APPLICATIONS

Historically, coded apertures have been used for gamma-ray and neutron imaging systems in medical physics, astronomy, and national security applications. However, no work has been done applying the concepts of coded apertures to optical imaging for event localization within a bulk volume as this work does. Until this work the mask patterns block the gamma-rays emitted by the source instead of the light produced by the gamma-rays in scintillator crystals. This section will provide an overview of previous coded-aperture applications and their results.

The earliest uses of coded-aperture imaging were in astronomy and medical physics applications [41]. The first mask patterns were Fresnel zone plates that are a circular pattern with

alternating rings of materials transparent and opaque to incoming radiation. This design was used by Mertz and Young to image X-ray stars. Soon after the coded-aperture technique was applied to medical physics.

2.8.A. CODED APERTURES IN MEDICAL PHYSICS

The earliest uses of pinhole-coded apertures (an aperture pattern of randomly placed pinholes that are transparent to gamma-rays with the non-open areas opaque to gamma-rays) in medical physics applications were in the mid 1970s [41] [42] [43]. In one of the first detectors, a multi wire proportional chamber [6] was combined with a random pinhole aperture pattern and used to image the human thyroid [41]. The energies of the imaged gamma-rays were 30 and 60 keV. The coded-aperture mask was made of 1.5 mm of lead in order to block the gamma-rays. For test point sources the lateral resolution was close to 3 mm while the depth resolution was 19 mm. While this imager was able to achieve good spatial resolution, the background signal was difficult to disentangle from the reconstructed image, thereby limiting the imager's effectiveness. Around the same time, a similar system based on a non-redundant array was used to image both human and canine hearts [42]. The X-ray source was moved to different points around the objects and the image was recorded using the shadowed X-ray signal on a diaphragm. This imager was able to distinguish between layers of the objects about 1 cm apart [42]. Still, background effects were problematic and hurt the resolution [42]. Another coded-aperture imager was developed for medical imaging applications that used a dual-plate time-coded aperture [43]. The way this worked was an aperture with multiple pinholes was stepped across a larger aperture plate. Each pinhole in the larger plate has an image that is decoded with the known aperture pattern of the smaller plate. For objects 4, 8, and 12 cm from the aperture plane, the lateral and depth resolutions were 4.2 mm, 12 mm, and 6.2 mm; and 17 mm, 8.2 mm, and 25 mm, respectively [43]. While the lateral resolution was an improvement over prior techniques, the depth resolution was still large relative to the geometry of the imager.

Lanza and Accorsi at MIT made a significant advancement in coded-aperture imaging in 2001 [44]. This was the first study to investigate the near-field applications of coded apertures and understand the properties and is discussed in previous sections in this chapter. The imager was designed for 140-keV gamma-rays. The mask plane was made of tungsten as it has excellent attenuation properties for radiation at the energy of interest. As the mask pattern was a physical

piece of tungsten, the pattern had to have no two holes touching. Thus, a MURA pattern was chosen and modified by inserting a constant number of opaque rows and columns between all of the rows and columns [44]. The imager had a field of view of 9 x 9 cm^2 and obtained lateral resolution of 1.67 mm with a depth resolution of 1 cm. This was a significant improvement, particularly in the lateral dimension.

2.8.B. CODED APERTURES IN ASTROPHYSICS

Coded apertures were originally applied in the medical field, but much of their technological advancement came from astronomical applications [45]. In the 1960s, after the earliest solar X-ray studies, higher resolutions were desired to image astrophysical objects [46]. In 1985 one of the earliest and most successful applications of coded-aperture imaging was developed for imaging the galactic center [46]. This was done using a dual coded-aperture system flown on the Spacelab 2 mission in the summer of 1985. Two aperture masks were used to give two resolutions of the imaged object. The coarse system was able to achieve an angular resolution of 12 arc min and the fine system an angular resolution of 3 arc min. The energies of the X-rays imaged were between 2.5 and 25 keV [46]. These results were the first time the galactic center had been successfully imaged in the X-ray regime.

E. Caroli summarized some coded-aperture astronomical applications. Various mask patterns were used in different projects including MURA patterns, Hadamard patterns, URA patterns and random patterns [47]. These projects were applied to X-rays and gamma-rays of various energies ranging from several hundred keV to 1000 MeV [47].

2.8.C. CODED APERTURES IN NATIONAL SECURITY

More recently coded-aperture imaging has been applied to nuclear security applications. This has proven especially useful as coded apertures allow one to image weak signals with respect to background. One of the earliest gamma-ray imagers for nuclear security applications was designed in order to allow remote and accurate inspection of radioactive materials (i.e. nuclear warheads) [48]. This system, called the Gamma-Ray Imaging System (GRIS), was designed with the goal of non-intrusively counting the number of warheads on an emplaced Peacekeeper missile. GRIS used a URA pattern between position-sensitive gamma-ray detectors and the source. The detectors were 5-mm-thick CsI(Na) crystals mounted to a position-sensitive PMT

[48]. The system was able to count warheads contained in missiles in a field test.

In 1999 a handheld imager was developed for uses in radiation management such as determining where a site is contaminated [49] [50]. The standard handheld radiation monitor does not give directional information so the RADCAM was developed in order to locate nuclear sources among high background signal. This system used a coded aperture between the source and a scintillator crystal coupled to a position-sensitive PMT. The mask pattern was a rank-19 MURA pattern. The device was successfully able to locate a ^{57}Co source at a distance of 70 m [49].

A large area imager was built in the early 2000s [50]. This detector was a much larger scale than previous coded-aperture imagers built for national security with a detector area of 0.57 m^2. This imager used a one-dimensional rank-19 coded-aperture mask. The detector was effective in separating nuclear sources from varying terrestrial backgrounds [12]. The imager successfully identified a source 50 meters away from the mask. A similar imager was built in 2008 [51] that used a rank-23 mask and a mask and anti-mask imaging method. The imager worked by recording two pictures of the scene; one with the opaque and transparent elements inversed (anti mask) of the original coded-aperture shadow pattern. This method helps to eliminate artifacts in the image reconstruction while still accurately imaging the peak.

Overall, coded-aperture technology has been successfully applied to a wide array of fields. So far all of the applications discussed use coded-aperture shadow patterns that block photons in the X-ray and gamma-ray energy ranges. The work in this dissertation uses shadow masks that image with optical photons. This event localization is then meant to be applied to imaging a gamma-ray emitting source outside of the crystal. The next section discusses the means to do this through Compton imaging and gives a historical overview of the theoretical principles as well as the most successful examples using this technique.

2.9. COMPTON CAMERAS

2.9.A. COMPTON CAMERA THEORY

Compton cameras offer a different method of imaging than the previously developed Anger camera with its mechanical collimator, and different than the coded-aperture system and its focus on shadow masks [8] [9] [10]. These detectors image by making use of Compton scattering events (Figure 15) and energy and momentum conservation. A gamma-ray interacts with an

unbound electron in a material, and both the energy given to the electron and the energy and direction of the recoiled gamma-ray are measured. Then, through Compton's formula, based on conservation of energy and momentum and which is derived below, the direction (or a cone of possible angles of incidence) of the original gamma-ray can be calculated.

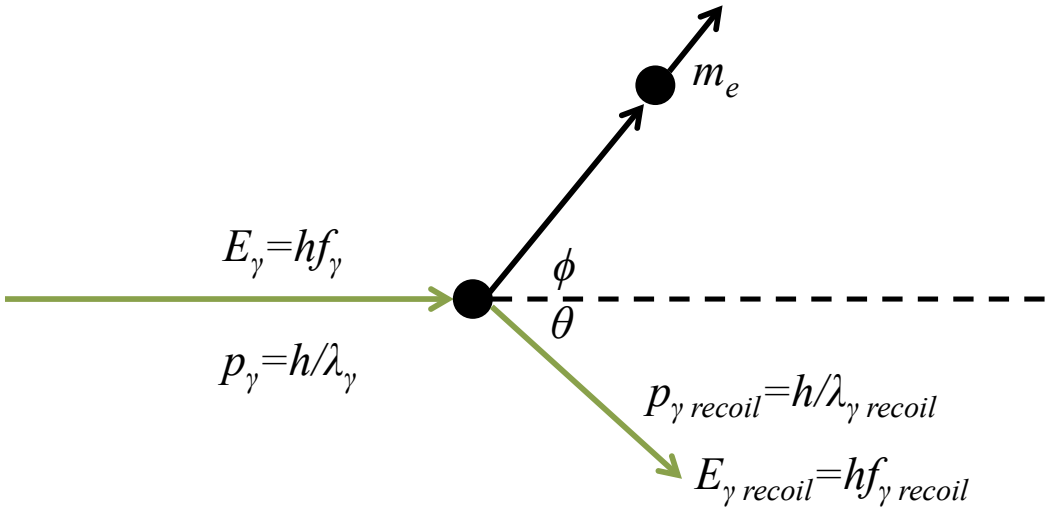

Figure 15. A photon interacts with a stationary charged particle (shown as a black circle) via Compton scattering. The photon transfers energy to the electron giving it a non-zero kinetic energy and the wavelength of the photon is shifted.

For a gamma-ray incident on an unbound electron with an initial wavelength λ_Υ and scattered by the electron (initially at rest) with a final wavelength, $\lambda_{\Upsilon\ \text{recoil}}$, the gamma-ray energy, $E_{\Upsilon\ \text{recoil}}$ is given by

$$E_{\gamma\ \text{recoil}} = \frac{hc}{\lambda_{\gamma\ \text{recoil}}}$$

Eq. 45

A diagram is shown in Figure 15, where h is Plank's constant, ν is the frequency, and c is the speed of light. This is related to the magnitude of the momenta *p* by

$$p = \frac{E}{c} = \frac{hf}{c} = \frac{h}{\lambda}.$$

Eq. 46

The gamma-ray interacts with the electron, which has final momentum $\boldsymbol{p_e}$. Conservation of momentum gives

$$\boldsymbol{p}_{\gamma} = \boldsymbol{p}_{\gamma\, recoil} + \boldsymbol{p}_{\mathbf{e}} \, .$$

Eq. 47

This can be written as

$$p_e^2 = p_\gamma^2 + p_{\gamma\,\mathrm{recoil}}^2 - 2\boldsymbol{p}_{\mathbf{e}} \cdot \boldsymbol{p}_{\boldsymbol{\gamma}\,\mathbf{recoil}} = p_\gamma^2 + p_{\gamma\,\mathrm{recoil}}^2 - 2p_{\mathrm{e}} \cdot p_{\gamma\,\mathrm{recoil}} cos\,(\theta) \, .$$

Eq. 48

Before the scattering, the energy of the electron is simply the rest mass energy equal to

$$E_0 = m_e c^2$$

Eq. 49

while the energy after the collision is

$$E_{electron} = (E_0 + p_e^2 c^2)^{1/2}$$

Eq. 50

Conservation of energy states that

$$E_\gamma \, + E_0 = E_{\gamma\,\mathrm{recoil}} + (E_0 + p_e^2 c^2)^{1/2}$$

Eq. 51

which gives

$$p_\gamma \, c + E_0 = p_{\gamma\,\mathrm{recoil}} c + (E_0^2 + p_e^2 c^2)^{1/2}$$

Eq. 52

Squaring the equation gives

$$E_0^2 + c^2(p_\gamma - p_{\gamma\text{recoil}})^2 + 2cE_0(p_\gamma - p_{\gamma\,\text{recoil}}) = E_0^2 + p_e^2c^2 \ .$$

Eq. 53

Using Eq. 48 and eliminating p_e gives

$$\frac{E_0(p_\gamma - p_{\gamma\,\text{recoil}})}{c} = p_\gamma \cdot p_{\gamma\,\text{recoil}}(1 - cos\ (\theta)) \ .$$

Eq. 54

Multiplying by $(hc/p_\lambda p_{\lambda\ recoil})E_0$ and using $\lambda=h/p$, Compton's formula may be written as

$$\lambda_{\gamma\,\text{recoil}} - \lambda_\gamma = \frac{h}{m_e c}(1 - cos\ (\theta)) \ .$$

Eq. 55

Replacing the wavelength terms with the energy equivalents and solving for $\cos(\theta)$ gives

$$\cos(\theta) = 1 - m_e c^2(\frac{1}{E_{\gamma\,recoil}} - \frac{1}{E_\gamma})$$

Eq. 56

where

$$E_\gamma = E_{\gamma\,recoil} + E_{electron} \ .$$

Eq. 57

If the energy of the electron and energy of the recoiled gamma-ray can be measured, then one can solve for θ. This defines a cone that contains the possible incidence directions for the gamma ray. With data from several gamma-rays emitted by a single source, the intersections of the cones indicate where the source that emitted the gamma-rays could exist. Compton cameras were developed to make use of this concept; classically, they consist of two planes of detectors with the Compton scatter and electron energy measurement occurring in the first plane, and the energy and direction measurement of the recoiled gamma-ray occurring in the second plane. This is shown in Figure 16.

The way that the recoiled gamma-ray energy is measured is through a photoelectric absorption in the second plane of the detector; if a photoelectric absorption occurs, all of the energy of the gamma-ray is deposited in the interaction and an accurate measurement of its energy can be obtained for the angle reconstruction. Utilizing this concept requires measuring four quantities. Each plane needs to be able to localize the interaction (Compton scattering in the first plane and photoelectric absorption in the second plane) in three dimensions. Additionally, the first plane must be able to measure the change in energy of the scattered gamma-ray (energy given to the electron) and the second plane to measure the final energy via a photoabsorption.

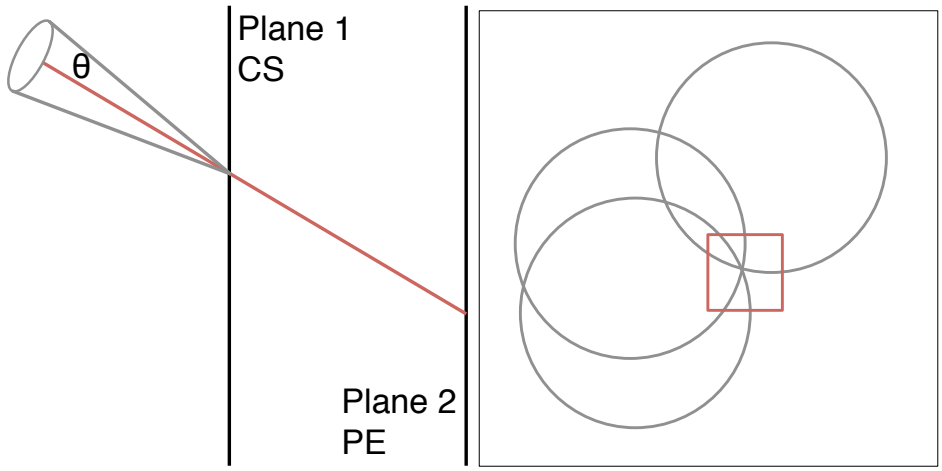

Figure 16. (Left) The gamma-ray interacts with the first plane and continues to the second plane. Each plane consists of a device that is able to locate a gamma-ray in two dimensions. By determining the x-y position and energy of the interaction in each plane, the scatter angle θ can be found that satisfies (Eq. 56). Since the recoil direction of the electron is unknown, all possible θ's form a cone. (Right) A projection of the cones onto a perpendicular plane from several different gamma-rays, each created by being able to determine θ (Eq. 56). The point source is located in the red box where all three cones intersect.

These measurement capabilities must each be optimized to minimize the angular uncertainty and, in turn, maximize the angular resolution. In practice, several design considerations are taken

into account. The first layer must be thin enough so that only one interaction (Compton scattering) is likely to occur. Additionally, a material should be selected that maximizes the probability of a Compton scatter interaction. The second layer must be thick enough and of a material so that the recoiled photon interacts via photoelectric absorption in a large percentage of cases to make use of as many events as possible.

In the photoelectric absorption event, a photon is completely absorbed and a photoelectron is ejected; the most probable shell for the absorption to occur is the most tightly bound shell (K shell) of the atom as this is closest in energy to the incident gamma-ray at the energies of interest. The photoelectron receives energy

$$E_{e-} = hf - E_b$$

Eq. 58

where f is the frequency of the incident photon and E_b is the binding energy of the photoelectron in the atom. The binding energy is on the order of tens of keV, so for a several hundred keV gamma-ray the photoelectron contains most of the gamma-ray's original energy. This process is the predominant interaction for relatively low photon energy and materials with high Z. The probability of this interaction occurring is proportional to [6]

$$\frac{Z^n}{(hf)^3}$$

Eq. 59

where n is between 3 and 4 and depends on the energy of the interacting gamma-ray, and f is the frequency of the photon. Thus, high-Z materials are needed for Compton imaging in order to ensure the photon experiences a photoelectric absorption in the second plane versus an additional Compton scatter.[2] An extensive analysis of the material chosen for this project is presented in Chapter 4.

The accuracy with which the direction of incidence is determined is given by the angular resolution measure (ARM) [21]. This is a distribution that can be derived from the scattering

[2] Note that in high z materials, the probability of emission and subsequent photoabsorption of a K-Shell fluorescence photon is high so that the full energy of the recoiling gamma ray is

angles given by Compton kinematics [21]. This is done by calibrating a system with a known source location and comparing the true source position to the measured scatter direction. It includes terms from uncertainties in event energies and locations. From Compton kinematics and reconstructing the angle with respect to the position measurement, the uncertainty from geometric contributions is given by the uncertainty in determining the line connecting the two interaction sites and is approximately inversely proportional to the distance between the first and second detection planes. The total geometric uncertainty is the sum of each dimension's uncertainty added in quadrature [14]

$$\Delta\theta_{geometric} = \sqrt{(\Delta\theta_{geometric})_x^2 + (\Delta\theta_{geometric})_y^2 + (\Delta\theta_{geometric})_z^2}\ [14].$$

Eq. 60

Defining $\vec{u}$ as the distance between the Compton scatter and photoelectric absorption interactions,

$$(\Delta\theta_{geometric})_x = \frac{\sqrt{2}}{|\vec{u}|}\sigma_x\sqrt{1 - \left(\frac{\vec{u}\cdot\hat{x}}{|\vec{u}|}\right)^2}\ [14].$$

Eq. 61

The uncertainties for the other two dimensions are the same for their respective directions. In a full volume detector (where the interaction is localized in a bulk volume instead of two separate planes), if it is assumed that $\sigma_x \cong \sigma_y \cong \sigma_z = \sigma_x$, the equation can be reduced to

$$\Delta\theta_{geometric} = \frac{2\sigma_x}{|\vec{u}|}\ [14]$$

Eq. 62

As seen in Eq. 62, a larger separation distance between events minimizes the angular uncertainty. Also, the uncertainty in each dimension of localization (both lateral measurements and the depth for each plane) contributes to the angular uncertainty and should be minimized to improve the angular resolution. Early Compton cameras avoided problems of disentangling simultaneous events that occur in a region smaller than the individual event position resolution of the detector by using only two detector planes instead of a bulk detector. Because of this, and the uncertainty

given in Eq. 62, they often occupied large overall volumes just to have enough separation between the first and second planes.

The angular uncertainty in a two-detector system also has a contribution from the energy measurements in each plane [52]. The uncertainty contributions from the energy measurements vary based on which plane is used to determine the energy. Again from Compton kinematics, if one holds the energy uncertainty of the first plane fixed, the uncertainty due to the second plane's energy measurement can be calculated. For a system where the energy discrimination is only the first plane (assuming the incident gamma-ray energy is known), the contribution to the scattering angle uncertainty due to the scattering energy uncertainty is given by

$$\Delta\theta_E = \frac{m_0c^2}{\sin(\theta)(E_\gamma - E_{electron})^2}\Delta E_{electron}$$ [53].

Eq. 63

As seen in Eq. 63, the uncertainty in the angle determination is greater for smaller scatter angles.

The scattering angle uncertainty from the energy measurement only in the second plane can also be calculated. The scattering angle is found with

$$\cos(\theta) = 1 - mc^2\left(\frac{1}{E_{\gamma\, recoil}} - \frac{1}{E_\gamma}\right)$$

Eq. 64

and the uncertainty is given by

$$\Delta\theta = \frac{mc^2\Delta E_{\gamma\, recoil}}{\overline{E_{\gamma\, recoil}}^2 \sin(\theta)}$$

Eq. 65

where $\overline{E_{\gamma\, recoil}}$ is the mean value of the measured photo-absorbed interacting gamma-ray.

A final model exists where the incident gamma energy is unknown and both energy measurements have contributions to the angular uncertainty [52]. In this case the scattering angle is given by

$$\cos(\theta) = 1 - \frac{mc^2}{E_\gamma}\frac{E_{electron}}{E_{\gamma\, recoil}}$$ [52].

Eq. 66

The uncertainty is given by

$$\Delta\theta = \frac{mc^2}{E_\gamma \overline{E^2_{\gamma\, recoil}} \sin(\theta)} \sqrt{(\overline{E_{\gamma\, recoil}} E_{electron})^2 + (\overline{E_{electron}} E_{\gamma\, recoil})^2}$$ [52].

Eq. 67

As seen in Eq. 63, the energy measurement of the electron contributes to the uncertainty in the angular distribution. Because the electrons in materials are not actually free (as assumed in the Compton equation), there is an uncertainty associated with the electron's initial motion. This term is called Doppler broadening and can become a limiting factor in the angular reconstruction [54]. Higher Z materials have larger electron motions that worsen this effect. Additionally, as discussed above, higher Z materials favor photoelectric absorption, so a low Z material is preferred in the first plane in order to both minimize the effects of Doppler broadening and, in turn, improve the energy resolution, as well as to favor Compton scatters as opposed to photoelectric absorption. Conversely, high-Z materials are favored in the second plane to increase the probability of photoelectric absorption.

The next section will highlight several significant Compton cameras built in the last few decades. While great advancements were made in effective area relative to the overall size of the system, these instruments still could not remedy the problem of needing a large area (1 m^2) detector while being cost effective and relatively easy to maintain in the field.

2.9.B. COMPTON CAMERA OVERVIEW

Several fundamental Compton cameras have been built in the last few decades using different technologies and detector materials. This section will highlight the most significant instances.

Throughout the 1980s and 1990s, COMPTEL, a Compton camera used for astrophysical source gamma-ray imaging was developed and used by NASA and several other astronomy agencies and research groups to image the gamma-ray sky from 1 to 30 MeV [9]. The instrument used the classic two-plane design with a scattering plane area of 4188 cm^2 and an absorption plane area of 8620 cm^2. The two were separated by 1.5 m, giving a large overall volume relative

to an effective area of only 20-50 cm^2 [9]. The upper plane that detected the Compton scatters was made of liquid scintillator and the lower one used NaI crystals. Both scintillators were read out by PMTs. While it returned significant astrophysical results [9], its very poor effective area compared to its size provided motivation for the development of more compact Compton cameras.

A main goal in the next generation of Compton cameras was to make use of a larger percentage of the overall volume of the instrument. One example built with this goal in mind was the Liquid Xenon Gamma Ray Imaging Telescope (LXeGRIT) [55] [56]. The project investigated using several noble liquids for scintillation material including argon, krypton and xenon. LXeGRIT used a liquid xenon time projection chamber to image cosmic gamma-rays from 200 keV to 20 MeV. The volume was much smaller than COMPTEL ($6.3x10^6$ cm^3) at only 10,000 cm^3 but had a much higher effective area of 400 cm^2 [56]. While effective for this specific situation, due to the complexity in engineering problems of this system and the cost of liquid xenon it is not suitable as an easily maintained, cost-effective, large volume system for use in national security applications [14].

More bulk volume Compton cameras were developed throughout the early 2000s. A Cadmium Zinc Telluride (CdZnTe) detector was developed by a group at the University of Michigan that had a field of view of 4π steradians and consisted of a single volume of CdZnTe. The volume of the detector was 3.3 cm^3 and resolution in the lateral positions was 1.2 mm with 1 mm depth resolution [57]. The two lateral dimensions were found with a pixelated array, while the depth dimension was found using timing signals. The detector was able to achieve adequate angular resolution of 17° and an energy resolution of 2% at 662 keV. While this system possessed good spatial resolution, its use for standoff detection purposes is limited since a much larger detector area is needed than can be achieved with CdZnTe when cost restrictions are considered.

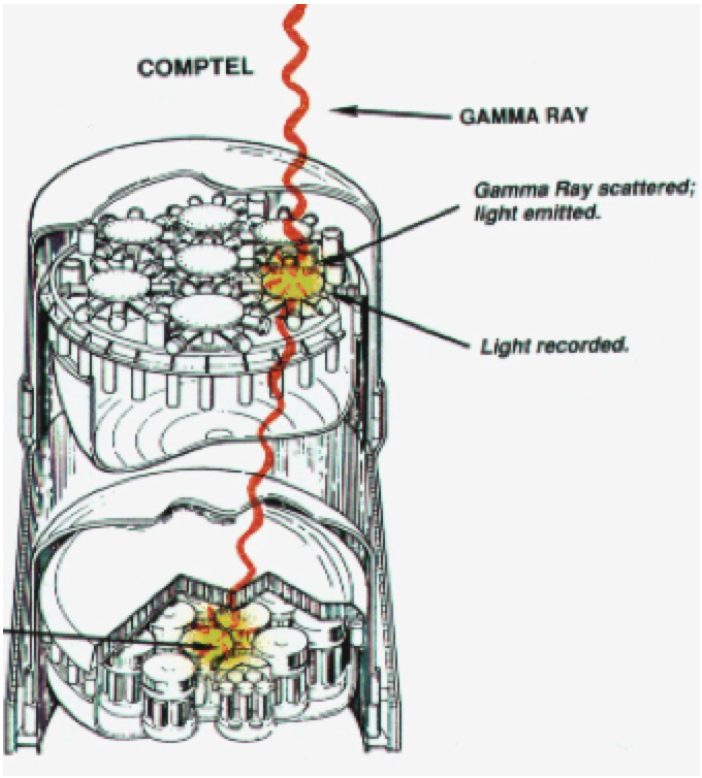

Figure 17. From [9]. An image of COMPTEL. The upper and lower planes are separated by 1.5 m, resulting in a large volume relative to the effective area of the detector.

Also developed in the early 2000s, the Nuclear Compton Telescope (NCT) was designed primarily by a research group at Berkeley to image astrophysical sources emitting gamma-rays between 200 keV and 20 MeV [55]. With the goal of creating a compact Compton camera of similar effective area as COMPTEL, it consisted of ten high purity germanium (HPGe) detectors within a small volume; each detector had three-dimensional photon measurement capabilities. When a gamma-ray Compton scattered in one HPGe module and was fully absorbed somewhere else in the instrument, the position of each interaction and deposited energy were measured [55]. NCT was able to achieve effective areas close to that of COMPTEL while being a fraction of the volume. COMPTEL had a volume of 6.3×10^6 cm^3 while NCT had a volume of about 1500 cm^3 [8]. The effective areas of each are shown in Figure 18.

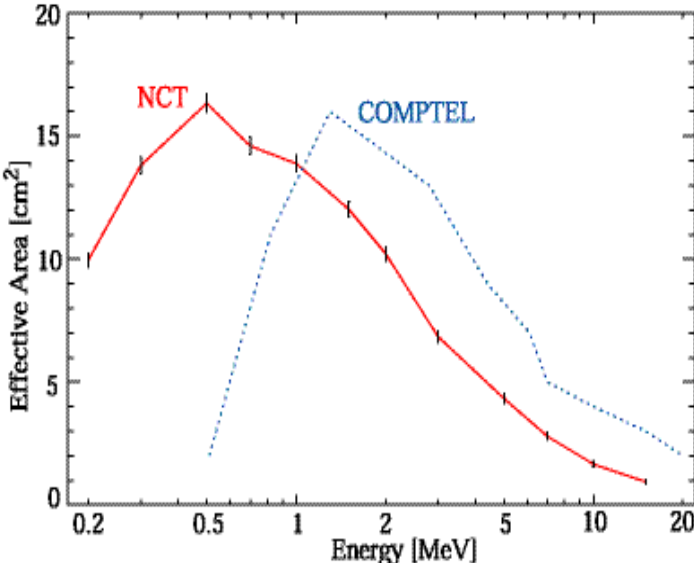

Figure 18. Adapted from [8]. The effective area vs incident gamma-ray energy for the Nuclear Compton Telescope (red) and COMPTEL (blue). The NCT was able to achieve the same effective area while being a fraction of the volume.

While NCT provided a significant improvement in volumetric efficiency over the previous generation of Compton cameras, as with CZT, HPGe is too expensive for projects with cost restrictions seeking to instrument a large volume.

In 2004, a group at the Naval Research Laboratory utilized silicon strip detectors to image using the Compton camera method [57]. This detector used three 57 x 57 x 2 mm^3 silicon strip detectors to build a three-plane gamma-ray imager. They were able to achieve an excellent angular resolution of ~1° [57]. While effective, the volume was limited as silicon detectors are expensive. Additionally, the detectors require cooling, limiting their uses in field applications. The low Z also means that one has to deal with multiple Compton scatters before a final photo-absorption occurs, significantly complicating the imaging analysis.

In 2005, a Japanese group used a combination Compton camera consisting of silicon strip detectors as the Compton scatter plane and CdTe detectors to photo electrically absorb the scattered gamma-rays [58]. This configuration was chosen because Si detectors have a low atomic number (14) resulting in a large ratio of the Compton-to-photoelectric cross sections. Conversely, Cadmium (48) and Telluride (52) have high atomic numbers, resulting in a high

percentage of photoelectric absorption interactions. The detector was able to achieve good energy resolutions of 9.1 keV and 14 keV, for 356 keV and 511 keV gamma-rays, respectively. The angular resolution was 3.9 degrees for 511-keV gamma-rays. However, as a two-plane system, it is volumetrically inefficient and the semiconductor materials make for a large cost-per-unit volume.

Each system discussed made improvements to the energy and angular resolution from the original COMPTEL system. However, due to the high cost or lack of portability and possible complications in maintainability of these detector systems, it remains impractical to instrument a large area detector with noble liquid scintillators, silicon-based PT or CdZiTe detectors or HPGe detectors. As introduced in Chapter 1, the motivation for this project is to be able to allow for instrumentation of a bulk volume Compton camera using a scintillator crystal. Thus, the next section discusses methods of event localization in crystals. This specific capability is the focus of this dissertation.

2.10. EVENT LOCALIZATION IN BULK SCINTILLATORS

Locating an event within a scintillator crystal is useful to several scientific communities including astrophysics, nuclear medicine, and national security. One of the earliest applications of event localization in scintillator crystals was the Anger camera [20] as discussed in Section 2.1. An array of PMTs is coupled to a bulk crystal, and because the scintillation light is emitted isotropically, the PMT closest to the interaction sees the most light. The spatial resolution of the anger camera is given by the full width at half maximum (FWHM) of the distribution measured across the PMT array. This is dependent on the size of the photo transducers used in addition to the ability to centroid the collected distribution. Original Anger cameras in the 1960s achieved spatial resolutions of ~15 mm [59] while modern cameras achieve resolutions of 3.0 mm [60].

2.10.A. CENTROIDING METHOD IMPROVEMENTS

In the 1980s position-sensitive PMTs with better spatial resolution were able to improve upon the coarse event localization resolutions. Using an NaI(Tl) bar 500 mm long, 50 mm wide, and 25 mm thick one group was able to obtain a spatial resolution of 4.0 mm in the horizontal dimension [15]. This method used a perpendicular collimator to restrict events to only include gamma-rays with incoming directions perpendicular to the crystal as seen in Figure 2. Advancements in PMTs have also improved the ability to find the centroid of a distribution.

They will be discussed in Section 4.3.

Most improvements in centroiding methods have come in electronic and signal processing. PMTs with small pixels have also significantly helped to improve the ability to find the centroid of a distribution. Current technology is able to obtain ~3 mm per 1 cm thickness of scintillator crystal [59]. This resolution has been achieved in several applications. In an X-ray imaging system designed for the 20-to-400 keV energy range [16], a crystal coupled to light guide used a system mounted to a photocathode followed by dynode amplifiers and finally crossed-wire anode (the photocathode to anode section is a commercially available PMT). The system then found the centroid of the charge cloud collected to locate the event within the crystal. The system obtained ~2 mm spatial resolution with a 2 mm thick NaI crystal directly coupled to the PSMPT. Better than 2 mm spatial resolution was obtained for a 1.6 mm thick CsI crystal also directly coupled to the PT. [16]. Another more recent study measured the size of the light cloud for NaI crystals from 2 mm to 20 mm thick. This method used a novel geometry for the crystals coupled to the PMTs; they used crystals with glass plates coupled to each side and an aluminum reflecting material coupled to the face opposite the PMT [17]. With this technique applied to measuring the light cloud of 511-keV gamma-rays, for a 2 mm thick crystal the spatial uncertainty in the lateral dimension was 2.3 mm [17]. For the 20-mm-thick crystal the uncertainty obtained was 6.58 mm. These results are significant improvements over the original event localization capabilities developed for Anger cameras. Various other methods to localize an event in a scintillator crystal in addition to the standard centroiding approach have also been investigated; the next sections will discuss these further.

Much advancement in the field of event localization has been motivated by efforts to improve Positron Emission Tomography (PET) imaging capabilities, so a discussion of this field of research will be presented. First, a method of event localization in segmented crystals is presented, as they are often used in PET imagers.

2.10.B. SEGMENTED CRYSTALS

One of the most common ways to localize a gamma-ray interaction in a scintillator crystal is to use a segmented crystal, as seen in Figure 19 [61] [62] [63].

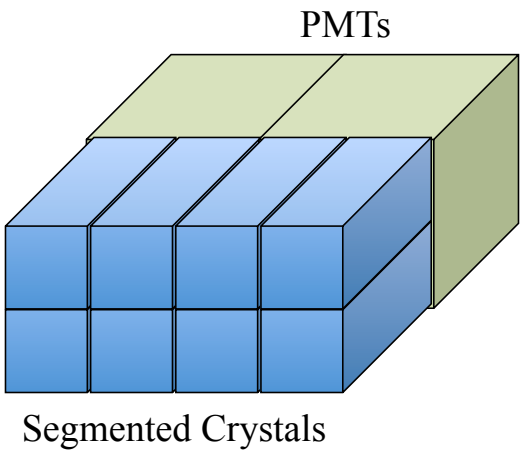

Figure 19. An example of segmented crystals with coupled PMTs. The light from an event in a segmented region spreads to multiple PMTs. The ratio of light in each PMT gives a specific segment that the event interaction occurred within. This system is known as a block detector.

In this design, the transverse position is given by the amount of light received from each segmented section (centroiding). However, if the crystal segments are too small, then the energy within each segment can leak to neighboring sections through finite electron ranges and Compton scatters [61] [64]. While this improves the position resolution, the energy resolution is sacrificed as the segmentations absorb light and lower the signal for each event. Assuming a fixed gamma-ray energy (as in PET), the depth of interaction information is given by the absolute height of the pulse recorded from the photo sensor (or in some cases by a second PMT on the opposite side of the crystal), where the ratio of signals in each PMT give the depth within the crystal segment Figure 22b. However, in order to achieve good stopping power and to maintain a high spatial resolution, the segments must be much larger in the depth dimension than the transverse dimension with respect to the PT (phototranducer) readout devices. This places the PT entrance window farther from some events than others that occur in the same crystal, resulting in less light reaching the PT [64]. Additionally, the segmented crystal has a lower sensitivity per area because of the dead space in between segments. They are also more expensive to manufacture [64].

In 1999 a camera designed for breast cancer imaging used 2 x 2 x 3 mm^3 CsI(Tl) crystals with 0.25 mm spacing between each segment. These segments were coupled to Hamamatsu R3292

position-sensitive photo multiplier tubes (PSPMT) on one side and parallel collimation segments on the other with one collimator opening per crystal segmentation as seen in Figure 20. In regards to source localization measurements (not events within the crystal but localizing an emitting source), this setup was able to achieve spatial resolutions of 1.6 mm and 1.8 mm for events 0 mm from the collimator and 2.7 and 4.0 mm for events 2-3 mm from the collimator [64]. Other applications of this method have been successfully implemented, but as the spatial resolution improves the system becomes significantly more complicated and expensive [63] [64].

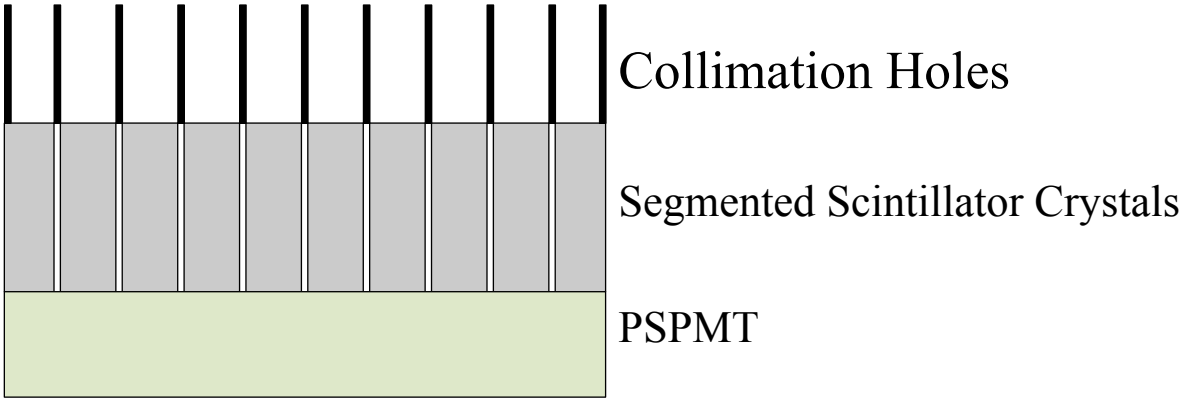

Figure 20. Adapted from [64]. The gamma-rays enter through the collimation holes and interact in the segmented crystals. The PSPMT then records the output in a nearly square shaped spatial signal.

2.11. POSITRON EMISSION TOMOGRAPHY OVERVIEW

PET imagers are medical systems that can produce images of functional processes that occur in the body (used in both humans and animals). While the functions of PET imagers are different than this dissertation work, they rely on the ability to localize events within scintillator crystals. Therefore, a review of PET imagers is given in this section in addition to advancements specific to their application that involve event interaction resolution in scintillators.

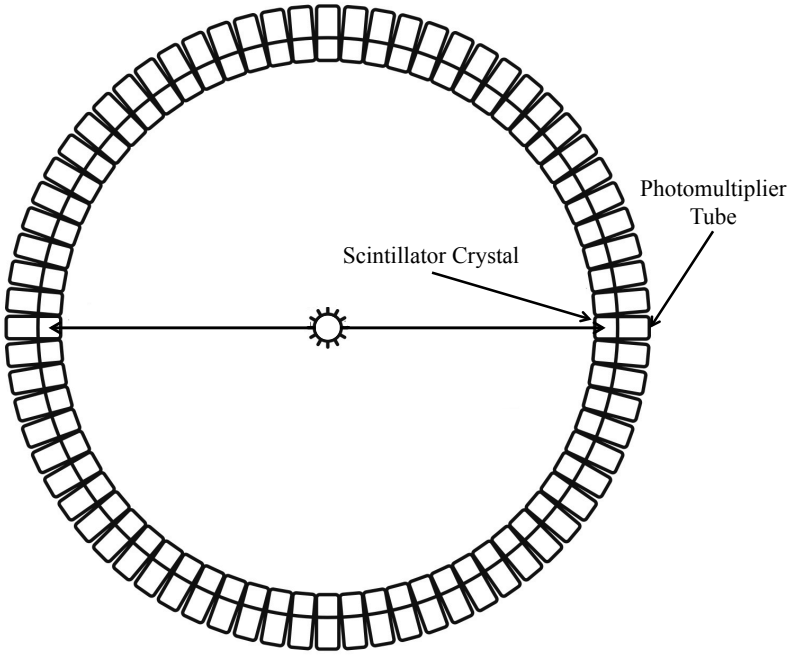

Figure 21. Adapted from [65]. The object to be imaged is placed in the center of a ring of detectors. Each detector module consists of a scintillator crystal, which is coupled to a PMT. The positron emitted from the radionuclide interacts and annihilates with a nearby electron and emits two 511-keV gamma-rays back to back. The detection of both photons 180° from each other gives the line on which the source of the photons must fall.

With an object (patient) placed in the center of a PET imager (Figure 21), the patient to be imaged is given via injection or ingestion a radionuclide that emits positrons. ^{18}F, ^{11}C, ^{13}N, or ^{15}O are the most commonly used isotopes [66] [67]. As the isotope decays, the emitted positron interacts with a nearby electron and annihilates. The annihilation produces a pair of 511-keV photons that are produced at 180 degrees relative to one another [66] [67]. By detecting the simultaneously produced photons, a line (called a chord) on which the annihilation occurred can be constructed. Using a method called computed tomography, the chords can be combined to construct the spatial distribution of the radioisotope. The gamma-rays are detected on a position-sensitive ring of detectors surrounding the object to be imaged as seen in Figure 21 [65].

The main requirements for the detector portion (scintillator crystal and PMT modules) of the

imager are as follows: high detection efficiency of the emitted scintillation photons, high spatial resolution, low cost for the crystal region, a short dead time to deal with high counting rates, and good timing resolution to be able to detect the coupled pairs of emitted photons [67]. Two primary detector materials are used that satisfy these goals: NaI and bismuth-germanate (BGO) [66]. The scintillator crystal block is coupled to several smaller PMTs, and through analysis of the PMT signal, the interaction position within the crystal can be obtained. This method uses the same centroiding approach discussed earlier. Full body commercial PET scanners currently can achieve spatial resolutions of 6.3 mm for imaging objects at the center of the ring (Figure 21) and ~10 mm at the edge of the field of view relative to the center [65]. The uncertainty in event localization in the crystal segments that contributes to this overall resolution is currently stated to be as low as 2.2 mm in the lateral dimension [65]. In addition to larger systems for imaging human subjects, small-animal systems also exist. These systems are typically about 12 cm in diameter. Current models can obtain spatial resolutions of ~1.4 mm, but the photon sensitivity of the systems are low (<10%). Improvements in both the spatial resolution and detection efficiency would greatly impact the field and the ability to more accurately image subjects.

2.11.A. DEPTH OF INTERACTION (DOI) AND HORIZONTAL SPATIAL RESOLUTION IN PET IMAGING

The depth of interaction determination in PET imaging is an issue that greatly affects the spatial resolution at the imaged object. The detector modules consist of segmented crystal elements as seen in Figure 19. When a gamma-ray does not travel directly through the center of the detector ring, it enters the detector region obliquely and can pass through several crystal segments before interacting and being detected [67]. This is the largest contribution to degrading the spatial resolution of the image and is worse for objects farther from the center of the detector ring. If the detector modules were capable of accurately determining the depth of interaction in the crystal segments, this uncertainty could be significantly reduced or eliminated. With improvements in the depth of interaction measurements, the likelihood of assigning the event to the wrong crystal segment could be decreased. The chord then would have a finer resolution as it passes through the source and extends between two points instead of between two crystal segments. Several approaches to improve the depth of interaction measurement have been investigated [67].

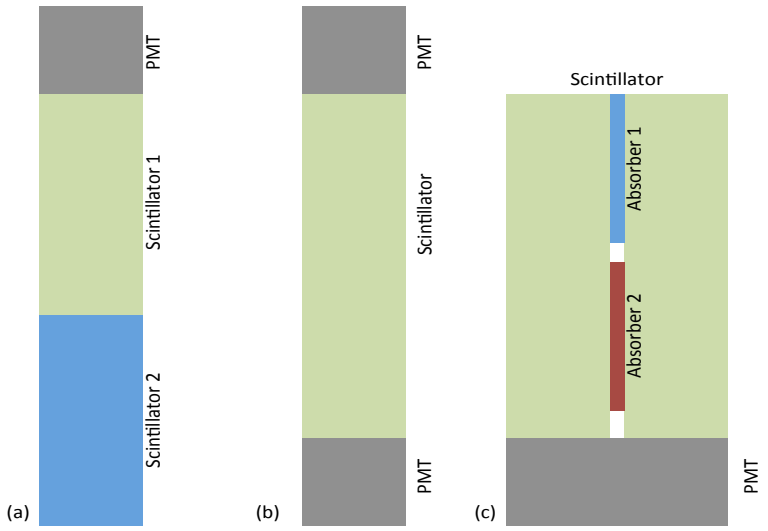

Figure 22. Adapted from [68]. Techniques to find depth of interaction in segmented crystals. (a) Different scintillator materials with different decay times, so the response from the PMT can be used to determine where the interaction occurred. (b) Coupling a PMT on each side of the scintillator allows one to use a ratio of the signal from each PMT to determine the depth of interaction. (c) The different absorbers between the scintillators share different amounts of light in each section, which can then be used to determine which segment the event occurred in.

One of the earliest approaches to measure the depth of interaction was to have layers of different scintillators with different decay times coupled to a PMT as seen in Figure 22a. As different scintillators give different pulse shapes for the same energy gamma-ray, a pulse-shape discriminator can be used to determine which depth the event occurs in [68]. While effective in depth measurements, this method is costly to realize because machining the different crystals to be the same size and optically matching them is expensive. [68]. Another approach that has been investigated is placing phototransducers at both ends of the segmented scintillator crystal as seen in Figure 22b. By comparing the ratio of the light recorded on each end of the crystal a DOI in the crystal can be calculated. So far this method has produced depth resolutions of about 2 mm [68]. Another method is to place several light absorbing materials between coupled crystals at different depths relative to a photo transducer as seen in Figure 22c [68]. When an event occurs in one of the crystals, the depth determines how much light from each crystal each photo

transducer sees. The ratio of the light in each crystal then determines the depth of the event. This method has been able to obtain depth spatial resolutions of 3-4 mm [68]. These methods use segmented crystals but PET imaging systems can also be constructed with larger continuous crystals. One method to determine the DOI in larger crystals is to use larger slabs of crystals with avalanche photodiode arrays between each layer [68]. This method has been able to achieve 1.4 mm depth resolution for 8-mm-thick crystals.

Another method developed for PET imaging is the Maximum Likelihood method [69] [70]. This approach involves modeling the light shape distribution in simulations of radiation interactions at various depths within a bulk crystal and then using the results to estimate the depth of a recorded event by comparing the model to the signal. Additional work in simulating individual PMT channels for a given depth and horizontal position has been able to achieve results of 1.4 mm depth resolution for an 8-mm-thick crystal [69].

Several other methods for event localization in crystals for use in PET imagers have been investigated. One method was to treat the surface of a scintillator crystal with different surfaces including raw cut, finished, polished optical finishes, and chemically etched surfaces [71]. The best DOI results obtained were about 3.5 mm with the chemical etching technique when the crystals were coupled to avalanche photodiode detectors [6]. Another method used retro-reflective tape along the top of a scintillator coupled to position sensitive PMTs [72]. For a 20-mm-thick CsI crystal the reflector tape improved the best measurement of the lateral resolution from 7.5 mm with standard Teflon tape (which diffusely reflects the light) to 7.3 mm.

As the DOI and horizontal position measurements are one of the largest contributions to uncertainty in the overall spatial resolution of PET imagers, minimizing this resolution is of great importance. The work in this dissertation could have a practical and significant impact on PET imaging resolution as optical coded apertures could be applied to the detector ring on a PET imager.

As the concepts required for a detailed understanding of the work in this dissertation were introduced in this chapter, the next chapter (Chapter 3) introduces the full concept of a bulk volume Compton camera. As stated before, it should be emphasized that while the motivation of the project was to build an operational Compton camera, due to several factors the dissertation results focus on event localization in the crystal. Future work with the concept may allow for a full Compton camera to be instrumented building on this project's success.

CHAPTER 3. THEORETICAL OVERVIEW

3.1. CRYSTAL COMPTON CAMERA THEORETICAL OVERVIEW

If it were possible to distinguish between two events (Compton scatter followed by photoelectric absorption) in a single scintillator crystal within a small volume, then a detector with a high percentage of effective volume could be built. We built a bulk scintillator detector that uses a coded-aperture shadow mask pattern to locate the events in the crystal using coded-aperture methods, and, in turn, is an enabling technology for a bulk volume Compton camera. While standard coded-aperture masks indirectly image gamma rays, this design uses the same principle to indirectly image scintillator light from the crystal before it reaches a PT. This system is cost effective and much more spatially efficient than a traditional Compton camera.

The overall design of the system consists of a bulk scintillator crystal optically coupled to a light guide which is coupled on the other end to a pixelated PMT array as seen in Figure 23.

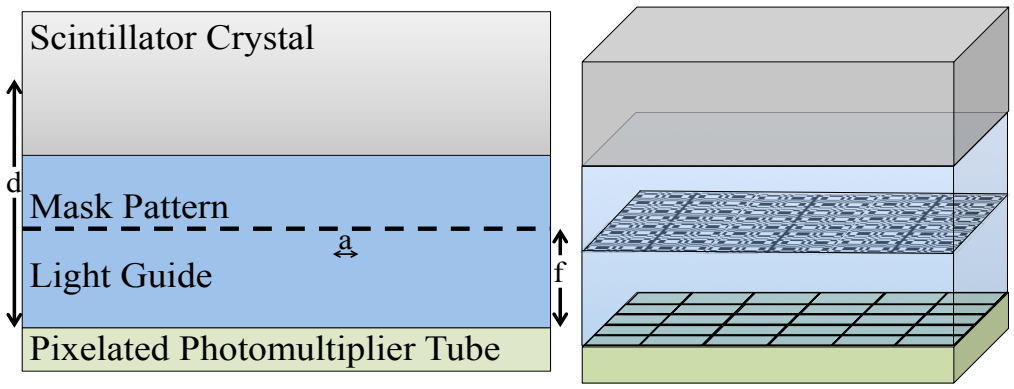

Figure 23. The physical setup of the system (left) and a three-dimensional view (right). The distance from the PMT plane to the event in the scintillator crystal is d, the distance from the PMT plan to the mask plane is f, and the size of the mask feature element is a. On the right, the mask plane is shown as a repeating pattern of rank 19 base patterns.

An optical coded-aperture shadow pattern is located in the light guide between the crystal and the PMT plane. The gamma-ray interactions in the scintillator crystal project the mask pattern

onto the detector with a magnification dependent on the event's depth in the crystal. In reconstruction the image is "focused" (processed with different assumed magnifications) until the correct depth of the interaction is found. Once that depth is located the lateral positions are found in the other two dimensions from the reconstructed image. Two systems were built and analyzed; a two-dimensional prototype system in 2013 and a three-dimensional system in 2014.

3.1.A. ADVANTAGES OF NEW METHOD

As mentioned above, the detector design uses a shadow mask pattern between the crystal and the PT. The basic design is shown in Figure 23. The events of interest interact via Compton scattering followed by photoelectric absorption in a small volume. The events are virtually simultaneous. Based on cost and the goal of building a system with a large enough volume to prove the method effective, the overall system has been chosen to be several centimeters thick and tens of centimeters wide in each horizontal direction. The final version of the system constructed for national security purposes is planned to have an area on the order of 1 m^2, so this is a reasonably sized prototype.

When using a system with a crystal coupled to a PT and no mask pattern, the method to localize an event in the horizontal direction in the crystal is either to segment the crystal into small voxels or to locate the centroid of the event. Segmenting the crystal results in loss of photons that reach the PT; not only does this lower the energy resolution, but the degree of light loss frequently depends on location within the segment [18]. When finding the centroid of the event, the fundamental uncertainty in locating the center of the light distribution at the PT is given by

$$\delta x \sim \frac{w}{\sqrt{N}} \text{ [6]}$$

Eq. 68

where w is the width of the light distribution (usually the FWHM) and N is the number of photoelectrons. In our case, the type of scintillator crystals used generate between 20,000 and 40,000 photons per MeV. The scintillator design considerations will be discussed later in Section 4.2. For a 400-keV event, the system will detect several hundred photons after accounting for losses between the event site and the PMT: first, only half of the light goes downwards towards the PT, half of that light is lost due to the mismatch in the index of refraction, and the quantum

efficiency of the PMT is about 20%. The current methods of locating the centroid of the distribution have resulted in spatial resolutions of ~ 3 mm per 1 cm thickness of crystal [13] [59]. The resolution worsens as the thickness of the system increases, so this method does not provide fine enough resolution for our needs. This problem is remedied when using the coded-aperture mask pattern between the crystal and the PT. The resolution at the image plane with a mask pattern is given by [13]

$$\delta x \sim \frac{\sigma}{\sqrt{N}}, \text{ where}$$

Eq. 69

$$\sigma = \frac{a}{f} d.$$

Eq. 70

The shadow mask pattern decreases the amount of light seen by the PT by a factor of two. While this would hurt the ability to localize the interaction in a crystal using the centroiding method, the resolution overall is improved when using the coded aperture. For a system several cm thick, σ is on the order of a few millimeters while w is a few centimeters. To make use of this approach, the PT must be able to resolve the projected features of the mask for events at the top of the crystal; these events have the smallest magnification factor, and thus the smallest magnified features projected onto the PT.

The crystal selection will be discussed in detail in Section 4.2, but the most important requirement is to maximize two factors: the number of events where a Compton scatter is followed by a photoelectric, and the number of scintillation photons per event reaching the PT plane. Because of the low energy of the events, a crystal with a decent light output is required. A light guide of borosilicate glass or quartz is coupled to the crystal on one side and to the face of the PMT on the other. Each surface is coupled using standard silicon optical grease.

3.2. OVERALL SYSTEM DESIGN

In designing the overall system two conditions (Figure 24) for events at the bottom and top of the scintillator crystal must be balanced. A single gamma-ray event in the crystal would not illuminate the entire mask, so the mask will be made up of many repetitions of a smaller uniformly redundant array (RA). Each RA-sized area will project a complete pattern onto the

detector and can be reconstructed to a point source in the image plane. To minimize systematic noise in the images, each event should illuminate a full cycle of the pattern. To approximate this, the RA pattern size is set to ~ the size of the smallest possible FWHM of the light cloud at the mask. This occurs for an event at the bottom of the crystal, as the light spreads less than for events at the top of the crystal. To determine the size of the light cloud we derived an expression for the size of the light spot after going through an index change from the crystal to the light guide [73] [74]. This derivation and result for an approximate expression are given in Appendix 1. From the theory developed and final expression given in the appendix, the size of the light spot at any plane after an index change can be estimated with high accuracy in order to determine the overall geometry of the system. This method is implemented and the results for a variety of possible geometries are given in Sections 4.5, 4.6 and 4.7.

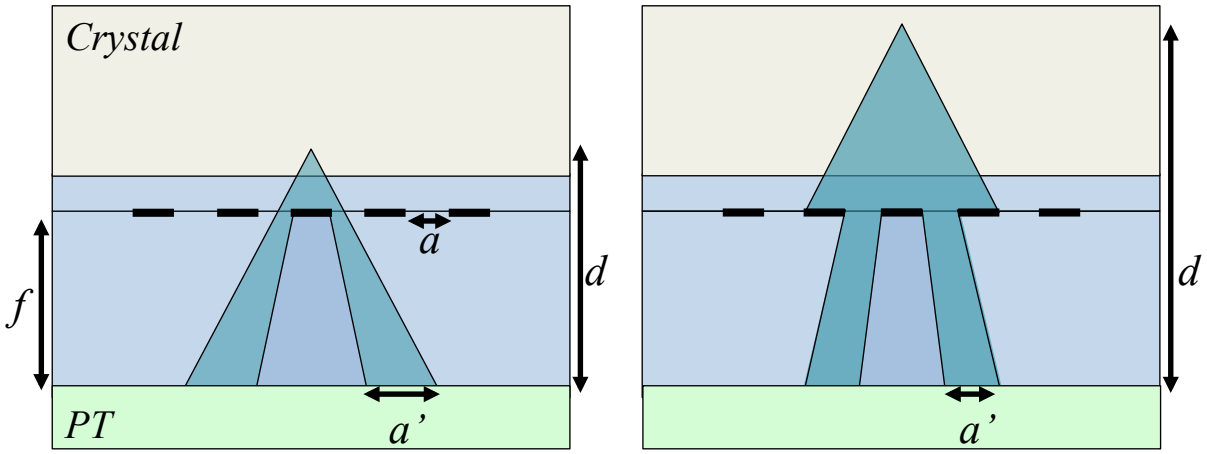

Figure 24. For an event at the bottom of the crystal, the light spot must project an entire mask pattern cycle in order to be able to do an image reconstruction. The magnification is the largest for these events. For an event at the top of the crystal, the PT must be able to resolve the magnified mask feature size a'. This means that the pixel size of the PT must be close to, or only slightly larger, than a'.

The other design consideration is important for coarse localization of events at the top of the crystal. Because we have many repetitions of the base pattern, we need to localize each event to

the correct one using only centroiding of the original light pattern (Appendix 1). This is hardest for an event at the top of the crystal since the light distribution is broader for those interactions. This sets a requirement that enough light must reach the face of the PT so that the event can be localized to the correct cycle of the mask pattern before performing the coded-aperture reconstruction. The mask feature size depends on the rank (base size) of the mask pattern, pixel size of the PMT and the minimum magnification for an event in the crystal. The rank is chosen from a set of known mask patterns and the pixel size of the PMT is restricted by the cost of readout electronics.

A full and comprehensive simulation study was performed and the methods used and results of the study are given in Chapter 4. This, along with analytic considerations discussed in this chapter are what dictated the design parameters of the first prototype (2-D localization) and final (3-D localization) system.

3.3. EVENT PROCESSING AND IMAGE RECONSTRUCTION

To explain how the images are created, this section will work in the purely theoretical case of a detector reading in data from the gamma-ray interactions modulated by the mask pattern. For now, the physical size and rank of the system are not important. The specifics of these parameters will be discussed in Chapters 4 and 5.

Once the data are collected, the events are parsed and assigned to the physical detector array. This array includes the gaps in the PMTs and the pixel geometry. The specifics of this procedure for all three cases (simulation detector array, 2-D system and 3-D system) will be explained in detail in Sections 5.1.A and 5.2.A. Once the data are assigned to the physical pixels, a coarse lateral position is found to determine the approximate center of the raw (pre-imaged) distribution. This gives a point in the lateral dimension (dimensions for the 3-D imager) that will be used for the entire depth range.

Once the coarse position is found, the detector data are rebinned in however many dimensions that the system laterally images (i.e. one-dimensional strips for the 2-D imager and two-dimensional squares for the 3-D imager). The size of the bins depends on the magnification given by the estimated depth that the reconstruction occurs. An image is then reconstructed at each depth over the range of the scintillator crystal, and the sharpest image (Section 3.3.B) is used as the best estimate of the event's depth. The absolute lateral information of the event is then found using the image at the best depth.

The next sections give each step in greater detail with visual examples.

3.3.A. COARSE LATERAL LOCALIZATION

In order to find the approximate center of the raw data signal and be sure the reconstructed image is linked with the proper cycle of the mask pattern, several methods can be used. Among them are a weighted mean, a two-dimensional Gaussian fit or a one-dimensional Gaussian fit of the collapsed data in each dimension. A visual representation of the Gaussian fit method for one-dimensional system is shown in Figure 25 (left) and an example of the same method is shown for simulation data in Figure 25 (right).

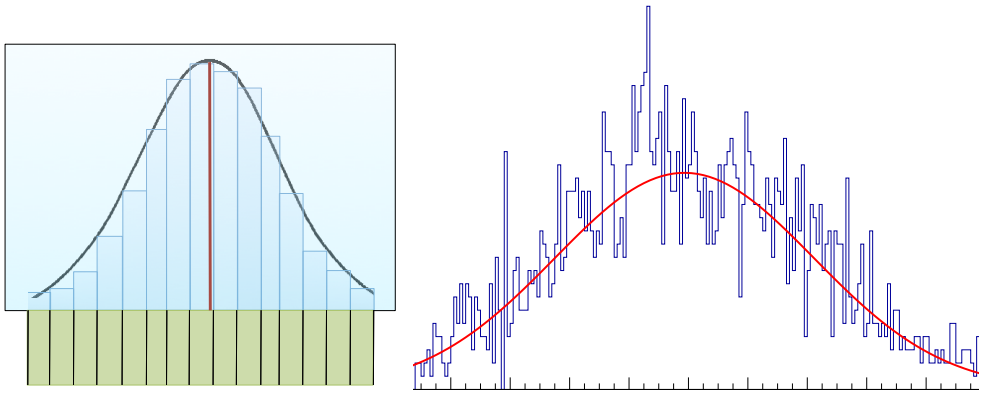

Figure 25. (Left) A one-dimensional example of how to find the coarse center of the distribution. The blue bars within the larger blue rectangle represent the response of a pixelated PT (Green rectangle where each section is a pixel) to a light event near the center of a crystal. The black curve is a Gaussian function fit onto the raw detector data. The center vertical line on the left is where the fit finds the approximate center of the signal. (Right) An example of a Gaussian function fit to a simulated pixelated PT response to an event in a scintillator with a mask pattern between the bottom of the crystal and the PT. Due to the modulation of the mask pattern, the fit provides a reasonable coarse localization but is statistically a poor fit. The simulation consists of 500 photons detected within a scintillator crystal in the geometry shown in Figure 24.

The simulation was performed with GEANT4 [75]. For this discussion, the relevant simulation

details are that 500 optical photons were launched from a single point within a crystal in the geometry shown in Figure 24. The PT had a finite pixel size and each bin represents one PT pixel. Fitting to the flux density expression in Appendix 1 was also tried as a coarse lateral localization method. The effectiveness of each of these methods will be discussed in the next chapter.

3.3.B. DEPTH DETERMINATION

Once the coarse horizontal center of the data is found, the detector data are binned at a certain bin size for each depth over the entire range of the crystal, and these rebinned data are used to construct an image. This is done by initially binning the raw data read out from the detector into bins that are the size of half of the magnified feature size in each dimension, or *a'/2*, centered around the coarsely found center. The magnification of the mask features are given by

$$m = \frac{a'}{a} = \frac{d}{d - f}$$

Eq. 71

and the size of the magnified feature by

$$a' = a\frac{d}{d-f}.$$

Eq. 72

By oversampling the data by a factor of two in each dimension, the image peak height versus reconstructed depth is less sensitive to events that fall between pixels, as opposed to centered in the middle of a pixel. The bin sizes relative to one another (PT pixels, magnified feature-sized bins and oversampled bins) are shown in Figure 26.

Once the data are binned for a given depth, an image is reconstructed. The general approach for reconstructing the image is described above (Section 2.3.A) and for our purposes uses the two-dimensional matrices where $I_{i,j}$ is the reconstructed image, $M_{i+m,j+n}$ is the mask function and $D_{m,n}$ is the rebinned detector. M_{closed} and M_{open} are determined by what kind of mask is being used (URA, MURA, etc.)

$$I_{i,j} = \sum_{m,n} M_{i+m,j+n} \times D_{m,n}$$

Eq. 73

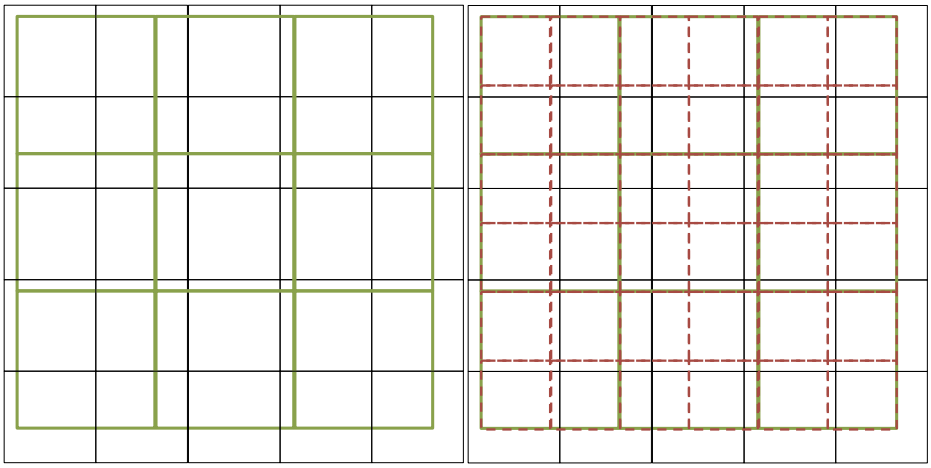

Figure 26. (Left) An example of a pixelated photo transducer in black with the magnified feature sizes overlaid in green. (Right) The rebinned oversampled magnified feature size (red) overlaid onto the detector and magnified feature sizes. The red bins are used for the image reconstruction and give better image pixel resolution compared to the larger magnified feature bins.

The uncertainty at each image pixel is determined by the total counts in the detector

$$\delta I_{i,j} = \sqrt{N}.$$

Eq. 74

The elements of the mask pattern that are used in the image reconstruction are determined by the coarse lateral position localization. The reconstruction is done around the center of the data and the image has a size of

$$2 \cdot rank - 1.$$

The physical position of the reconstructed image is known because the center of the reconstructed image corresponds to the absolute position of the coarse lateral localization as seen in Figure 27b (center). This will be discussed in detail in the simulation chapter below.

Once the image is reconstructed the data are rebinned to the magnification of the next depth and a new image is constructed there. This process is repeated over either the entire range of the scintillator crystal, or a limited region that is preselected based on the raw detector response before any imaging is performed. In certain cases a coarse depth location is estimated from the raw detector data and the depths that the event are imaged over are restricted to a distance less than the entire thickness of the crystal. Specific algorithms, and where they are applied, will be discussed in the Section 6.1.B.

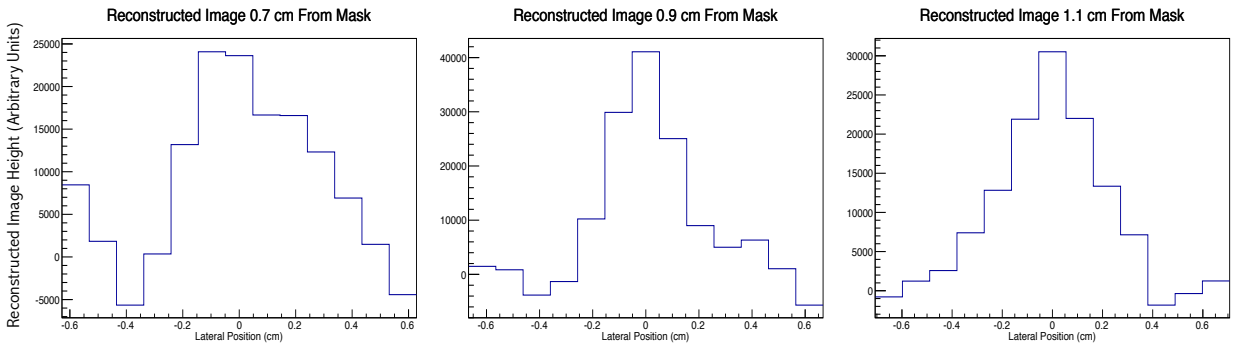

Figure 27. Some sample reconstructed 1-D images. These are from a GEANT4 [75] simulation for an event located at 0.9 cm from the mask. As seen in the images at 0.7 and 1.1 cm, the peak height is the largest at the true depth. This is how an image is localized in a crystal. This process and particular simulation data are described in much greater detail in Section 4.6.

For each image, the pixel with the maximum counts in the reconstructed image is recorded with the reconstructed depth. The event location is taken as the location of the maximum image pixel. The overall depth resolution of the detector is given by the width of the distribution in depth for many events.

3.3.C. LATERAL POSITION DETERMINATION

The coarse lateral position determination dictates which elements of the mask pattern the event is imaged around. After the coarse position is found and the depth determination made, the absolute lateral position is determined from the reconstructed image at the best depth. This can be done using several methods. The first option is to use a weighted mean of the image distribution. In one dimension this is a simple procedure to return a value from 0 to 2*rank-1 that gives the weighted mean of the image. In two dimensions the image pixels are collapsed in one dimension and the weighted mean of those collapsed elements gives the lateral position of the image peak. The entire image is not used; from an analysis of simulation data [75] it was found best results were obtained when using a smaller section of the image. For example, if the mask is a rank-7 mask, the image will consist of 13 × 13 image pixels. To compute the weighted mean in x we would use only the maximum bin position and one element on either side of the maximum of the collapsed x-histogram. This calculation is done independently in both the x and y dimensions to determine the two-dimensional event position. Another option for finding the lateral position of the peak is fit to a Gaussian. This may be done by either fitting a two-dimensional Gaussian to the imaged data, or by collapsing the data in each direction and fitting the collapsed distributions individually to a one-dimensional Gaussian. As in the weighted mean case, analyzing simulation data indicated that it is better to use a smaller segment of the image rather than the entire image for the Gaussian fit.

Once the lateral peak location is found from the reconstructed image, the absolute position of the image can be determined. The size of each image pixel for a given depth is known from the size of the mask element and the distance into the crystal the event occurred. Because the center of the image is located at the position of the coarse localization, the location of the peak in the image and the size of the image pixels give the absolute position of the event location. Like the depth measurements, the resolution of the imager is given by analyzing many events. The lateral event localization is described in detail in the simulation chapter below.

3.4. METHODS USED IN EVENT PROCESSING

3.4.A. REPEATING CYCLES

The fact that the mask pattern is a cyclic repetition of a smaller base pattern can be used to improve imaging abilities. This was originally shown in [13]. When an event occurs in the

scintillator crystal the entire mask pattern is projected onto the detector. The pattern directly under the event is illuminated most brightly, with outlying patterns progressively less illuminated the farther the patterns fall from the center of the event. Because the outer cycles are the same as the central cycle they can be used in the reconstruction to improve the peak-to-background count ratio in the image. This is done by adding all of the outer images to the center image; it has been shown effective in both simulations and the physical system. A quantitative discussion of the impact of this method is included in Sections 4.7.C (simulation) and 6.2.B (experimental).

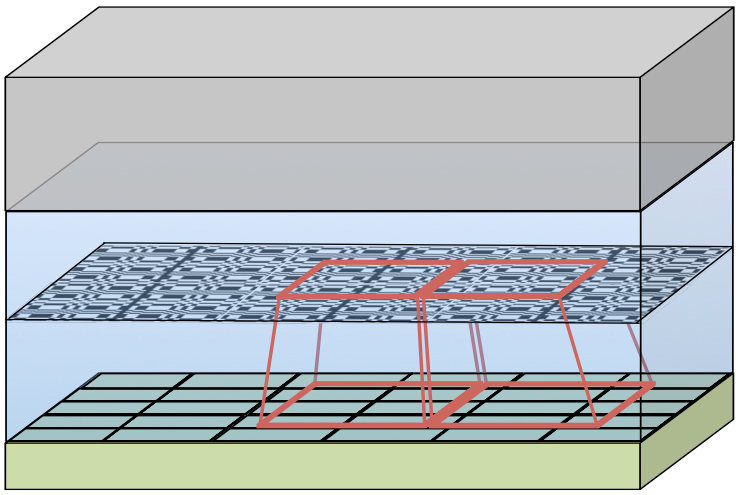

Figure 28. The center red square shows the central base pattern in the mask plane. When reconstructing the image, the outer cycles, such as the one in the red square to the right of the central cycle can be used in the reconstruction and help improve the peak-to-background ratio of the image.

3.4.B. INDEX OF REFRACTION DEPTH CORRECTION

As described above, as the light rays move from a higher index of refraction in the scintillator crystal (typically ~1.8) to a lower index of refraction of a quartz or glass light guide (~1.5), the rays bend outwards from the point of origin as seen in Figure 29.

As the detector sees the light after it has undergone the shift, the reconstructed image is in the

physical space of the lower index. Thus, this has an effect on the absolute depth reconstruction and the reconstructed event is found to be lower in the crystal than the true location. The relationship between the amount of light guide and the equivalent depth into a thick crystal was found using GEANT4 [75] simulations. This relationship is shown in Figure 30 and the slope is equal to 0.63.

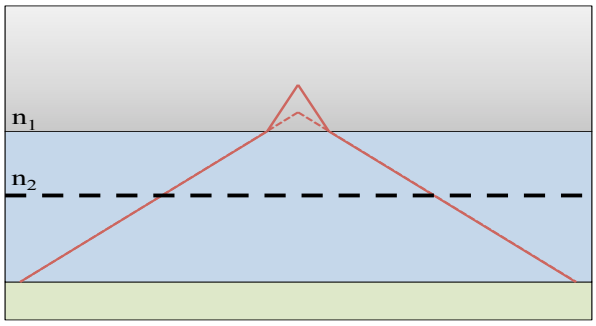

Figure 29. The light from the event in the scintillator crystal spreads outwards as it undergoes an index change from a higher to lower index. The image is reconstructed to a lower depth than it actually occurs. The point where the dashed lines converge shows where the image appears using the coded-aperture analysis.

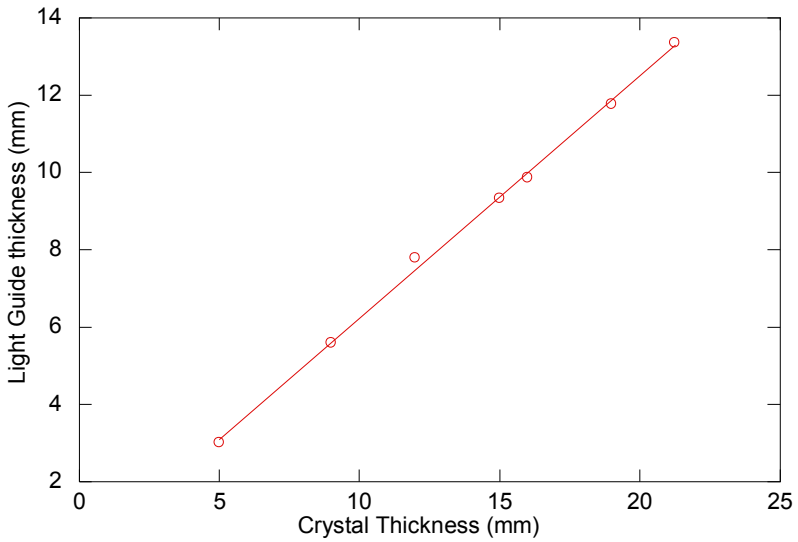

Figure 30. The relationship between an event's location in a thick crystal and the apparent location in a low index light guide. The slope is equal to 0.63.

This result has several effects on the system. First, the absolute reconstructed depth of an event is found to be at a lower depth relative to where it actually occurs. This effect has little to no impact at the bottom of the crystal (<1 mm from the upper light guide), as the resolution of the system is less than the correction factor. Second, two simultaneous events located at different depths are found to be separated by a smaller distance vertically than they actually are separated by. This is of particular importance as this system is designed to work as a Compton imager for simultaneous events. Finally, when a physical system is built, one effective way to obtain the imaging performance of the system is to restrict the actual event locations to within a thin crystal. For gamma-rays of energies of interest to this project, the gamma-rays interact uniformly within a thin (several mm) scintillator crystal. This can then be used to obtain a FWHM of a depth reconstruction distribution where the actual gamma-ray events are known to occur within the given range where the thin crystal physically exists. The index of refraction effect spreads out this measured result as it reconstructs to the lower index space without taking the higher index into account. The correction must be applied to the final results to obtain the imaging resolution.

CHAPTER 4. EXPERIMENTAL OVERVIEW

4.1. SYSTEM PARAMETERS AND SIMULATIONS

This chapter outlines the design parameters and component features needed to make the system work. This discussion will combine analytical concepts as well as simulation results simultaneously. In 2011, a feasibility study was performed by Klaus Ziock et al. to study concepts of the project. The study included extensive simulations into the crystal selection, mask pattern selection and physical geometry [13]. Between 2012 and 2014, Mark Harrison (ORNL), Donald Hornback (ORNL) and I investigated the project further and redeveloped these simulations. Unless cited to the original publication of the first simulation results, it can be assumed that simulation results are from the latter study.

4.2. SCINTILLATOR SELECTION

4.2.A. INTRODUCTION

Detecting radiation using scintillation light is one of the oldest methods used in the field. Knoll [6] describes the characteristics of desired scintillators. The kinetic energy of the incoming particle should be efficiently converted into detectable light, the amount of output light should have a linear relationship to the energy of the interacting particle, the material should be transparent to the wavelength of the output light as to allow highly efficient light detection, the decay time of the luminescence should be short to allow for quick pulses to be generated from the PT, the material should be able to be manufactured in the large areas required for practical detector designs, and the index of refraction should be near that of glass to allow efficient coupling to light guides and entrance windows of PMTs [6]. In practice, not all of these properties are relevant for all applications, and for this project in particular some factors are less important than others.

Organic-based liquids and plastics, and inorganic alkali-halide crystals are the most commonly used scintillators [6]. Inorganic scintillators generally have the best light output and linearity properties while organic scintillators are faster but yield less light. Also, inorganic scintillators generally have higher Z values and high density making them better for gamma-ray detection. As the work of this dissertation is for gamma-ray imaging, only inorganic scintillators will be reviewed.

4.2.B. MECHANISMS FOR LIGHT GENERATION

In a pure crystal lattice the energy band structure consists of a conduction band and a valance band. A particle can interact with an electron in the lattice and transfer its energy to the electron, which promotes it from the valance band to the conduction band. When the electron returns to the valance band a photon is emitted. In a pure crystal this is an inefficient process and the typical energy gap is too large for the emitted photon to exist in the visible range [6]. To create more effective scintillators, activators are added to sites in the lattice to create energy states in the crystal between the valance and conduction band that were previously forbidden. With the lower energy state, electrons from the valance band can be excited to the new energy states and emit photons in the visible spectrum when they de-excite.

When a charged particle passes through the scintillator, a large number of electrons are elevated from the valance band to the conduction band and, in turn, a large number of electron-hole pairs are created. The holes are the lack of an electron at a position in a material. Thus, they behave as positively charged objects that move inside the crystal. The positive holes drift to the activator sites and ionize them, as the ionization energies of the sites are less than that of the pure lattice sites. The electrons move through the crystal until they encounter the ionized activator sites and form a neutral configuration with its own set of excited energy states [6]. The activators are chosen so that these formed states are excited states that can decay to an activator ground state (higher energy than the valance state of the crystal) and emit photons in the visible range. These state transitions occur quickly; a single charged particle event can induce many emitted photons in the visible spectrum by interacting multiple times. Another possibility is that the electron-hole pair moves through the crystal in a loosely bound state; this is called an exciton [6]. It drifts until it reaches an activator site, at which point it can form an excited activator state and emit visible photons.

It is also possible for the free electrons to form states that do not have an allowed de-excitation to the activator ground states. These states require additional energy to be excited to a higher state that can then de-excite to the ground state. This extra energy is often thermal energy and this slows the de-excitation process and is the source of a slow component of the scintillator light emission called phosphorescence [6].

Yet another possibility is for an electron to be captured at an activator site for which there are allowed transitions between excited states and the ground state that do not emit visible photons.

This is called quenching and is equivalent to a loss in energy between the ionizing radiation and the scintillator emission signal.

By using activator sites to create scintillation light the crystal can remain transparent to visible light. In a pure crystal the energy required to excite an electron-hole pair is approximately the same as is released when the pair recombines. This results in the emission and absorption spectrums overlapping significantly and thus a large amount of self-absorption. With an activator added to a crystal the emission spectrum is shifted to lower energies, thereby significantly decreasing self-absorption [6].

4.2.C. EFFICIENCY

As mentioned above, scintillator crystals provide an extremely cost effective way to instrument a large area detector. In selecting the crystal, several factors were considered. To select the best material, the angular resolution (for a Compton camera) and detection efficiency should be optimized. A gamma-ray in a crystal can interact once in a crystal via pair production or photoelectric absorption, multiple times via Compton scattering followed by pair production, or photoelectric absorption. It is also possible for a Compton scattered photon to leave the crystal without depositing its full energy in a subsequent absorption event. For Compton imaging the most easily useable sequences are the Compton scattering-photoelectric absorption or Compton scattering-Compton scattering-photoelectric absorption ones. While these sequences can occur within very small distances, the realistically useable sequences are limited to events that are separated by our minimum spatial resolution in the crystal. Thus, the detection efficiency is given by

$$\varepsilon = \frac{N_{CS-PE}(r_{12}>r_{min})+N_{CS-CS-PE}(r_{12}>r_{min})}{N_{incident}}$$

Eq. 75

where $N_{CS\text{-}PE}(r_{12}>r_{min})$ is the number of Compton scattering-photoelectric absorption sequences with distances between the events greater than the minimum resolvable distance (r_{min}), and $N_{CS\text{-}CS\text{-}PE}(r_{12}>r_{min})$ is the number of Compton scattering-Compton scattering-photoelectric absorption events with distances between the first and second events greater than r_{min}. Mark Harrison performed a crystal selection study in GEANT4 [75] in 2012 to determine which crystal to use.

He used the parameters listed in Table 1. Each parameter was used with all of the others in every category; i.e. a simulation for each possible combination was run.

Table 1. Parameters and Intervals used in Crystal Selection Study. From July 2012 Project Review (Credit Mark Harrison)

Z	10, 25, 40, 55, 70
Density (g/cm^3)	2.25, 3.50, 4.75, 6.00, 7.25
Gamma-Ray Energy (KeV)	200, 400, 600, 800, 1000
r_{min} (mm)	1, 2, 3, 5, 10

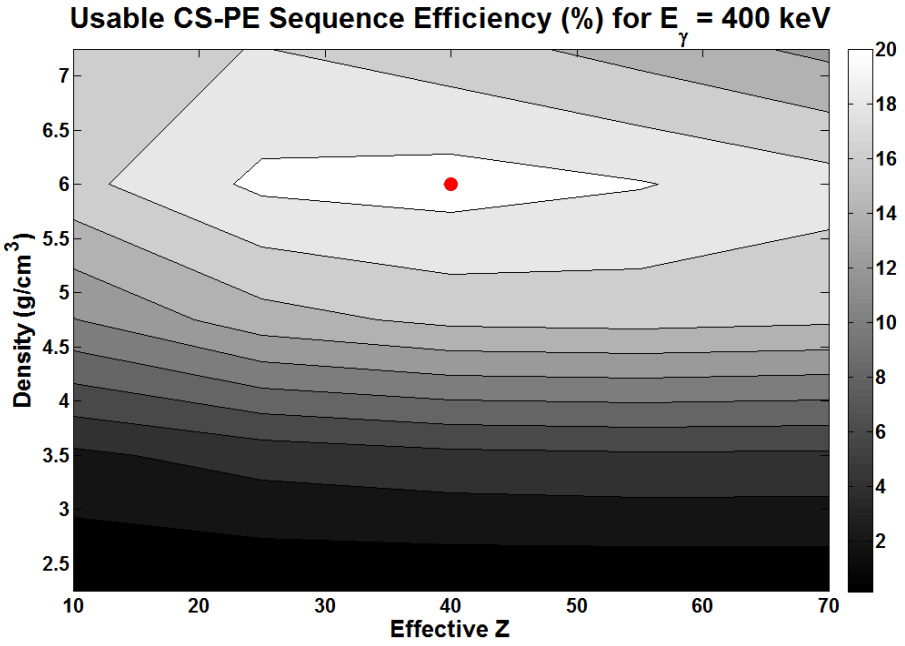

Figure 31. A greyscale map of the parameters described in Table 1. The maximum efficiency that can be obtained is approximately 20%. From July 2012 Project Review (Credit Mark Harrison).

The gamma-rays were normally incident onto a 3-cm-thick scintillator with area 50 x 50 cm^2. As seen in Figure 31, the optimal efficiency is obtained for density near 6 g/cm^3 and Z of 40.

Several materials were selected that had properties near the optimum range and are plotted in Figure 32.

Based on the results, the final crystals in consideration were Cesium Iodide (CsI(Na)) or NaI(Tl), and calcium fluoride (CaF_2(Eu)). CsI(Na) and NaI(Tl) output nearly the same number of photons and have nearly identical indices of refraction. The only practical difference between the two is that NaI(Tl) is more hydroscopic than CsI(Na). Thus, the simulation looked at CsI(Na), but the results apply to both crystals. CsI(Na) outputs about 40,000 photons per MeV (NaI(Tl) outputs 38000 per MeV), while CaF_2 outputs about half of that. The advantage of CaF_2(Eu) is that it has a lower index of refraction equal to 1.43, so by coupling it to a glass light guide the light losses from the index of refraction change are minimized. The challenge in this case is that CaF_2(Eu) produces half of the light per MeV of either CsI(Na) or NaI(Tl). Because of this and as seen in Figure 32, CsI or NaI(Tl) provide the best option for this application.

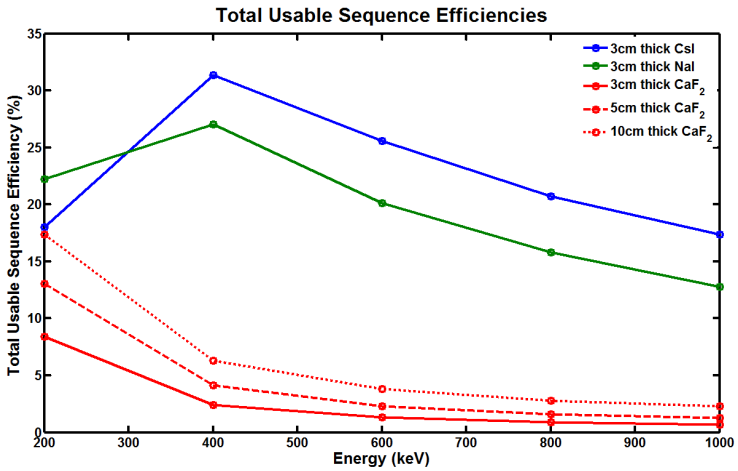

Figure 32. Total useable sequence efficiencies versus energy of the gamma-ray. While CaF_2 has an index of refraction of 1.47 that would minimize light losses from the smaller index change, the crystal outputs about half the number of photons per MeV of the gamma-ray, and the efficiency is much lower at energies around 600 keV. The low efficiency is a result of the low Z and density as the second photon escape probability is higher. From July 2012 Project Review (Credit Mark Harrison, ORNL).

4.2.D. LIGHT GUIDE MATERIAL

The motivations for choosing the scintillator crystal are discussed above. CsI or NaI(Tl) both provide good options for this project. While slightly different in light output (40k photons per MeV or 38k), the index of refraction is nearly identical. CsI(Na) and NaI(Tl) have an index of refraction of 1.84 and 1.85, respectively [76]. It is the high refractive index of these materials that are a problem. Several physical effects result in light losses at the optical boundaries of layer transitions; namely Fesnel losses and total internal reflection. Fresnel equations give the reflected and transmitted amplitude of the incident light based on the index of refractions of the first and second materials that the light moves through [77]. These are described in detail in Appendix 1 and were taken into account in developing the flux density expression used. Fresnel losses can be minimized by matching the indices of refraction of the materials. With total internal reflection, a fraction of photons are lost at the index boundary. This is discussed in detail in Section 4.5.

When optically coupling materials with different indices, a coupling compound is used to minimize light losses due to both Fresnel and total internal reflection. Ideally, to minimize Fresnel losses this material should have an index halfway between the two materials to be coupled, although practically it is frequently chosen with the index of one component or the other. In this case its use is simply to avoid an air gap (n=1), which would significantly worsen the coupling. Thus, there are three possible options in building the optics system (stack): standard optical coupling grease such as BC-630 [76] (n=1.5) can be used to couple the crystal to a quartz or glass light guide, a high index light guide such as sapphire can be used with a high index coupling compound, or a high index material can be used with a low index coupling compound.

Initially, due to the light losses from the index change, a high index light guide (n~1.8 [76]) such as sapphire was thought to be the best choice in order to minimize the overall losses. A search for a high index-coupling compound was conducted and only one candidate material was found. Cargille Labs [78] is the only manufacturer of a commercially available high index optical coupling material. A sample of their high index optical grease with n~1.8 was ordered and measured for its transmission to light in the visible spectrum using an Absorption Spectrometer by the Physical Organic Chemistry Group at ORNL [79]. As seen in Figure 33, the material is not suitable for use with either the CsI(Na) (peak emission 420 nm) or NaI(Tl) (peak emission 415 nm) due to its high absorption in the blue portions of the spectrum.

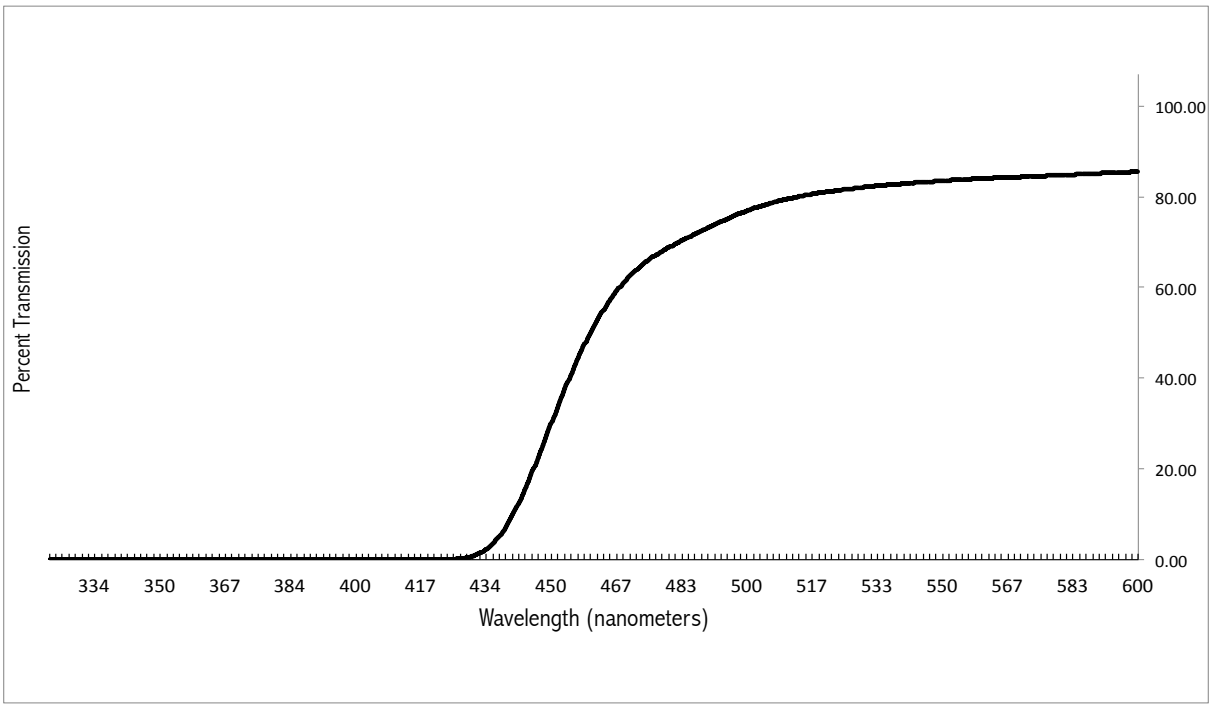

Figure 33. The measured percent transmission vs. wavelength for a 2 mm thick cell of the high index Cargille material. Depending on the type of doping material used (CsI(Tl) or CsI(Na)), the crystals have a wavelength of emission maximum at 420 and 500 nm respectively [93]. As seen in the plot, the transmission drops to ~50% around 450 nm, making it unusable for photon starved applications.

This coupling compound was the only high index material available; thus, BC-630 was chosen as the coupling medium. However, once a single low-index coupling joint was included, the simulations showed that all benefits from a high-index light guide were lost. Hence, quartz was selected as the light guide material due to its good light transmission across the visible wavelength range and its index of refraction close to that of BC-630.

In addition to the light loss from the index change, we note that there is a distortion of the projected mask pattern when light is transmitted from the high index crystal to the lower index light guide as shown in Figure 34.

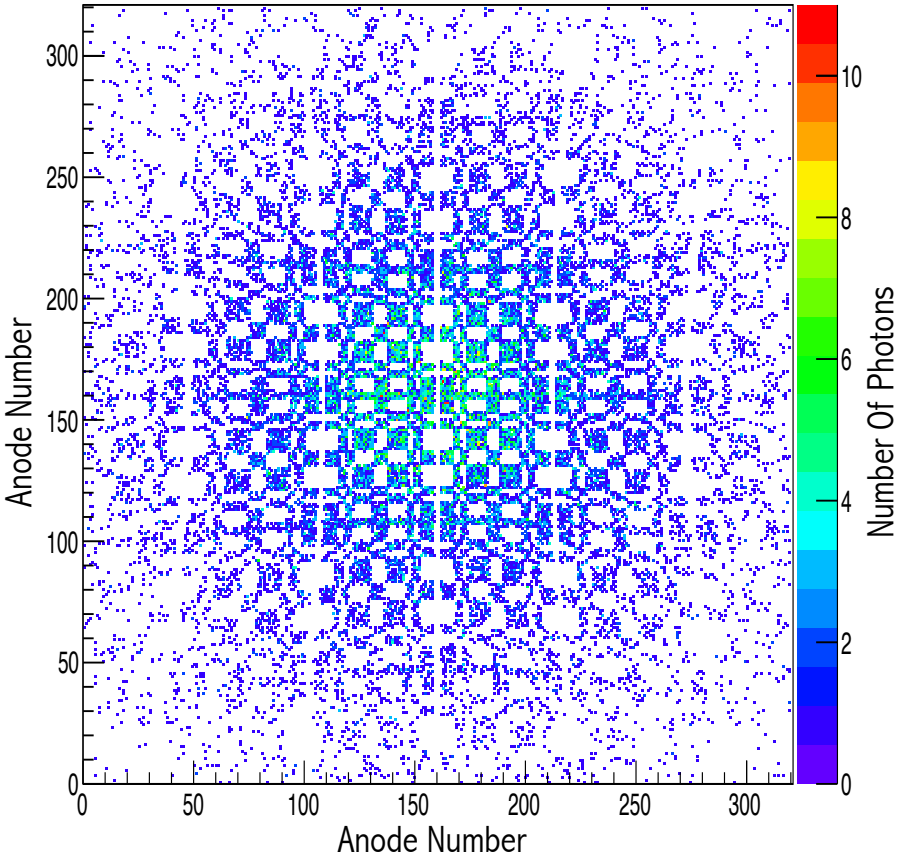

Figure 34. The detector pattern with an ideal 0.8 mm pixel PT array for 40k launched photons from a single point (lateral position of (160,160) 20 mm from the bottom of the crystal. The physical setup is the same as that shown in Figure 24 with a rank-17 mask, 1.0 cm light guide between the bottom of the crystal and the mask pattern, and 2.2 cm between the mask and the PT plane. The detector response clearly shows a warping of the light signal due to the index change that is more pronounced further away from the photon launch point.

The image was generated using the second generation of Monte Carlo simulations for the optical coded-aperture system. The simulation consists of 40k photons launched from a single point 20 mm into a CsI(Na), which is optically coupled to a quartz light guide with a 1.4 mm feature size, rank 17 MURA mask pattern 1.0 cm below the bottom of the crystal. The PT plane is located 2.2 cm below the mask pattern. The PT plane has an ideal array of 0.8 mm square pixels. There are no gaps or non-uniform pixels throughout the detector array.

Figure 34 conveys the warping of the light signal due to the index change. While it does distort the signal, the cross-correlation reconstruction method discussed in Section 2.3.A. has been shown to work with no high-impact negative effects from the index change. While it is possible the index change may affect the ability to use outer mask cycles due to the warping of the pattern, this was not found to have a significant impact in simulation data. Additionally, only the center cycle and outer ring of cycles are used, so the most extreme effects towards the edge of the image in Figure 34 do not impact the image reconstruction.

4.3. PHOTOTRANSDUCER REVIEW

The phototransducer must satisfy several requirements. It must have a low dark count rate due to the small number of photons that will reach the PT plane from the scintillator crystals selected, and, in turn, must be able to detect on the order of single photon signals. It also must have a small pixel size in order to resolve the magnified features of the mask pattern. Finally, it must be cost effective to instrument a large-area detector. There were several options considered for this project; silicon photomultipliers (SiPT), charge-coupled devices (CCD) and electron charge-coupled devices (emCCD), and pixelated photomultiplier tubes. As described above in the scintillator section, for gamma-rays of energies relevant to national security applications of several hundred keV, a scintillator crystal typically outputs a few hundred photoelectrons resulting in several thousand photons. This is one of the primary factors in considering the type of PT to use. Accounting for all factors in which the light is lost from the crystal to PT plane, the resultant signal is on the order of a single photon per mm^2.

4.3.A. SILICON PHOTOMULTIPLIERS

As with all of the PTs discussed, the SiPT converts photons into an electric signal. The photons emitted from a scintillator crystal are incident on silicon, which due to its photon absorption spectrum in the visible light range makes it useful for detecting light emitted from the selected scintillator crystal [6]. A photon interacts with bound electrons in the valance band of the material, moving them to the conduction band.

The silicon consists of an n-type side and a p-type side. The n-type side conducts electrons while the p-type side conducts holes. When a positive voltage is applied to the n-side of the material, the natural potential difference between the regions is made larger, allowing for a net current from the movement of electrons to the n-type material and holes to p-type material. With

a large enough applied electric field the charge carriers can create secondary charge pairs (electrons and holes) through impact ionization that amplify the signal. For a thick enough amplification region, this process repeats and an ionization cascade is created [80]. Thus, a large current can be obtained from a low initial photon signal. In a SiPMT, this operation works as an on or off signal of photon detection [80], while in an avalanche photodiode (APD), the device is designed so the output signal is proportional to the number of input photoelectrons. (These devices are too expensive for instrumenting a large area system).

In a SiPMT, arrays of densely packed and individually isolated photodiodes (each called a microcell) allow for a PT that gives a signal proportional to the number of photons detected. These typically have 100 to 1000 photodiodes per mm^2 [80]. The signals from all of the microcells are summed and this allows for an analog-type signal based on the number of incident photons [80].

Thermally excited electrons that then cause a cascade through the semiconductor material are responsible for the primary noise in SiPTs [80]. The noise is typically about 100kHz/mm^2 [80], making them unsuitable for extremely low light situations. The cost of these detectors is also high at about \$1000/cm^2 [13]. Thus, instrumenting a large area for this project would result in both large noise signals and an unfeasible cost.

4.3.B. CHARGE-COUPLED DEVICES

Charge-coupled devices (CCDs) were developed in the 1970s by researchers at Bell Laboratories. The fundamental principles concerning the light interaction mechanism that govern their operation are similar to those of a SiPT; however, the signal production from the light uses different principles. As discussed above, atoms in a silicon material have electrons in discrete energy bands known as the valance and conduction bands. An incoming photon interacts via the photoelectric effect and excites an electron from the valance band to the conduction band. In a CCD, a gate, held at a positive voltage relative to the rest of the device is connected to the semiconductor material by an insulator. The electrons are held in place by the positive charge of the gate and because of the insulator cannot move through the separating plane. Once the image is captured on the entire surface, the voltages of the gates adjacent to the pixel being read out are shifted and the electrons migrate in the direction of a readout system at the end of a row of pixels. The rows are read out in two directions; the parallel direction and serial direction. The

parallel direction moves the captured electrons line by line to be readout by the measurement electronics. The serial direction reads each line to the measurement electronics.

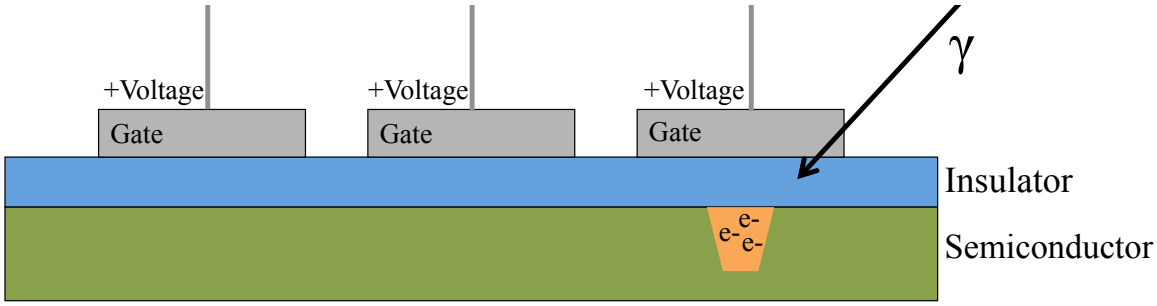

Figure 35. Diagram of the operation of a CCD. The gamma-ray interacts via photoelectric absorption in the semiconductor and frees electrons. The electrons are stored in a potential well due to the gates being held at positive voltage relative to the semiconductor. The voltages of the gates are then shifted one by one so the electrons are moved to readout electronics. This process is repeated for multiple rows of gates to give a two-dimensional signal.

Like SiPTs, because CCDs use silicon as the charge generator they suffer from large amounts of thermal noise. These thermally excited electrons cannot be distinguished from the actual photo-electrically excited electrons. Cooling the CCDs significantly helps this problem. For every 6-7° C of cooling there is about a two-fold reduction of dark current [81]. Practically this is a challenging problem, especially when using the devices in a detector to be used in the field. Additionally, with slow read times the noise can be reduced.

CCDs typically are able to have very small pixel size. Current devices can have pixels as small as 3 x 3 μm^2 [82]. These can be coupled together in order to form larger pixel sizes. While the pixel size is excellent, for this project the slow readout time in addition for the need for a large number of CCD's coupled into larger pixels would be impractical.

Due to the method of reading out the signal and the typically large amount of pixels, readouts for a full frame of a large area CCD are usually only able to read about 1 image (or event) per second [6].

4.3.C. ELECTRON MULTIPLYING CHARGE-COUPLED DEVICES

Andor Technology first introduced the electron multiplying charge-coupled device in 2001 [82]. They work the same as conventional CCDs but have a multiplication register placed between the serial register and the signal output amplifier. While CCDs are unable to resolve signals on the order of single photons due to their high thermal noise and lack of amplification system, emCCDs are very good at detecting low light signals.

The gain register works in a similar manner of the other registers. As the charge is moved through the register, two pixels at a time act to both move and amplify the signal. One is held at a voltage that is responsible for moving the charge along the register to be read out (the voltage electrode). The neighboring pixel is held at a much higher voltage (usually 40-60 V) in order to accelerate the charge through register (the clocked electrode). The large electric field between the two pixels amplifies the signal through impact ionization. The impact ionization gives the emCCDs large gains, making these devices a good choice for low signal applications. However, they are too expensive for use in this application.

4.3.D. PHOTOMULTIPLIER TUBES

Photomultiplier tubes coupled to scintillator materials provide an effective way to detect radiation and are the most widely used method in the field. A photomultiplier tube consists of two main components; the photocathode that converts individual photons to free electrons and an electron multiplying system that amplifies the number of initially freed electrons, between the photocathode and the readout stage [6]. The photocathodes available can be sensitive to photon energies as low as the near infrared range and as high as the ultraviolet range of the electromagnetic spectrum.

The scintillation photons initially interact with the photocathode via the photoelectric effect. The energy that can be transferred to the electron is determined by the energy of the incident photon energy. The freed electron then migrates to the surface of the photocathode, and under an applied electric field moves into the vacuum that the photocathode exists in. It is then guided by focusing electrodes to the first dynode stage [6]. Once the electrons are emitted from the photocathode and accelerated to the first dynode they must be multiplied to increase the signal. The emitted photoelectron typically has a kinetic energy of about 1 eV. The dynode is held at several hundred volts so that the photoelectron is accelerated towards it and gains a significant

amount of kinetic energy by the time it reaches it. The dynode material usually has a bandgap of 2-3 eV, so to create an excited electron the initial photoelectron must have a kinetic energy greater than this. Because the dynode is held at a high voltage the photoelectron can create many secondary electrons. However, the secondary electrons are emitted in random directions, and due to interactions within the material many do not have enough energy to overcome the work function when they reach the material barrier. For standard dynode materials and incident photoelectron energies, the ratio of emitted secondary electrons to one incident photoelectron is 4-6, but can be as high as 10 for higher energy incident electrons [6]. The dynodes are repeated in order to gain large responses for a single incident photoelectron on the first dynode. This value is defined as

$$\delta = \frac{number\ of\ secondary\ electrons\ emitted}{primary\ incident\ electron}$$ [6].

Eq. 76

In reality, δ is not a constant but depends on the initial number of incident electrons. Also, the number of secondary electrons emitted is a statistical process that follows a Poisson distribution [6]. For a photoelectron incident on the first dynode, the number of secondary electrons emitted has a mean value of δ with a standard deviation of $\sqrt{\delta}$. The variance is equal to $1/\delta$. For *N* identical processes (dynodes), the mean number of final electrons is given by δ^N. From Poisson statistics, for *N* dynodes the variance is given by [6]

$$\frac{1}{\delta} + \frac{1}{\delta^2} + \frac{1}{\delta^3} + \cdots + \frac{1}{\delta^N} = \frac{1}{1-\delta}.$$

Eq. 77

For small δ, the distribution width of the final output pulse recorded is dominated by the first dynode electron output. Conventional dynodes typically have $\delta = 5$, while negative electron affinity (NEA) materials can have $\delta = 25$ [6]. In an NEA material there are added acceptor sites due to doping the material with something such as gallium phosphide. This brings the vacuum potential to escape from the material below the conduction band, allowing electrons that are excited to the conduction band to escape the material as long as they can move to the surface of the material. This allows for many more secondary electrons to be emitted and, in turn, higher

gains. In a typical PMT, there are 10 stages with $\delta = 5$, which results in a gain of about 10^7. This is the basic operation and gain multiplication method of the PMT. Now, moving back to the initial signal collection, the first stage is discussed.

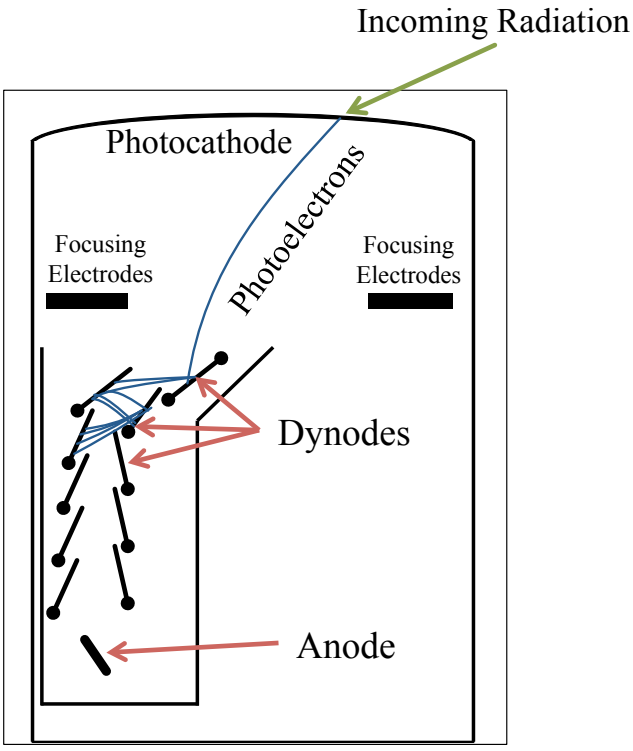

Figure 36. Adapted from [6]. An incident photon interacts with the photocathode and frees electrons that are then directed to the first dynode. The dynode material reemits more electrons than were incident on its surface. This process is repeated through the dynode chain until the charge is collected on the anode and an output signal is collected.

At the first stage, for the electron to overcome the potential barrier that exists at the boundary of the material to the vacuum it must have energy greater than the work function of the material. The energy available is the energy of the incident photon ($h\nu$, where h is Planck's constant and ν is the frequency of the light) minus the work function of the material. A typical signal from a photocathode depends on the quantum efficiency of the material. The quantum efficiency, or

ratio of emitted photoelectrons to incident photon number, is one of the more important parameters in choosing a photocathode material. A quantum efficiency of 0.2 (20%) results in 1 electron per 5 incident photons. Commonly used photocathodes are currently able to obtain quantum efficiencies of 20-30%, with more recent work obtaining values as high as 40% [6] [83]. Most common PMTs use one of several standard photocathode materials. Solar Blind photocathodes are more sensitive to UV light and have a lower wavelength cutoff of about 200 nm [89]. The two most common photocathode materials are S11 (SbCs) and Bialkali (Sb-K-Cs). The S11 was developed first and is rarely used today as Bialkali has better response in the 400 nm range where most scintillators emit, with lower thermal emission rates. Hamamatsu has also developed Ultra-Bialkali and Super-Bialkali, which have wider spectral ranges of sensitivity (from UV to 850 nm) and higher quantum efficiencies in the visible region.

For a standard photocathode material using a compound such as Bialkali, the work function is between 2 and 2.5 eV. The electron may lose energy through electron-electron collisions before it escapes to the vacuum [6]. Because of this, the rate of energy loss that electrons experience as they move through the photocathode material to the vacuum should be as low as possible so that electrons freed from photoelectric interactions are able to escape the material.

In addition to the wavelength sensitivity for photoemission and the rate of electron interaction, spontaneous electron emission also plays an important role in selecting a photocathode material. Thermal conduction electrons in the conduction band of the photocathode material have energies of about 0.025 eV [6]. However, it is possible that some conduction band electrons have thermal energies high enough that they may overcome the work function and be spontaneously emitted. In metals, the emission rate is about $100/m^2s$. Semiconductors have a lower work function and, in turn, much higher thermal emission rates. Thus, metals are better choices when working with low light signals.

The most common type of noise in PMTs is due to the thermionic electrons emitted by the photocathode. In this case the noise signal is that from a single electron, and most of the time it is easily discriminated against an actual signal. In cases where one wishes to detect signals from a single electron, as the number of thermionic electrons emitted is proportional to the photocathode area, the PMT with the smallest photocathode area should be selected for the application [6].

4.3.E. MULTIANODE PHOTOMULTIPLIER TUBES

For this project the photo transducer must have a small enough pixel size to resolve the magnified mask features, so a standard PMT will not work. Knoll lists many commonly used PMTs with the smallest having a diameter of 10 mm. Position-sensitive photomultiplier tubes (PSPMT) were designed in order to have a PMT device that is able to have spatial resolution where an incident photon on one part of the device can be localized to a region smaller than the overall size of the tube. The way these devices work is that the photocathode is placed closely to a focusing mesh that directs photoelectrons to the first dynode.

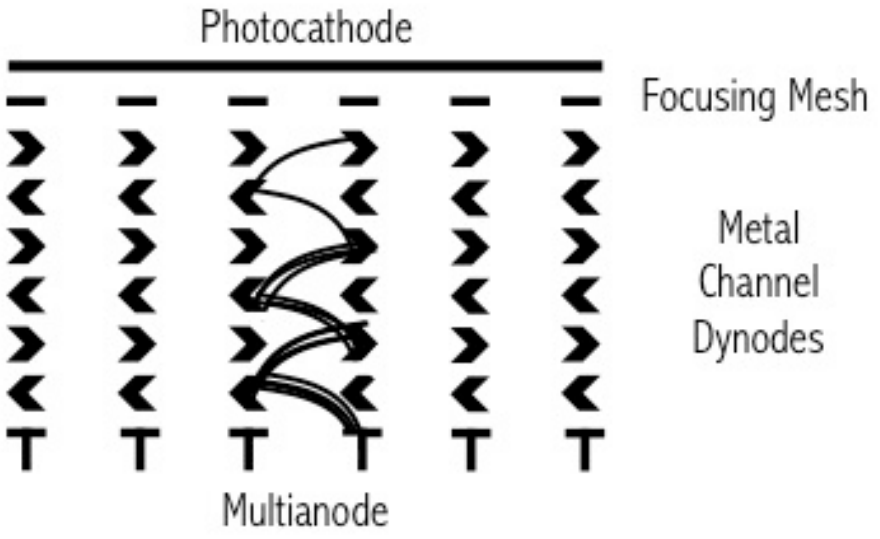

Figure 37. Adapted from [83]. A multianode PMT schematic. The incident photons interact with the photocathode at the top and electrons are directed to the dynodes.

The signal is then multiplied to the following dynodes in a spatially coherent structure that has minimum spatial spread of the freed electron signal. The signal is then read out at a multi-anode plane with pixelated anodes as seen in Figure 37. Hamamatsu Corporation [84] is a main manufacturer of this type of PSPMT. They offer options with pixel sizes as low as 3.04 x 3.04 mm^2. The gain of these devices is similar to that of standard PMTs. Current devices using

materials such as Super-Bialkali and Ultra-Bialkali are able to achieve quantum efficiencies as high as 43%. These are currently available in multi anode PMTs [84].

While these photo transducers are appealing in terms of small pixel size, low noise (the same as a standard PMT) and ease of use and instrumentation, issues such as pixel crosstalk, non-uniform gain across the channels, and dead space on the outer edges are all important factors.

4.4. PHOTOTRANSDUCER SELECTION

For this project there are several factors that drive the choice in selecting a photo transducer. The PT must have a small enough pixel size so that it can resolve the minimally magnified mask features for events at the top of the crystal. It also must have a low dark count rate (i.e. low thermionic noise) and be able to be instrumented in a large array with minimal dead space between individual PT elements. Additionally, the device needs to be capable of detecting low light signals ($O(1)$ photon). The readout time is also important; the ideal system has an event detection rate of 10,000 events/second, so a fast readout time is required. All of these factors make a pixelated PMT the best option for this system. Their low noise, ability to detect low light signals (see Section 4.5.A), fast readout rate, and ability to be closely coupled in a large array give the system the best overall performance at the PT plane.

Specifically, these requirements make the Hamamatsu 9500 a good choice for this project. The size of the face of the PSPMT is 52 x 52 mm^2 with an active area of 49 x 49 mm^2 [85] [84]. Each pixel is 3.04 x 3.04 mm^2, except for the outer square of anodes, which have pixel sizes of 3.22 x 3.22 mm^2. Because there is only a 1.5 mm dead space on the outer edge of the device, they are easily arranged in a large array with dead areas comparable to a pixel size. The quantum efficiency and sample gain uniformity across the face of the PSPMT are shown in Figure 38.

These devices satisfy all of the requirements for the project. They are able to be placed in a square array with a very small dead space between modules, have small and nearly uniform pixel size, and are very easy to maintain in the field (no cooling, leaking, etc.) and are sensitive to the wavelength of light that the chosen crystals, NaI(Tl) or CsI, output.

4.4.A. SINGLE PHOTON RESPONSE

To investigate the single photon capabilities of the H9500, a study was performed in Spring 2012 at ORNL. The motivation for this study was to confirm that the H9500 could indeed detect single photons localized to a single anode. NaI(Tl) produces on average 38k photons per MeV of

incident photon energy. For this system, half of the light goes up away from the photo transducers, the remaining signal decreases by ½ because some is blocked by a ~50% opaque shadow mask pattern, the signal again decreases by ½ due to the index of refraction change from the crystal (n=~1.8) to the lightguide (n=~1.5), and the PMT has a quantum efficiency of about 20%. This results in several hundred photons distributed across the entire face of the PMT array with individual anodes being required to detect a maximum of *O*(10) photons.

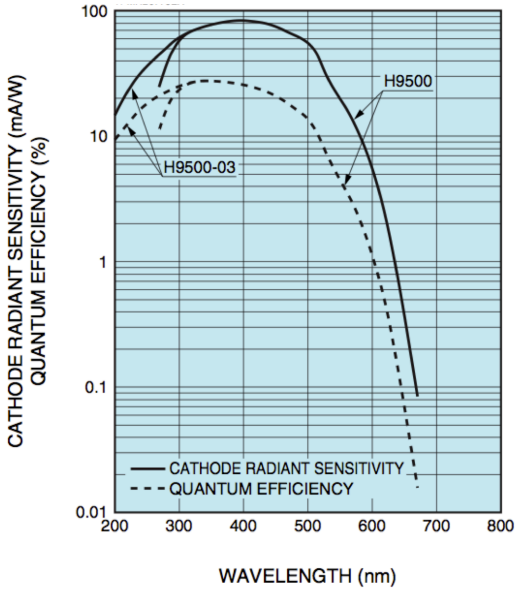

78	78	86	79	83	92	92	92	93	90	91	93	88	87	77	84
79	77	77	74	81	87	91	91	87	85	80	80	69	69	74	83
72	43	74	77	86	91	96	99	100	97	90	76	54	59	80	85
63	61	66	67	71	77	80	89	94	90	84	74	51	51	79	87
52	52	57	58	63	69	74	80	83	84	84	77	63	59	78	88
50	48	52	53	61	66	67	76	78	78	79	83	71	68	79	89
46	44	48	49	57	57	61	69	74	71	74	84	73	73	82	90
43	41	44	46	54	55	59	66	71	72	75	84	78	72	79	93
42	38	43	45	51	54	57	62	69	70	76	86	77	71	77	92
39	39	43	44	50	53	55	63	71	71	73	85	71	67	77	94
39	39	42	44	51	56	55	65	73	71	75	83	68	58	77	94
39	39	42	42	49	57	64	70	78	79	79	79	64	53	75	91
38	39	44	44	50	56	64	71	82	81	81	79	64	55	74	84
38	42	48	52	58	63	72	79	83	80	79	80	71	69	72	79
35	38	48	51	54	56	61	62	71	69	68	71	63	59	55	66
29	40	53	52	55	57	58	55	65	60	59	65	61	61	52	48

Figure 38. From [85]. The quantum efficiency (left) and gain map of a typical H9500 (right). The quantum efficiency shows a response peaked at the typical output wavelength of scintillators like NaI(Tl) and CsI(Na). The anode uniformity map given by Hamamatsu was made using a 3 mm square blue light signal. The signal varies by as much as 3 on the outer edges. Other studies have measured variations as large as 1:4 [85] [84].

For the study, a H9500 was mounted in a light-tight box with an LED diode mounted several cm above it as seen in Figure 39. The LED was driven by a function generator at 1 kHz and made to pulse and output a single or double photon with each 10-ns-wide pulse.

The waveforms were recorded with a Strück 3305 waveform digitizer [86] and the triggering was done with the output of the pulse generator (a forced trigger). Initially, the dark count rate

of the PMT in coincidence with the LED trigger (the LED itself was turned off but the trigger pulse to the PMT was turned on) was measured to ensure the last dynode triggers were only causing true signals to be recorded. For an hour-long data set, only three waveforms were recorded with maximum waveform amplitude height much lower than that of true signals (~250 arbitrary units compared to ~500).

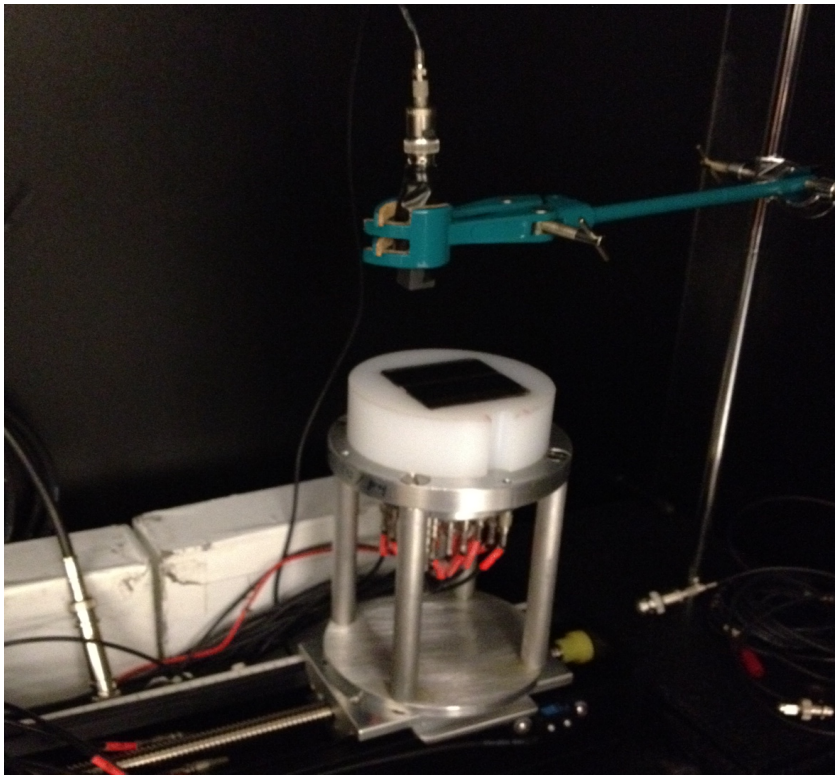

Figure 39.The apparatus to measure the response of the H9500 PMT. An LED was mounted above the PMT in a light tight box. The PMT was read out using a custom board to read the center 16 anodes (a 4 x 4 square). The signals were then connected to a waveform digitizer. These waveforms were then analyzed using a constant fraction discriminator function implemented in software [6].

Once the noise was verified to be low relative to the true signal, the LED was turned on and the system recorded waveforms from the collimated LED. The recorded waveforms fell into

three classes; true single-photon waveforms, "stacked" double-photon signals, and waveforms with pileup. Sample waveforms for each case are shown in Figure 40.

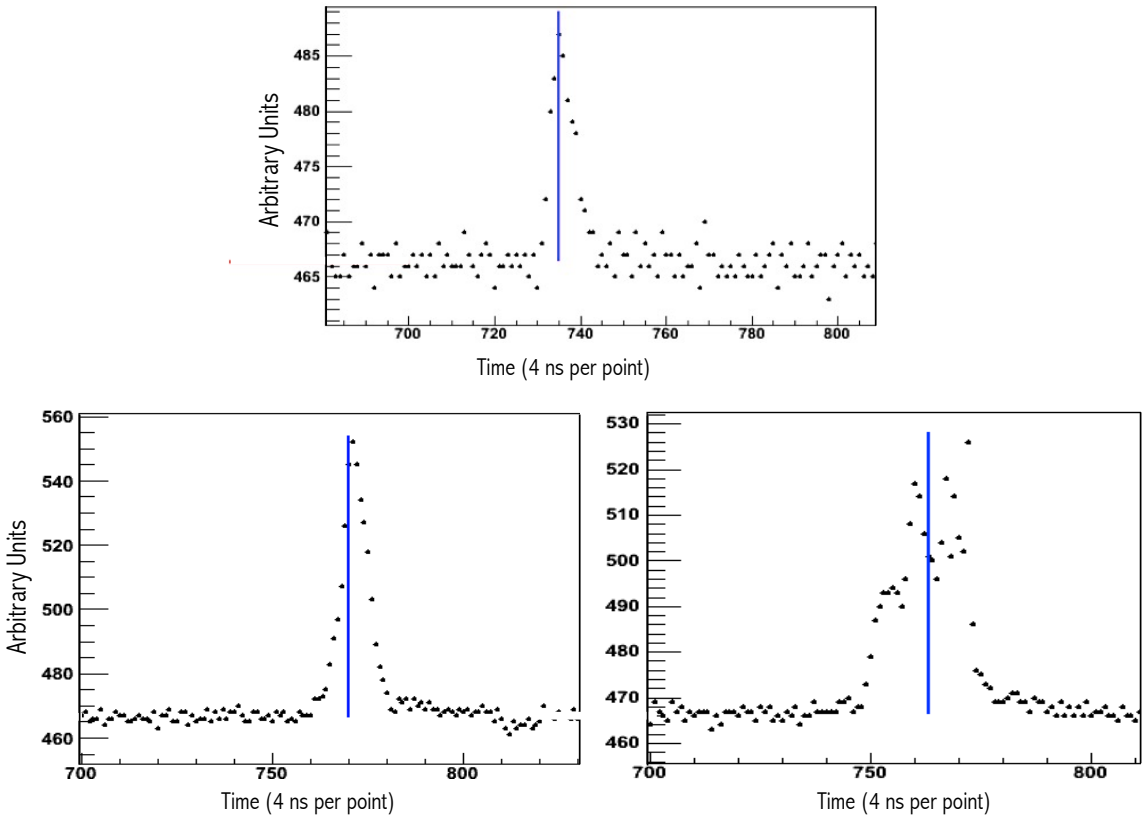

Figure 40. Three classes of waveforms were observed in the H9500 output signals. The true single photons are shown in the top waveform. This class of waveforms was demonstrated to truly be single-photon responses through the use of neutral density filters (discussed below). The lower left waveform has the same structure as a single photon, but the amplitude indicates a double or triple photon signal. The lower right waveform is a "stacked" signal. This was due to piled up photons (i.e. not clean single or double photon outputs from the LED). In each case, the blue line is where the software found the peak.

To differentiate between the different types of signals, two parameters were optimized so that only the single photon signals were selected. The peaks were integrated and the value of the integral in addition to the width (half width) was selected so that the double signals and stacked

signals were filtered out. Once these parameters were selected, a neutral density filter with a light transmission value of 0.502 was placed between the LED and the H9500. If the LED were truly outputting single photons, a histogram of the number of counts per channel (integrated waveform value) would be reduced to half as many counts for data sets with the same number of triggers, while the location of the peak would not shift. Figure 41 shows the histograms for each case.

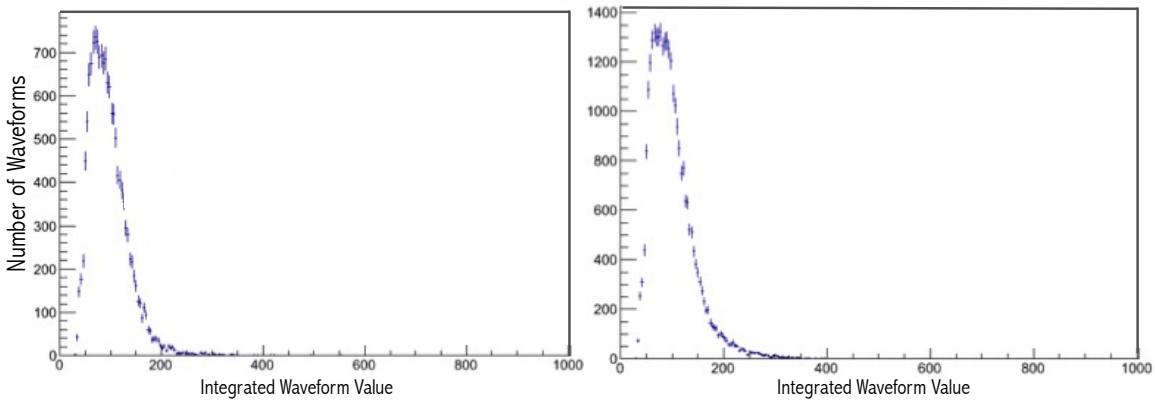

Figure 41. The left histogram is with the 50% transmission neutral density filter between the LED and the H9500. The right is without the filter. Each data set contains the same number of LED pulses. Each entry in the histograms is the integrated signal per waveform for one event. Because the total number of LED events is the same in both data sets (i.e. histograms) and one has a 50% light transmission filter above the PMT, the number of single photon events recorded by the PMT is reduced by two with the filter, as half of the single photon pulses are absorbed in the filter. In other words, half of the LED pulses are not captured by the H9500 and are absorbed in the filter, while those that make it to the PMT have the same integrated waveform values.

This study proves the H9500 is capable of detecting single photon pulses and is adequate for this project's photo transducer requirements.

4.5. SIMULATIONS

With the scintillator crystal, PT device and light guide material selected, the system was ready to be studied with extensive simulations. The parameters such as the mask rank, mask feature size, distance between the bottom of the crystal and the mask, and the distance between the mask and PT plane (called the focal length) are all included under the moniker of "optical geometry".

As discussed above, two separate simulation studies were performed. Both were done using GEANT4 [75]. While the first established the concept as feasible, it did not take into account a realistic detector array. Thus, the second, which included this effect and was part of this dissertation work, will be discussed in detail. The earlier simulations are described in [13].

The simulations were originally developed by Mark Harrison (ORNL) in 2012 and adapted in 2013 to include visualization tools and two-dimensional mask pattern capabilities. Monochromatic photons were launched from a single point inside a scintillator crystal. The scintillator, optical coupling layers and light guide materials were all set to materials included in the GEANT4 [75] framework; this dictated several parameters such as the index of refraction, density, light transmission, etc. of the materials. A wide range of optical geometries were considered, with each layer using the parameters listed in Table 2.

Table 2. The parameters used in the GEANT4 simulations. The photons were launched in the crystal in all directions, as seen below in Figure 42. Each material was given an elemental composition as indicated.

Material	**Density (mg/cm^3)**	**Index of Refraction**	**Element Composition**
NaI(Tl)	3.76	1.8107	Sodium, Iodine
Light Guide	2.203	1.466	Silicon, Oxygen
Optical Grease	1.06	1.471	Carbon, Hydrogen, Silicon

An image from the simulation with varying numbers of launched photons is shown in Figure 42.

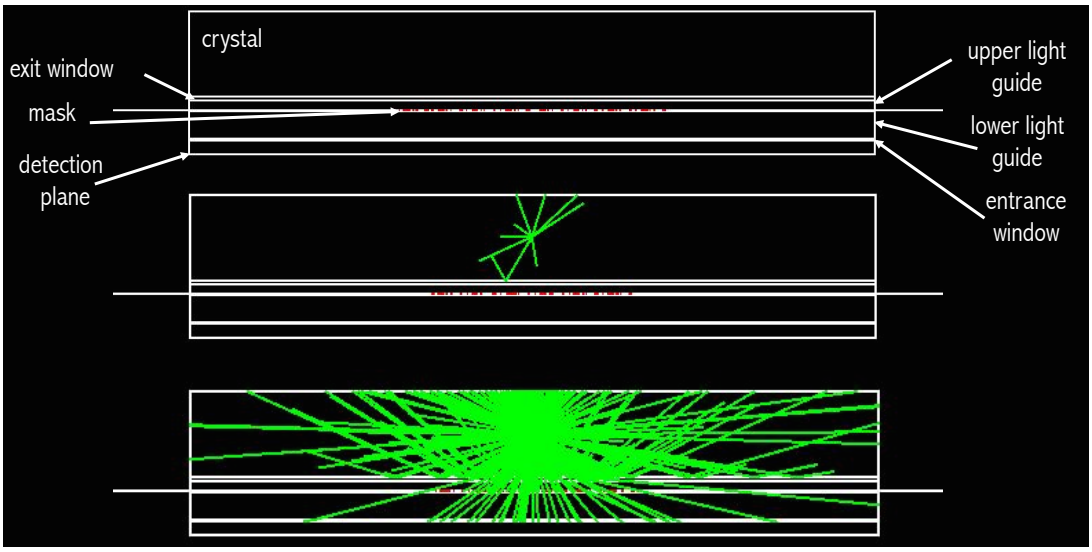

Figure 42. The top image has no photons launched. The red and white patterns show a rank-19 MURA shadow mask pattern, with red elements representing opaque portions of the mask. The middle images show the same geometrical setup with 9 photons launched. The lowest image shows 400 photons launched from a single point. In all cases, the crystal is 30 mm thick, its exit window is 3 mm thick, the upper light guide is 7 mm thick, while the lower light guide is 2.1 cm thick, and the PT entrance window is 1.5 mm thick. The entrance window is made of the same material as the light guide and represents the entrance window of the photomultiplier tubes. In the middle and bottom simulations the photons are launched halfway into the crystal (15 mm from the bottom).

The photons were launched uniformly in 4π. A lateral view of the geometry with both a small and large number of photons are shown below in Figure 43. As seen in Figure 42, many photons do not make it past the crystal light guide boundary due to the index change. These are the traces that bounce back upwards from the mask layer boundary. When going from a higher to lower index of refraction, the critical angle, or angle at which a light ray undergoes total internal reflection, is given by

$$\theta_c = \arcsin\left(\frac{n_2}{n_1}\right)$$

Eq. 78

where n_2 is the higher index and n_1 is the lower index.

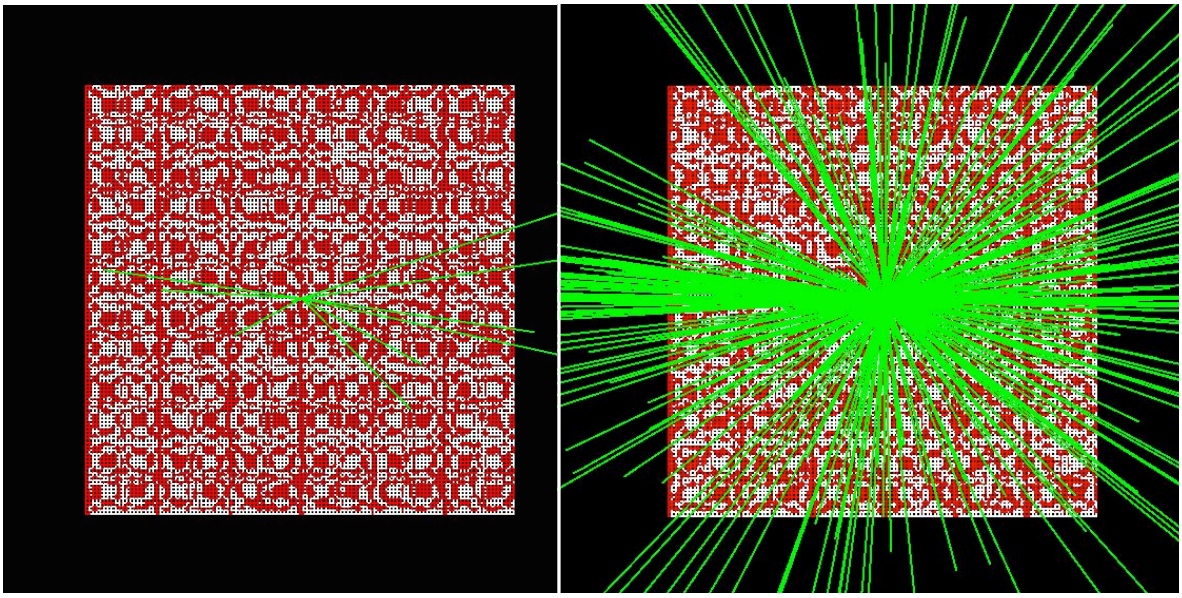

Figure 43. A lateral view of optical photons launched over the MURA rank-19 shadow mask pattern. The pattern is repeated outwards for 8 cycles.

The locations where the optical photons hit the detector plane were recorded in both lateral dimensions without binning. In the event processing and reconstruction code the locations were then binned into either an ideal or real PMT anode array.

4.5.A. OPTICAL GEOMETRY SELECTION

In the two-dimensional system, the optical geometry was chosen based on analytic conclusions as opposed to a full Monte Carlo study. However, the three-dimensional system was chosen from a comprehensive simulation study.

4.5.B. TWO-DIMENSIONAL SYSTEM OPTICAL GEOMETRY

As mentioned above, the overall system parameters are primarily dictated by the light spot size for events closest to the mask pattern and the magnification coupled with the mask feature

size for events farthest from the mask pattern. Also, the overall thickness of the system needs to be kept thin to ensure that enough light falls on the PMT array, as the overall PMT area is a fixed size.

In choosing the mask pattern, as discussed above, this project benefited from using a URA or MURA pattern over a random pattern. As these patterns allow for repetitions of a base cycle, the overall size of a single cycle can be chosen independently of the size of the individual features. The overall size of one cycle can then be chosen based on the size of the light spot at the mask plane. Figure 44 gives the sizes of the light spot for a relative flux density of 50% (FWHM of the light spot) to 30% for varying upper light guide (distance from bottom of crystal to mask) thicknesses. These values were found using the analytic expression for the size of the light spot after an index change as derived above, and are for an event 0.1 mm from the bottom of a crystal with an index of refraction of 1.85 coupled to a light guide with an index of 1.52 [73].

Table 3. The upper light guide thickness and flux density of each system.

Upper Light Guide Thickness (mm)	**30% (mm)**	**40% (mm)**	**50% (FWHM) (mm)**
1.0	2.19	1.85	1.57
2.0	4.24	3.50	2.96
3.0	6.13	5.18	4.38
4.0	8.13	6.87	5.81
5.0	10.12	8.56	7.24
6.0	12.13	10.25	8.66
7.0	14.12	11.9	10.09
8.0	16.12	13.62	11.52
9.0	18.12	15.31	12.94
10.0	20.12	17.0	14.37

The upper light guide thicknesses vs. the FWHM of the light spot size are plotted in Figure 44.

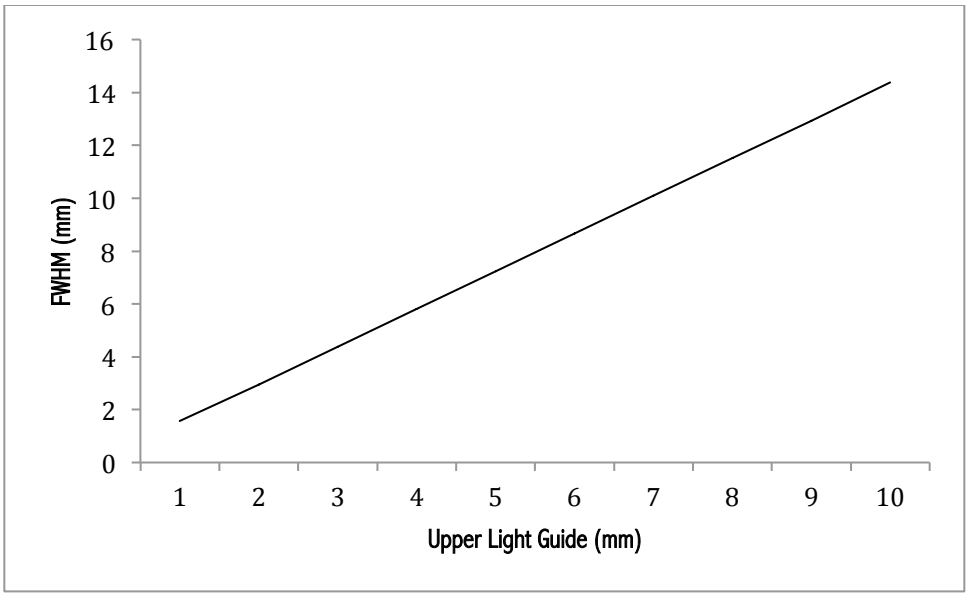

Figure 44. The full width half maximum of the light spot versus the upper light guide thickness for an event at the bottom of a scintillator crystal. These values were found using an analytical expression derived in Appendix 1.

In the first prototype (2-D system), the method of picking the optical geometry was as follows:

1. Select a maximum system thickness; this is done by determining the flux density of the photons. A thicker system results in the light cloud being more spread out and, in turn, less photons per channel at the PT plane.
2. Select the crystal thicknesses (20 mm in 2D).
3. Select the mask base cycle size based on the overall thickness of the crystal and the FWHM of the light spot as discussed above.
4. Select the mask rank and hence feature size; a higher rank mask pattern with smaller features can be chosen to have the same base cycle size as a lower rank with larger feature sizes. Additionally, based on the size of the base cycle, calculate the uncertainty (δx) in finding the centroid of the distribution for events at the top of the crystal to be sure that one can reconstruct in the correct mask cycle.
5. Calculate the smallest magnified feature sizes (event at top of crystal) and select lower light guide thickness to ensure that the PT pixels can resolve these features. A longer

lower light guide allows the light to spread out more than a thinner one, resulting in a larger magnification. This thickness is restricted by the overall size of the system.

These considerations were all taken into account when selecting the optical geometry. Additionally, basic simulations were carried out in the 2-D system to verify the event localization ability of the imager.

4.6. TWO-DIMENSIONAL SIMULATION RESULTS

The two-dimensional system simulations were developed beginning in 2012 and continued to be adapted through 2013. The simulations allowed for several parameter choices including:

1. Thicknesses of all layers (PT entrance window, light guide and crystal thicknesses, optical coupling layer thicknesses, etc.).
2. Material and index of refraction selection.
3. Launch location of, and number of photons generated.

In addition to these parameters, all aspects of the mask (thickness, material, opacity, location, rank, type, and feature size) could also be selected.

To construct the simulation to match the physical system as realistically as possible, the analysis started with the amount of light seen at the PT plane for a typical event. A gamma-ray interaction in the crystal results in several thousand photons being launched from a single point in the crystal. An approximate calculation gives

$$\begin{aligned} &Initial\ Photon\ Emission \cdot 0.5_{Half\ of\ light\ detected\ in\ downwards\ direction} \cdot 0.5_{Index\ losses} \\ &\quad \cdot 0.5_{50\%\ Open\ Mask\ Pattern} \cdot 0.25_{Typical\ PMT\ QE} \\ &\quad = Photons\ Detected\ At\ Photocathode \end{aligned}$$

Eq. 79

NaI(Tl) and CsI(Na) output 38k and 41k photons per MeV respectively. As discussed in Chapter 1, a 400-keV event provides a good representation of a real gamma-ray energy for a source of interest to national security applications. Thus, the simulation data will focus on events with the number of photons equal to that of a 400-keV gamma-ray interaction in NaI(Tl) and CsI(Na).

The following simulation results are for a rank-7 MURA mask as described in earlier chapters, with the optical geometry as follows:

- 1.4 mm mask feature size,
- 2.485 cm focal length (detection plane to mask), and
- 1.0 cm upper light guide (mask to crystal bottom; includes entrance window)

The recorded detector response will be shown in this section, with a discussion of the imaging results presented with the physical experimental data. An event 15 mm from the bottom of the scintillator crystal with no mask pattern is shown in Figure 45. While the number of photoelectrons in a real gamma-ray interaction event is on the order of a few hundred, the following detector patterns are each shown with 200k photons in order to clearly show the system behavior. Additionally, the detector pixels are 0.65 x 0.65 mm^2. While a Hamamatsu 9500 anode size is larger (~3 x 3 mm^2), the smaller pixel size is chosen to effectively see the resolved illuminated mask pattern onto the detector.

The warping of the mask patterns due to the index change is seen in both the 1-D and 2-D cases.. There was no correction applied in the imaging of this data and it was found to work well regardless. The experimental results and associated simulation results to explain effects seen in real data will be presented in Chapter 5.

For each event, a coarse lateral position estimate needs to be performed to localize the event to the correct mask cycle. This will be discussed in detail below; for now, one can assume there exists a coarse lateral position determination method to correctly localize an event to the correct base cycle of the larger mask pattern.

Once the coarse lateral position is found, the data are rebinned as discussed in Chapter 3 and reconstructed using the coded-aperture decoder array and the cross-correlation reconstruction method. Figure 46 shows the reconstructed images for a single 400-photoelectron event at various depths in the crystal. The true event depth is 1.28 cm from the mask pattern. As seen in the figure, the image reconstructed at this depth gives both the largest maximum value and the narrowest image distribution. In the automated imaging code, the depth with the maximum peak value gives the event depth.

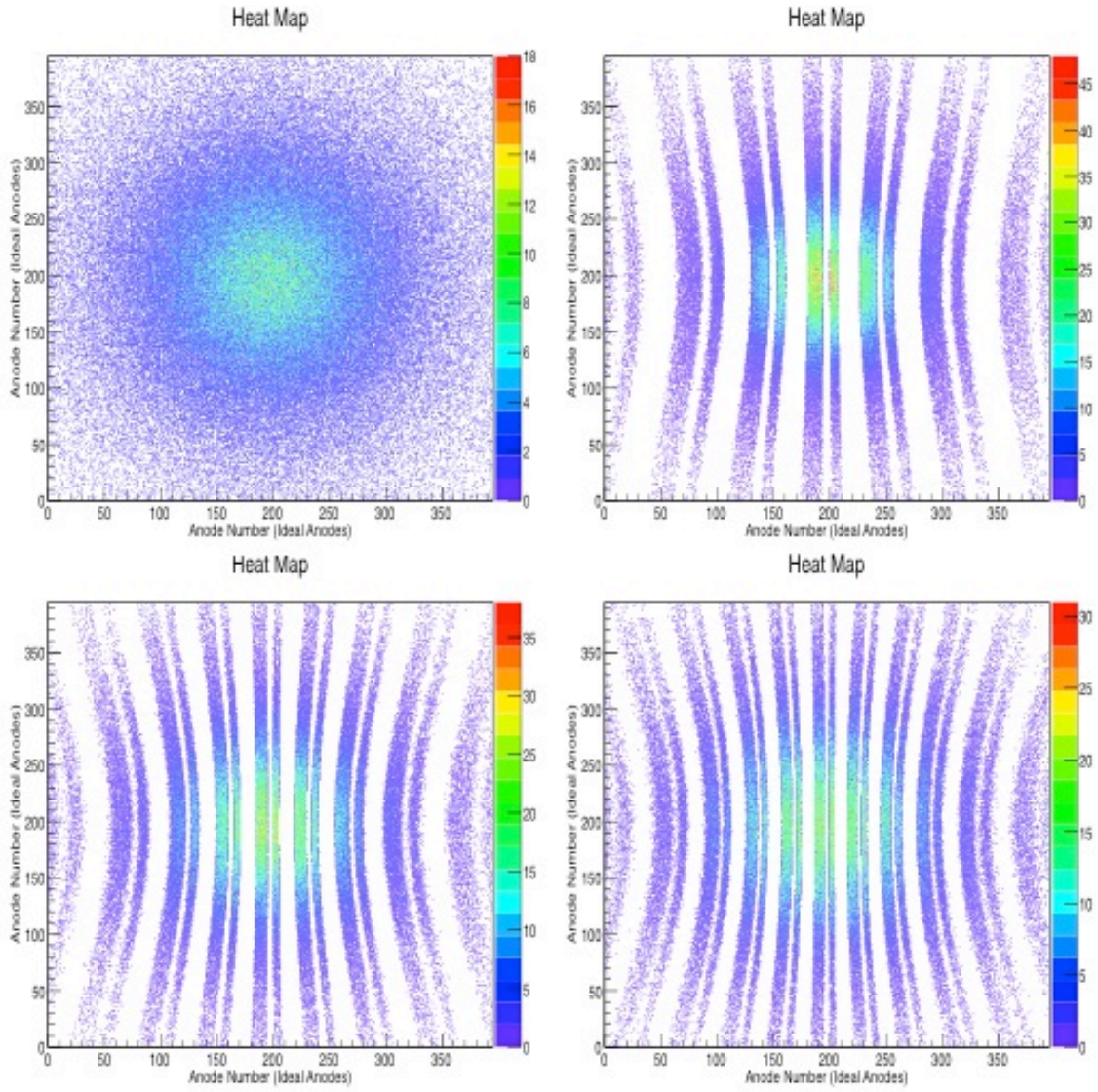

Figure 45. All heat maps shown with 200k photons launched from a single point. Every scenario besides the top left uses a rank-7, 1.4-mm-feature-size, MURA mask pattern located 24.85 mm from the detection plane, with an upper light guide distance of 6 mm. (Top left) An event with no mask pattern launched at the top (farthest from the light guide plane) of the crystal (30 mm from the light guide). (Top right) Event launched 0.5 mm from bottom of crystal. (Bottom left) Event launched 10 mm from bottom of thick crystal. (Bottom right) Event launched from top of 30 mm thick crystal. The simulation uses a larger area than the physical experiment. With 0.65 x 0.65 mm^2 pixel size and 400 pixels, a 260 x 260 mm^2 area was used. The area of the 3 PMT array was 156 x 52 mm^2.

Figure 46. The reconstructed images of a single 400-photon event with all photons launched from a single point (1.28 cm from the mask) within a scintillator crystal with the optical geometry described. As seen in the figure, as the assumed depth from the mask used to generate images increases, the image begins to form. It is the sharpest at the correct depth of 1.28 cm, and disintegrates as the distance decreases after that. The y axis is in arbitrary units.

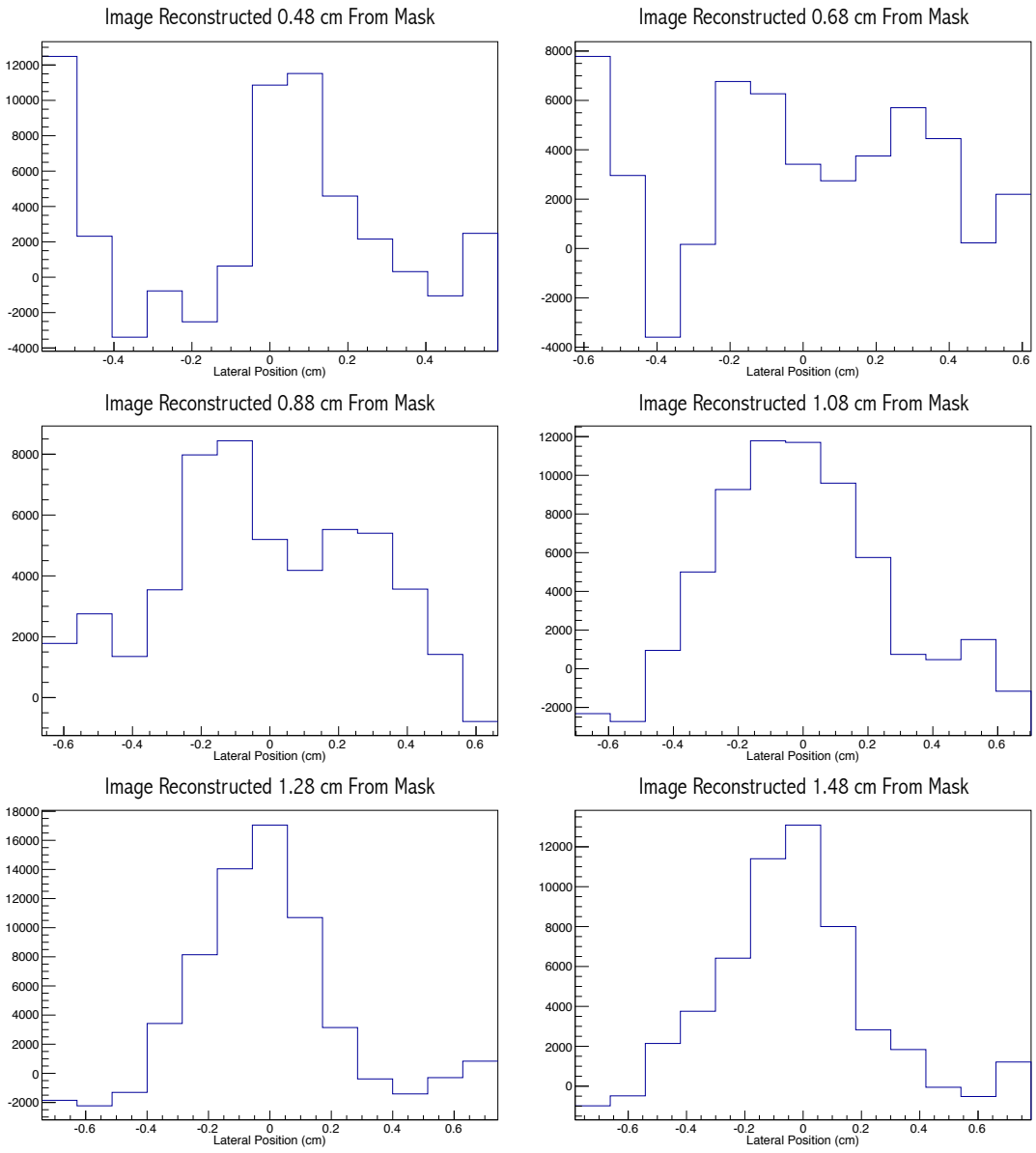

Figure 46. Continued.

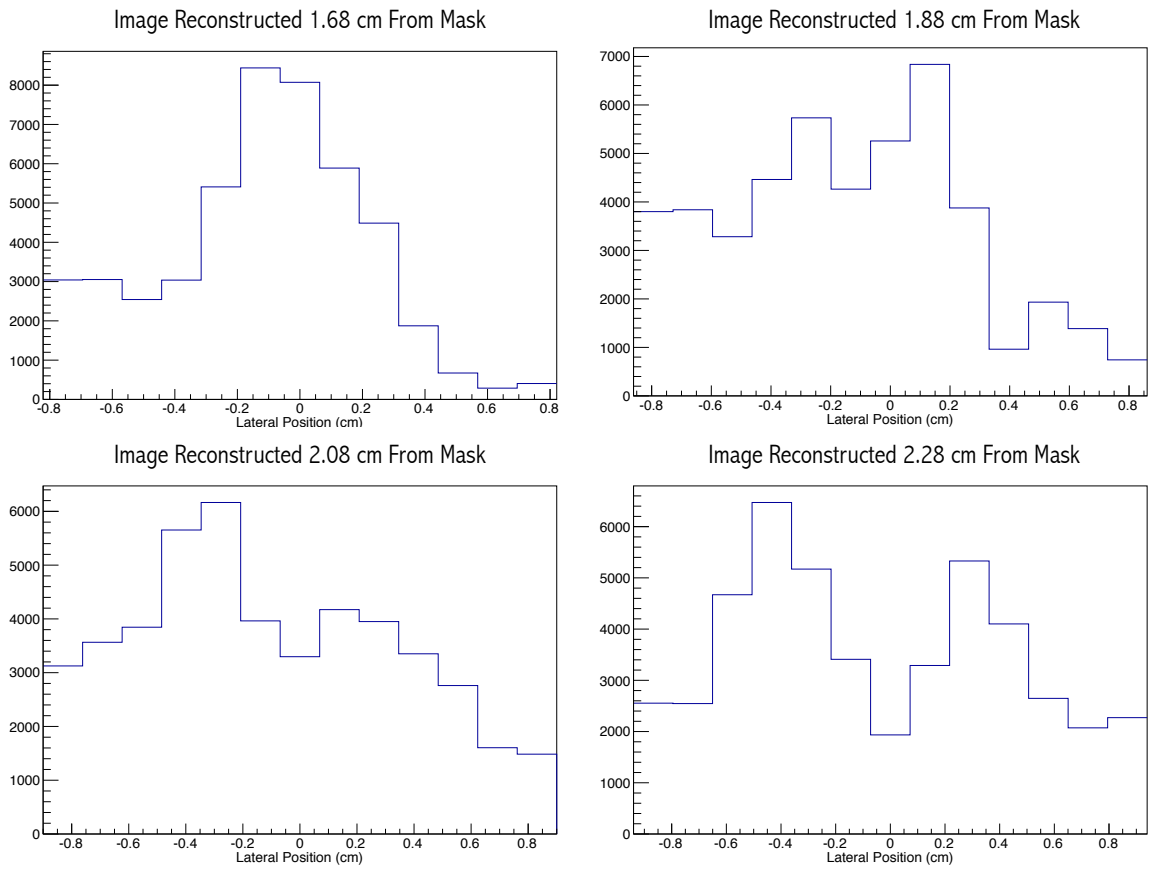

Figure 46.Continued

.

Once all of the images are constructed for the entire range of depths throughout the crystal, the maximum peak heights for each image are stored and the results are searched for the depth with the maximum peak. The peak height versus depth of reconstruction for the event shown in Figure 46 is plotted in Figure 47. As seen in the plot, the peak height of the reconstructed images increases before the true depth of the event and decreases after reaching a maximum at the correct depth. While there are other peaks throughout the depth range, they are significantly less than the true depth peak height and do not cause discrepancies in simulation event reconstruction results. Using a Gaussian fit of the peak was investigated to find the mean, but simply taking the depth with the maximum bin was found to work better to localize the events.

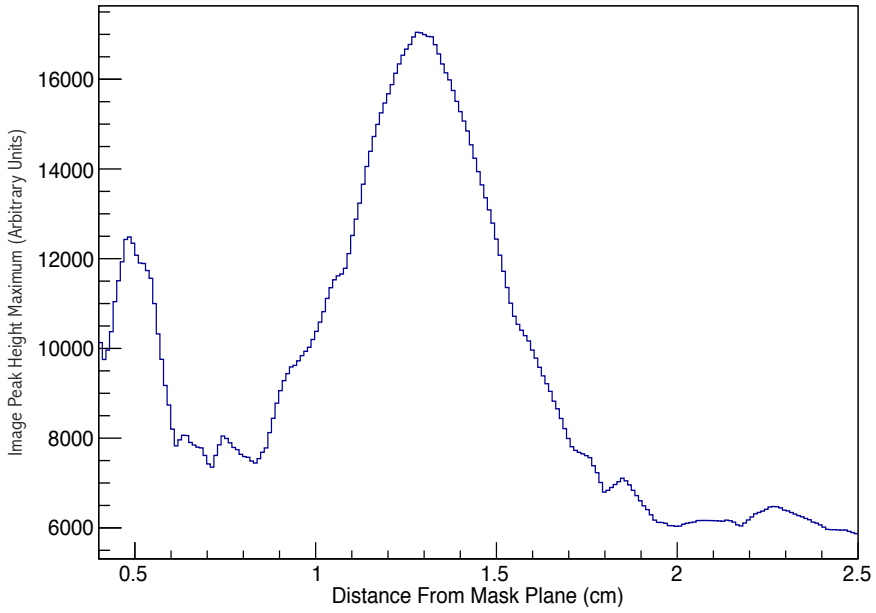

Figure 47. The maximum peak heights of each reconstructed image plotted for the range of depths from the mask pattern. The true event occurred at 1.28 cm, which is where the maximum value occurs in the plot.

Once the images are reconstructed and the depth is found, in order to find the true (imaged) lateral event location, a weighted mean of the peak location from the image at the correct depth

is used to correct the event location from the initial global event location found earlier in the analysis.

The global lateral event localization works by calculating which mask element the event is approximately centered over, and then finely adjusting the lateral position with the reconstructed image. For this to work, the coarse localization method must find the event to within one base cycle of the true location. In an ideal case, all coarse locations will be found under a single (and the correct) cycle of the base pattern. With a poorer coarse localization, the distribution of fully reconstructed events would posses "wings" that are spaced one base pattern cycle size away from the true lateral position point of the events. Several methods were tried to calculate which cycle of the mask pattern the image falls over.

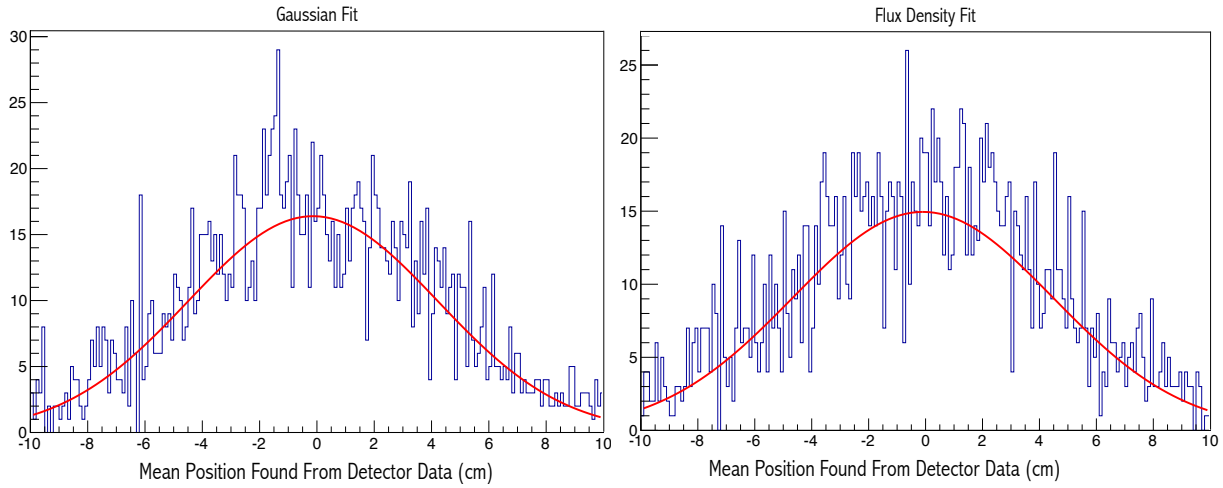

Figure 48. Histograms of the mean for each fitting method (left, Gaussian fit; right, flux density distribution) for 400-detected-photon events launched from a single point. Each entry on the histogram is the lateral location of where the fit found the mean of the raw mask modulated detector distribution. The mean from the Gaussian fit of the histogram on the left is -0.1298 cm, and the right is -0.09555 cm. The width of each is σ=4.36 and σ=4.57 cm, respectively. The width of these distributions indicates how many of the events are found under the wrong mask pattern; i.e. the larger the width, the worse the fit. As they are nearly the same for both cases, both fits work equally well.

Figure 48 shows the mean position found for 250 400-photon events launched from the same point in the scintillator crystal using either a Gaussian fit or a fit to the flux density (Appendix 1). As the detector response includes the mask modulation, the fits are significantly worse than they would be without mask modulation. Each histogram plots the mean of the fit found for each event. Each of the histograms shows a Gaussian fit of the histogram that was used to determine the mean of the distributions.

Once these fits (Gaussian or index of refraction flux density) were compared, the Gaussian was then compared to the weighted mean fit. To compare the weighted mean against the Gaussian fit, the final imaged results for the same 1750, 400-photoelectron events were compared. The absolute lateral position was calculated as described above for a single event.

As seen in Figure 49, the weighted mean approach (right) resulted in 100% of the events being found in the correct base cycle, while the Gaussian fit (left) has outer "wings" in the distribution. These wings are events that were found one base cycle to the left or right of the true cycle for the events. This problem with the Gaussian fit was found to be even more apparent in actual experimental data and will be discussed in Chapter 6. Thus, the weighted mean was used to coarsely localize the events to the correct base cycle. The simulation results indicate that the imager should work well for single events; the overall detector position resolution is given by the width of the depth and lateral event position reconstruction for many events over a range of depths. The results of the simulation data are shown in Figure 49 for various depths using the geometry described.

In order to measure the imaging resolution of the system for events at known depths in the thick crystal range, a thin crystal can be used to mimic a thick crystal setup. Because the transition of high to low index occurs lower for events higher in a thick crystal relative to a thin crystal with light guide, the absolute depth of events is not equivalent when emulating a thick crystal event in a thin crystal. This is discussed in detail in Section 5.1.B. From the index of refraction correction discussed in Chapter 3, a 14.5 mm thick light guide with a thin (1 mm) scintillator crystal is equivalent to 22.5 mm of high index crystal. Figure 50 shows the simulation results for a range of thin crystal locations, with all but the highest giving a depth resolution of better than 1 mm. At the upper depths (row 3, right), a bimodal structure is seen beginning to develop in the depth reconstruction distribution. The bimodal structure becomes more pronounced at the higher depth (bottom). This effect is also seen in the experimental data

(Section 6.1). It is presumably due to both the size of the magnified feature and the mask rank. Simulations show that by using a higher-rank mask, the onset of this effect can be delayed until higher depths in the crystal. With the rank-7 mask, this effect is seen when the anode size is close to the magnified feature size.

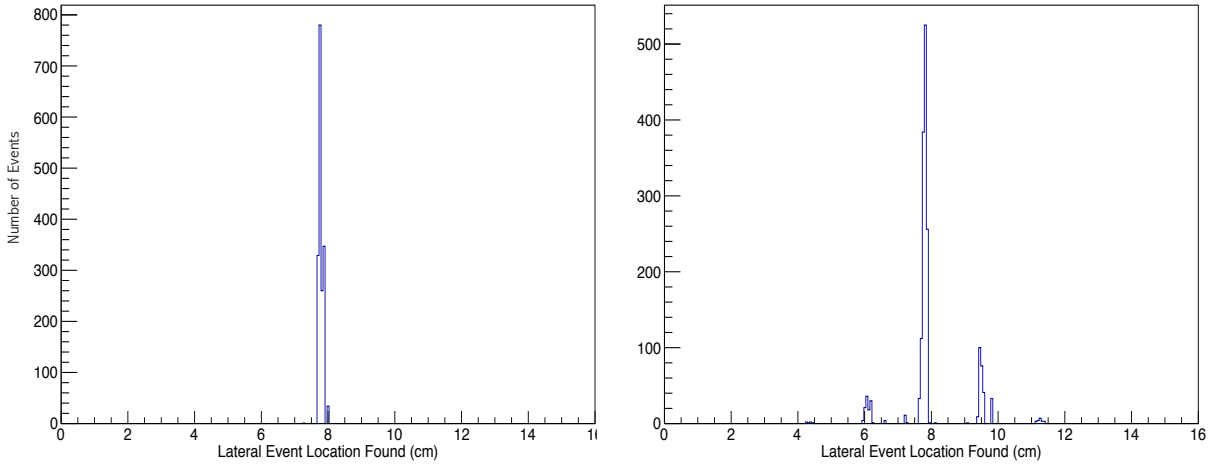

Figure 49. The imaged and absolute lateral position found with the coded-aperture imaging method using the mean (left) and Gaussian fit (right) approach to obtain the coarse localization. The outer wings in the Gaussian plot are events incorrectly coarsely localized, as all of the events are launched from a single point in the crystal. The events using the weighed mean method (left) are all found within the correct base cycle of the mask. The events using the forced Gaussian fit (right) have 25% of the events incorrectly localized. This poor fit is due to the modulation of the mask pattern on the recorded detector response, in addition to the shape of the light spot not being a true Gaussian distribution.

Figure 50. The found depth for 1000 events emulated at different depths in the crystal. The events in each plot are all launched from the same point in a thin crystal with the thickness of the light guide labeled in the figure. The range of the light guide thickness used is equivalent to a 20-mm-thick bulk scintillator crystal. The FWHM of each distribution gives the depth resolution at each depth. Each bin is 0.25 mm, so the FWHM for all depths up to 20 mm are less than 1 mm wide.

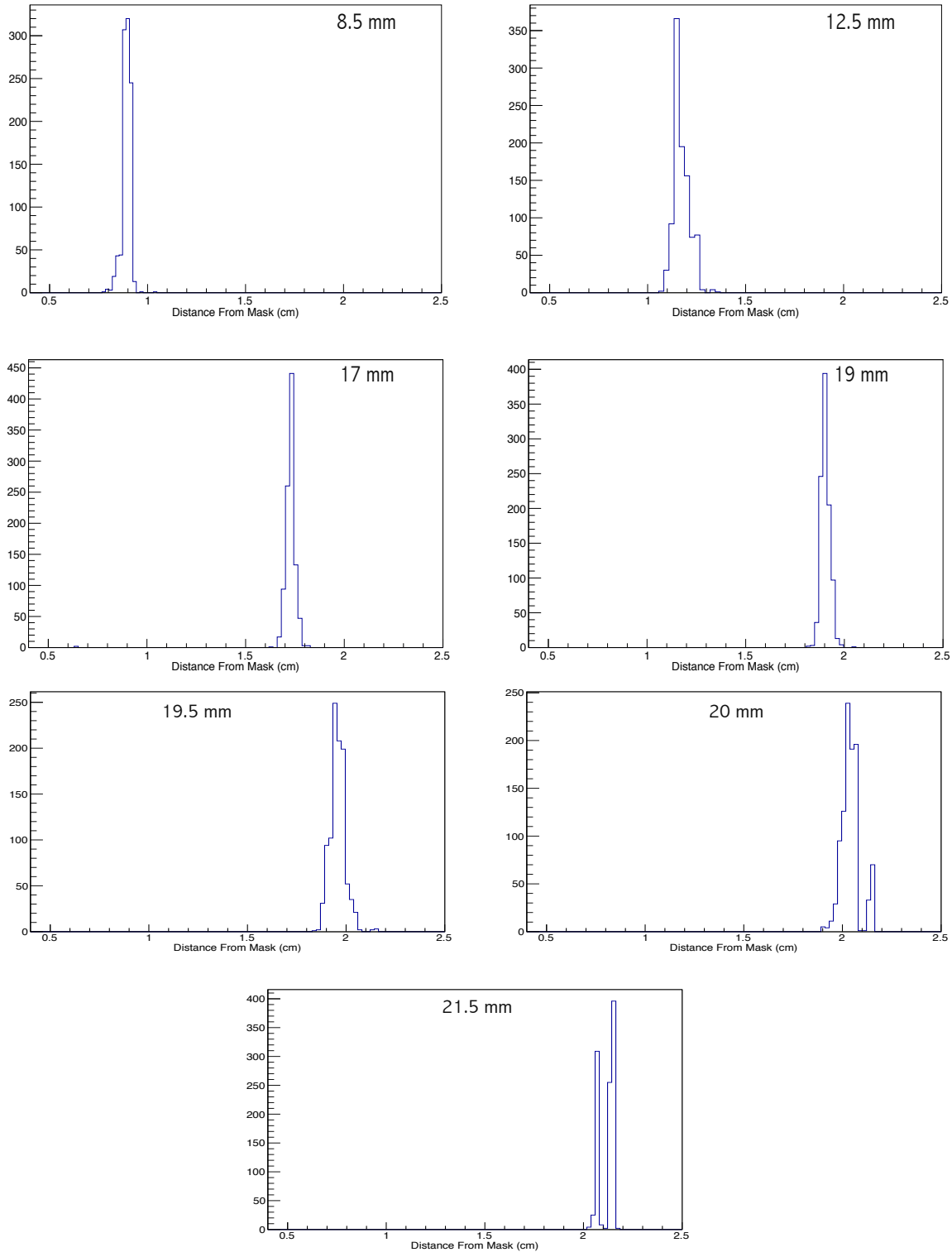

Figure 50. Continued.

The lateral position resolution results are shown in Figure 51. Each bin is 0.6 mm, so the lower depth (5.0 mm) FWHM is better than 0.6 mm while the upper depth FWHM is about 1.4 mm.

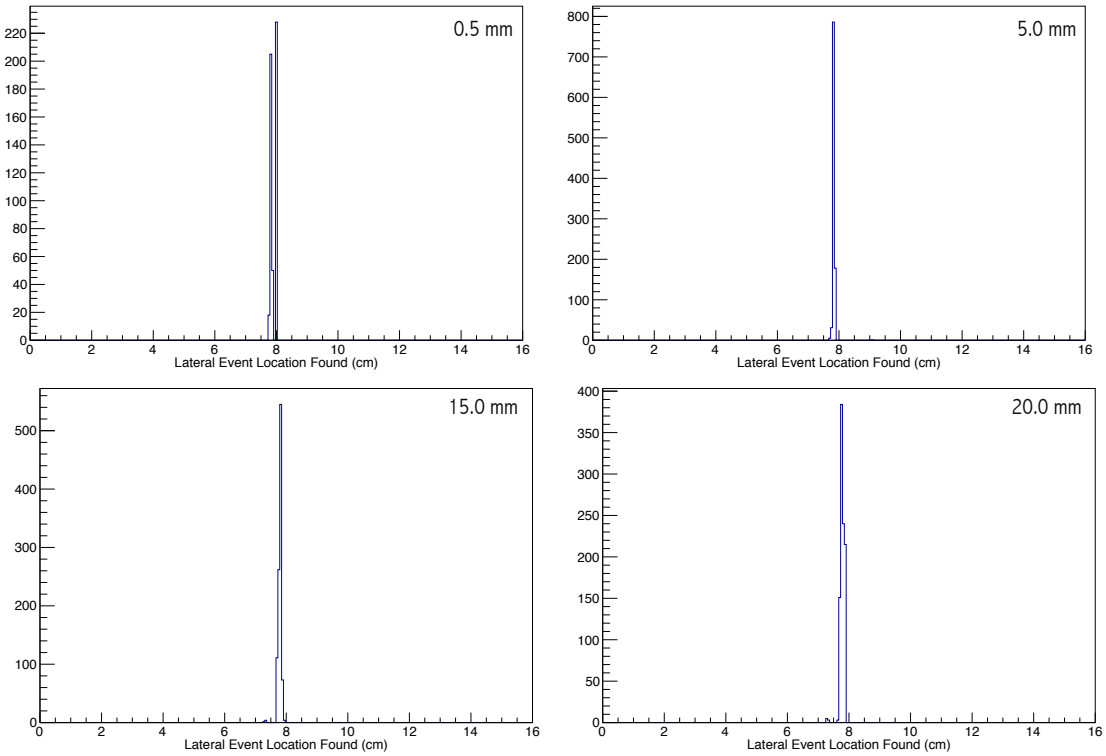

Figure 51. The lateral position reconstructed location for 1000, 200-photoelectron events. Each bin has a width of 0.6 mm for all depths. All events were launched from the same lateral point in the bulk crystal at the depths indicated in the plots. The events at the lowest depth have a worse resolution, presumably because the events do not project a full base cycle of the pattern. This results in poorer lateral position resolution, as the detector does not record all of the information required for reconstruction.

These simulation results provided the framework for selecting the parameters of and building the physical two-dimensional experiment. The results of the real imager will be compared to the simulation results in Chapter 6.

4.7. THREE-DIMENSIONAL SIMULATION RESULTS

A full simulation was performed for the three-dimensional system in order to select the best optical geometry of the physical system. This system was selected using the same method to select parameters as listed above; i.e. the mask ranks, feature sizes, focal length, and upper light guide thickness. The cases simulated are given in Table 4. Based on simulation results, the system was built with a rank-19 mask with 1.3 mm features, a focal length of 2.2 cm, and an upper light guide thickness of 1.0 cm. The detector patterns for several detector configurations are shown in Figure 52. While the true magnified pattern is much clearer with ideal (0.65 mm) pixel sizes as opposed to an array of Hamamatsu 9500 PMTs, the imaging still works well to locate the events, as the magnified features can still be resolved by the larger pixel sizes. The size of the magnified features can clearly be seen to be decreasing, as the event launch point is further into the crystal from the mask plane, as shown in Figure 52. As will be shown later in this chapter, even for cases with an extremely low number of photons, as seen in the two rightmost columns in Figure 52, the imager still locates the events in all three dimensions.

The reconstructed images are generated as described in Chapter 3; first the data are rebinned as appropriate to the bin size at a given depth. Then, the peak height of the reconstructed image at each depth is found. Finally, the event depth is set to the depth with the largest peak height. The reconstructed image at the found depth is then used to determine the lateral position of the event, as the absolute position of the image pixels are known, and the peak in the image gives the finer localization.

The three-dimensional system is more complex than the two-dimensional imager discussed above. In this case, the coarse localization and rebinning are more complicated. In order to get a coarse lateral position location the data are collapsed in each direction across the entire face of the detector. This concept is shown in Figure 53.

Unlike with the two-dimensional case, in the three-dimensional system the Gaussian fit is found to work better than the weighted mean. As shown in Figure 54, while the shape of the light spot is not a Gaussian, due to the fact that the mask pattern is washed out when the data are collapsed, the Gaussian fit works well in obtaining the mean as a fit parameter.

Table 4. The ranks of the mask patterns, feature sizes, focal lengths and upper light guide thicknesses for each system considered for the full three-dimensional system. The parameters were chosen analytically before performing the simulation study.

Mask Rank (MURA)	**Feature Size (mm)**	**Focal Length (mm)**	**Upper Light Guide (mm)**
13	1	28	8
13	1.4	26	10
13	1.6	22	10
13	1.6	22	11
17	1.45	22	10
19	1.3	22	10
19	1.4	23	11
19	1.3	23	10
19	1.3	22	10
19	1.5	22	11
19	1.4	22	11
19	1.25	25	10
19	1.2	30	10
19	1.2	28	10
19	1.0	22	8
23	1.15	23	10

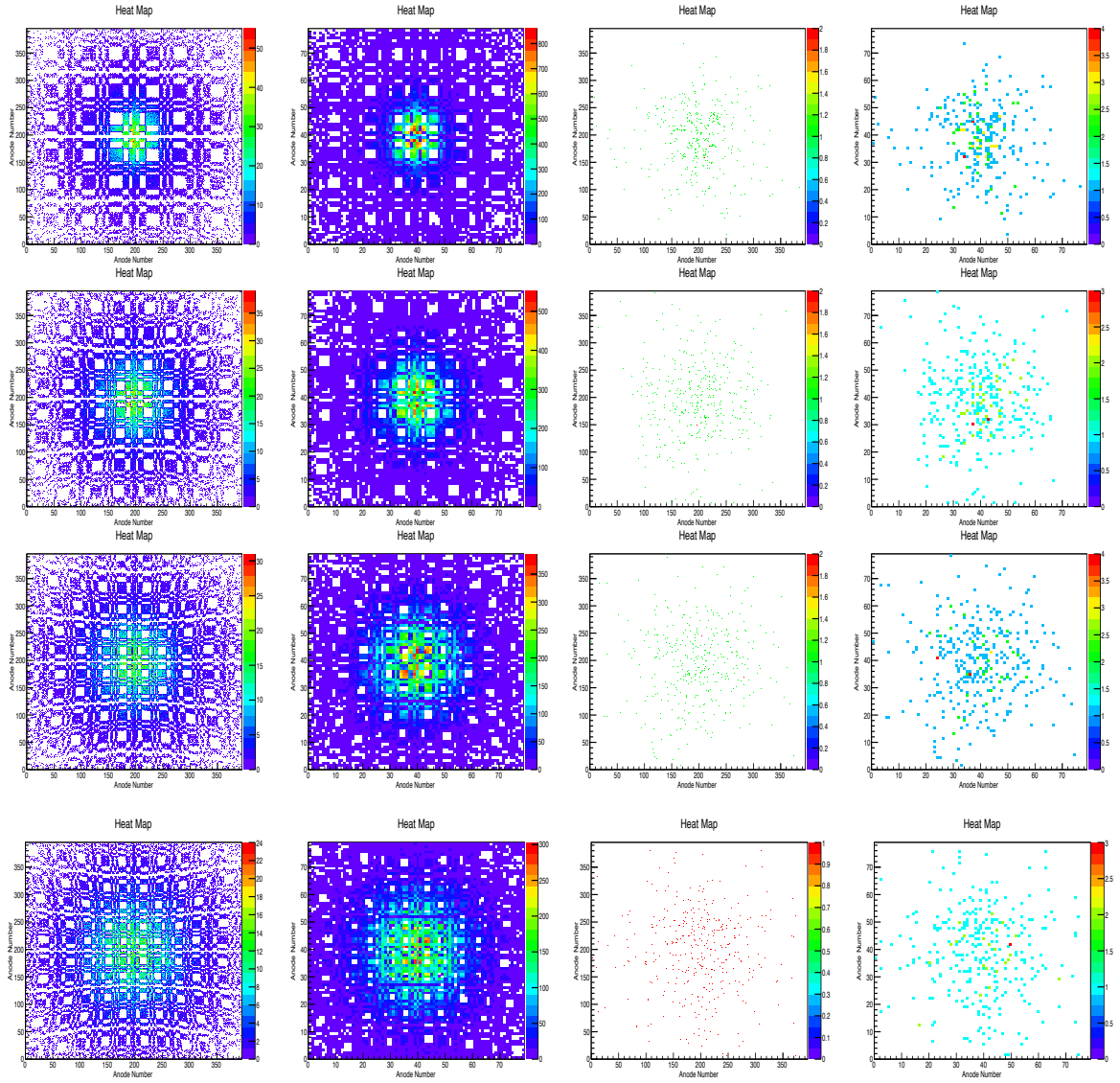

Figure 52. Detector responses for various detector geometries and numbers of photons per event for locations in a 30-mm-thick crystal with the optical geometry of a rank-19 mask, 1.3 mm feature sizes, 2.2 cm focal length and 1.0 cm upper light guide. The rows from top to bottom correspond to events launched 1 mm, 10 mm, 20 mm and 30 mm from the bottom of the thick crystal. The columns from left to right are for 200k photons with an ideal (0.65 mm) anode pitch, real H9500 PMT pixel size pitch, 400 photoelectrons with .65 pixel pitch and 400 photoelectrons with real H9500 pixel pitch. Although the detector patterns for 400 photoelectron show extremely weak signals, the image reconstructions still work to localize the events. This will be shown below.

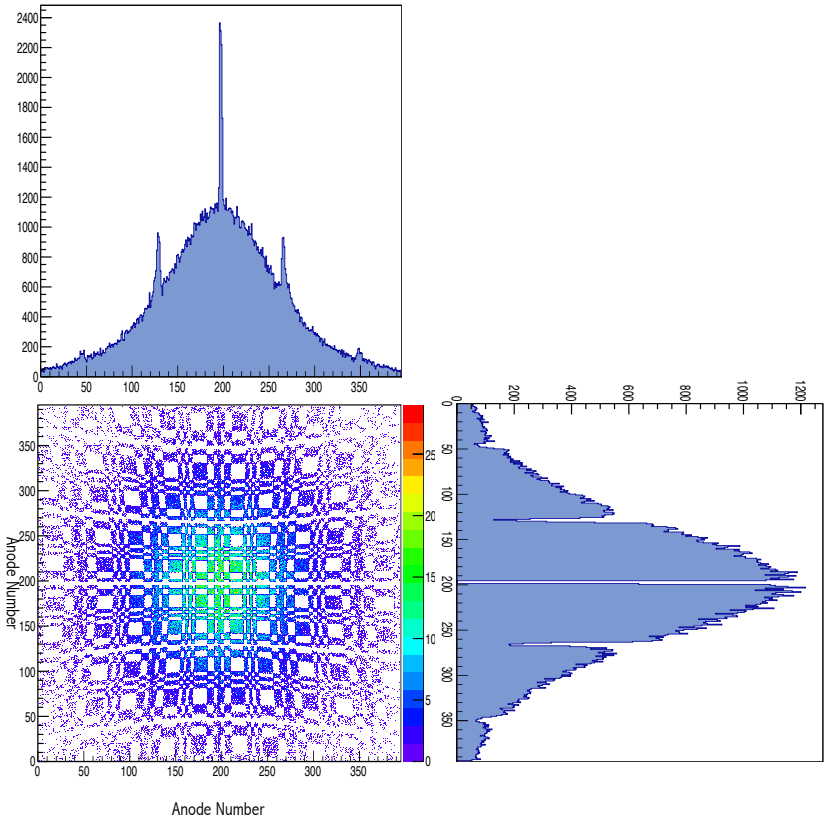

Figure 53. (Bottom left) The heat map for 200k photoelectrons with an ideal anode pixel array. (Upper left) The 200k-photoelectron detector data collapsed in the y (vertical) direction. As seen, except for the central closed elements, the mask pattern is mostly washed out. This shape allows for a good fit with either a Gaussian or weighted mean in order to obtain coarse localization to the correct mask cycle. (Lower right) The 200k-photoelectron detector data collapsed in the x (horizontal) direction for 200 bins. As seen, the mask pattern is mostly washed out except for a central peak on an entirely open line of the mask.

While the distribution of the events for a very large number of photoelectrons (O(100k) is uniform enough to use a Gaussian fit, a realistic number of photoelectrons (400) has a much less uniform collapsed detector distribution. Figure 55 shows the collapsed detector distributions in the x and y directions for a realistic anode mapping with 400 photons. As see in the top left (x collapsed data), the distribution is too modulated by the mask pattern and low number of counts to provide a good fit; this distribution is similar to the one-dimensional case where the weighted mean proved to work significantly better than a Gaussian. To prove this, the distribution of the

initial found x locations for 400-photoelectrons events with a realistic detector is shown in Figure 56.

Once the coarse localizations are determined, the data are rebinned in two dimensions using bin sizes of half of the magnified feature size as previously discussed. Each set of rebinned data for each depth is then reconstructed using the cross-correlation, two-dimensional reconstruction method. A sample event's images over a range of depths with 200k photons detected from an event at the bottom of a thick scintillator crystal are shown in Figure 57. The true depth is located at 1.01 cm; the reconstruction at 1.01 cm has the greatest peak height value. A clear peak is seen against a much lower background. As seen in the upper right surface plot in Figure 57, the image has a very sharp peak with a small background structure. The non-flat background is due to the large anode size and non-uniformity of the anode map.

Once the individual images are reconstructed, the one with the maximum bin height is selected as the event depth. A plot of the peak pixel versus reconstruction depth for a single event is shown in Figure 58.

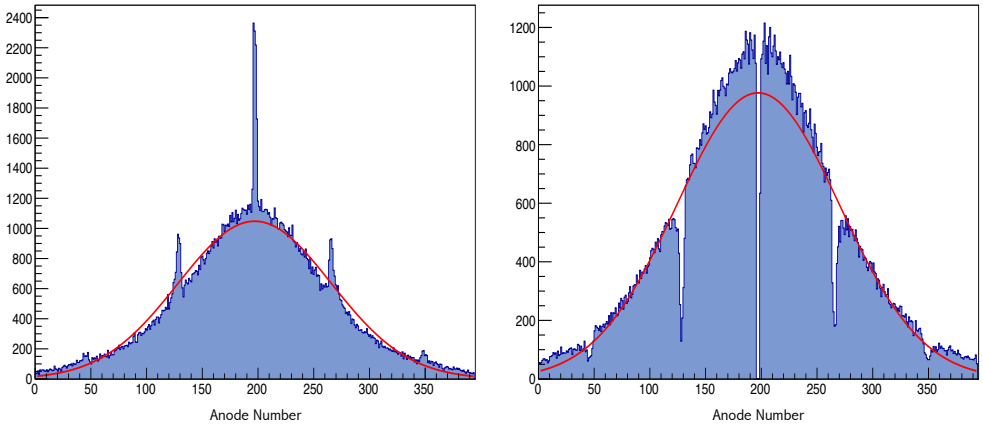

Figure 54. The collapsed data with a Gaussian fit. (Left) The x-collapsed data shows a peak where the open line of the mask exists. This feature does not degrade the Gaussian fit's ability to find the center of the distribution. (Right) The y data has a closed section where the mask has an opaque line. It should be noted that while the shape of the light spot is not a Gaussian and is in fact known [73] and derived in Appendix 1, the ease of use of the Gaussian fit makes it an attractive and simple way of obtaining the coarse localization for the collapsed data.

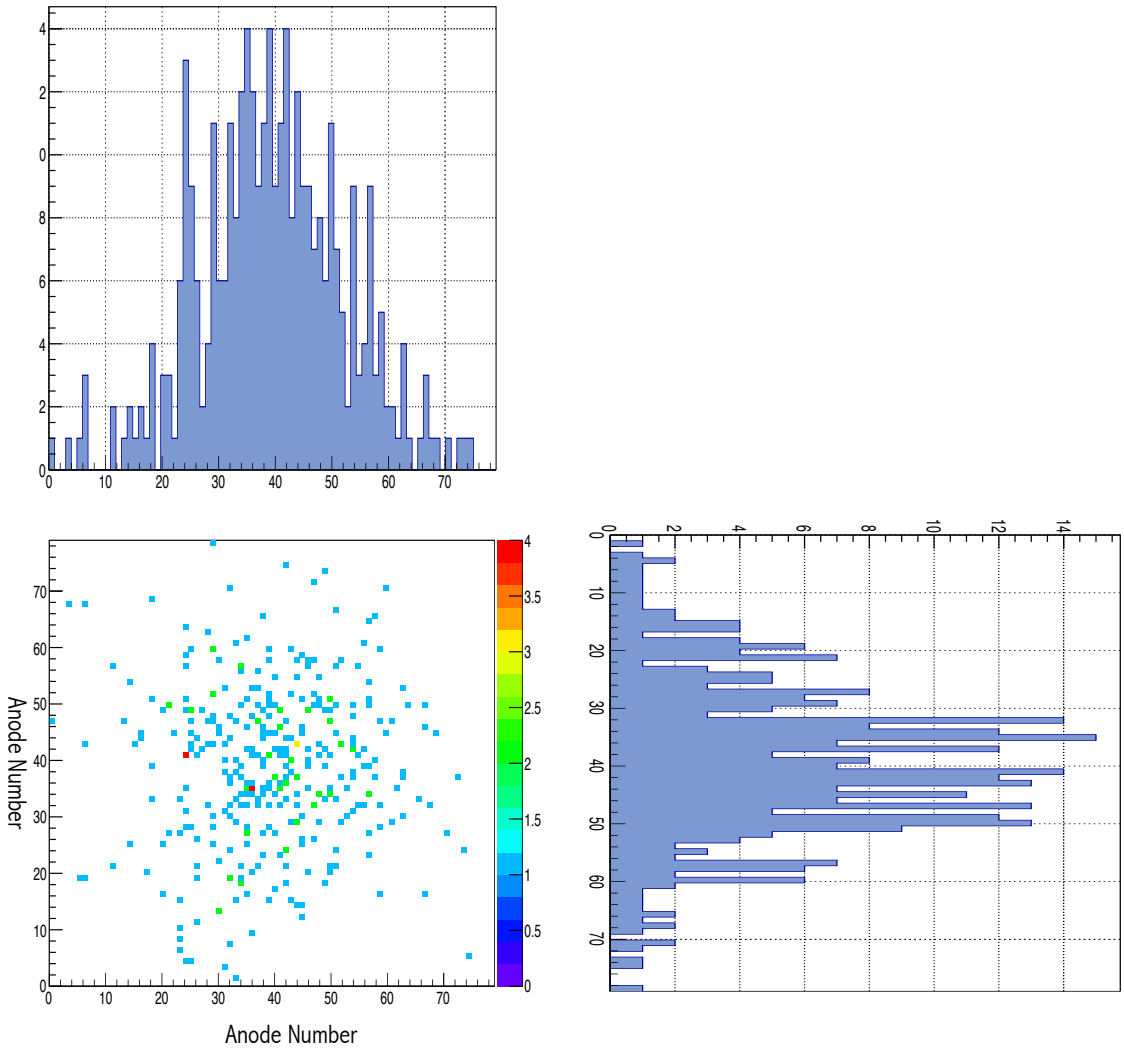

Figure 55. Collapsed data in the x (top) and y (right) directions for 400 photoelectrons with a real detector array. As seen in the images, due to the low number of photoelectrons, a Gaussian fit does not work as well as with a very large number of photoelectrons.

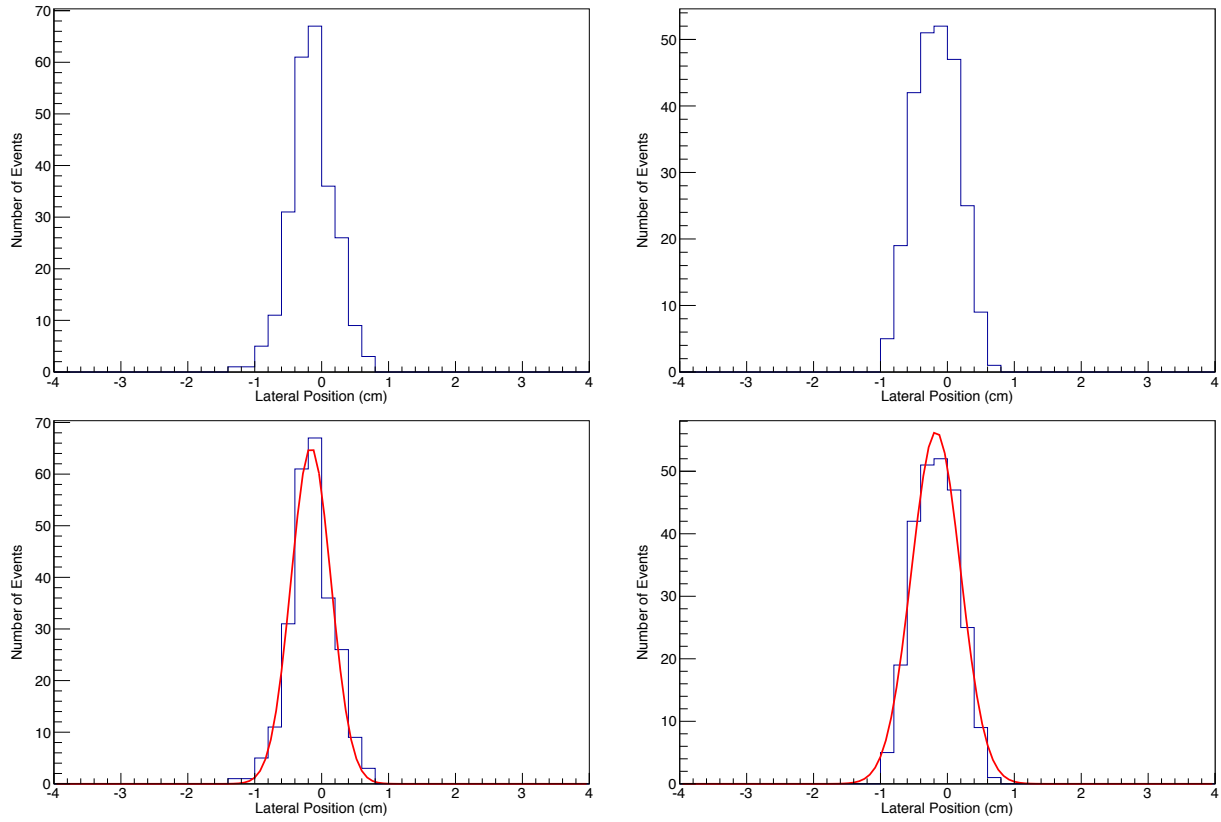

Figure 56. The histograms of the coarse x position found for 250 400-photoelectrons events 20 mm from the bottom of a thick scintillator crystal with a real detector array. The top left image was made using the weighted mean with the collapsed detector data. The top right uses a Gaussian fit. The events were launched at x=0.0 cm, so the method with the narrowest FWHM around 0.0 works the best in localizing the events coarsely in the lateral dimension. The bottom left and bottom right images show each distribution with a Gaussian fit to obtain the width and mean of the histograms. The weighted mean method has a mean of -1.56 mm and σ=6.9 mm, while the Gaussian method has a mean of -1.7 mm and σ=8.61. Thus, the weighted mean method again provides a narrower (and more correct) coarse localization method.

Figure 57. The reconstructed images at various depths for a 200k-photoelectron event 1.01 cm from the mask pattern. The image reconstructed at 1.08 cm has the largest peak value as well as the peak image closest to the shape of a delta function. The image in this case would be found at 1.01 mm.

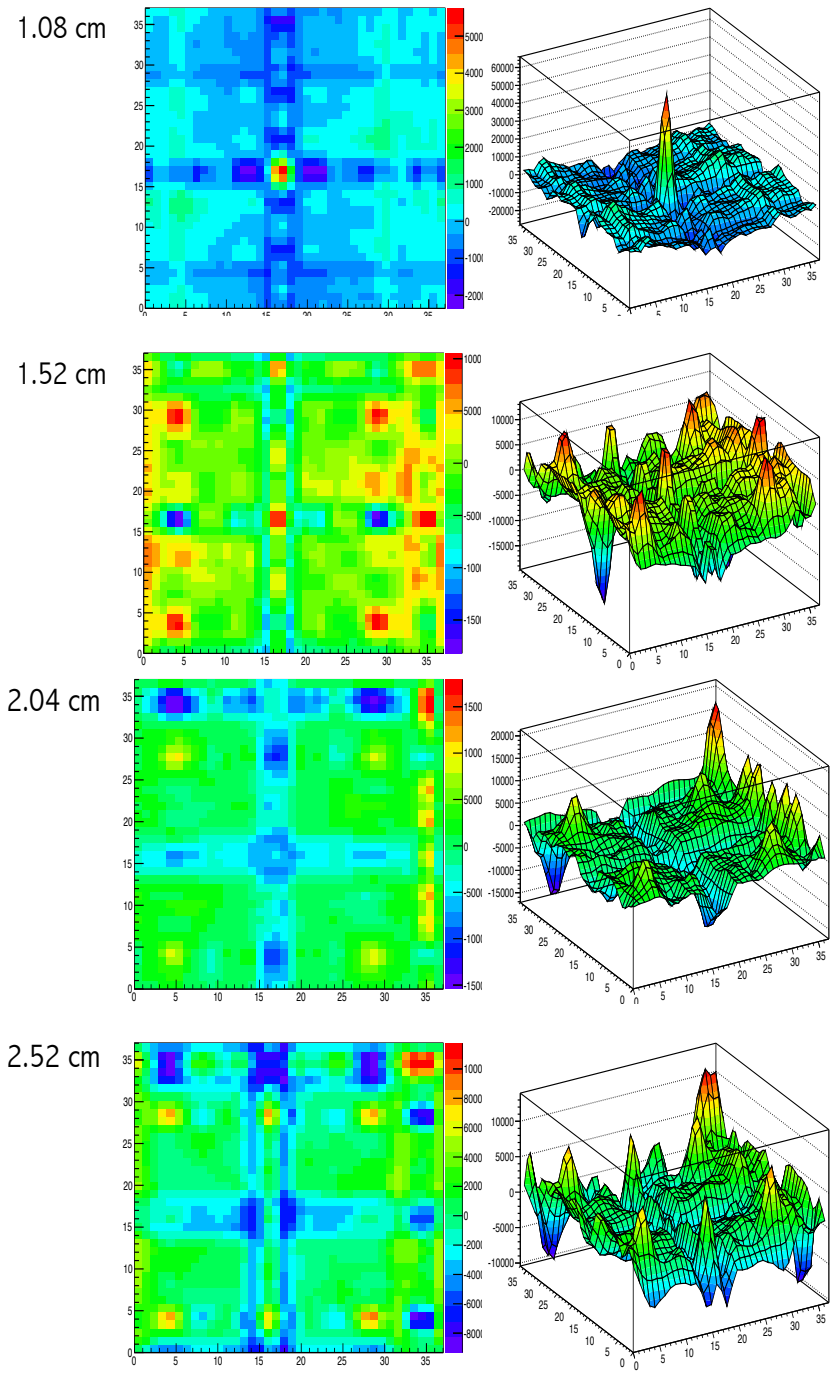

Figure 57. Continued.

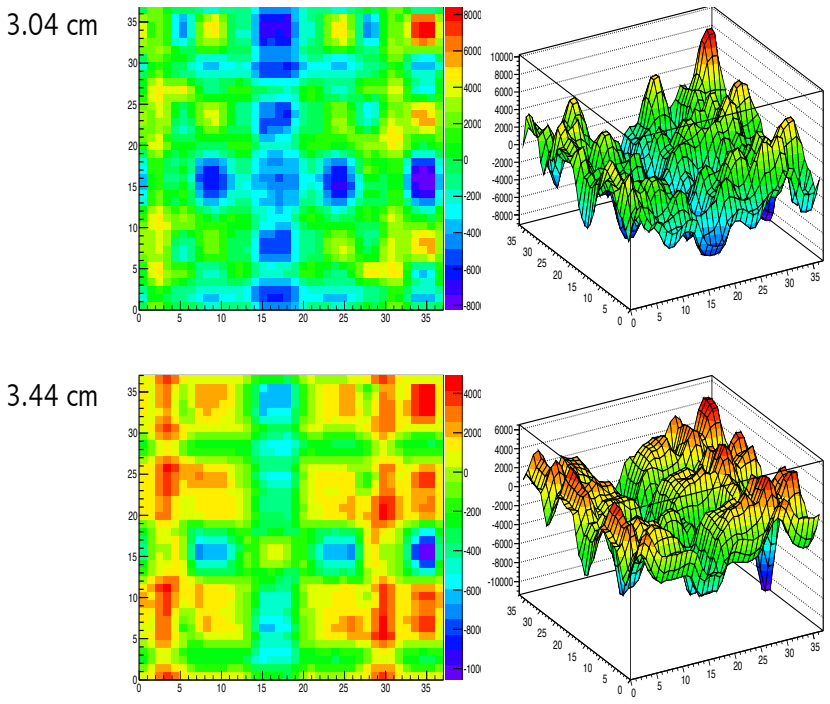

Figure 57. Continued.

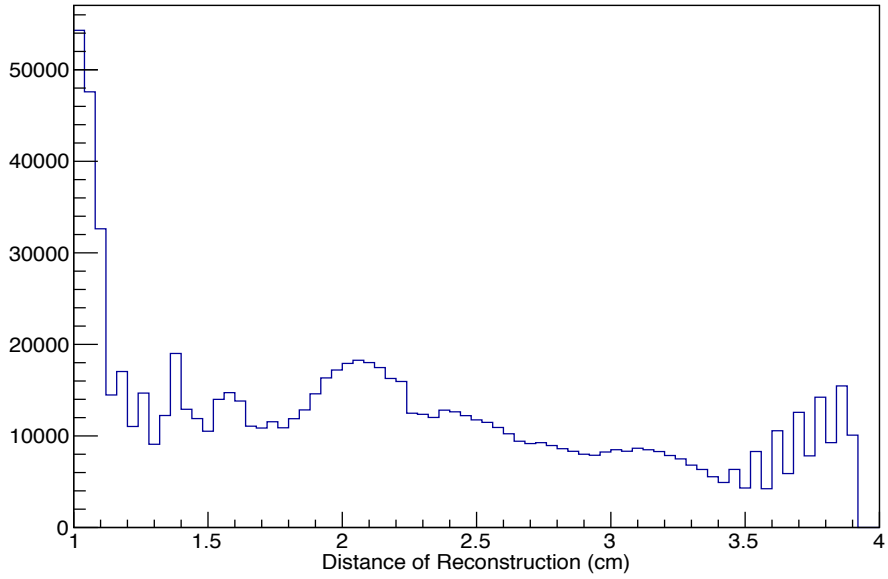

Figure 58. The maximum peak height from the individual images in Figure 57 plotted against the depth each image was reconstructed for. This particular event would be found to exist at the lowest bin. 200k photoelectrons were detected from an event launched from a single point at the bottom of a thick scintillator crystal.

The simulations were performed extensively over the range of a 30-mm-thick un-segmented crystal. The step size for image reconstruction can be selected to any increment; these simulation reconstructions used 0.4 mm steps.

To understand the shape of the reconstructed distribution as a function of the number of detected photons, Figure 59 shows an event 17 mm into the scintillator crystal (17 mm from the bottom side coupled to the upper light guide) with the top row consisting of a single 300k photoelectron event, and each lower row consisting of an event in the same location with a decreasing number of detected photons. The left column shows the detector response with a 25 Hamamatsu 9500 PMT array, and the right shows the reconstructed image peak height for 0.4 mm depth step sizes. As seen in the figure, the general shape of the reconstructed peak stays the same as the number of photons detected decreases, but the ratio of the peak height at the correct depth against the background decreases when the number of photons is $O(1000)$. As this is the realistic number of photons collected from

Figure 59. (Left) The heap maps and reconstructed events (right) for the number of detected photons labeled to the left of the heat map. The shape of the reconstruction remains as the number of photons decreases to a realistic value, however the cleanness and ratio of maximum peak value to incorrect image reconstructions depths decreases.

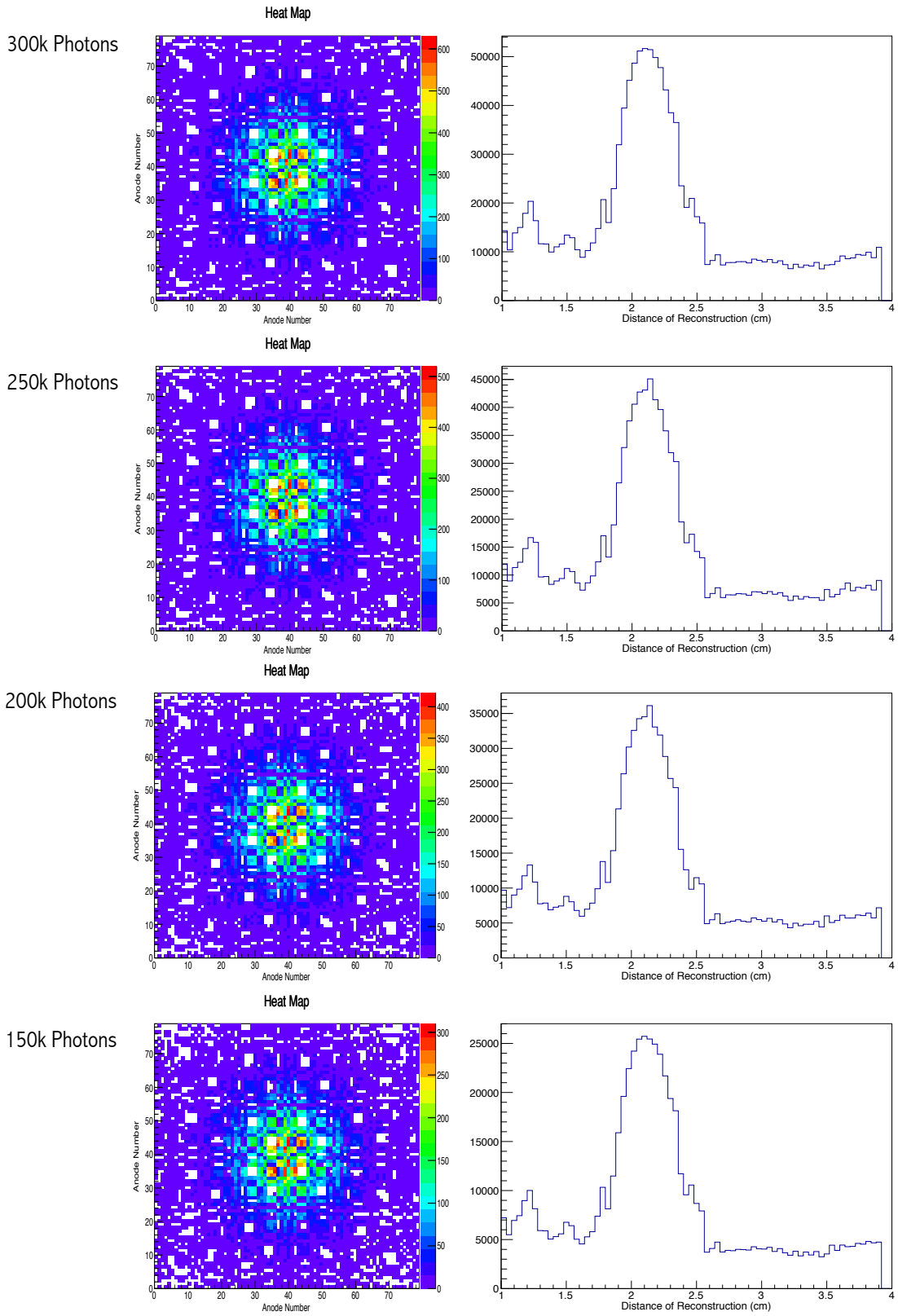

Figure 59. Continued.

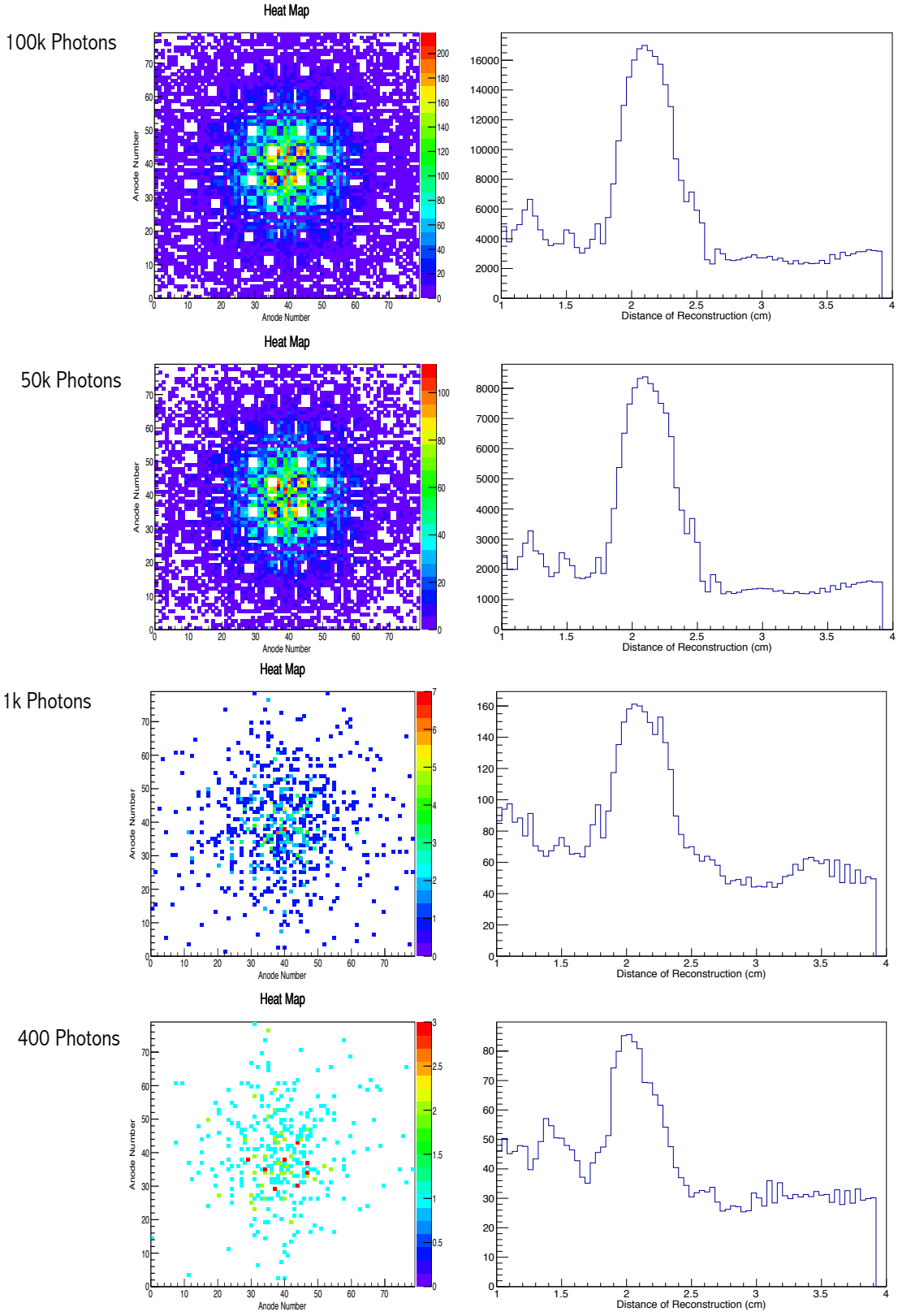

Figure 59. Continued.

a several-hundred keV event in a currently available crystal, it shows the system should work for a low number of photons, however the more photons collected the cleaner the peak.

4.7.A. DEPTH RESOLUTION

As with the 2-D case, while the system has been demonstrated to work for single events, the imaging resolution can be determined by the ability to localize many events to the correct depth. Figure 60 shows the depth localization distribution for 250, 400-photoelectron events at various depths throughout the bulk crystal. Each distribution is fit to a Gaussian with the FWHM of the fits given on the plots and in Table 5. As seen in the figure, all depths have good depth imaging resolution. Nearly 1 mm resolution is obtained throughout a 30 mm range of crystal. While the prototype does not indicate sub 1 mm resolution will be achievable, by using an anode map with slightly smaller pixel sizes and a higher mask rank with smaller features, it is expected that the depth resolution can be further improved. These results will be compared to real experimental data in Section 6.2.H.

Table 5. The depth of the launched events and FWHM (depth resolution) at each depth for 400 photoelectrons.

Depth in Scintillator Crystal (mm)	FWHM (mm)
0.5	0.28
10.0	1.03
20.0	1.15
30.0	1.12

4.7.B. LATERAL DIMENSION RESOLUTION

The lateral dimension results are shown in Figure 61 and given in Table 6. As mentioned above, the detector array used in the simulation is geometrically identical to that of the physical system. However, the QE of the PMTs and noise were not present in the simulation results. In the lateral dimensions, the system breaks down above 26 mm; as seen in Table 6, the results are *O*(1 cm). The results for events 25 mm into the crystal are (3.35 mm, 2.82 mm) for (X, Y).

Figure 60. The depth reconstruction for 250, 400-photoelectron events at various depths throughout a bulk crystal. The left column shows the histogram for the depth found. The right column shows the same histograms with a Gaussian fit used on each to obtain the width of the distributions. The values in the upper right corners of the left figures indicate the depth of the events, and the values in the upper right corners of the right column indicate the imaging resolution at each depth. Nearly 1 mm-uncorrected depth resolution is obtained. The true resolution in physical space is slightly broadened due to the index of refraction change [73].

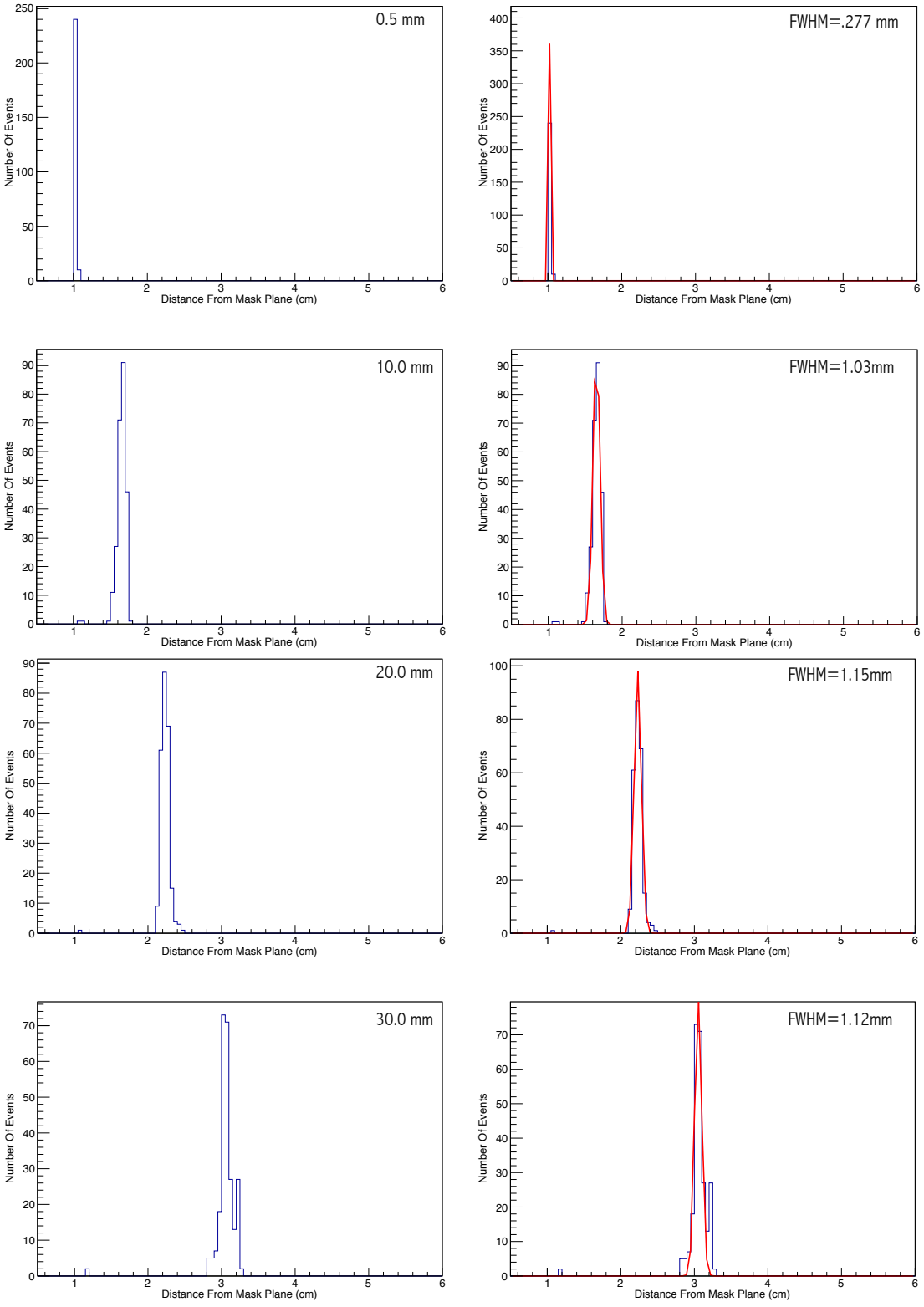

Figure 60. Continued.

Table 6. The X and Y resolutions for each of the depths for 400 photoelectrons.

Depth in Scintillator Crystal (mm)	X FWHM (mm)	Y FWHM (mm)
0.5	2.72	2.69
10.0	1.82	2.17
20.0	2.13	2.25
30.0	12.4	14.4

4.7.C. MULTIPLE MASK CYCLES

As mentioned earlier, due to the repeating nature of the overall mask pattern used, the outer repeated cycles of the base mask pattern can be used to increase the image peak counts relative to the background counts surrounding the point source peak. This was examined in an initial feasibility study [13]. While the study produced quantitative results on the improvements of outer cycles, the simulated imager used an ideal anode mapping instead of a physical detector array with variable pixel size and dead space. Thus, in order to compare to the experimental data that will be presented, new simulation results will be used to show the improvements of using outer cycles. The improvements in adding the outer cycles are easily apparent with both a small and large number of photons.

Figure 62 shows the results with reconstructing an event 20 mm from the bottom of the crystal at the correct depth both not using (left column) and using (right column) the outer ring of repeated mask cycles. In doing so, it was verified that this can be done in two ways with identical results; the rebinned data can either be added to the center array before the reconstruction, and then reconstructed with the decoder array a single time, or each outer cycle can be reconstructed and added in image space to the center reconstructed cycle image. While the results are identical, in practice the method of adding the rebinned data and performing the reconstruction a single time is much faster computationally, and thus this was the method selected. As seen in the figure, the outer cycle additions significantly improve upon the reconstructed peak height against the background signal.

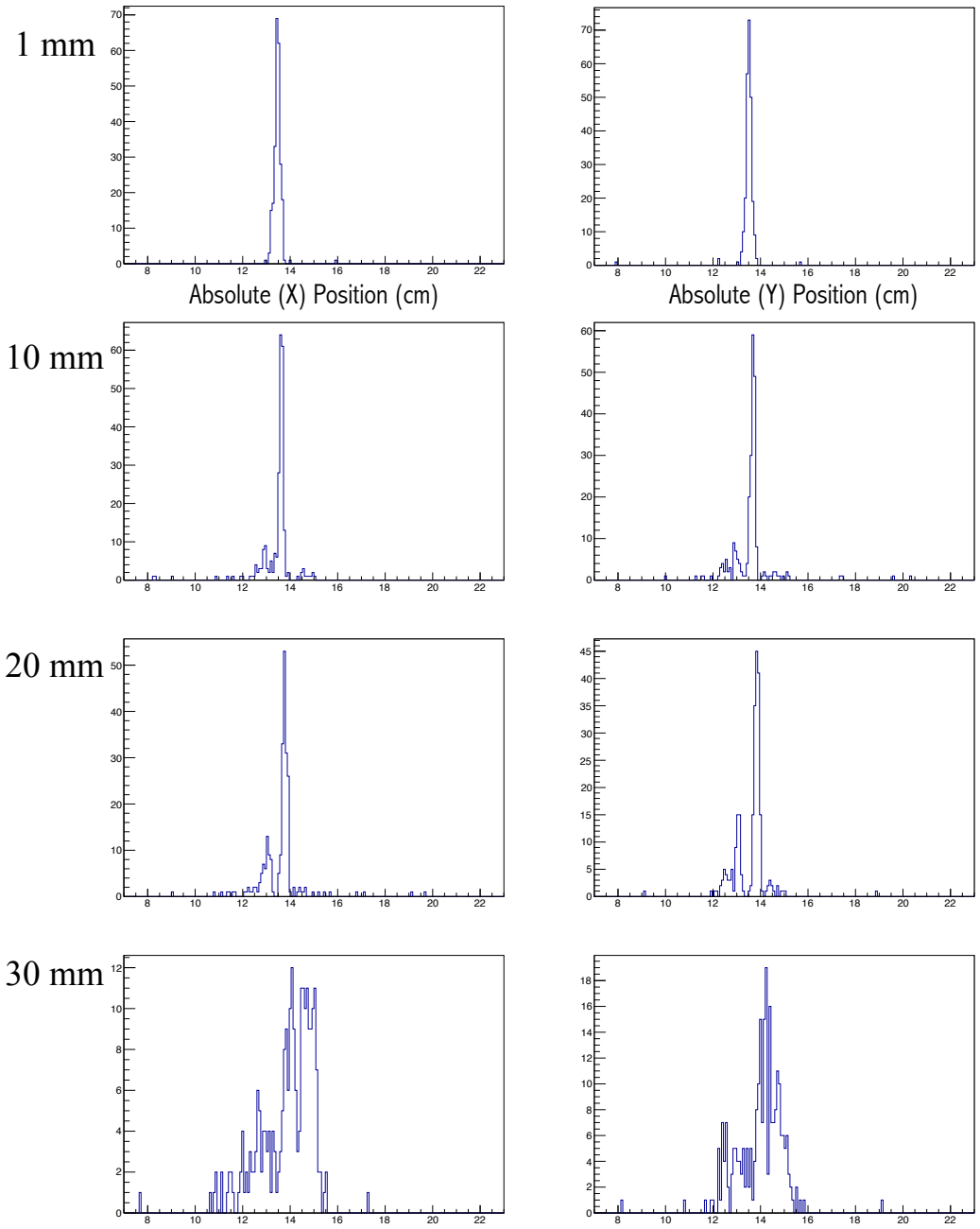

Figure 61. The lateral results for events at 1 mm, 10 mm, 20 mm and 30 mm into the scintillator crystals. The X results (left) and Y results (right) show good behavior until the upper-most depth. The bimodal structure beginning at 10 mm and showing strongly at 20 mm are due to events that are not found within one base cycle size of the true event location, shifting them one cycle width.

With 100k photoelectrons the peak height is improved by nearly a factor of 3, and with a realistic 400 photons the peak height is improved by about 2. While this indicates the next cycle outwards may help the peak height even more, this has been investigated, and due to both the scarcity of photons in the outer edges past the first ring of repeated cycles as well as the more extreme index of refraction distortions in the mask pattern, the next ring outwards does not impact the image quality in the simulation results.

The prior simulations in 2010 and 2011 [13] were able to show a significantly greater impact from using outer cycles; for events at the bottom of the crystal, using the outer ring of patterns alone increased the signal by 3.7, and for an event at the top by 7.6. This greater benefit is due to the fact that the simulation used a much smaller mask pattern that was 9.5 x 9.5 mm^2 and these results use a pattern of size 24.7 x 24.7 mm^2. The older results could use a smaller pattern because the anode array simulated used 0.5 mm^2 pixels with no dead spaces or variable pixel size. In order to make the system work for the much larger H9500 pixels, a larger mask element feature size is required.

Figure 62. The reconstructed images at the correct depths for events 20 mm from the bottom of the crystal. The top row is for 100k photoelectrons and center and bottom rows are for 400 photoelectrons. The left images use only the single center mask cycles in the reconstruction, while the right images also use the outer cycles; in the right images, 9 total cycles are used (1 center and 8 surrounding). As seen in the image amplitudes (color scale), the outer sum additions improve the top row nearly by a factor of 3 and the bottom row by over a factor of two.

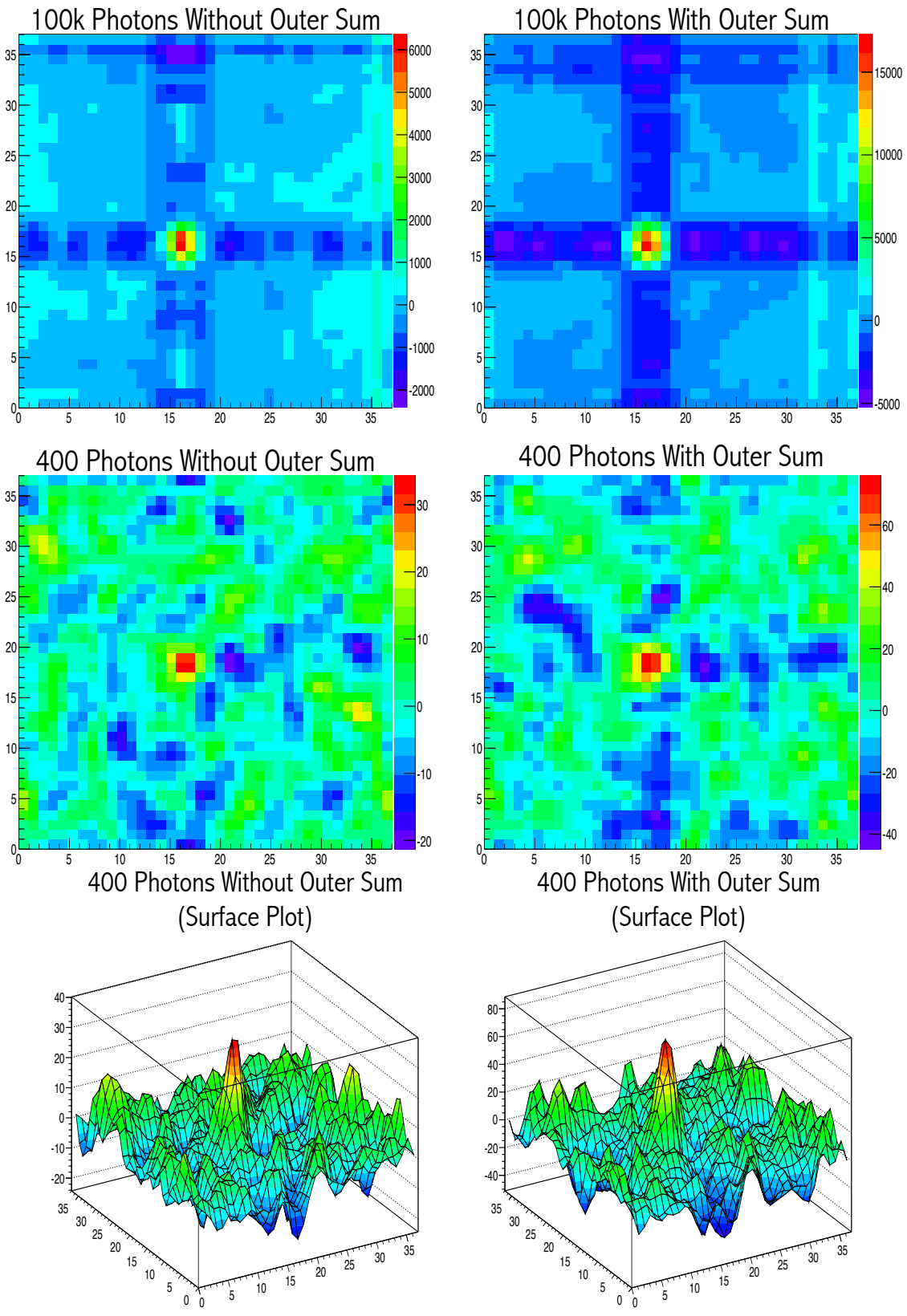

Figure 62. Continued.

CHAPTER 5. EXPERIMENTAL DESIGN

Two systems were designed, instrumented, and built. The first of the two was constructed in 2013 with data collection occurring in the summer of 2013, and the analysis through the fall of 2013. The second system was designed and built between December 2013 and the summer of 2014, with data collection and analysis occurring from July 2014 to the fall of 2014. As discussed in Chapter 4, each system's parameters were chosen using an analytical method and narrowed by running extensive GEANT4 [75] simulations to analyze the event localization capabilities. This chapter will provide a detailed overview and guide to each component of both detectors, including but not limited to: the electronics, software, event-processing imaging code, physical hardware, detector instrumentation procedures, and data collection methods. The final results (event localization, or imaging capabilities) obtained with each system will be presented in Chapter 6.

5.1. TWO-DIMENSIONAL SYSTEM

5.1.A. ELECTRONICS OVERVIEW

The two-dimensional system used three Hamamatsu 9500 PMTs to demonstrate the proof of concept for optical coded-aperture imaging. As the Hamamatsu 9500 was the type of photo transducer selected for the full system, it was appropriate to use the same PMTs for the smaller two-dimensional system. Due to initial cost restrictions, while a larger 6400-channel readout system for the full 3-D system was being developed, a maximum of 64 electronics channels were available to read out the initial H9500 array. The readout electronics were designed to allow for compact coupling of the PMTs. Two readout options were designed and built; one allowed for individual anode readout and the second coupled "strips" of 16 anodes into a single channel. The anode mappings of each option are shown in Figure 63.



Figure 63. The two options for the PMT readout configurations in the two-dimensional system. The PMT map is shown in the upper left without any readout diagrams in order to see the full, unmarked mapping. In the first readout board configuration (top right), the center 64 anodes of the H9500 can be read out individually. The second configuration (bottom) coupled each vertical strip of anodes into one signal. The figure shows 48 strips drawn onto the PMT array, with each strip yielding one channel.

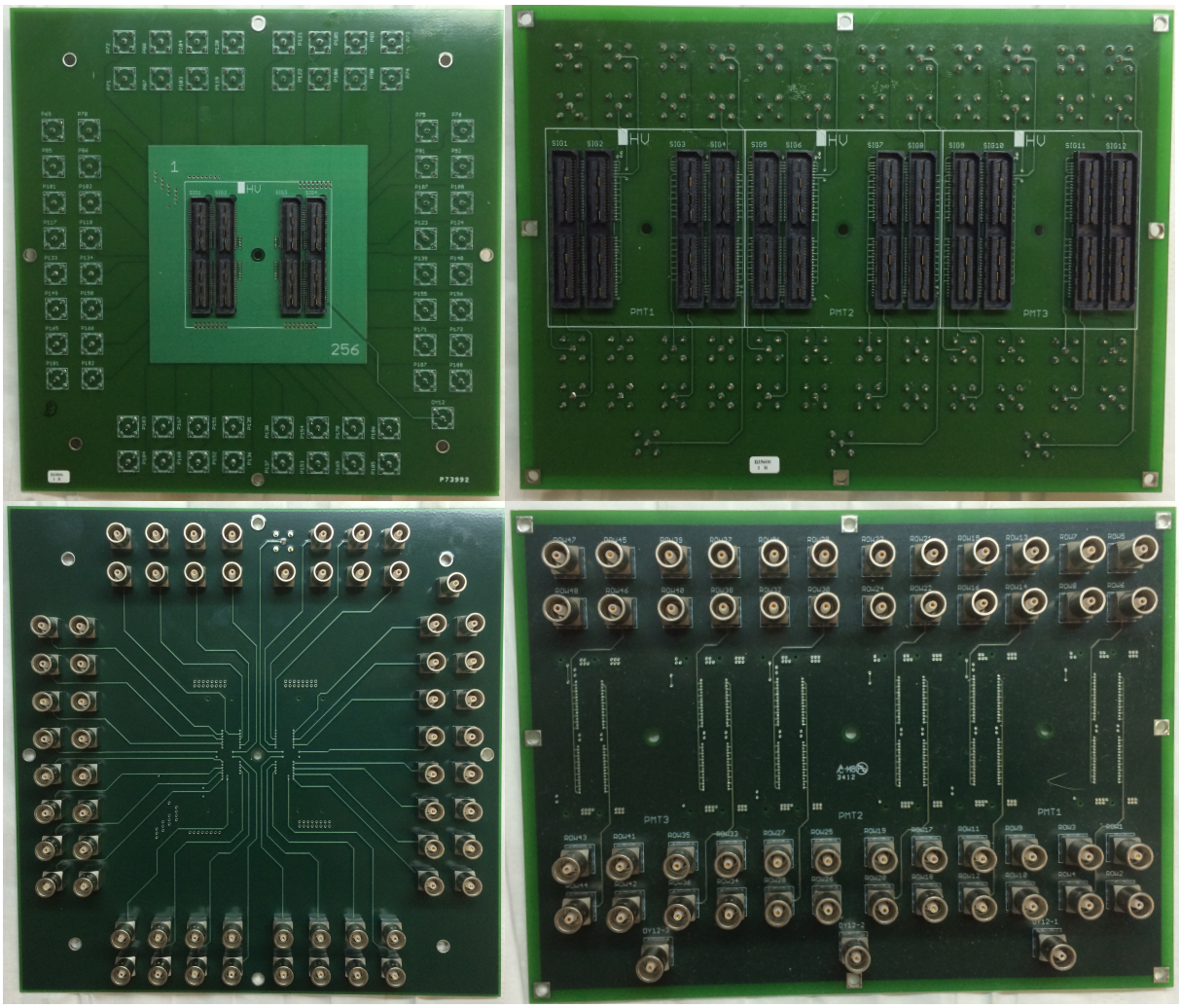

Figure 64. PMT side (top row) and cable side (bottom) of the two readout boards corresponding to the PMT readout anode configurations in Figure 63. The H9500s mount on the black connectors seen in the top row and LEMO cables are connected to the silver connectors in the bottom row. In the board on the right, the PMTs are closely coupled with the boundaries touching. This results in a dead space between active detector area equal to 3 mm, or slightly less than the size of a single anode width.

5.1.A.i. STRÜCK WAVEFORM DIGITIZERS

STRÜCK Waveform Digitizers [86] were used to record the signals from the PMT anodes read out through the readout board configurations. The experiment used four 16-channel, 250-

MHz digitizers (STRÜCK 3316). The readout speed results in a recorded data point from each anode every four nanoseconds. The digitizers were operated in a VME crate and read out by a personal computer. The digitizer and USB 2.0-to-VME Readout Controller used are shown in Figure 65.



Figure 65. From [86]. A 16-channel digitizer (left) and the VME-to-USB controller (right).

The PMT's last dynode signal was used for triggering. In the first configuration (single PMT), only one dynode signal was available. In the second readout configuration, the last dynode of the center PMT was used for the system triggering. The last dynode signal was split; one copy was sent to a channel of a digitizer to be recorded, while the other copy was sent into a Constant Fraction Discriminator (CFD) [6]. The output of the CFD was sent into a linear fan out NIM module and sent back into each trigger input of the 3316-digitizer cards. Thus, a last dynode was

used as a global trigger for the entire system in both cases (either in the 64-square array or the 48-channel linear array). The trigger threshold level was set physically in the CFD NIM module. Once the digitizers received the duplicated trigger, each channel opened a 3200-nanosecond window to record the waveforms.

A CFD was used because the timing jitter is less than for a leading edge or fixed level discriminator. As stated in [6], the method "produces an output signal a fixed time after the leading edge of the pulse has reached a constant fraction of the peak pulse shape". This allowed for use of last dynode signals because the CFD ensures that the true dynode signal always occurred at the same time in the integration window. Thus, the events with the desired dynode signal can be picked out. The waveforms will be discussed in detail in later sections.

5.1.A.ii. SIGNAL AND WAVEFORM ANALYSIS

Originally the waveform digitizers were set to high input impedance (1 kΩ). However, as seen in Figure 66 this setting produced unwanted noise due to signal reflections from the ends of the 50 Ω Lemo cables used in the system. The figure shows traces from 16 channels on the same plot. The 3200 ns window includes 10 e-foldings of the scintillator light decay time and captures the full signal from each event. As seen in Figure 66, the waveforms possess high-frequency oscillations that degrade the recorded signal. In order to eliminate the noise and collect a clean signal, the digitizers were set to a low input impedance of 50 Ω. However, this lead to unacceptably high noise levels because the size of the input signals were mismatched to the dynamic range of the digitizers.

To boost the signals from the readout boards, Phillips 776 amplifier modules [87] with a factor of 10 gain were used. This setting changed the recorded signal from the one shown in Figure 66 to that shown in Figure 67, and allowed the digitizer to record single packets of photon emissions over the entire decay time of the crystal. Sample waveforms from a single anode strip are shown in Figure 67. The upper left figure shows the complete waveform collected from a single channel. The upper right figure is zoomed in on the waveform in the vertical direction. The waveform shows low-frequency oscillations of the baseline throughout the entire integration period. The lower plot is zoomed into the waveform in the horizontal direction; the small separated peaks are the groups of photons arriving from the event in the crystal to the photo transducer (the crystal bleeds out the light over several hundred nanoseconds).

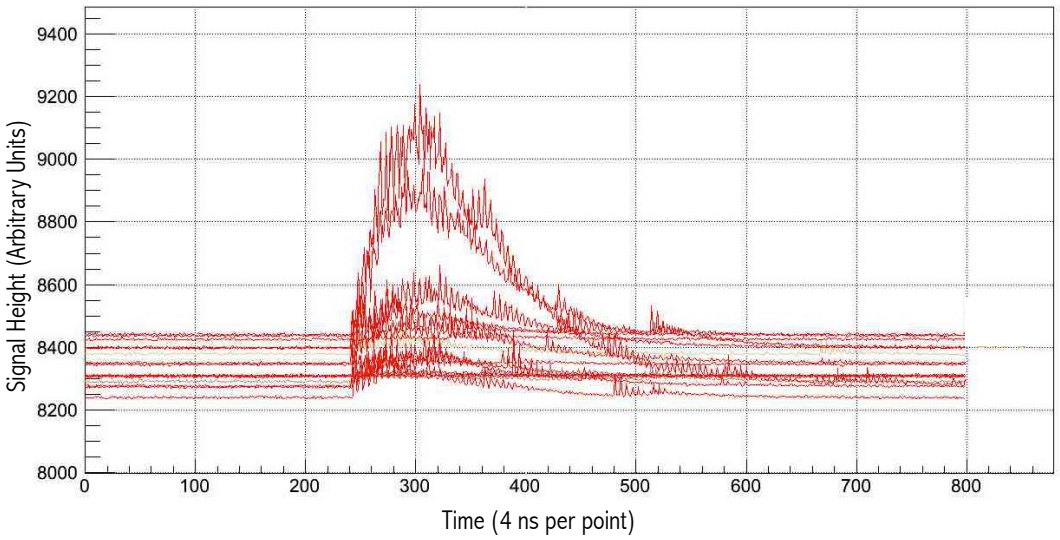

Figure 66. The recorded waveforms for 16 channels in a 3200-nanosecond integration window. The waveforms were recorded with the STRÜCK waveform digitizer on the high impedance setting (1 kΩ). As seen in the figures, while the general shape is what one would expect from a signal, the waveforms contain high-frequency oscillations that significantly degrade the signal and make it impossible to obtain a clean integrated value and, in turn, a high quality event energy measurement

Traditionally, one would extract the signal from the recorded waveform by extrapolating a baseline value, integrating the entire signal, and subtracting the baseline to obtain the signal above the baseline. Because of the low-frequency oscillations seen in the upper left plot of Figure 67, this method does not work, as the initial baseline integration does not give a reliable average value.

To overcome this, we opted to obtain the signal from the "peaklets" without relying on the baseline integration. Software was developed to do this automatically by selecting several parameters chosen after studying many waveforms individually. The algorithm developed was an adapted version of a ROOT-based [88] data-analysis framework. Three parameters were needed to extrapolate the signal from the peaklets; an initial threshold, a backward integration distance and a forward integration distance. Integrating only while the signal was greater than the threshold was not adequate in collecting the entire peaklet signals; as seen in the figure, the peaklets have structures distributed over several bins that often contain signal before the

maximum bin location. Without the backward and forward integration, the integrated signal would only contain the bins with values above the threshold. The threshold was set at 90.0 above the first data point value in the waveform (the baseline), with a backward and forward integration distance of two bins. This means that the threshold took into account an absolute offset in the recorded waveform points. Thus, every small peaklet with a value over 90.0 from the baseline was integrated one bin before and one bin after the peak. The baseline used was an average of the first 100 data points in the waveform. As will be shown in later sections, this method yielded good signal collection as seen by the energy resolution obtained.

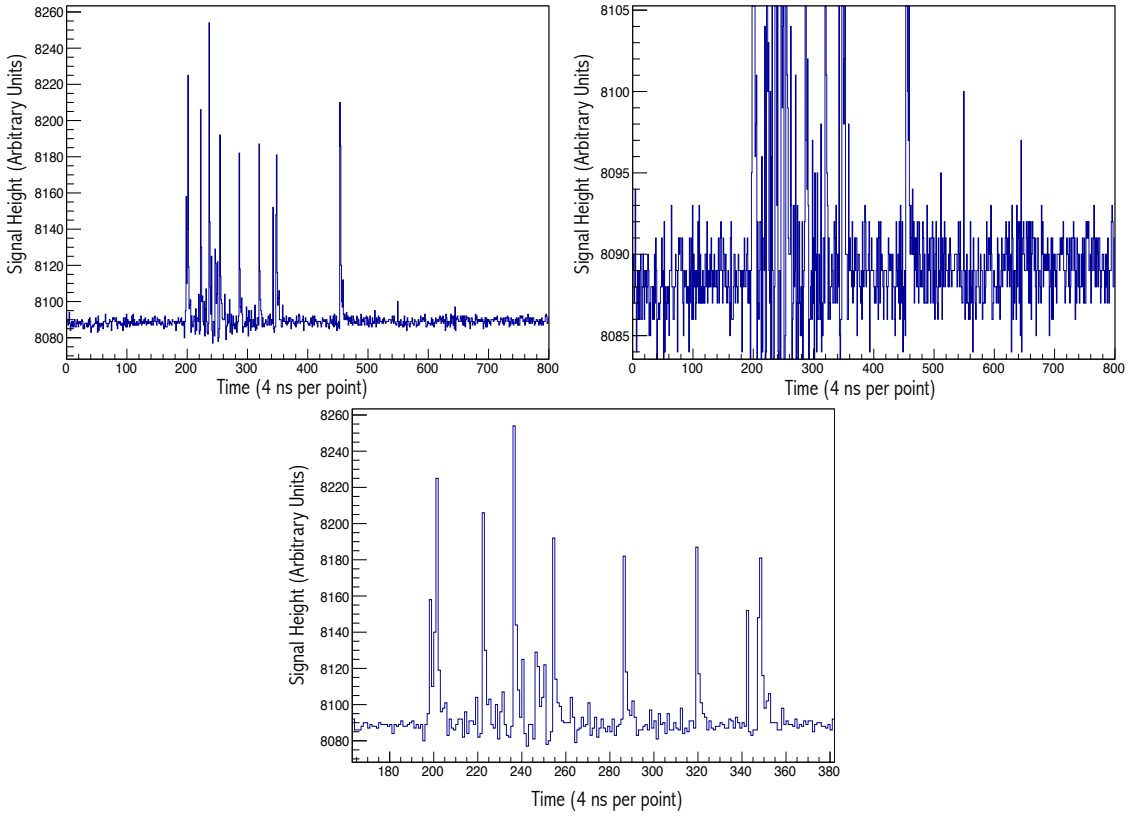

Figure 67. (Top left) The entire recorded waveform for a single anode strip with the digitizer set on low impedance. (Top right) The same waveform zoomed in on the vertical scale. The baseline fluctuates throughout the entire signal, making a classic baseline calculation and subtraction a poor method to acquire the true signal. (Bottom) The same signal zoomed in on the horizontal scale to the section with the peaklets.

5.1.B. TWO-DIMENSIONAL SYSTEM HARDWARE

The hardware was designed with several goals in mind; the most important being to allow one to measure the imaging resolution of the method at various depths of a bulk scintillator crystal. This was accomplished by fixing the PMT anode array positions, mask optical geometry (pattern, rank, feature size, etc.), focal length, and upper light guide while varying the amount of additional light guide between the top of the upper light guide and a thin scintillator crystal. This concept is shown in Figure 68 and Figure 69.

The approach uses a thin crystal at different distances from the readout surface to emulate events at a known depth in a bulk crystal. This is viable because at this stage in the system development, the top surfaces of the crystal (both thin and notional bulk crystal) are blackened to avoid reflections of light that is directed upward from the scintillation site. In order to truly emulate a thick crystal system, several specifics must be considered. First, the alignment of the PMT anode map, mask plane, and collimator must be fixed even when changing the upper light guide thickness. This is a complicated problem due to the need to make optical contact at all planes. In particular, the optical grease that must be used is a highly viscous material and in order to spread it evenly throughout the plane and get rid of air bubbles, the materials must be pressed together and moved circularly while applying pressure on each plane. The vertical and horizontal stresses are significant on each plane, so a rigid, reliable fixed position to which to align the mask, even when breaking and making optical contact with higher planes is required. Thus, hardware designed with multiple planes and the ability to lock each plane in place was designed and manufactured. A diagram of each plane and which planes are locked laterally are shown in Figure 69.

The entire structure was built vertically off of, and used the support of, a light-tight aluminum box. Using the aluminum frame as a support, the entire stack including the PMT readout boards, the focal length light guide, the photomask plane, the upper light guide, and the crystal were vertically mobile.

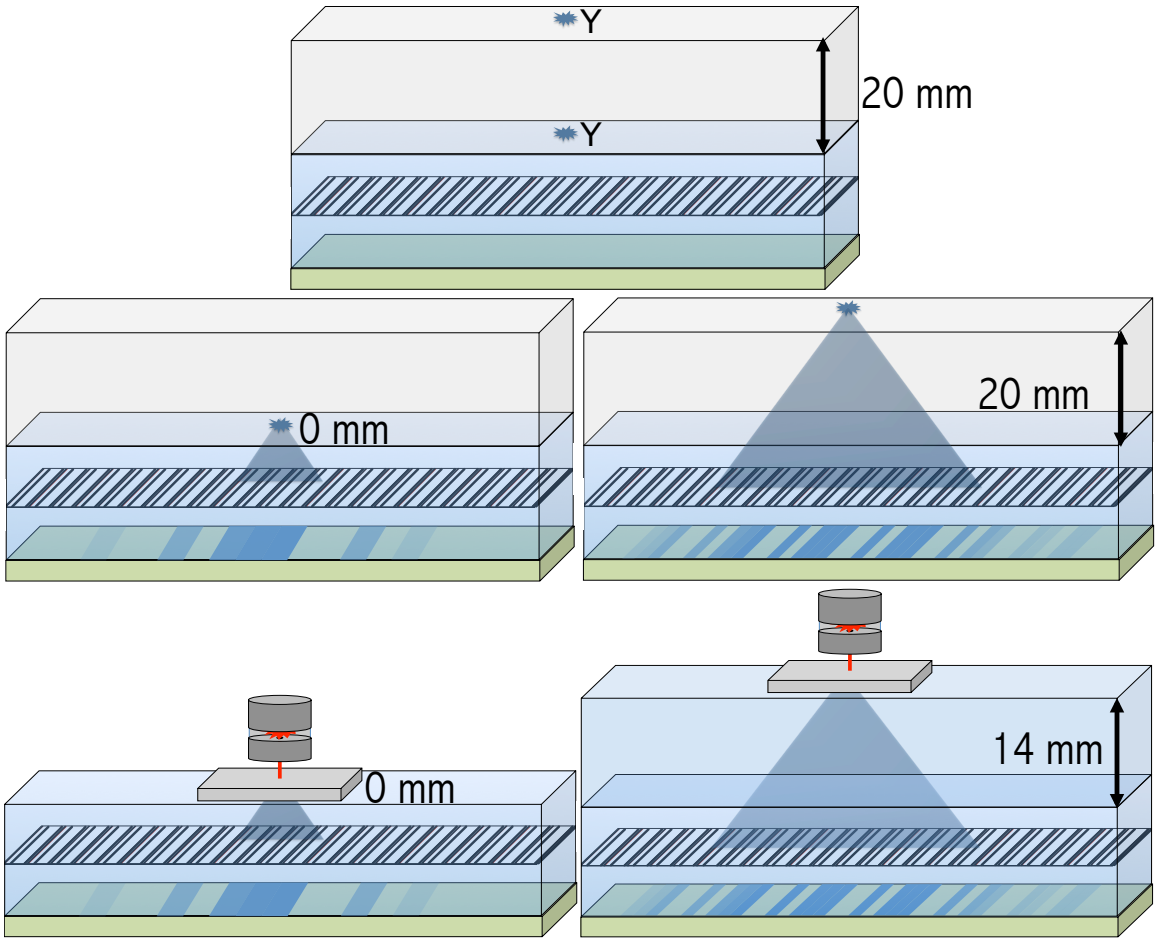

Figure 68. A schematic of the concept used to determine event location in a thick crystal. A 20-mm-thick crystal can be emulated with a thin crystal and light guide variation. To mimic an event at the bottom (second row, left) of the crystal, no extra upper light guide would be added (bottom row, left) and the magnified pattern on the detector from a gamma-ray event in a thin crystal would be the same as an event at the bottom of a thick crystal. For an event at the top of a thick crystal, additional upper light guide can be added between the upper light guide and the bottom of a thin crystal to emulate the event. The event in the thin crystal will project the same magnified pattern as the event at the top of a thick crystal. As discussed earlier, because of the index of refraction change, less additional quartz upper light guide is needed than crystal thickness to have equivalent magnified patterns at the PMT plane.

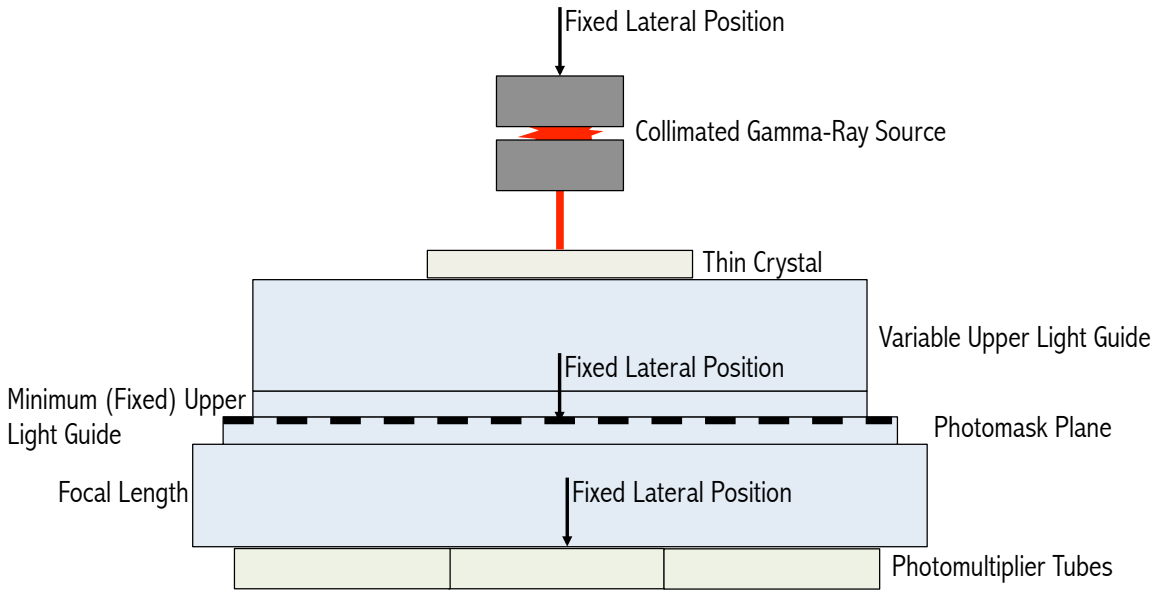

Figure 69. Each individual plane that the hardware is designed to hold with the required alignment labeled. The collimator, mask plane and PMT plane are the only planes that require lateral alignment. As the mask pattern is one dimensional, the other lateral dimension (into the page) of the mask does not matter. The PMTs were held in place by a mount around the readout electronics boards. The mask was held in place with plastic screws to lock onto an edge, and the collimator was mounted on two linear slides with the ability to move both automatically and manually in 10-micron increments.

As indicated in the figure, the readout board and PMTs were locked laterally, with the photo-mask plane moveable laterally using two linear Velmex Bislides [89]. In practice, the mask plane moved slightly and the data had to be adjusted in the data analysis. The process to assemble the system is given below:

1. The stack with the focal length, the photomask, and the upper light guides was built as seen in Figure 70. Each plane was optically coupled together using BC-630 [76] optical coupling compound.
2. The stack was optically coupled to three "floating" PMTs using BC-630. While the PMTs were arranged in the same orientation, the exact position of each was not fixed at this point.

3. The stack was flipped upside down and the PMTs were guided to match the readout board position and coupled to it using the relevant connectors. The stack-PMT-Board assembly was then flipped back over. It was initially supported by the PMTs, but was then lowered to just make contact with an aluminum frame that supported the weight of the focal length, the photo-mask plane and the upper light guide.
4. The photo-mask plane was locked into place and the upper light guide thicknesses could then be broken and remade while the PMT and photo-mask positions were maintained to a tolerance of several tenths of a millimeter.
5. The crystal was mounted to the top of the stack between the additional upper light guide plane and the collimator.

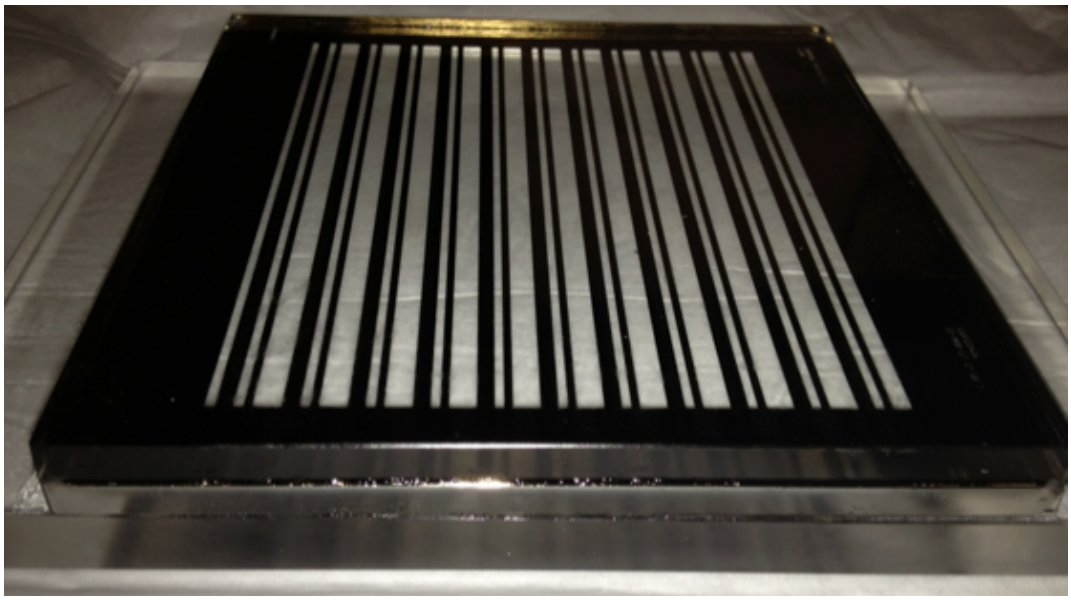

Figure 70. The stack consisting of the focal length plane (bottom), the photomask (middle) and upper light guide (top). As seen in the figure, the top of the photomask is a dark chrome material that is 99.968% opaque to ~420 nanometer light. The crystal (not shown) couples to the top of the stack.

The hardware described is shown in Figure 71. The rotating lever to the right of the collimator raised and lowered the entire apparatus including the readout board. The figure shows the system

with only a single PMT, but the fully assembled 2-D system had an additional PMT on either side of the central 9500.

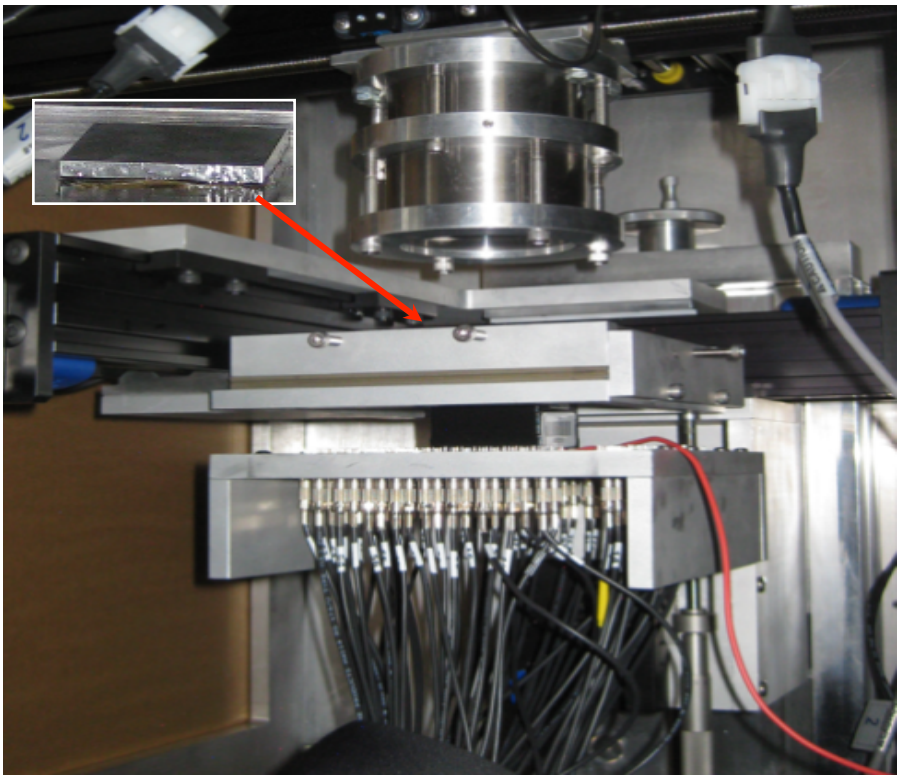

Figure 71. The hardware of the two dimensional system. The collimator was mounted on to linear slides. The entire system could be raised and lowered with respect to the collimator. The readout board in the image is the 64 single anode configuration with a single PMT. The stack shown in Figure 70 above is optically coupled to the PMT and sits in the aluminum frame in the middle of the image. The thin crystal is coupled on top of the stack and is shown in the inset image in the upper left.

As stated, the entire enclosure was built into a light-tight aluminum box. The light seal was verified by examining the last dynode signals from the system. The source collimator was made of tungsten with a design that accommodated any commonly used source shape. It allowed for a 1 or 2 mm diameter collimation pinhole with at least 1.35 inches of shielding in all directions.

5.1.C. ENERGY SPECTRUM CALIBRATIONS

Once the system was assembled and the data acquisition system was programmed and tested, the first step was to perform energy spectrum tests and calibrations. In order to obtain a full mapping of the system response, several nuclear sources with a range of spectral lines were used. To test the low-energy response of the system, a ^{57}Co (dominant spectral line at 122 keV) source was used.



Figure 72. A one-dimensional binary mask pattern with alternating 2-mm transparent and opaque elements made by Toppan Photomask [90]. In addition to being used for magnification verification tests (discussed in the next section), the pattern was useful for energy spectrum calibrations and sanity checks to verify that the light received at the PMT plane was halved when a binary mask was placed between the crystal and the PMTs.

In addition to the rank-7, 1.4-mm, MURA mask pattern, two one-dimensional binary masks were ordered; each had alternating transparent and opaque lines with 1-mm and 2-mm spacing (Figure 72). For a simple energy calibration, two data sets with the same system were used with

and without a binary mask pattern. As the binary mask blocks half of the light per event (50% open), the signal per event should be half of that without a mask pattern.

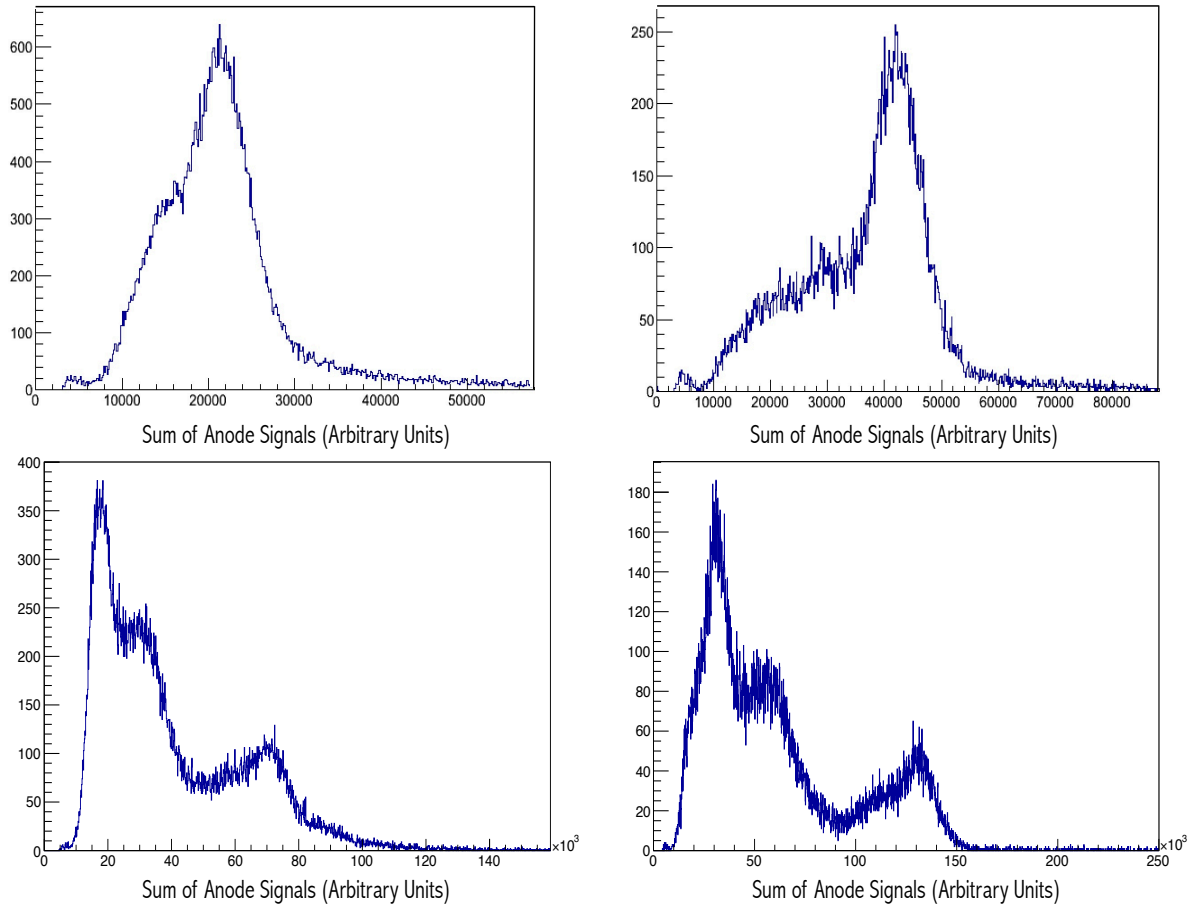

Figure 73. The energy spectra with (left) and without (right) the 50% binary mask pattern using a 2-mm-thick NaI(Tl) crystal. The upper row is for a ^{57}Co source with the large peak at 122 keV. The bottom row is with a ^{133}Ba source, with the right-most peak at 356 keV. As seen in both energy spectra, the overall shape of the energy distributions do not change when the binary mask is inserted, but the peak locations for the same energies are halved, as half of the light per event is collected at the photomultiplier tubes due to the mask.

As seen in the figure, the shape of energy distribution remains the same with and without the mask, while the light per event is cut in half. This verifies the light collection difference one

would expect to see with a simple binary pattern. While the overall shapes are similar, the reduction in light reduces the energy resolution. The energy resolution of the 356-keV peak is 21% without the mask pattern and about 30% with the binary mask. This is as expected, as a decrease of half of the light per event should give a factor of a $\sqrt{2}$ decrease in energy resolution. Additionally, the 356-keV energy spectrum obtained with the last dynode signals gives 15% and 21% without and with the mask, respectively.

5.1.D. MAGNIFICATION DIFFERENCE VERIFICATION

Once the energy behavior with the mask pattern was checked, the ability to detect magnification differences with different size mask features was studied. While simple, this check was fundamental in verifying that the mask concept would provide 3-D position resolution since the magnified pattern differences allow the system to properly discern an event's depth. First, one-dimensional magnification tests were performed. Both a 1 mm and 2 mm binary mask pattern manufactured by Toppan Photomasks [90] were used. The ^{133}Ba source was used with a 1-mm-thick NaI(Tl) crystal, a 3-mm-thick upper light guide (mask to crystal), a 12.85-mm focal length and 2-mm binary mask pattern. This geometry gave a magnification of 5.28 and, in turn, a magnified feature size of 10.56 mm. As the H9500 has pixel sizes of 3.04 mm, this magnification resulted in the binary pattern magnified to about three pixel widths. An image of the setup is shown in Figure 74. The exit window of the crystal was 3 mm and was used as the upper light guide. The 2-mm mask pattern is seen coupled to a several-cm-thick piece of quartz, which is mounted to the PMT. The three-PMT-strips readout board was used with one PMT for the measurements.

A second configuration was used to show that the system could resolve smaller magnified features. A single event is shown in Figure 76. The system used a 1-mm-thick crystal with a 4-mm-thick upper light guide, a 7.85-mm focal length and the 2-mm binary mask. This resulted in a magnification of 2.96 and a magnified feature size of 5.9 mm. The 2-pixel-wide magnified pattern is clearly seen in the figure.

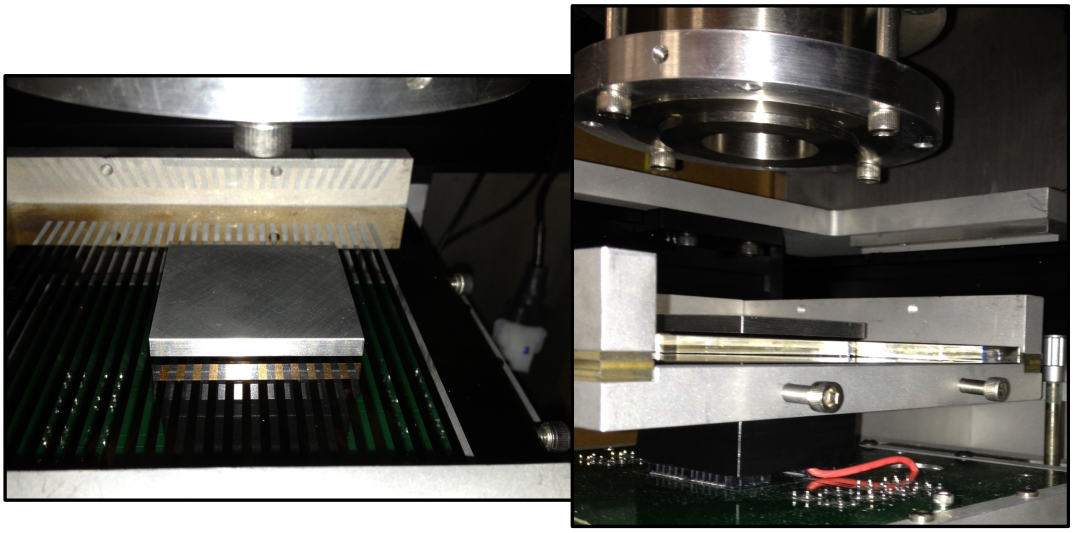

Figure 74. Images of the magnification test setup. The crystal is coupled to the 2 mm binary mask pattern, with the PMT read out using the one-dimensional anode strips readout board.

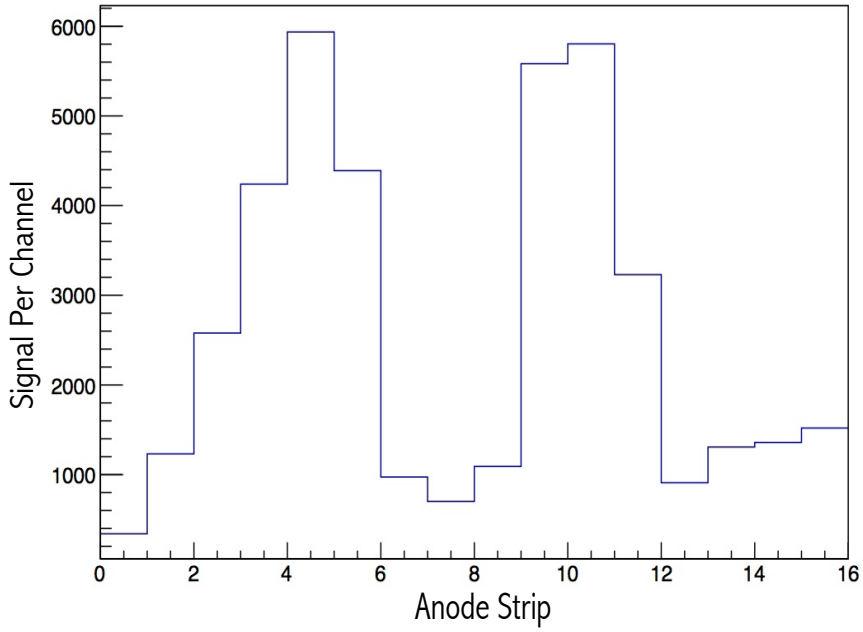

Figure 75. A one-dimensional binary magnified pattern for a single, 356-keV, gamma-ray interaction. The magnified three-pixel pattern can clearly be seen in the signal, with the event centered over the center opaque region.

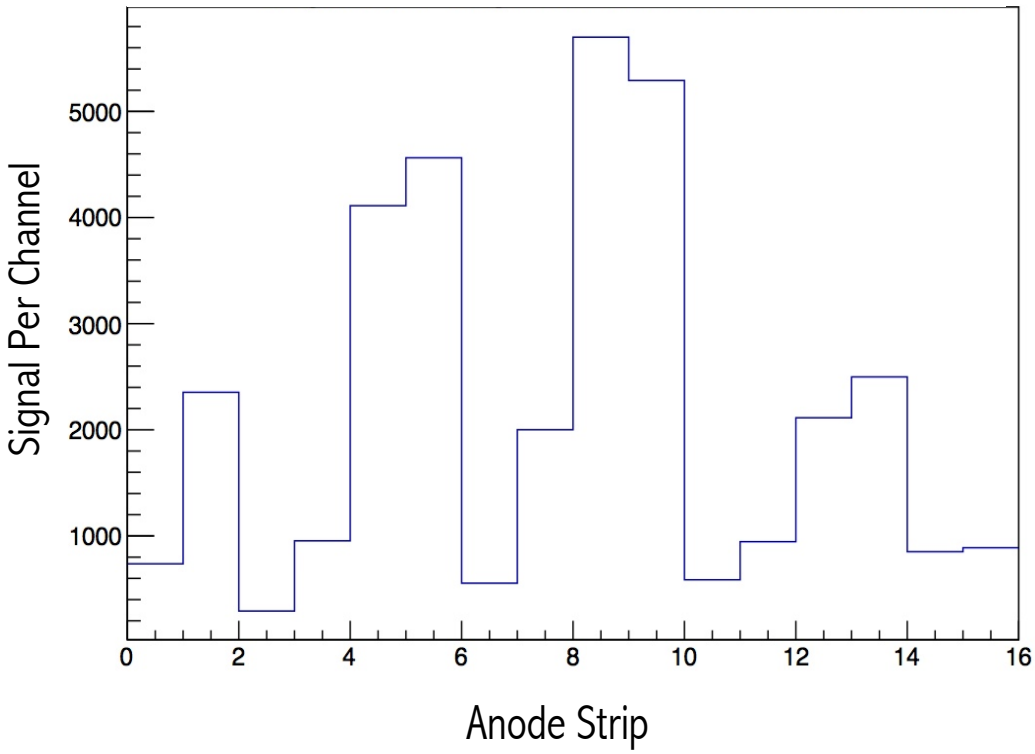

Figure 76. Sample event from the second configuration used to demonstrate the ability to detect pattern magnification differences. The magnified features are about 2 pixels wide.

As a regular two-dimensional mask pattern was not available, the two one-dimensional binary masks were used with the strips oriented orthogonal to each other to create one. One binary mask had 2 mm features and the other had 1 mm features, so the magnified features of the 2-D pattern were rectangles with a 2:1 length-to-width ratio. An optical geometry was chosen so that the magnification was 3.01, resulting in the 2-mm pattern being magnified to 2 anode pixel widths and the 1-mm pattern being magnified to 1 anode pixel width. The result for many events is shown in Figure 77. The 2-mm magnified mask is easily visible in the aggregate image. In the vertical direction the pattern is less well defined. This is due to blurring due to the beam width. The collimator diameter was 1 mm and the spread of the beam by the time it reached the crystal was ~1.2 mm, so the gamma-rays were being deposited at a spread slightly larger than the mask pattern size. As such, the magnification for many events in this direction is somewhat washed out.

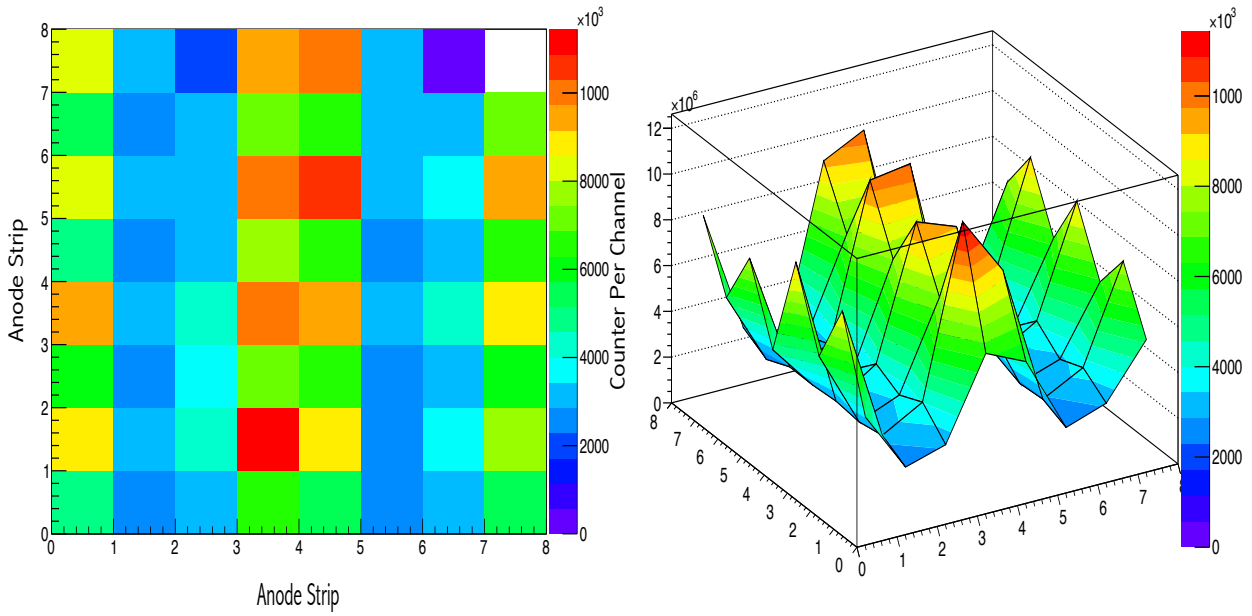

Figure 77. Many aggregated events with the two-dimensional readout board. The upper right pixel is empty as it was used for the last-dynode data of the PMT. As seen in the heat map, the two-dimensional magnified mask pattern is clearly seen in the signal. The larger horizontal magnified feature is more cleanly defined than the smaller 1-pixel-wide feature because the beam spread at the crystal (1.2 mm) was comparable to the size of the mask features (1 mm), resulting in a blurring of the pattern when many events were combined.

In addition to the aggregate events, it was important to verify that the PMT array could resolve two-dimensional magnification differences for single events. Several single-event patterns are shown in Figure 78 with each heat map collapsed in both dimensions, shown in the histograms to the bottom and sides of the detector hit patterns. The figure clearly shows the system's ability to resolve the magnified mask pattern with different size magnified features.

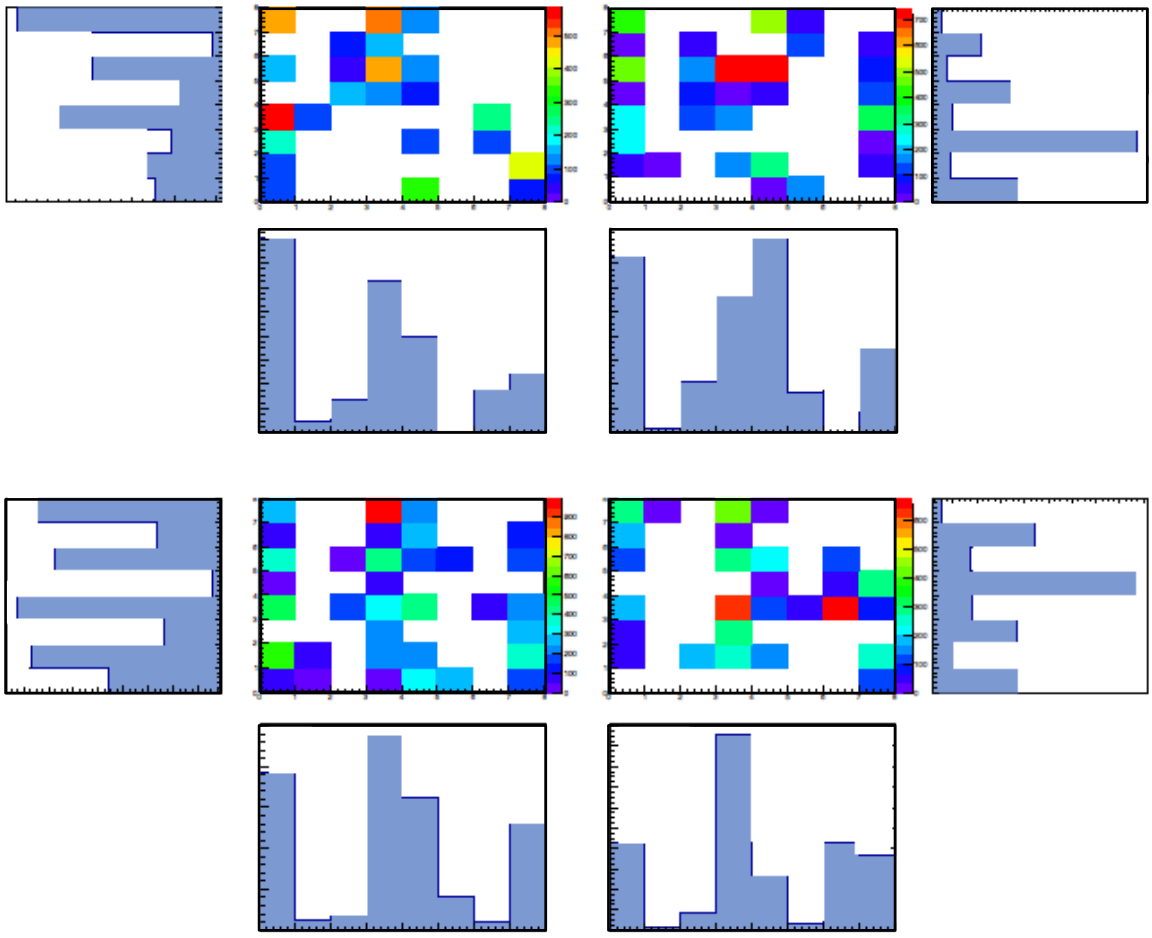

Figure 78. Single events from the same data set as the aggregate events shown in Figure 77. Histograms to the sides and below each heat map show results when data for the event are collapsed in each (x and y) direction to enhance the one-dimensional magnified pattern for each event. The one-pixel-wide magnified pattern in the vertical direction and two-pixel-wide magnified pattern in the horizontal direction are clearly seen for each event.

5.1.E. EVENT PROCESSING

The individual events were processed in the same method as the simulation events described in Chapter 4. The overall processing steps are:

1. Input data were raw waveforms (800 data points per waveform) recorded on disk for each channel for each event. Each event also included a last-dynode-integrated value.

2. The waveforms were analyzed using the peaklet integration method discussed above. Each waveform signal value was then saved to disk in a new file.
3. The extrapolated waveform signals from step 2 were read and assigned to physical detector anode (strips) positions.
4. A weighted mean of the detector data was used to determine the coarse lateral position information about which image deconvonlution was performed.
5. A coarse depth parameter was determined to constrain the depth search. This is described in detail in Section 6.1.B.
6. The data were rebinned to half of the magnified feature size (oversampling by two) for each depth.
7. An image was made at each depth and the depth with the maximum image height was used as the event depth.
8. A weighted mean for the event location in the image for the event depth (step 7) was used with the coarse position information (step 4) to give the absolute lateral position of the event.

However, before these steps could be applied there were some additional steps added to account for experimental parameters. These are discussed in the next two sections.

The data sets were collected in June 2013. Once the bottom portion of the stack was built (focal-length quartz, photomask plane and minimum upper light guide), the assembly thickness was increased to the desired thin crystal center location by adding quartz planes above the upper light guide (Section 5.1). The stack was then flipped over and the PMTs were coupled to the bottom. It was then flipped again and mounted on the readout boards. The mask position was then locked relative to one of its corners to obtain approximately the same position for each mask element in every data set, even when new upper light guide was added. The final results will be presented in the next chapter along with a coarse depth localization method.

5.1.F. GAIN CORRECTIONS

Hamamatsu 9500 tubes are known to have significant overall gain/QE variations [84]. Unfortunately, the system was disassembled before a full gain map and subsequent anode gain correction were applied to the system. However, due to the multi-anode nature of the anode strips, the strip-to-strip gain variations were less than those of individual anodes. Worse, the PMT positions were not maintained between different data sets, so a full mapping was

impossible after all of the data sets were collected. Instead, aggregate data of many events were used to smooth out the overall light shape for a gain calibration. This is shown in Figure 79.

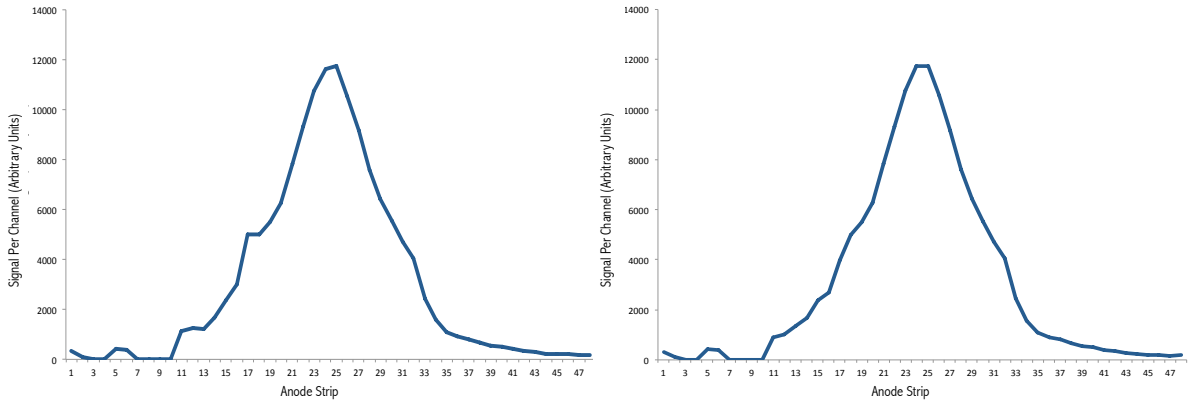

Figure 79. The anode response for many events in a thin crystal 22 mm from the PMT plane. The shape should be a smooth distribution, but as seen in the response there are discontinuities at anodes 16 and 17. These were smoothed out and the same data with the gain corrections applied are shown on the right.

5.1.G CENTER LOCATION ADJUSTMENT

The photomask plane was intended to remain stationary relative to the PMT anode array throughout all measurements, but in practice it was found that it shifted by several millimeters in each measurement. This was a result of the force required to break and remake the optical connections in the upper light guide planes. Thus, in post-processing a small correction was added in each data set to laterally center the reconstructed image peaks to the center of each image array. It was done once per data set, so all events at each depth were constructed with a single offset value.

5.2. THREE-DIMENSIONAL SYSTEM

This section will present the details of the three-dimensional system, including the design parameters, hardware and electronics design, and instrumentation. As discussed in the simulation

in Section 4.7, a wide variety of optical geometries were investigated and a rank-19 mask was found to have the best performance for the system.

5.2.A. ELECTRONICS

The electronics were designed and manufactured by XIA LLC [91] [92]. The system was designed to readout 25 H9500 PMTs closely packed into an array as seen in Figure 80, although only 20 were used.

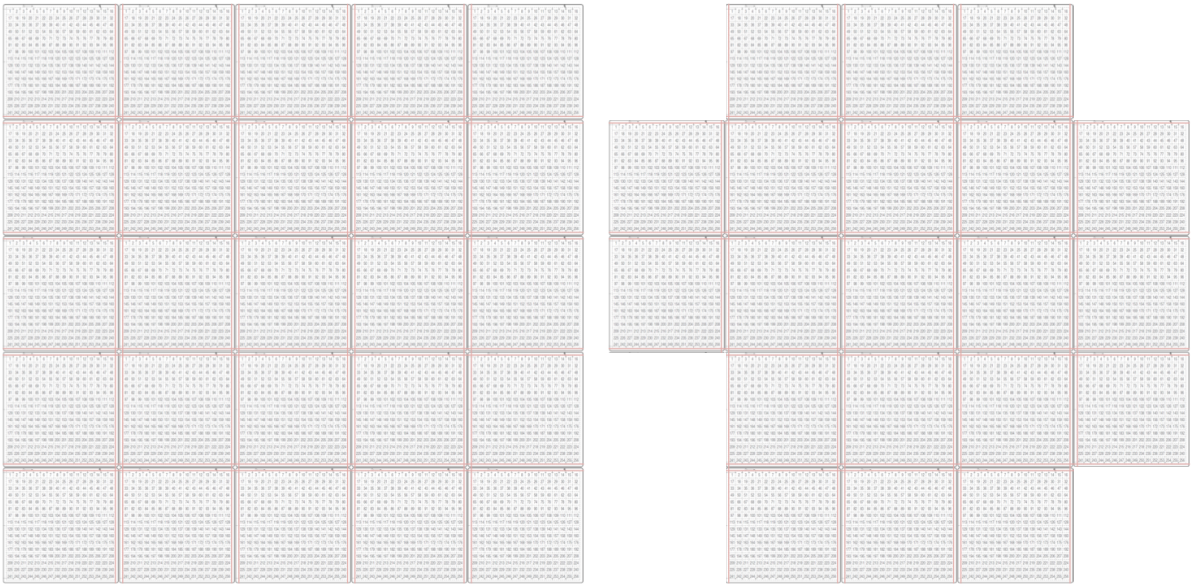

Figure 80. (Left) The 25 H9500 close packed array for which XIA designed readout modules. The modules were designed to allow a closely packed array without adding separation to the small gap between the PMTs. The figure on the right shows the array that was used in the actual system. The PMTs in the corner were not used and only 20 modules were instrumented.

Originally, we planned on using 21 H9500s with Photonis Planacon modules [93] on the corners of the system. The Planacon modules have smaller pixel size (1.6 mm^2), but due to cost restrictions the original design called for four pixels to be summed to one channel. Designing the requisite board to read out the corner modules was dropped due to both cost and time restrictions of the project. The final system only used 20 H9500s due to one dead PMT.

5.2.A.i. DATA ACQUISITION SYSTEM

In addition to the physical requirements, the data collection system was designed with several goals in mind. The system required a global triggering system, to capture low light (O(1 photon)) signals (and thus have low readout noise), and the capability to handle high count rates [100]. In addition, cost constraints set a goal of $50.00 per channel [92].

The XIA data acquisition system consists of three main sections:

1. PMT front-end readout electronics that collect the signals from each anode of each PMT. This is called the PMT256. This records the 256 anode signals and outputs them as 32 multiplexed signals.
2. Digitizer that collects the 32 multiplexed signals from each PMT256. This is called the MPX-32D. The MPX-32D then communicates the anode signals to a desktop computer via a PCI interface.
3. A trigger module that both supplies power to each PMT256 module and controls the triggering of all modules.

5.2.A.ii. FRONT-END READOUT MODULE

The front-end readout module that mounts on the PMT can work with the close-coupled design of the H9500 array without adding any additional dead space between the PMT edges. A PMT256 module is shown in Figure 81.

Each PMT256 contains 64 analog integrators that feed into 8 multiplexers [100]. The multiplexer allows for the system to read 8 channels with a small number of electronic components, reducing the cost per channel of the data acquisition system. The integrators use dual op-amps with a time constant of 20-50 microseconds. This allows for a high count rate (up to 3×10^5 counts per second). The integrator and multiplexer cards in each PMT256 are paired with an end cap that communicates with the MPX-32D card for timing information. The sampling rate of each anode was 1.04 MHz.

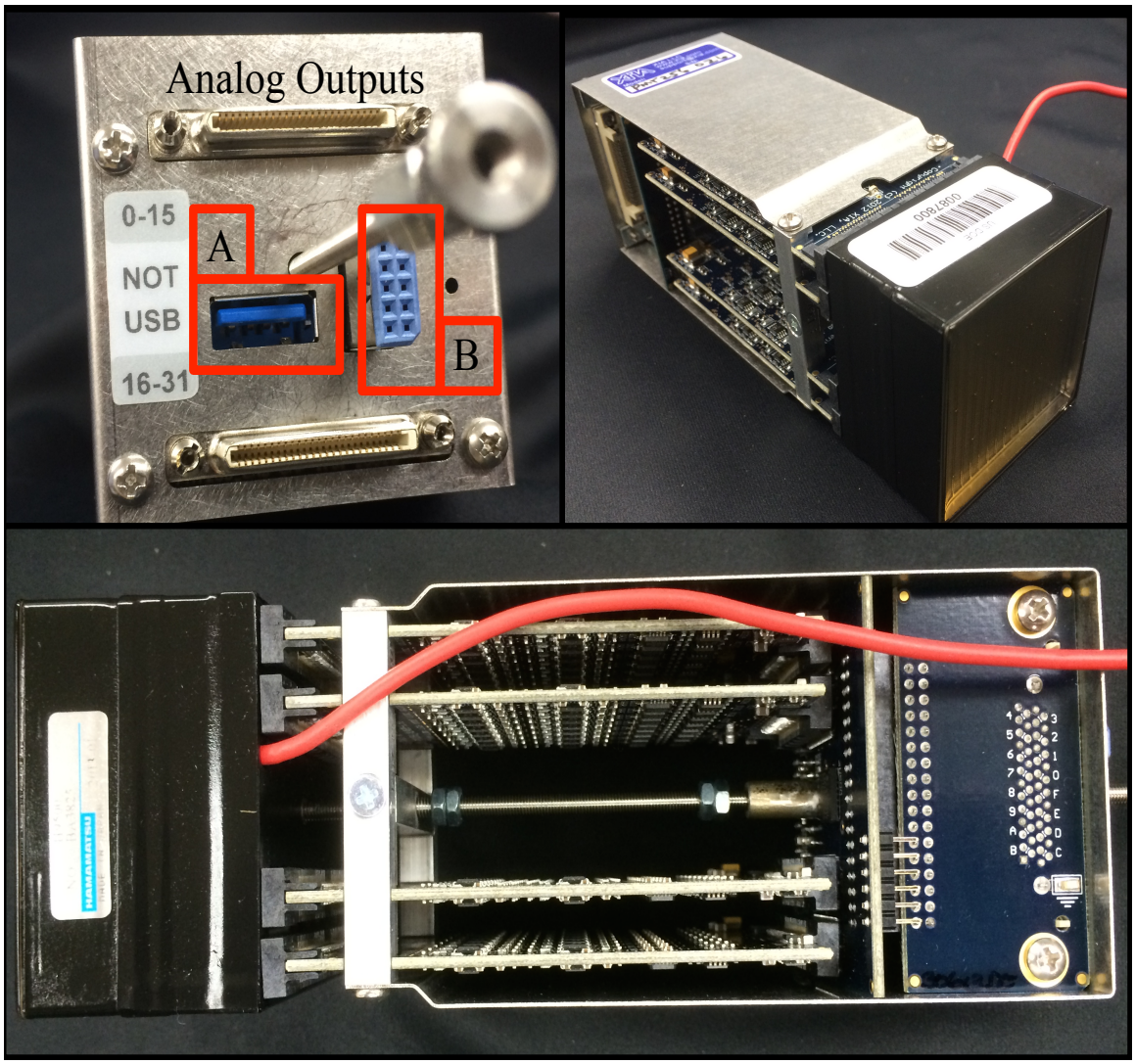

Figure 81. (Top left). The connectors on the back side of the PMT256 module. The top and bottom analog anode connectors output 32 multiplexed, integrated signals containing the signal for 256 anodes. (Top right, bottom). The PMT256 connected to a H9500. The module adds no dead space between the anodes in the PMT array.

Each analog signal carries 8 channels, as shown in an anode map of a single H9500 in Figure 82.

H9500 Anodes

0	16	32	48	64	80	96	112	128	144	160	176	192	208	224	240
1	17	33	49	65	81	97	113	129	145	161	177	193	209	225	241
2	18	34	50	66	82	98	114	130	146	162	178	194	210	226	242
3	19	35	51	67	83	99	115	131	147	163	179	195	211	227	243
4	20	36	52	68	84	100	116	132	148	164	180	196	212	228	244
5	21	37	53	69	85	101	117	133	149	165	181	197	213	229	245
6	22	38	54	70	86	102	118	134	150	166	182	198	214	230	246
7	23	39	55	71	87	103	119	135	151	167	183	199	215	231	247
8	24	40	56	72	88	104	120	136	152	168	184	200	216	232	248
9	25	41	57	73	89	105	121	137	153	169	185	201	217	233	249
10	26	42	58	74	90	106	122	138	154	170	186	202	218	234	250
11	27	43	59	75	91	107	123	139	155	171	187	203	219	235	251
12	28	44	60	76	92	108	124	140	156	172	188	204	220	236	252
13	29	45	61	77	93	109	125	141	157	173	189	205	221	237	253
14	30	46	62	78	94	110	126	142	158	174	190	206	222	238	254
15	31	47	63	79	95	111	127	143	159	175	191	207	223	239	255

PMT256 Multiplexed Signals

0	2	4	6	8	10	12	14	16	18	20	22	24	26	28	30
0	2	4	6	8	10	12	14	16	18	20	22	24	26	28	30
0	2	4	6	8	10	12	14	16	18	20	22	24	26	28	30
0	2	4	6	8	10	12	14	16	18	20	22	24	26	28	30
0	2	4	6	8	10	12	14	16	18	20	22	24	26	28	30
0	2	4	6	8	10	12	14	16	18	20	22	24	26	28	30
0	2	4	6	8	10	12	14	16	18	20	22	24	26	28	30
0	2	4	6	8	10	12	14	16	18	20	22	24	26	28	30
1	3	5	7	9	11	13	15	17	19	21	23	25	27	29	31
1	3	5	7	9	11	13	15	17	19	21	23	25	27	29	31
1	3	5	7	9	11	13	15	17	19	21	23	25	27	29	31
1	3	5	7	9	11	13	15	17	19	21	23	25	27	29	31
1	3	5	7	9	11	13	15	17	19	21	23	25	27	29	31
1	3	5	7	9	11	13	15	17	19	21	23	25	27	29	31
1	3	5	7	9	11	13	15	17	19	21	23	25	27	29	31
1	3	5	7	9	11	13	15	17	19	21	23	25	27	29	31

Figure 82. From [91]. (Left) The H9500 anode mapping from 0-255. (Right) The multiplexed channels with each number corresponding to 8 anode signals.

When the signal is fed into the next stage in the electronics (MPX-32D), the signals contain the integrated anode signals. Connection A in Figure 80 is the power supply for each PMT256 and also carries the last dynode signal for each PMT for each event to the trigger module. It also carries run control information such as the integration window, sampling rate, etc. Connection B carries the dynode threshold and buffer read statuses to the module.

5.2.A.iii. DIGITIZER

The MPX-32D digital spectrometry card consists of 32 analog inputs, digital I/O ports, field programmable gate arrays (FPGA), and a PCI interface. The analog inputs receive the multiplexed signals from the PMT256 and the signals are de-multiplexed in the FPGAs. They are then passed to the desktop computer via PCI connections. The I/O ports control the PMT256 operations. Each PMT256 connects to one digitizer card; there are 20 MPX-32Ds used in addition to one for the trigger module.

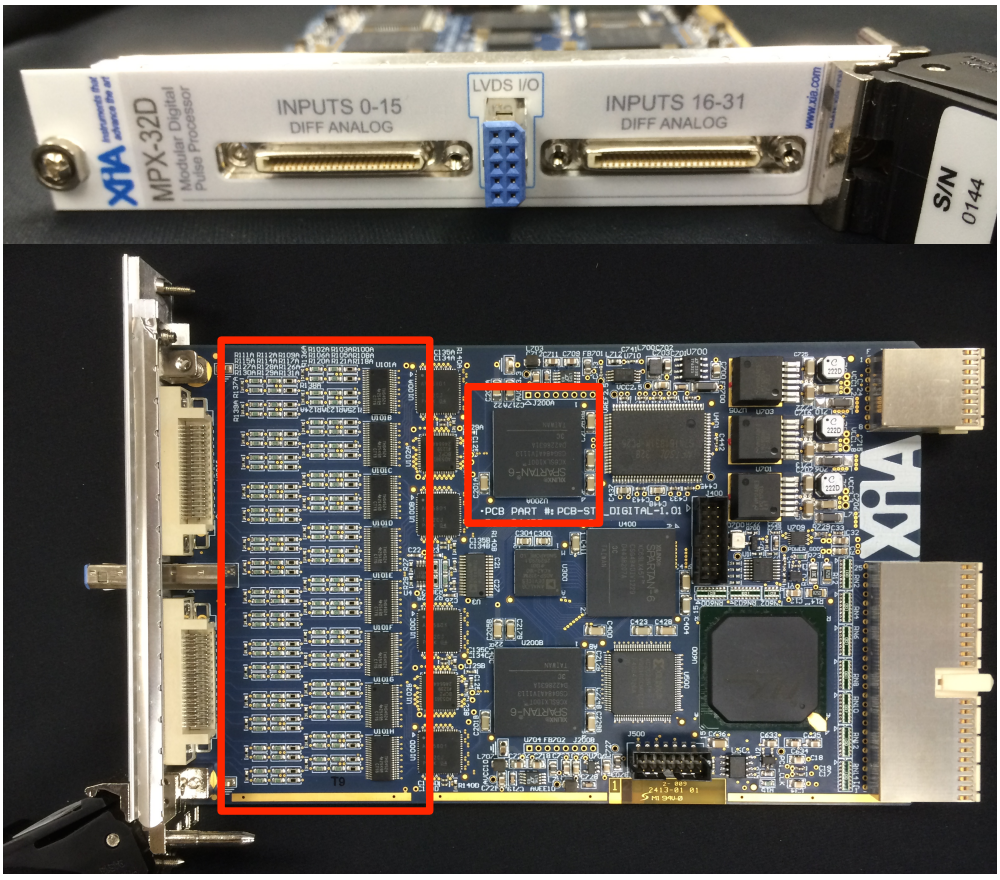

Figure 83. An MPX-32D digitizer card. Each card sits in a National Instruments PCI PXI Express crate [94]. The left rectangle shows the 32 anode channels that receive the multiplexed integrated signals from the PMT256. The right-most red box is the FPGA that de-multiplexes the signals into 256 channels.

5.2.A.iv. TRIGGER MODULE

Connection A on each PMT256 module outputs the last dynode from that tube to the trigger module. A multiplicity setting sets how many last dynode signals were required for triggering; i.e. a single last dynode above the threshold could globally trigger the system, two last dynode signals could be required to be above the threshold, etc. Due to the nature of the system that required events with different light distributions (different depths) to trigger the system, a single signal was chosen to trigger the system (multiplicity of one). This triggering setting allows for

events at the bottom of the crystal to trigger the system when the majority of the light spot falls over a single PMT.

5.2.A.v. ELECTRONICS NOISE

A full noise study was planned after the final thin and thick crystal data were collected. However, due to a lack of information from XIA some parts of the study were not completed. In particular, we wanted to be able to understand the exact filter applied to the raw waveforms read from the PMT channels. This would allow us to understand the step between the read and the integrated signal multiplexing. They would not provide the specifics of the filtering used (timing, baseline information), so we were forced to use other methods to extrapolate the noise characteristics of the system. As will be discussed in this section, the system behaves well with very low noise on the baseline signals (with no input signal from the PMT). However, the integrated signal fluctuates greatly when an input signal with a pulsar test card is used. Additionally, as will be shown, the system was found to have non-working triggering behavior on several of the center PMT and module systems.

To measure the noise the PMTs were turned off (no high voltage) and the system was triggered with an external pulse card that allowed for an input signal from a function generator to be directly routed to a PMT256 module. This forced the entire system to trigger on a known signal. From this, three useful plots could be made. First, a histogram of the root mean square (RMS) of each anode signal for all of the events was made. This was in the units of integrated anode signal (ADC units). It is shown in Figure 84. Each entry in the histogram corresponds to one root mean square (RMS) value for a single anode (5120 entries).

As seen in the figure, there are essentially two types of values; those centered at 0.5 ADC counts and those centered between 1 to 1.5 ADC counts. The baseline signal of a digitized anode trace with no signal and examined using different software was found to be about 400 (with a ^{137}Cs source, the typical peak of a digitized anode signal is ~700). The width of the lower peak using a Gaussian fit gives a FWHM equal to 0.35 ADC counts. Thus, the calculated RMS seen in the figure in addition to the width of the distribution is extremely low relative to any true signal. Even so, because of the bimodality of the distribution, a heat map of the individual anode RMS values was made to determine which anodes gave the higher RMS values. This is shown in Figure 85.

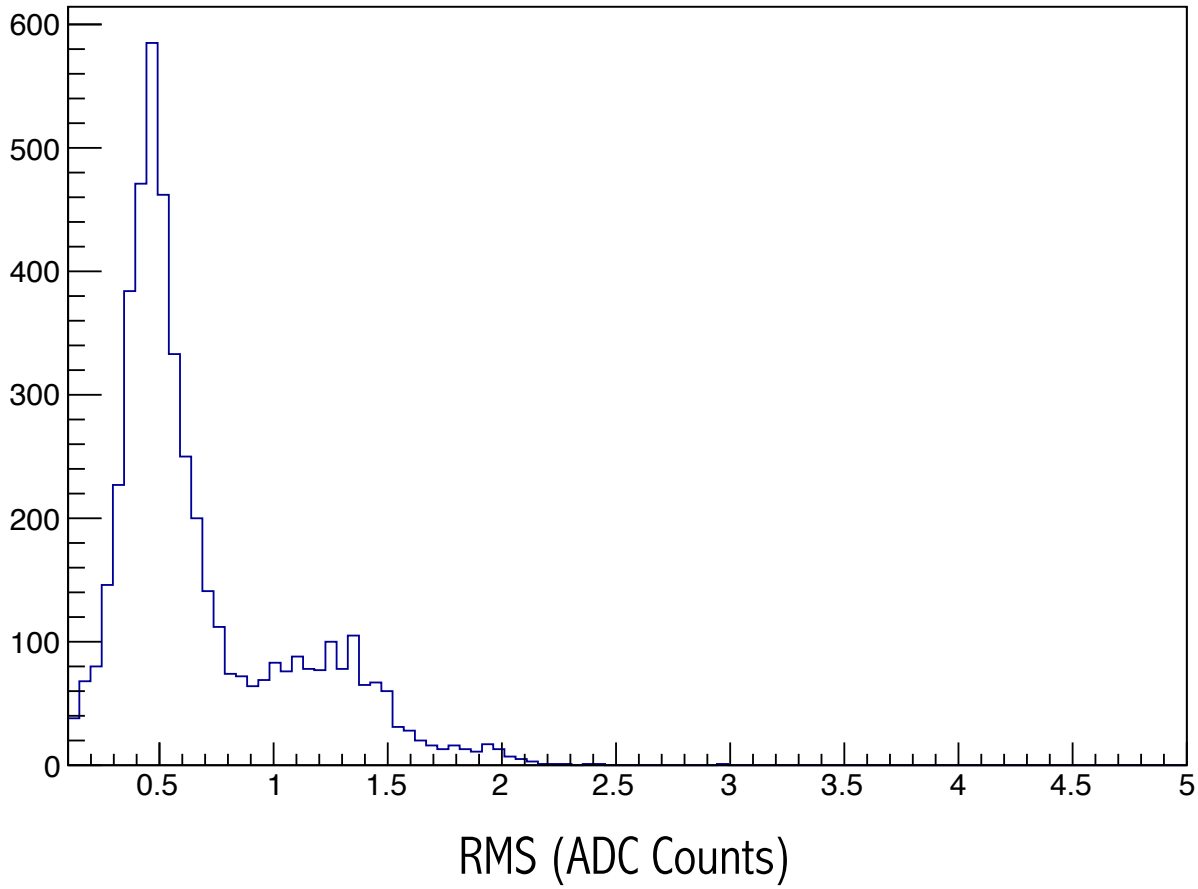

Figure 84. A histogram with each entry being the RMS of a single anode for 3800 force triggered events (no PMT signal).

As seen in the heat map, the anodes with a higher RMS do follow general PMT trends; i.e. the individual PMTs generally have either many of the higher RMS anodes (x=16,y=0) or very few (x=0, y=32). Two conclusions can be made from this; first, the PMTs with many high RMS anodes tend not to fall in the center of the array where the focus of the data collection occurs. This is due to simple chance of not picking what appears to be a noisier module to go in the center of the array. Secondly, even while there are noisier modules, as stated above, the RMS values of 1-2 ADC counts are still very small compared to the true signal minus the baseline (~300 ADC counts).

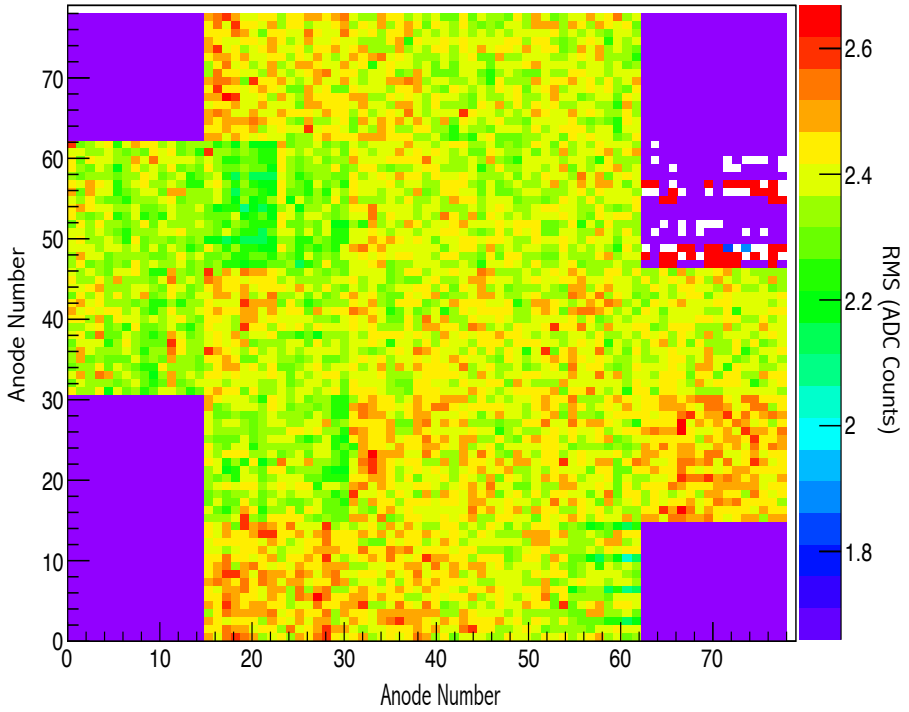

Figure 85. A heat map of each anode's RMS value for 3800 forced trigger events. The signal at (x=64, y=48) is the module with the pulsar test card attached to the PMT256. This specific region is discussed below.

The signals at (x=64, y=48) are the calculated RMS values of those anodes where the test card was connected. Ideally, the pulsar test card would input the exact same signal in every event to the same channels. If it were working correctly, it would be the regions of sixteen x and six y pixels (two groups of three at (x=64 to 79, y=48 to 49 and x=64 to 79, y=56 to 57)) seen as the red points in the heat map. However, when the test card was used with other modules in initial system tests, it was observed that depending on the module some of the channels appeared to receive no signal. The "dead" signals changed depending on the module that was used. Therefore this was deemed a poor method to collect the response to a truly uniform input signal and was not used to calculate the anode noise.

Additionally, there were triggering issues that degraded the data collected with a thick crystal system that were originally attributed to electronics noise. These are shown in Appendix 3.

5.2.A.vi. DATA ACQUISITION SYSTEM SOFTWARE

The original design called for a system that embedded the data acquisition system controls with the imaging code. This software was designed to initialize the XIA system, begin a read and record and read using each buffer (the XIA system has a dual buffer design to store the data for readout) while switching between the two when the recording buffer was filled. The data could then be directly piped to the imaging code to begin the coded-aperture reconstruction. Due to complications with reading the buffers correctly this system could not be implemented. Instead, software provided by XIA was used to record the data sets to disk before being read into the imaging code post-collection. The XIA software allowed for the system parameters (trigger threshold, integration times, etc.) to be set and a maximum of 3854 events to be recorded per data set.

5.2.B. HARDWARE

The hardware for the three-dimensional system contained many components used to secure the functional parts of the system. The following requirements were considered when designing the system.

1. The PMTs needed to be optically coupled to a large glass plane in a closely packed array. The operational orientation had the PMTs facing up while assembly of the system occurred with them facing down. Thus, the PMT array needed to be able to be flipped without breaking optical contact or breaking the module cable connections.
2. The electronics modules needed to be coupled to the PMTs without inducing enough stress to break optical contact with the glass plate. The cables from the modules pull downward on the modules and, in turn, the PMTs, so the PMTs needed to be secured against the glass.
3. The modules needed to be held in place while the entire system was situated inside a light-tight box.
4. The cables had to be passed through the sides of the light-tight box without using bulkhead connections.

A schematic of the entire apparatus is shown in Figure 86. An inner system was designed that mounted PMTs against a solid aluminum bar in rows of 3 or 5 PMTs, depending on the position in the array (Figure 86). A small screw hole on the back of the H9500s was used for

this purpose. A small threaded rod connected the back of the PMT through a bored hole in the rigid aluminum rod to a bolt on the PMT256 module (see Figure 88). The rigid bar held the closely coupled PMT and modules in place and each was individually coupled to the larger quartz plane that was built into the outer frame.

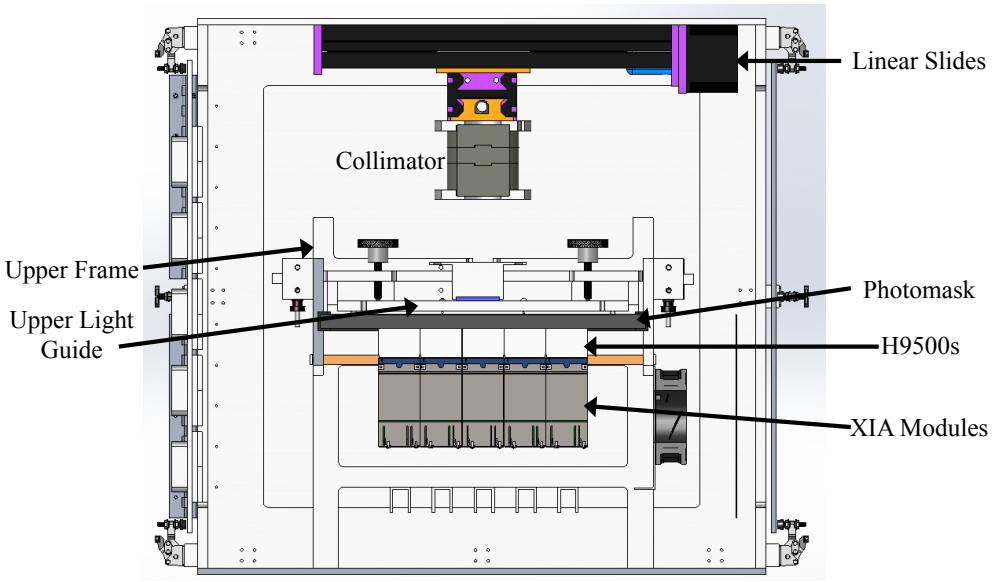

Figure 86. A schematic of the entire enclosed hardware system. The outer frame sits inside a light tight box with cable outputs using foam compressions around the cables. The PMT bars are built one by one (5 bars) and coupled to the quartz plane while the system is upside down. It is then flipped over and the entire frame is placed inside the box. The upper frame assembly is then built on top of the large 16 x 16 inch^2 quartz plane without disrupting the PMT optical coupling.

According to Hamamatsu the tube-to-tube variations of the height of the PMTs from the base of the connectors to the top glass face varies by up to 0.9 mm [85]. As the system (every individual PMT face) must be optically coupled to a flat rigid piece of quartz, a method was needed to ensure uniform height to within 0.001 inches in order to allow for the entire array to maintain optical contact. Originally, a rubber o-ring was placed between the aluminum bar and the back of the PMT. This was designed to apply pressure for a bar of PMTs with varying depths. However, when optically coupled, it was observed that the o-rings applied more pressure

to the center of a PMT than to those at the edge, resulting in the optical coupling breaking on the PMT edges when the system was inverted for several hours. Additionally, the o-ring did not possess enough dynamic range to level out each PMT to a constant height and acceptable pressure against the quartz plane. To fix this, the PMT heights were measured and plastic shims were cut to correct the distance between the different PMTs in the row. The shims were then placed between the bar and the PMTs to level the glass faces against the quartz plate. As seen in Figure 87, the PMTs could then be held at a uniform level and the system was inverted with all PMTs maintaining optical contact.

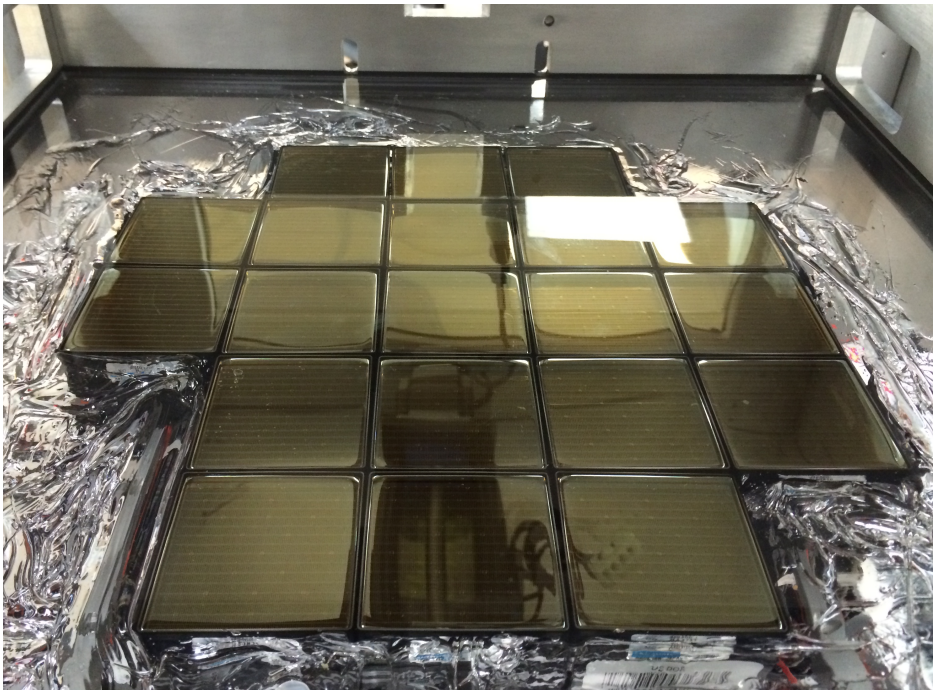

Figure 87. The PMT array optically coupled to the 17 mm quartz plate and mounted in the hardware assembly. Due a dead PMT the array is missing one PMT in the far left column. The corner positions were to be occupied by Planacon detectors but the needed adapter boards were never designed due to cost and time constraints.

While the system was initially conceived to use 25 PMTs and then built using 21, an inner PMT was found to be dead through initial tests using a pulsing LED. When examined, the

photocathode appeared to be degraded. The system was then torn apart and rebuilt with a PMT on an outer row moved into the dead position. The final configuration is shown in Figure 87 and consisted of 20 PMTs and PMT256 modules.

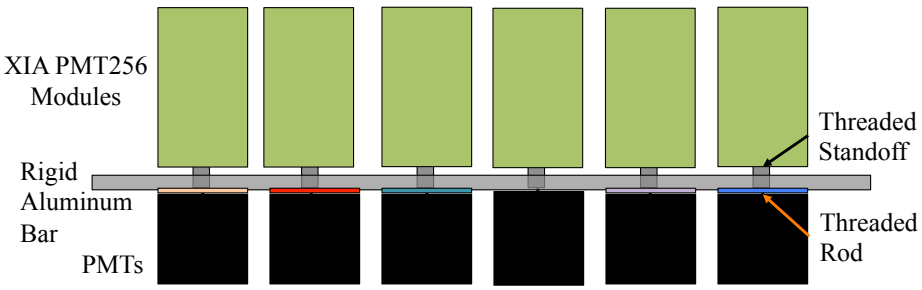

Figure 88. The system used to mount the PMTs to a uniform height. Due to the varying height of the PMTs from the connections to the face of the glass (varied by 0.9 mm), plastic shims were used to account for the height variations. This system allowed for the glass faces of the PMTs to sit uniformly against a glass plane while using the aluminum mounting bar to provide even pressure along the entire length of the PMT backing.

The mounted PMTs and glass plane within the outer aluminum frame were flipped and placed inside a light-tight box as seen above in Figure 86. The cables were fed through a door with individual cut outs and foam compressions around each cable; black cloth was then wrapped around the box. The tungsten collimator (the same one used in the 2-D experiment) was mounted to two linear slides above the entire system and was able to be moved in 10-micron steps across the entire face of the system.

The four bottom corners of the aluminum frame had threaded holes drilled so the system could be fixed to an absolute position. This allowed for a fixed coordinate system between the PMT anodes and the collimator. The system was also designed so that it could be rotated (the entire light box), so the upper-most frame has rubber stoppers that can be set to place pressure on the top-most glass plane. A 3-D plastic casing could then be made to hold the crystal in place. This system was never implemented, as the cables and data acquisition system restricted the movement of the overall system.

5.2.C. DATA COLLECTION AND SYSTEM PERFORMANCE

5.2.C.i. ENERGY CALIBRATIONS

XIA designed the electronics system to be able to detect single photon signals. Thus, the energy resolution for low-energy gamma-ray interactions is an important system characteristic. Three sources were used to calibrate the initial system; a 1-milliCurie ^{57}Co source (122-keV spectral line) and a 1-milliCurie ^{133}Ba source (80-keV and 356-keV spectral lines). A ^{137}Cs source (662-keV spectral line) was also used to both calibrate the system and record data with the mask plane present in the system. The energy spectrum data sets were collected with the apparatus enclosed in the light-tight box with ~17 mm of quartz optically coupled above the PMTs.

For the ^{57}Co, a thin 2 x 5 x 5 mm^3 NaI crystal was used [95]. It was enclosed in an aluminum casing with the sides and top painted black. It was optically mounted to a 2 mm quartz exit window with a 1 mm silicon pad between the crystal and quartz window.

The ^{133}Ba spectra were collected using a 30 x 150 x 150 mm^3 thick NaI crystal also painted black and enclosed in aluminum. The exit window was the same as that of the 2 mm crystal. Both crystals (2 and 30 mm) schematics are shown in Figure 89. Spectra collected with the 30 x 150 x 150 mm^3 NaI crystal are shown in Figure 90. The ^{57}Cobalt 122-keV peak has a FWHM resolution of 32%. A low-energy noise peak is also seen in the spectrum. The figure on the right shows the spectrum for the 356-keV peak from ^{133}Ba. The energy resolution is 19%. These initial spectra were only used for system instrumentation purposes; the energy resolution with the mask pattern and the analytical explanation for the result is given in Section 6.2.G.

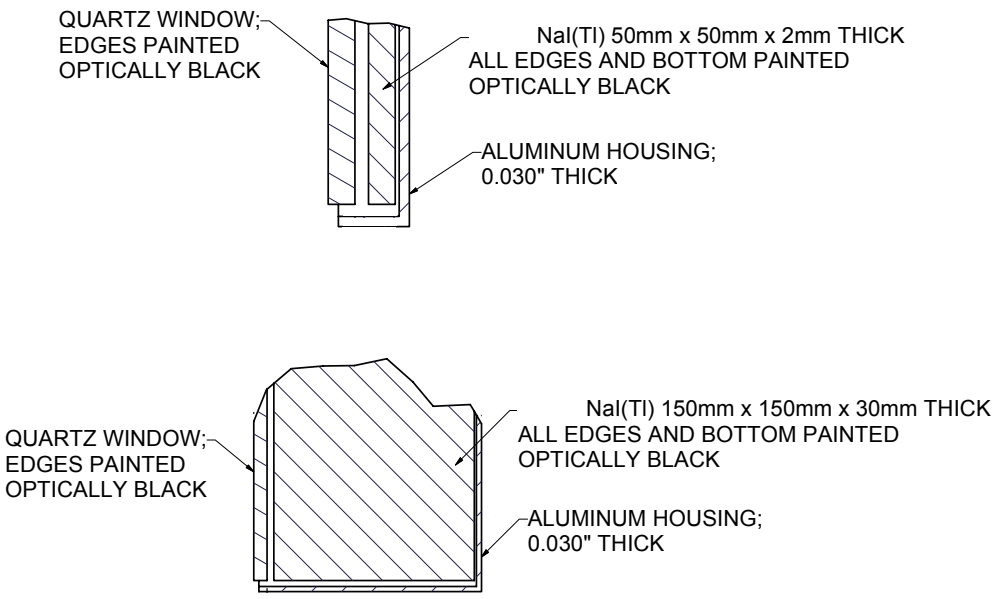

Figure 89. [95]. Crystal schematics for the 2 mm (top) and 30 mm (bottom) crystals used for energy calibrations. The top and sides of each crystal is painted black and absorbs any incident light.

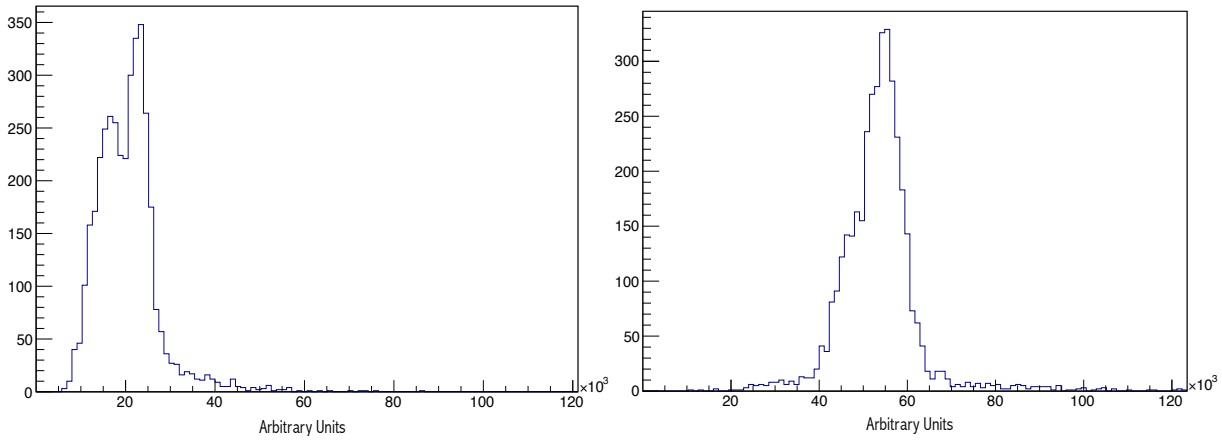

Figure 90. (Left) The energy spectrum for ^{57}Cobalt. The 122-keV peak is located at about 21 (arbitrary units). The lower peak is a noise peak. (Right) The ^{133}Barium spectrum. As expected, this peak is located at about 3 (2.7) times higher than the 122-kev peak of ^{57}Cobalt. The resolution of the 356-peak is 19%.

5.2.C.ii. PATTERN VISIBILITY CHECK

As in the 2-D system, once the 3-D system was able to resolve the energies of events, the next step was to try and see a mask pattern on the detector. However, in the 2-D system in order to see the magnification visually, the mask pattern could be moved in 10-micron steps with the linear slides to align the system so the mask pattern mapped well onto the anode array. Because this system did not have that capability, and due to the size of the mask features, (rank-19 1.3 mm^2 features) they were unresolvable visually. To check signal performance, the 2 mm 1-D linear pattern was optically coupled to the mask with an LED mounted above it. The pattern can be seen (Figure 91) on the anode heat map for the aggregate of many events.

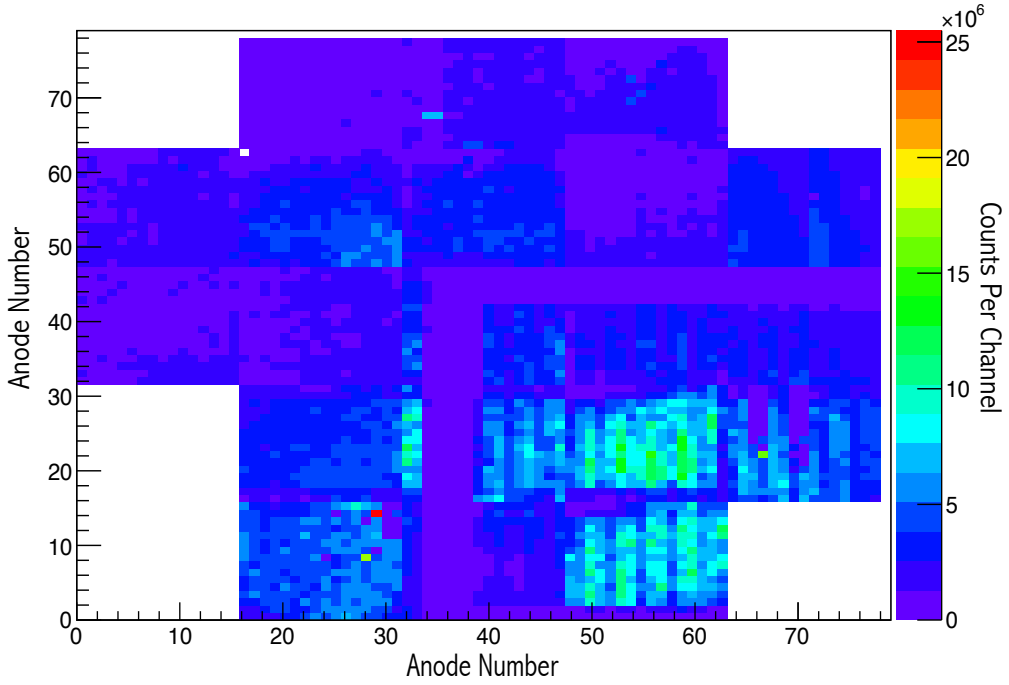

Figure 91. The 3-D system with the 1-D 2 mm binary lines pattern over the PMT array. The lower right PMT has an anomalously high gain relative to the other PMTs. This data was taken with an early generation of the system while bugs were still being worked out with the readout electronics.

5.2.C.iii. GAIN MAPPING

A gain mapping was required to correct for variations in anode and PMT gains. The most direct approach was to uniformly illuminate the PMT array with a uniform light source and make the corrections based on these measurements. However, to create a uniform light field over the full PMT array proved very challenging. Several approaches were investigated, and eventually a system using two planes of diffusing glass with an LED illuminator was chosen. The system consisted of two 3-mm-thick opal diffusing glass planes [96] with one wrapped in white Teflon tape. Each side of the tape wrapping operated as an additional diffusing plane. The unwrapped glass sat directly on the 17-mm-thick quartz plane coupled to the PMTs, and the wrapped plane was located 6.35 cm above it. An LED array shown in Figure 92 was mounted 24.5 cm above the upper plane. This allowed for the light to spread out before it reached the first glass plane, undergo diffusion by the first Teflon layer, diffused again by the opal glass, etc., until it reached the PMT array. The LED array consisted of 5 LEDs that emitted light at 415 nanometers.



Figure 92. The LED array. The outer LEDs are arranged at the corners of a square with a side length of 5 inches. The 5th LED is in the center of the square. They are connected in parallel to a function generator and driven with a negative pulse ranging from -1.1 to -2.2 Volts with a pulse width of 12 ns at a repetition of 1 kHz. The array allowed for a more uniform light distribution relative to a single LED.

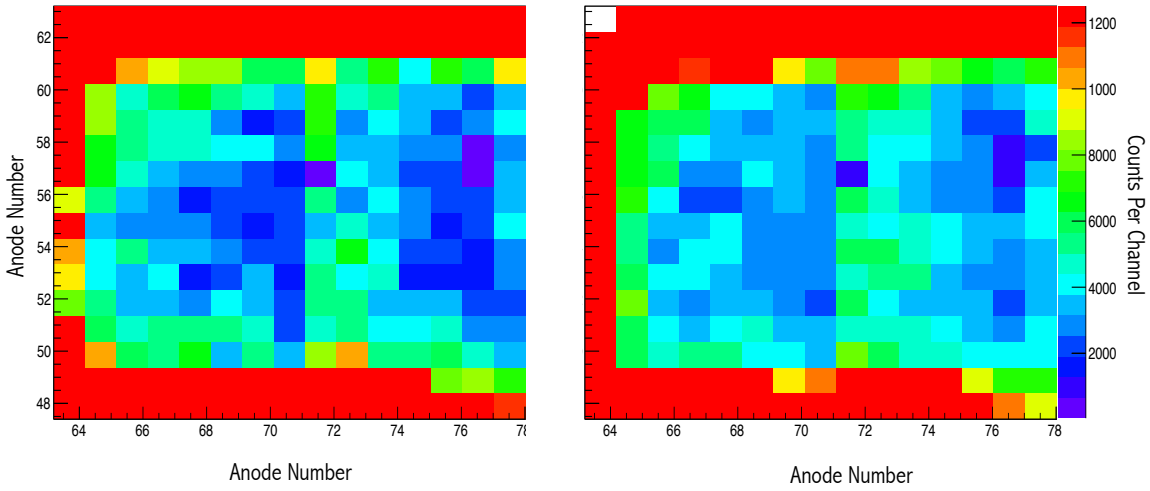

Figure 93. A single PMT signal taken with the diffusing glass planes and LED illuminator centered over the PMT (Left) and moved 4 cm from the center (Right). As the signal does not change even with the LED array moved, the light signal is proven to be approximately uniform and the signal variations are due to the gain differences in the anodes of the H9500.

As seen in the previous system (2-D system), adjusting for the gain corrections of the pixels improves the results of the imager. The full 3-D system was only gain mapped anode by anode for each PMT individually; no full array PMT normalization (using a uniform LED calibration) was done to adjust the voltages of each PMT in an attempt to normalize the response across the entire face of the detector. A gain mapping using the same post-processing "smoothing" of the signal was done when going through the collected data. Results with and without this gain mapping for a selection of events will be given in Section 6.2.C.

5.2.D. MASK AND MASK ALIGNMENT

Toppan Photomasks [90] made the mask pattern using the same lithography technology that was used for the one-dimensional mask patterns. However, due to the size of the pattern required to cover the entire PMT array (25 cm x 25 cm^2) a larger quartz plate was needed than they normally provide; thus, a 12 x 12 x 0.67 $inch^3$ plate of quartz was purchased from Prism Research Glass [97]. This had to satisfy the flatness tolerances required for the lithography method to work.

As in the previous system, the photomask plane needed to be locked in place in order to allow for multiple data sets to be taken while varying the thickness of quartz above the minimum upper light guide. An aluminum frame was built to the exact size of both the photomask plane and upper light guide. These are shown as A (photomask frame) and B (upper light guide frame) in Figure 94. The larger outer frame that holds the quartz that the PMT array mounts to is labeled C, and the rigid bar that holds the PMTs in place is labeled D. Each red line in the figure indicates a locking point between sections.

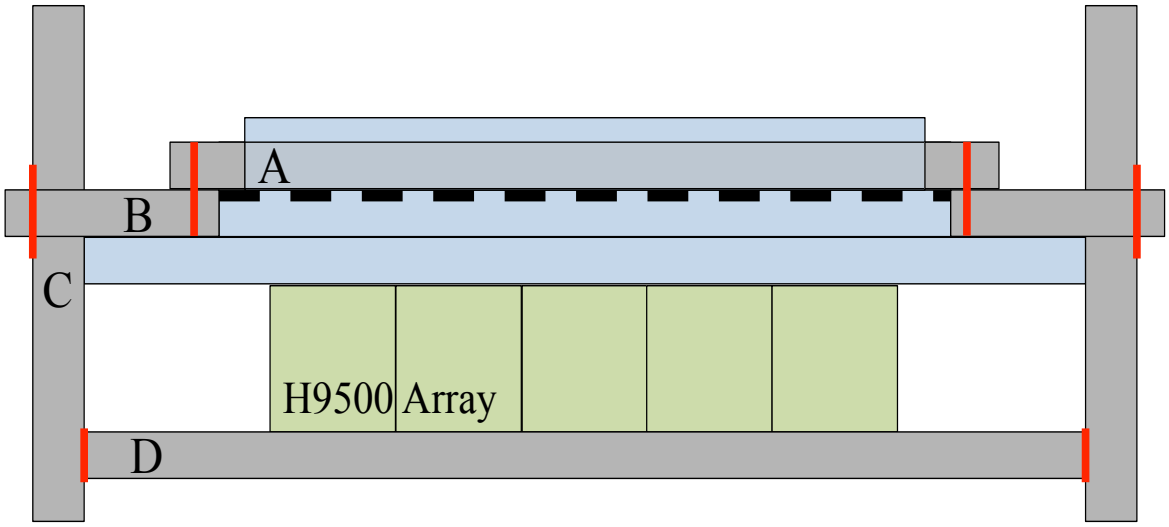

Figure 94. A simple schematic of the alignment hardware. A is the minimum upper light guide frame, B is the photomask frame, C is the outer frame and D is a bar that mounts between the PMT and PMT256 Modules. Each red line indicates a point where two frames lock together.

To assemble and lock the system after the frame is built with the PMT and electronic modules, the photomask quartz plane is optically coupled to the quartz coupled to the PMT array. Then the upper light guide quartz is optically coupled above the mask pattern. Next, frame B is placed around the mask and locked into C. Frame A is then locked into B. The system at various points in assembly along with the frames are shown in Figure 95. Once the system was locked in place, due to the high precision of frame B, the photomask could move no more than 100 microns when additional upper light guide was added or removed.

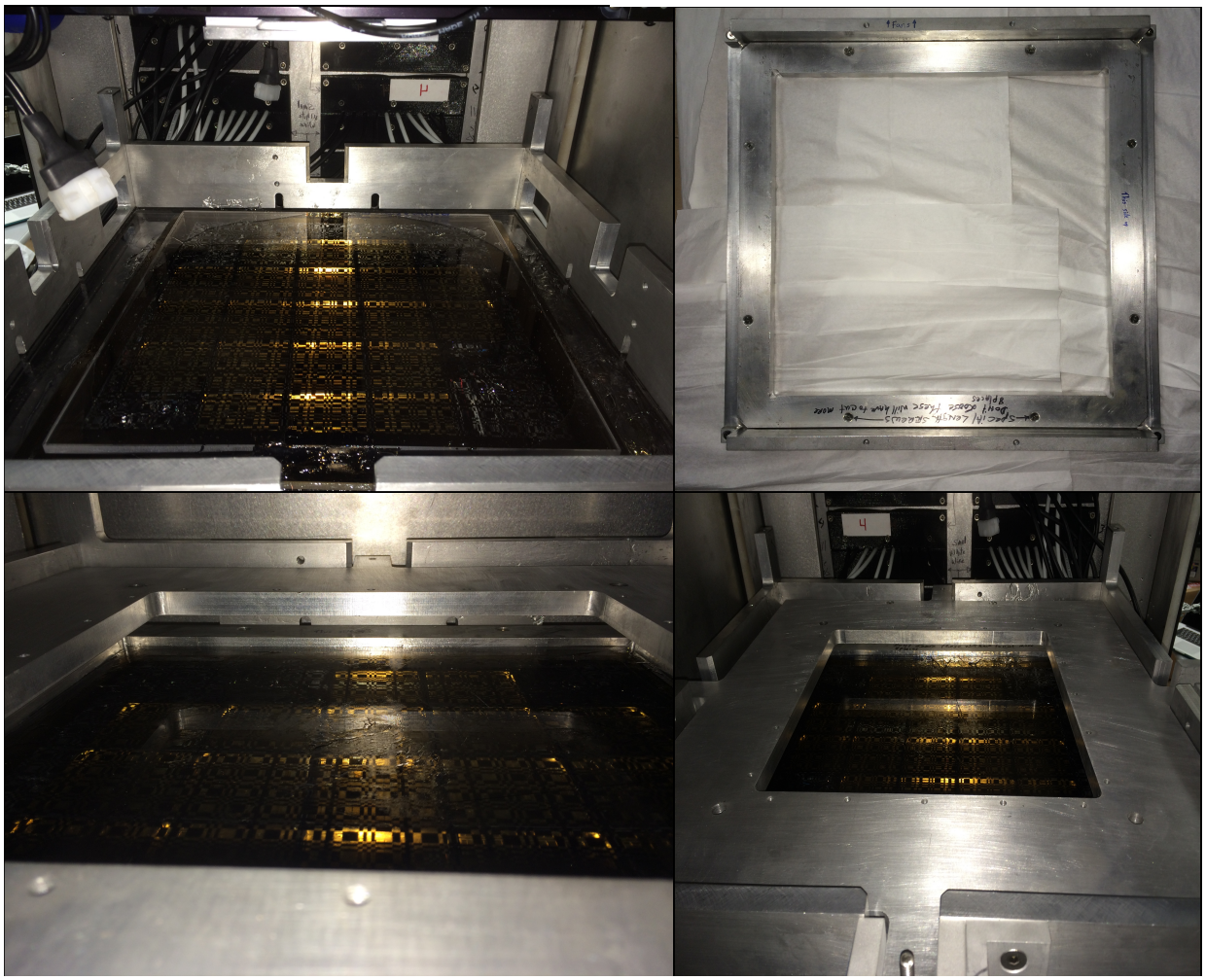

Figure 95. The photomask optically coupled to the focal plane (top left), the frame for the photomask plane (B in Figure 94, top right), the system mounted with the minimum upper light guide and outer frame (bottom).

Once optically coupled, the mask needed to be aligned so its offset with the PMT pixel array was known. Because of the lack of a linear slide system to finely adjust the position of the mask pattern, an LED illuminator over the edge of an opaque element of the mask to electronically position the photomask plate could not be used. To find the absolute position of the mask pattern, a picture was taken from directly above the mask element on the edge of the PMT array, and the location estimated from the features visible through the PMT window. This is estimated to be good to 200 microns.

5.2.E. IMAGING SOFTWARE

The imaging software for the full three-dimensional system was adapted from the two-dimensional-system analysis software. The same reconstruction and data-visualization software was used for both the GEANT4 [75] simulation data as well as the actual data. Originally, it was intended that the data acquisition system would be controlled within a larger custom built data collection and imaging software package built in Visual Basic [98]. Some work was done to control the data acquisition system within the Visual Basic framework, but due to firmware problems with the dynamic-link libraries provided by XIA, the pre-built XIA executable was used to collect the data sets instead. This software allowed one to view the waveforms from each channel; change parameters such as the integration window time, trigger threshold, number of events per buffer, etc.; and start and stop data set recording. Data sets were recorded as binary files and read into and parsed by the imaging code.

To begin, the binary file was read in to the software and assigned to an array. It was then parsed according to the anode positions; both locally in a PMT and globally in the larger 5 x 5 PMT array. Once assigned, the gain correction instrumentation files were read in and the gain-mapping array was used to gain map each PMT. Then, the event energies and last dynode information were calculated and energy cuts were used to select events for imaging.

If an event was chosen for imaging, the data were processed in the same way as a simulation event. First, the raw detector data were collapsed in the x and y directions (Chapter 4) and coarsely localized. The coarse lateral localization was then used as a rebinning center for each depth where the data were rebinned to half of a magnified feature size at that depth and an image was reconstructed using the cross-correlation reconstruction method. Originally, simulations showed that using any cycles outside of the 3 x 3 ring bordering the mask cycle below the event gave almost no improvement on the imaging capability (peak height vs. background), but when using experimental data, the imager's depth localization capability was significantly improved by taking another 2 outer rings of repeated cycles. This improvement will be discussed in detail in the next chapter with the final results.

The reconstruction software took ~4.3 seconds per event with 0.4 mm step sizes. While attempts were made to improve upon this, the timing was limited by the rebinning and reconstruction methods. As discussed in earlier sections, several methods in the imaging details can be varied such as using weighted means or Gaussian fits, as well as the number of bins in

each operation. While certain methods were found to work best for simulation data, in practice other parameters and fitting techniques were chosen for the actual data. The reasoning behind each decision and results will be shown along with the final results obtained with the system.

CHAPTER 6. FINAL RESULTS

This chapter will present the results from the 2-D and 3-D system as well as an analysis of the results. Specifically, selected single events from both systems will be shown along with the processing methods discussed in Chapter 4 (outer cycle additions, gain mapping, coarse depth localization, etc.). The chapter will specifically show the results using the thin crystal emulation for both systems with comparisons to simulation results. It will also present results using a thick scintillator crystal with the 3-D system.

6.1. TWO-DIMENSIONAL SYSTEM

As discussed in Chapter 5, the system's imaging performance (especially depth localization ability) can be studied by emulating events at a known depth in a thick crystal using a thin crystal and varying thicknesses of upper light guide. The two depth ranges (quartz and thick crystal) are not equivalent, and as explained in Section 3.4.A. the correction factor is equal to 0.63.

Several thin crystal location measurements were taken for the 2-D system; all of the data with the thin crystal and rank-7 mask were taken with a 1-milliCurie ^{133}Ba source. The thin crystal was originally thought to be 1 mm thick with a 2 mm quartz exit window, but when an X-ray of the wrapped crystal was taken and the layers were measured and accounted for, it was found to be 0.88 mm thick with a 1 mm silicon pad between the crystal and the 2 mm quartz exit window. This crystal thickness was then used to propagate errors in the final results and obtain the imaging resolution in the depth dimension for both systems.

The goal of the 2-D experiment was a first proof of principle with a small system that could localize events in two dimensions (the depth and one lateral dimension). The event processing routine was discussed in Chapter 5. As that discussion used only simulation data, the process using data from a real gamma-ray interaction event will be briefly reviewed here with a sample event. First, an individual event will be examined, and then the results for many events will be presented.

6.1.A. SINGLE EVENT RECONSTRUCTION

For a single event in a data set with 8.5 mm of quartz between the mask pattern and the thin (0.88 mm) crystal, once the data were collected, the event location was coarsely determined in x. The event was then reconstructed for the range of depths throughout the possible crystal

locations. Figure 96 shows the event reconstructed at three depths, and Figure 97 shows the peak height for each reconstruction versus the depth; the event was found to be at 9.2 mm[3].

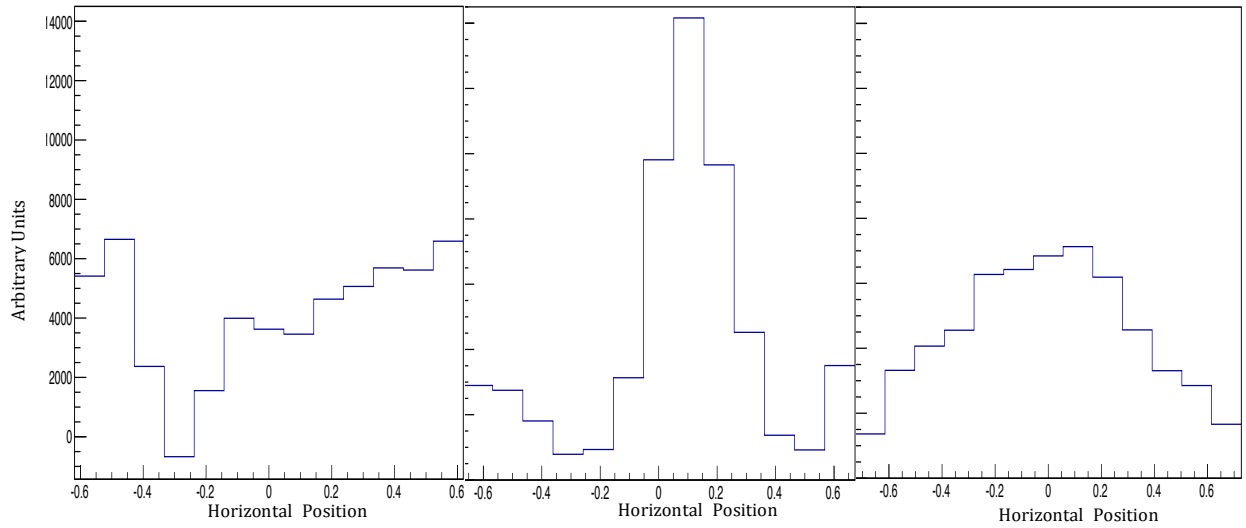

Figure 96. Single event reconstructions at 6.5 mm (left), 9.2 mm (center), and 12.0 mm (right). As seen from the images, the center is both the largest and sharpest peak; all three events have the same y axis.

Once the depth was found comparing the peak height versus depth, the absolute lateral position was found using the method described in Sections 3.3.C. and 4.6 (the location in the coded-aperture image was found using a weighted mean around the peak and this was added to the coarse localization found in the first step). Once it was confirmed that the method worked for several hundred individual images, the process was automated to go through many events.

[3] If the event was imaged correctly, it must be found within the range of the thin crystal (8.5 to 9.38 mm).

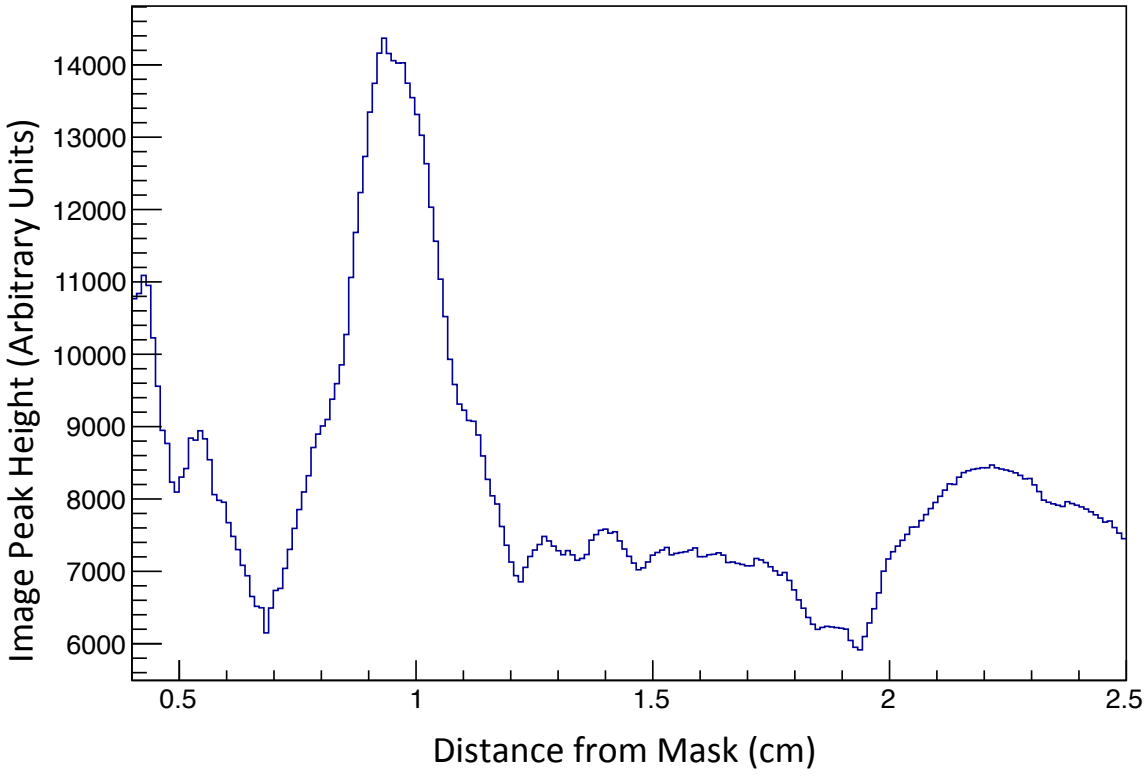

Figure 97. The peak pixel values versus the reconstructed distances for each depth reconstruction. The maximum occurs at the center image in Figure 96. The event was found to be at 9.2 mm; this is within the 8.5 to 9.38 mm where the actual thin crystal existed.

6.1.B. EVENT FILTERING

After several data sets (varying depths) with several thousand events each were examined, it was found that further event filtering algorithms were required. Figure 98 shows the result for one thousand events with 14.7 mm of upper light guide (22.5 mm depth in a thick crystal equivalent) between the minimum upper light guide and the bottom of the thin crystal. As seen in the reconstructed depth histogram, 18% of the events are found below 1.5 cm. As every single event actually occurred in the uppermost 0.88 mm, all of the events at the lower depth are incorrectly localized far outside of the width of the distribution. Thus, a method was needed to correctly place the misplaced events without either biasing events that actually occur deep (closest to the mask pattern) within the crystal towards the top (farthest from the mask), or creating a discontinuity in the depth reconstruction range.

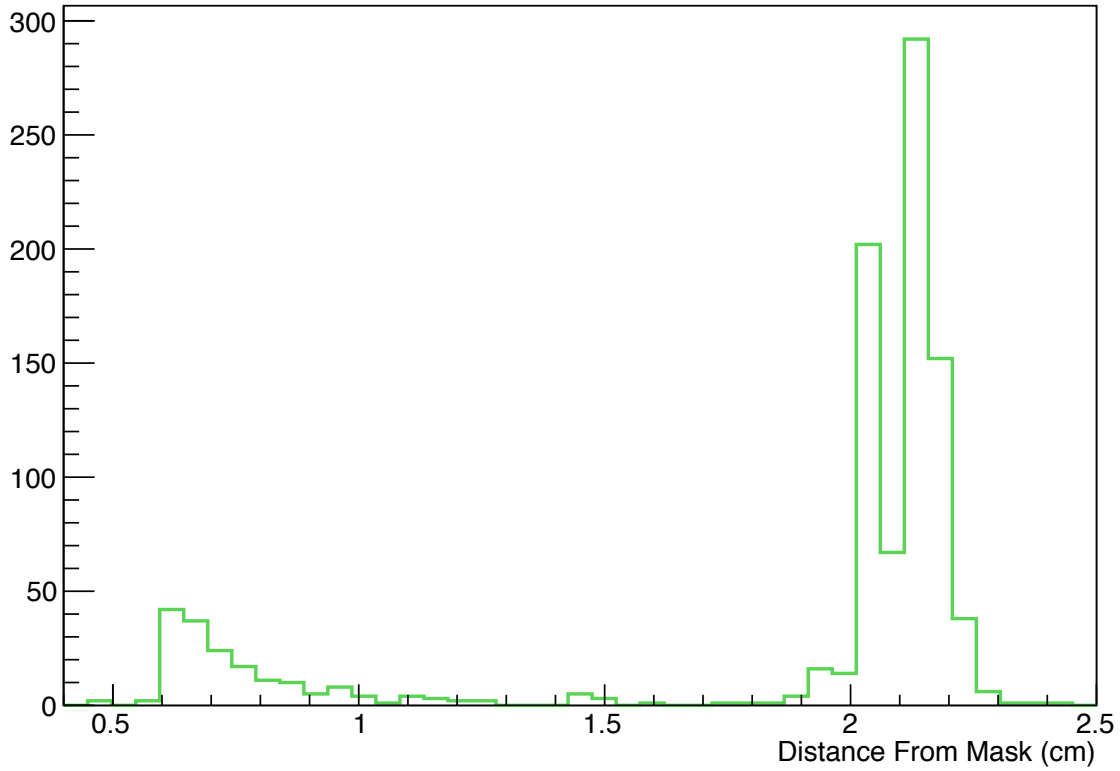

Figure 98. The depth results for 1000 events at the upper-most depth with 14.7 mm of additional upper light guide. The events near the bottom of the crystal are improperly reconstructed. The bimodal structure discussed in Section 4.7 is present in the data set. Every event in this histogram was within the 356-keV energy peak of the ^{133}Ba spectrum.

The parameter used for filtering could not be the total ADC counts, since that value gives the energy of the event, and due to the small detector size (3 PMTs) events deep in the crystal yield more collected light than events near the top of the crystal. Several parameters were investigated to give a coarse depth estimate including: the width of the light distribution at the detector fit to a Gaussian, the width of the Gaussian fit divided by the maximum value (height) in the detector distribution, and the kurtosis of the detector distributions. These were investigated in order to coarsely distinguish the low (closest to mask plane) and high (farthest from mask plane) events from the raw detector data; none of these yielded significant differences between the low and high depth events. However, the raw detector pattern did show different numbers of "crossovers" based on the depth that could be used for coarse depth localization. Figure 99 shows raw detector

data for single events from the high (left) and low (right) data sets. The red lines on each plot are drawn at 40% of the maximum peak values.

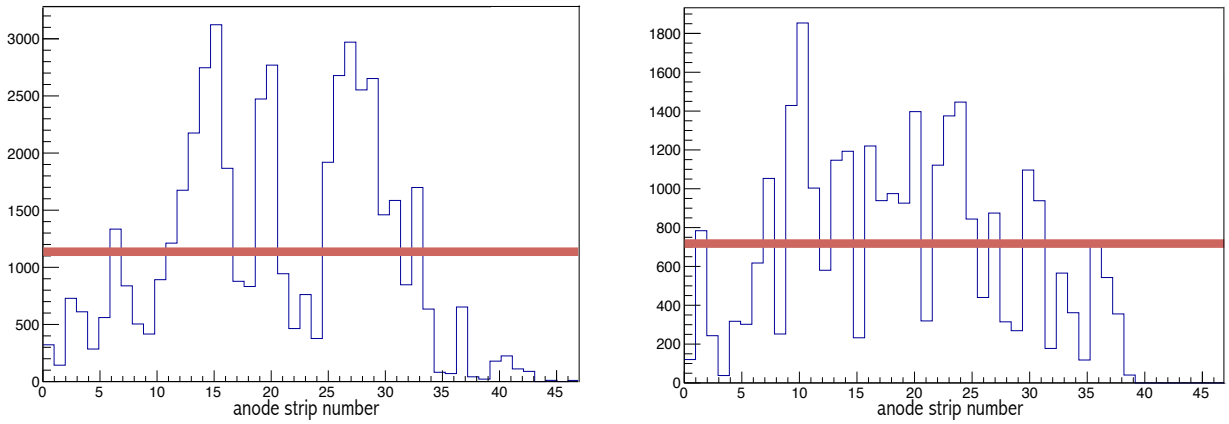

Figure 99. (Left) The raw detector patterns for a single event from each of the low (closest to the mask plane, largest magnified mask features) and (right) high (farthest from the mask plane, smallest magnified mask features) data sets. The red lines are drawn at 40% of the maximum peak values in each detector pattern. The x axis is the anode strip number (3 PMTs giving 48 anode strips).

The magnification in the data set for the top of the crystal is smaller than that for the bottom data set, hence the smaller features on the right. As a result, when counting the number of crossovers over the entire range of anode strips, the number of crossovers greater than 40% of the maximum value varies between the low and high data sets. This is shown in Figure 100 below.

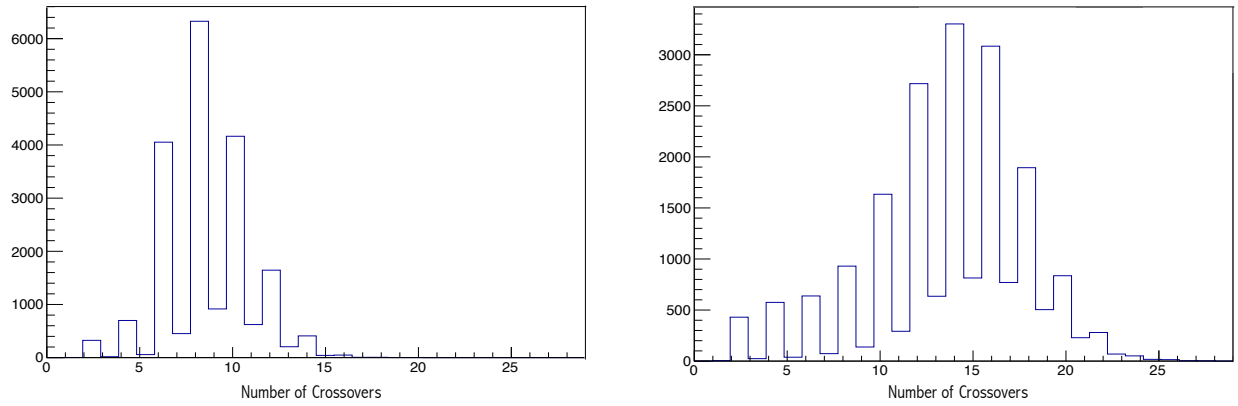

Figure 100. The number of times the raw detector data crosses 40% of the maximum bin value for the low (left) and high (right) data sets. There is a significant difference in the mean between the two histograms.

As seen in Figure 100, this parameter provides good separation of the value for coarse depth localization. The rest of the data sets were then analyzed for the same parameter and a function was fit to the mean values for each plot in order to give coarse depth localization. The function was fit using a 6th order polynomial given by

$$y = .00007283 \cdot x^6 - .06028 \cdot x^5 + 2.0594 \cdot x^4 - 37.171 \cdot x^3 + 373.867 \cdot x^2 - 1987.012 \cdot x^1 + 4361.167$$

Eq. 80

Originally, 18% percent of the events were incorrectly found at the lowest depth range while with the fit only 11% were found in the same region. The coarse depth localization improved the uppermost data set by about 7%. This is shown in Figure 101, with the blue showing the improved results and the red the results without the fit.

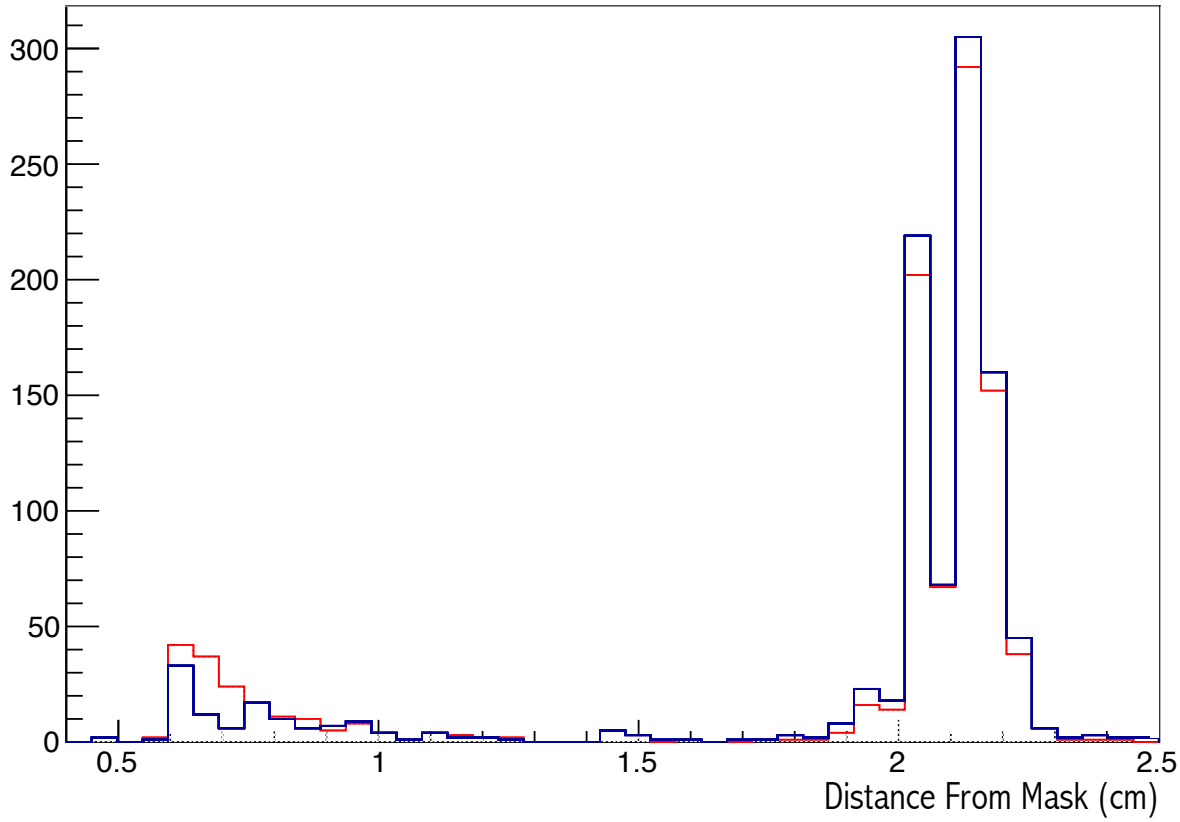

Figure 101. The results with (blue) and without (red) the coarse depth localization crossover counting method. The fitting function improved the results by about 7%.

While the crossover counting method was intended to make the most difference in the uppermost data set discussed above, it was included in the analysis of every data set as in a true bulk crystal there would be no basis to apply it to only certain events.

6.1.C. TWO-DIMENSIONAL FINAL RESULTS

Four data sets with varying amounts of additional upper light guide between the minimum upper light guide and thin crystal were collected. The final results for all depths for the two-dimensional system are shown in Figure 102.

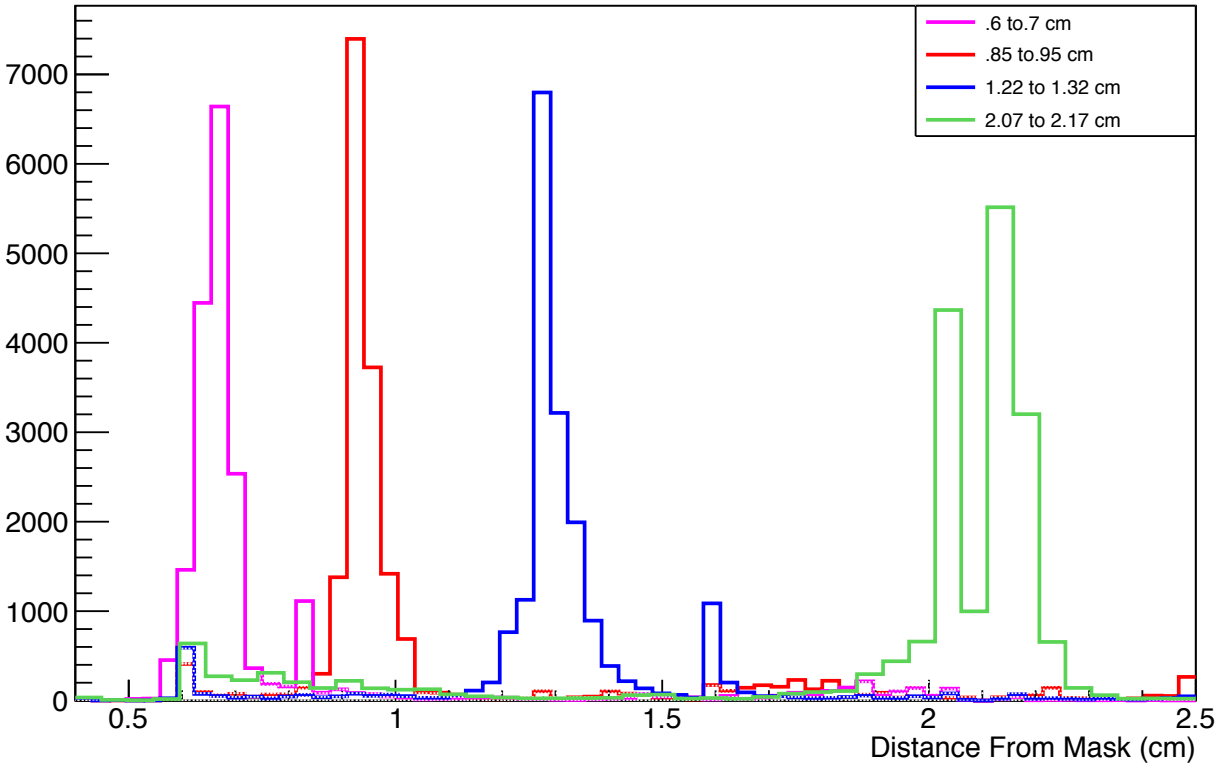

Figure 102. The final depth results for four data sets collected. Each data set contains 20 thousand events, all within the 356-keV peak from the 1-milliCurie ^{133}Ba source.

While the range of the quartz thickness varied by 14.7 mm, as discussed above, this is equal to a range of 22 mm inside of a scintillator crystal. The lowest three depths behaved as originally expected, with the upper depth possessing the bimodal structure also seen in simulations (Chapter 4). The quantitative results are given in Table 7. Additionally, with the final processing (including coarse depth localization) the percentages of the events found in the real (where the crystal is physically located) peak at each depth are shown in Table 8.

Table 7. The final depth and lateral results for the 2-D system.

Mask to crystal center (mm)	Emulated crystal center location (mm)	FWHM (mm)	Converted FWHM (mm)	Deconvolved FWHM (mm)	X-width (mm)	Deconvolved X width (mm)
6.5	0	0.65	1.03	<0.54	1.67	1.43
9.0	4.0	0.65	1.03	<0.54	1.22	.87
13.0	10.3	0.65	1.03	<0.54	1.45	1.17
20.7	22.5	1.67	2.65	2.50	1.16	0.78

Table 8. The percentage of events found within the correct peak for each depth. The correct peak includes events at the tail edges of the true peak.

Mask to crystal center (mm)	Emulated crystal center location (mm)	Percentage of Events in Correct Peak
6.5	0	81%
9.0	4.0	79%
13.0	10.3	81%
20.7	22.5	89%

The deconvolved results are found by the standard formula for error propagation where the total uncertainty in the measurement result is given by

$$\delta_{total}^2 = \delta_a^2 + \delta_b^2.$$

Eq. 81

In this case, δ_{total} is the FWHM of the measurement result, and δ_a and δ_b are the spread of either the gamma-ray beam from the collimator (lateral measurement) or crystal thickness (depth measurement), and the imaging uncertainty in each measurement. The width of the beam at the crystal was 1.2 mm. Thus, the lateral imaging uncertainty was found by

$$FWHM^2 = 1.2^2 + \delta^2_{Lateral\ Imaging\ Uncertainty}.$$

Eq. 82

The depth imaging uncertainty was found by

$$(\frac{FWHM}{.63})^2 = (0.88)^2 + \delta^2_{Depth\ Imaging\ Uncertainty}$$

Eq. 83

where the 0.63 factor on the measured FWHM in depth is from the index of refraction change; the measurement is in quartz space and needs to be converted to crystal space in order to be propagated with the thickness of the crystal. The lateral dimension results for the coarse localization are shown in Figure 103, and the imaged events are shown in Figure 104.

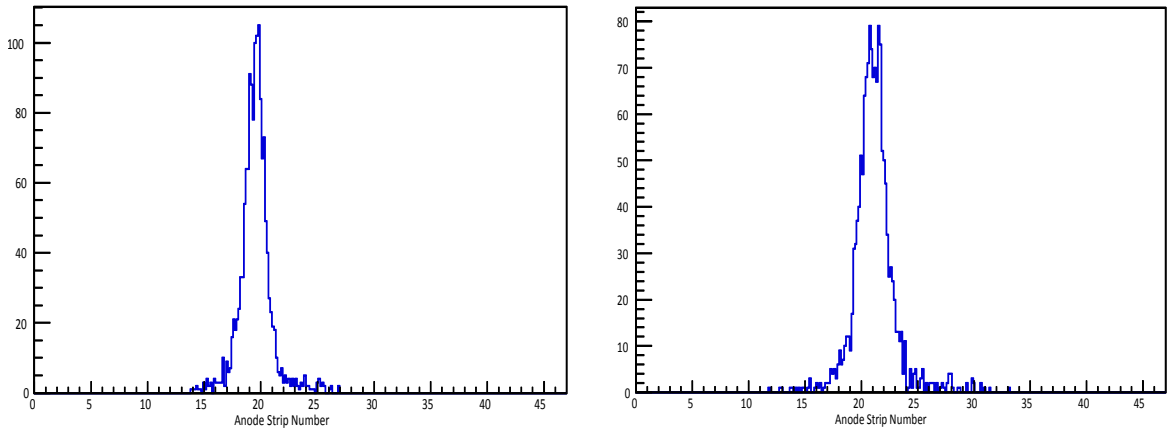

Figure 103. The coarse lateral event localization using a weighted mean of the raw detector data for the bottom data set (left, pink on the depth results) and top data set (right, green on the depth results) in Figure 102.

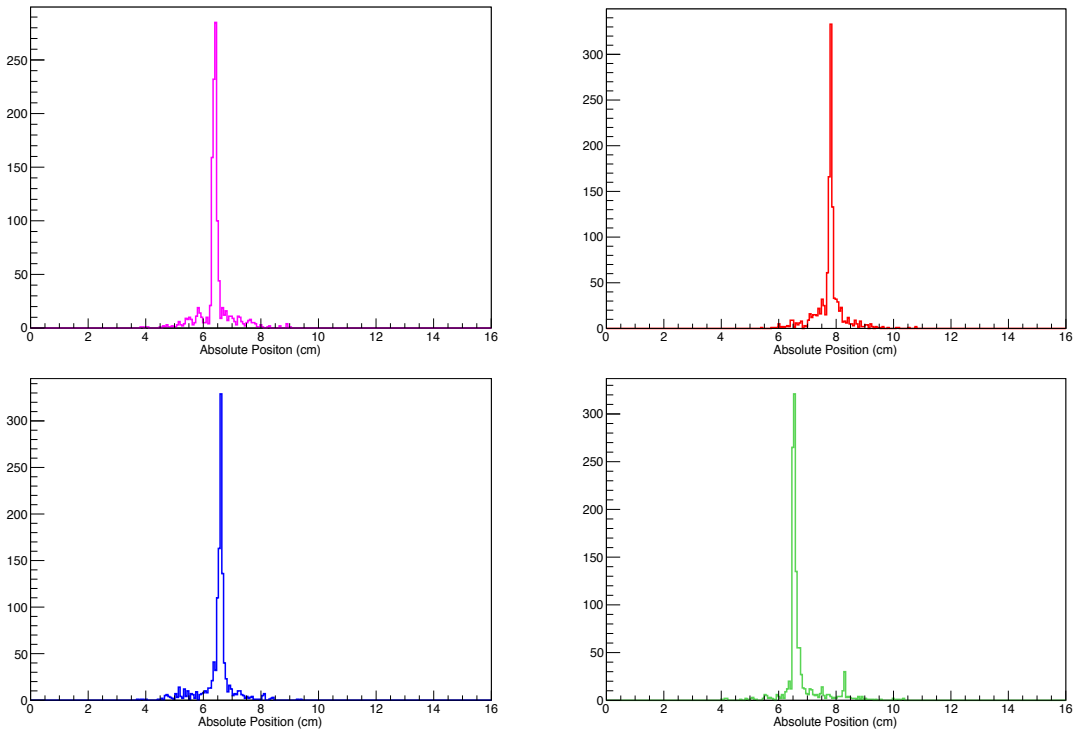

Figure 104. The lateral dimension event localization after the coded-aperture imaging. The bin width in these histograms is 0.6 mm. In the coarse localization plots (in anode space), the units are in anode strip space which are ~3 mm per anode strip. The widths of the coarse localization distributions are about 4 anodes, or ~12 mm. The widths of the imaged lateral dimensions are 1-2 mm. Thus, the imaged lateral results give much sharper peaks than the coarse localization distributions.

The collimator was moved around with respect to each data set, accounting for the small changes in the absolute position measurement. Unfortunately, the electronics used for this early work were borrowed and had to be returned before data could be taken both at the depth just before the bimodal distribution, as well as a data set with the collimator moved slightly laterally; although simulation studies indicate both cases would work as expected.

6.1.D. TWO-DIMENSIONAL COMPARISONS TO SIMULATIONS

The experimental results are shown compared to thick crystal simulation results in Figure 105. As seen in the figure, the general trend is the same, with the simulation results behaving

slightly better. The worse experimental results are likely due to the physical characteristics of the detector that are not present in simulations. For example, when a photon is launched in the simulation it is always seen in the simulation detector as long as it falls in the active detector area. While the simulation detector array is geometrically identical to the physics detector array, there was a major difference in the photon detection characteristics of each. The quantum efficiency of the detector array was not accounted for in the simulation. When a photon hits the photocathode in the H9500, it has some probability of being detected (given by the QE of the PMT). In the simulation the photon is always detected by the detector (QE=1.0). The error bars are given by the errors using the chi-squared iterative fitting method in ROOT [88]. In all cases using the chi-squared Gaussian fit method, the errors found on the widths were $O(10^{-3}\text{-}10^{-5})$ and are too small to be visible on this or any similar plots.

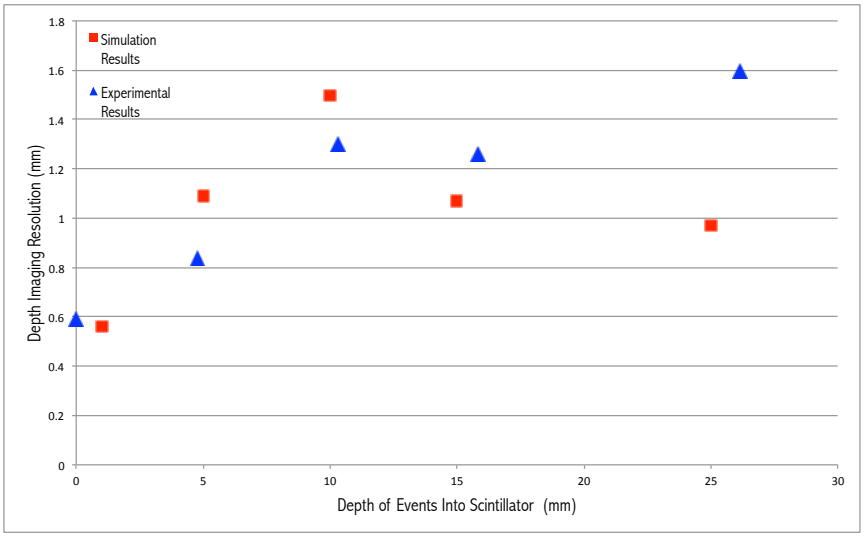

Figure 105. The simulation depth results (red squares) plotted with the experimental depth results (blue triangles) of the two-dimensional system. The general trend agrees in both cases, with the experimental results slightly worse at the upper depth. The error bars $O(10^{-3}\text{-}10^{-5})$ of each point are given by the uncertainty in the width of the fit using a chi-squared iterative fitting method [88], and are too small to be seen on all data points.

The lateral resolution results compared to simulations are shown in Figure 106. Again, the overall trend agrees between the two cases. However, in this case the experimental results are slightly better at both the lowest and highest depth.

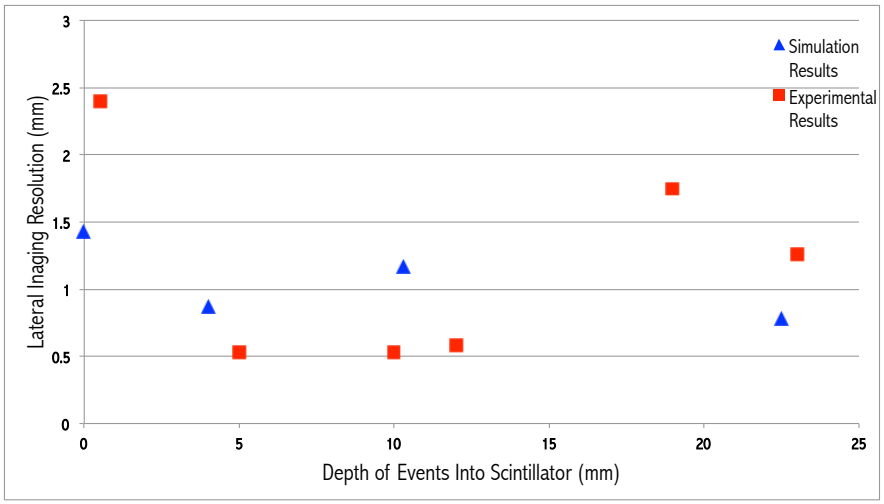

Figure 106. The simulation lateral results (red squares) plotted with the experimental depth results (blue triangles) of the two-dimensional system. The error bars are the same as described in Figure 105.

Overall, the system behavior closely resembled the simulation results.

6.2. THREE-DIMENSIONAL SYSTEM

Both ^{133}Ba and ^{137}Cs sources were used in collecting data with the full 3-D system. While the system was intended to work with the 356-keV peak of the ^{133}Ba, it was found that the resolution was worse than expected both in the peak width and the percentage of correctly found events in the general peak areas. This will be presented after the ^{137}Cs results are presented.

6.2.A. SINGLE EVENT RESULTS

Two techniques can improve the imaging capabilities; Chapter 4 discussed using outer cycles in imaging and how this method improved simulation results, while Chapter 5 discussed gain mapping and how a flat detector response helps imaging capabilities. Many events were looked

at one by one to understand these effects, and the results with and without each will be presented here for a single event. Then, the final results processed with both will be presented.

6.2.B. OUTER CYCLES IMPROVEMENTS

As discussed in Chapter 4, making use of the repeating mask pattern allows one to add data from the outer cycles to the center cycle (see Chapter 4). In the most recent simulations with a realistic detector, adding in one outer ring of mask cycles (resulting in 9 cycles) improved the peak-to-background results by approximately a factor of two. Going beyond that (adding cycles outside of the 3 x 3 center ring) did not show any improvement in the simulation data. However, the experimental data was improved using the outer cycles. A sample event with 10.0 mm of additional upper light guide and the 1-mm-thick crystal is shown in Figure 108. Each plot is the value of the maximum pixel for each depth plotted against the estimated depth of reconstruction with 1, 9, and 25 cycles. Figure 107 shows the pattern of cycles used. The labels (a), (b) and (c) correspond to which patterns are used in the reconstruction in Figure 108.

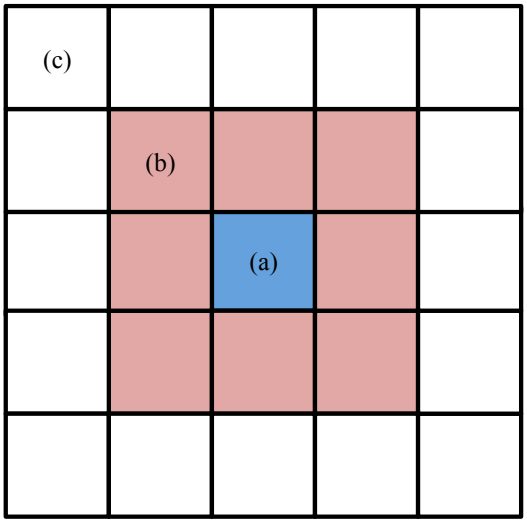

Figure 107. The colored regions with labels (a), (b) and (c) indicate which cycles were used in the reconstructions of the single event shown in Figure 108 below. Region (a) is the single base pattern, region (b) includes (a) and the 3 x 3 surrounding ring, and region (c) includes (a) and (b) in addition to the 5 x 5 outer rings.

When using no outer cycles (Figure 108a) the event would not be found at the correct depth. Figure 108b and Figure 108c show the improvement in the peak height as the outer cycles are used.

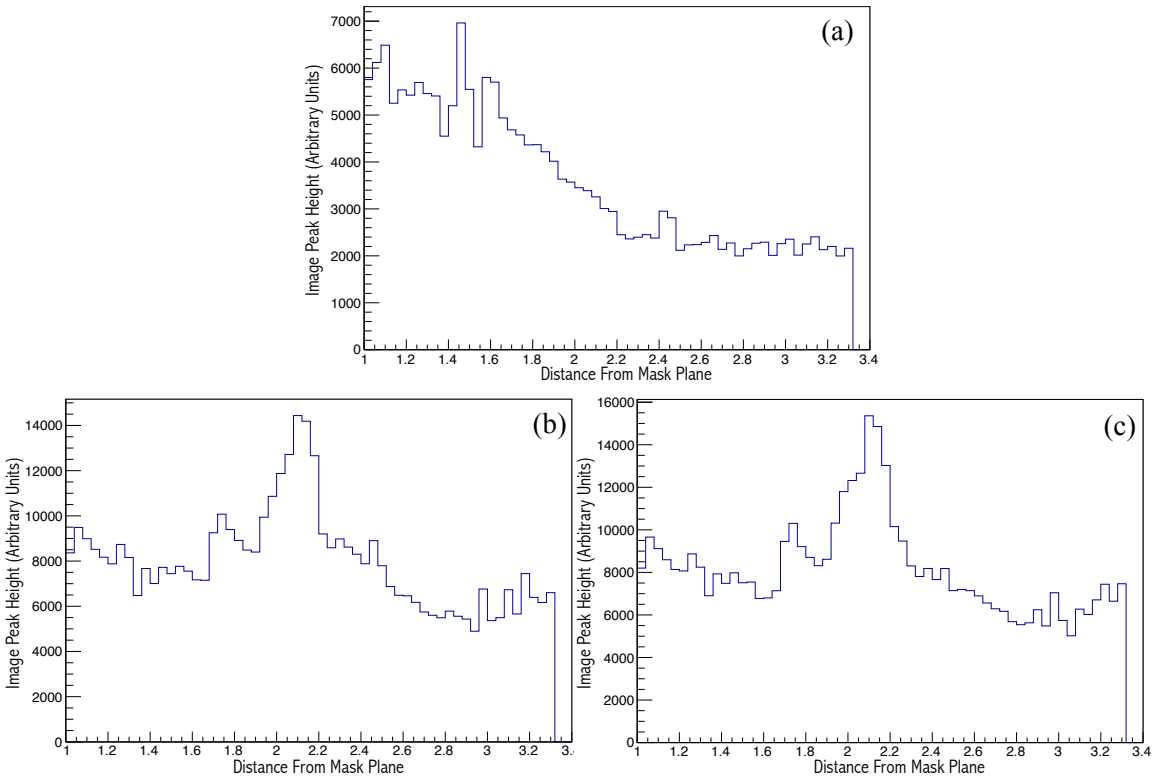

Figure 108. A single event in the 662-keV peak with 10 mm of additional upper light guide. The event is a total of 2.0-2.1 cm from the mask. In addition, a small offset is present due to the thickness of the layers of optical grease between several planes in the system. The top (a) uses only the center cycle data. The lower left figure (b) includes the 3 x 3 sum in addition to the center, and the lower right (c) includes the 5 x 5 cycle.

As seen for the single event shown, the maximum image values in the reconstructed events are increased using additional outer patterns, while the maximum values in the images at the non-correct depths are only slightly raised between the 3 x 3 and 5 x 5 reconstructions. This methodology was repeated for many events and the trend was true for all observed depths.
From this point on, all data shown will use the cycles shown in region (c).

6.2.C. GAIN CORRECTIONS

As discussed in Chapter 4, while the PMTs were initially gain matched anode by anode with a single PMT flood light field illumination, there was no initial gain mapping to calibrate one PMT against another throughout the array. Instead this was done post-processing by observing the aggregate heat map for many events and correcting for the most egregious gain variations. The uncorrected and corrected heat maps and associated single events using each are shown in Figure 109.

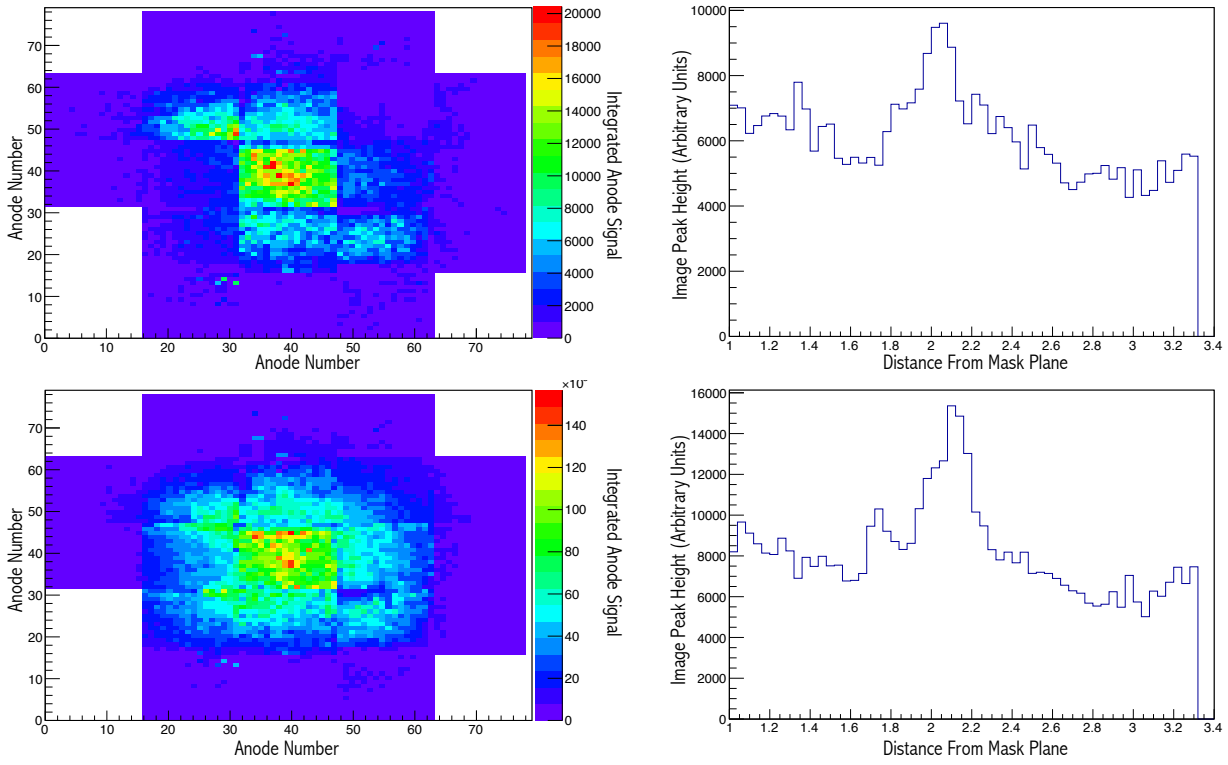

Figure 109. (Top left) The aggregate heat map for 3800 events without the post-processing PMT gain matching. (Top right) The same single event reconstructed with the gain mapping used in the top left image. (Bottom left) The heat map with the adjusted gain mapping to smooth out the response over the PMTs. (Bottom right) The same event reconstructed with the adjusted gain mapping.

As seen in the plots on the right of Figure 109, the maximum value in the image at the true depth is larger with the adjusted gain mapping than without it. This gain mapping was observed to have the same effect for other events as well as the one described, and therefore it was used in the final imaging code.

6.2.D. SINGLE EVENT DEPTH RECONSTRUCTION

The event discussed in this section will now be examined more closely. The images shown in this section used the full outer cycles in addition to the adjusted gain matching across the PMT array. The event was reconstructed over 2.1 cm in quartz space; this is equivalent to about 3.3 cm of a NaI(Tl). The step size between each depth reconstruction was 0.4 mm. The results from several depths are shown in Figure 110 to demonstrate the reconstruction. The image was reconstructed using the methods discussed in Chapters 3 and 4, with the setup discussed in Chapter 5. Processing of this event used the complete set of techniques discussed above.

6.2.E. LATERAL POSITION DETERMINATION

In the simulation study in Chapter 4, a weighted mean was found to work better to coarsely localize events than a Gaussian fit. This was initially used in processing the experimental data, but after observing the coarse localization results when different collimator positions were used, a Gaussian fit of the collapsed detector data was adopted since it worked much better. The heat map for the single event discussed thus far is shown in Figure 111 with the collapsed data in each direction.

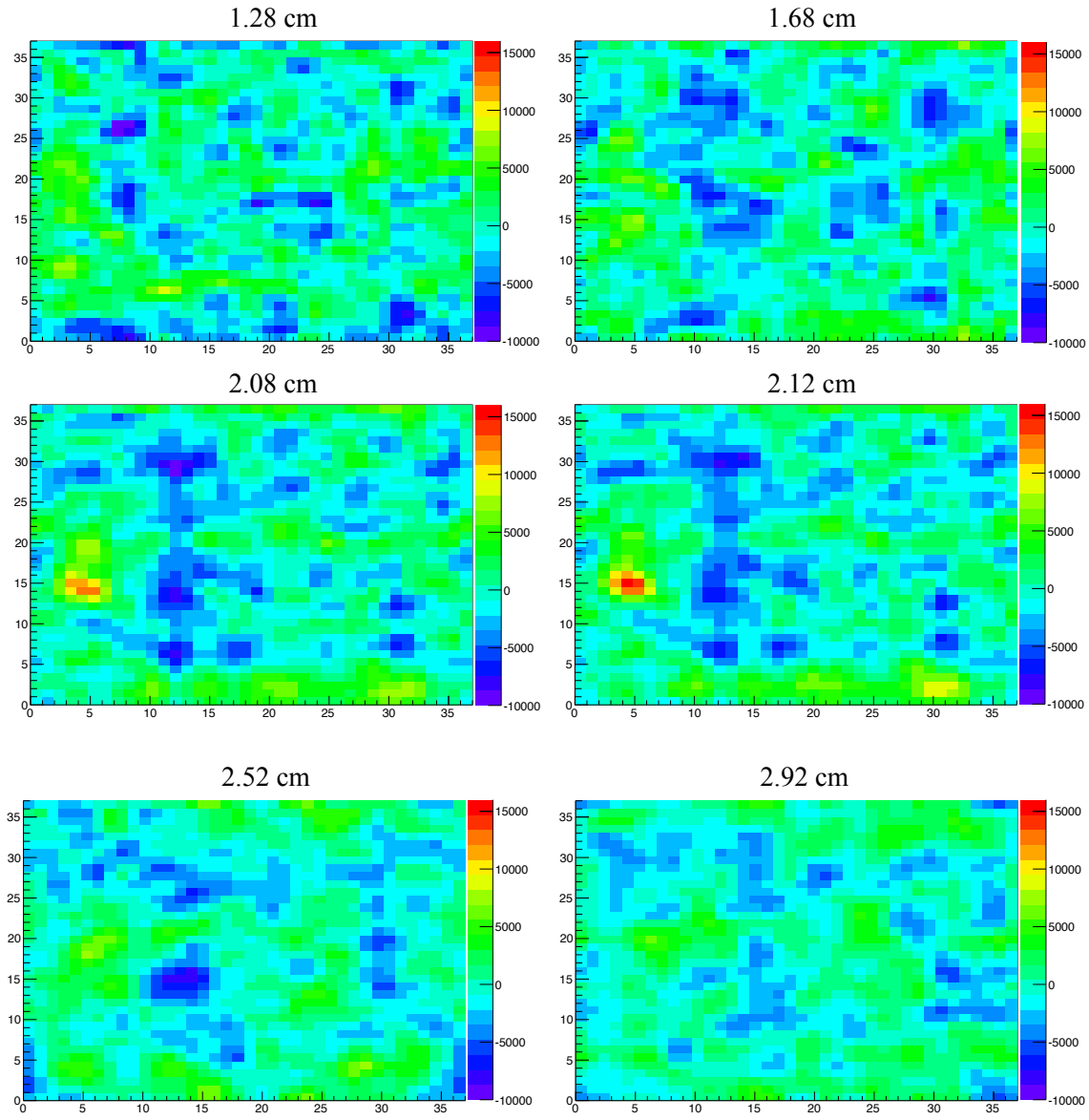

Figure 110. Reconstructed images over the depth range of the thick crystal emulation. The event exists at 2.12 cm. As seen in middle row, a peak is seen at image pixels (4, 15). This is the same event as in Figure 108 and Figure 109. The peak height versus the depth of reconstruction is shown in the figures above.

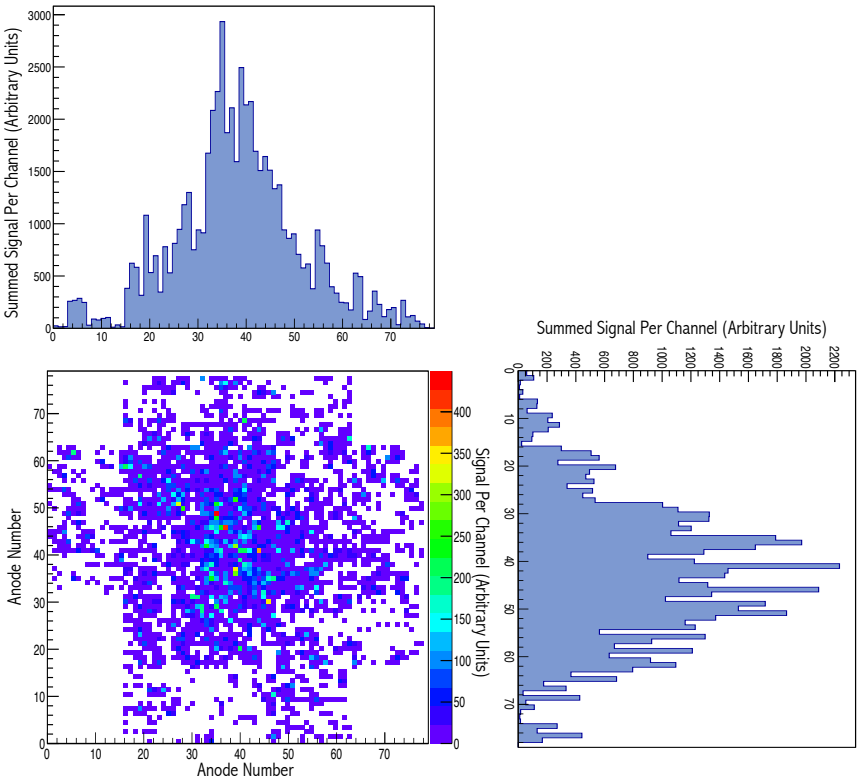

Figure 111. The heat map for the single event with the collapsed detector data in the x (top) and y (right) directions. As seen in the collapsed distributions, the mask modulations are easily visible.

When used on experimental data, the weighted mean coarse localization approach was not able to account for changes in the collimator position; i.e. when the collimator was moved 2 cm in the x or y direction, the position (mean) of the coarsely found localization peak in the dimension of the collimator movement did not move 2 cm. The Gaussian fit was used and it was found that coarsely binning the dimensionally collapsed data (x and y) into larger bins worked best. This means that from the first bin (far left on the heat map), one bin of the collapsed data contained 5 bins of anode strips for the x and 4 bins of anode strips for the y dimension. This method for the single event is shown in Figure 112.

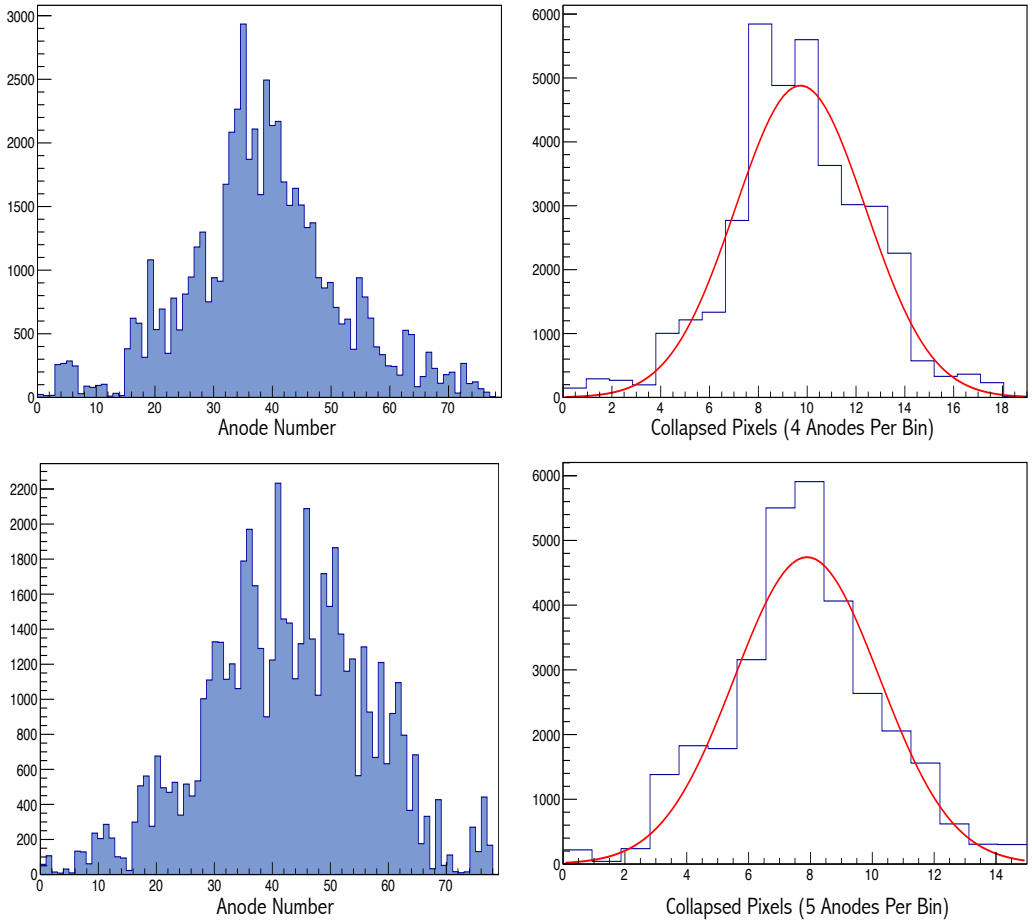

Figure 112. (Top left) The heat map data for the single event collapsed in constant x. (Top right) The x data collapsed into larger bin sizes. Each bin contains 5 bins in the adjacent histogram. This was then fit using a Gaussian function, and the coarse localization was given by the center of the Gaussian fit. (Bottom left) The y-collapsed data. (Bottom right) The y data collapsed into four anodes per bin. Again, the collapsed data was fit using a Gaussian to find the coarse y localization.

Each collapsed bin size was selected by looking at many individual events one by one and determining which collapsed bin size gave the best fit. This method was confirmed by verifying that the collimator movement agreed with the coarsely localized peak movement in both directions.

6.2.F. THREE-DIMENSIONAL SYSTEM THICK-CRYSTAL EMULATION FINAL RESULTS

The thick crystal emulation data were collected over a range equal to 26.3 mm in a thick crystal. The depth results are shown in Figure 113 with the quantitative results given in Table 9. As in the two-dimensional system, the imaging resolution was calculated using the index correction and the thin crystal de-convolution.

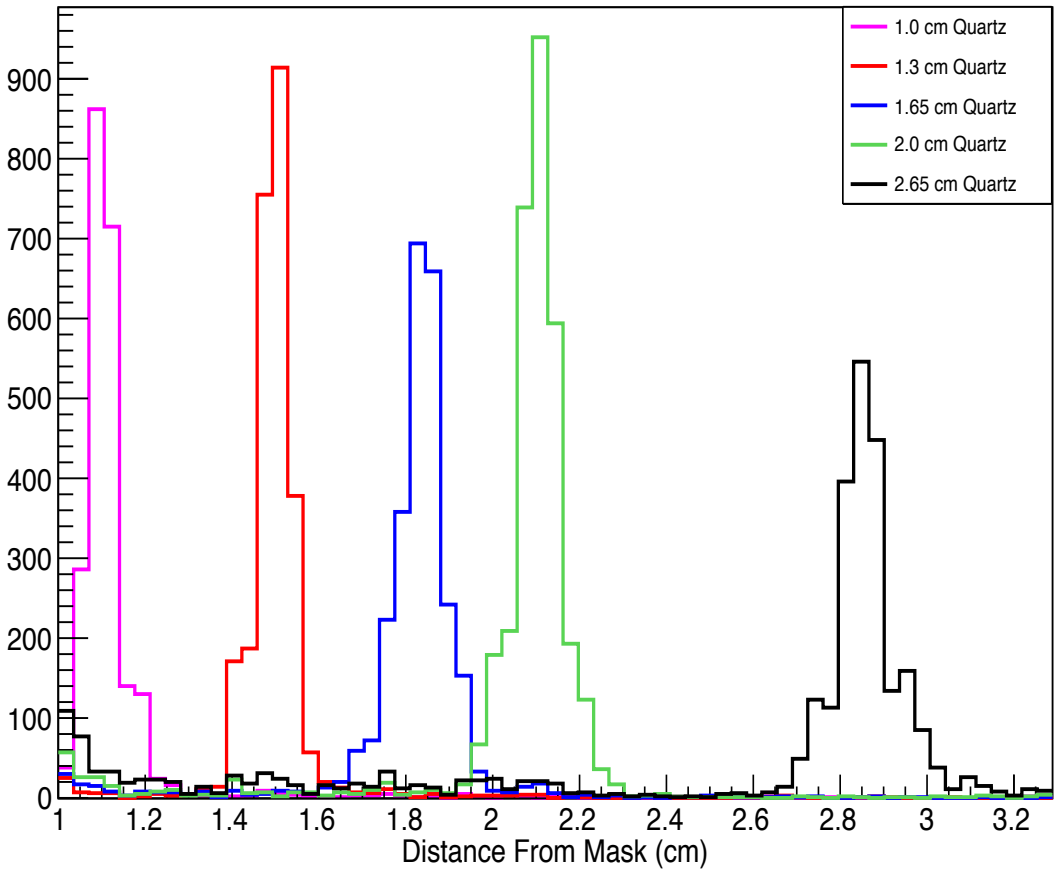

Figure 113. Five data sets with varying layers of additional quartz upper light guide. The de-convolved final results for each depth are given in Table 9.

The depth results are best for the events closest to the mask pattern. While the resolution worsens as the events are farther away, it is still less than 2 mm for events equivalent to 26 mm into a

bulk, un-segmented scintillator crystal; this is 2-3 times better than any previously published work of localizing events in an un-segmented bulk crystal.

Table 9. The final results of the full three-dimensional system.

Additional Upper Light Guide (mm)	Equivalent Depth in Crystal (mm)	Depth FWHM (mm)	Deconvolved Depth Resolution (mm)	Percentage of Events Found in Peak
0.0	0.0	0.67	**0.59**	91.8%
3.0	4.76	0.77	**0.84**	91.5%
6.5	10.3	1.0	**1.3**	86.7%
10.0	15.8	0.97	**1.26**	85%
16.5	26.1	1.15	**1.6**	61.5%

One item of note is the low percentage in the far right column for the highest depth. This is due to the shape of the peak height versus depth of reconstruction for the images. The overall height of the maximum value versus depth decreases as the estimated depth increases, and in the uppermost case some true peaks cannot be resolved over the fluctuations in the peak heights. In these cases, most of the incorrectly found events are found at the highest depth of reconstruction. The range of the depth reconstruction (in the imaging software) was performed over a thicker range than the 30 mm thick crystal; thus, the "badly" reconstructed events could be immediately recognized. The range above the 30 mm crystal that includes the reconstruction range is shown in Figure 114.

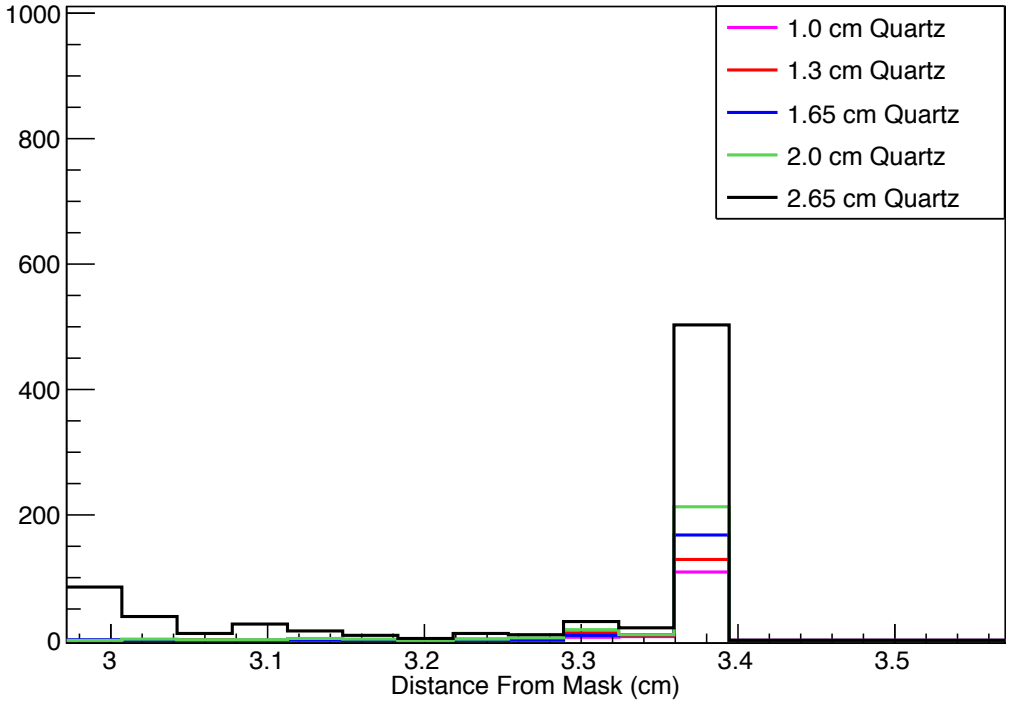

Figure 114. The range above the possible location of the 30-mm-thick crystal. This is located at 2.9 ((1.9/0.63-1) from the index change) on the horizontal axis. As the crystal does not exist above this depth, all events found above this are known to be improperly localized. The top data set has the most "badly" reconstructed events.

One could imagine algorithms or event filters that look back through the peak profile to help correctly localize some of these events. One simple filter was tried but was not successful in improving the results without degrading the true peak resolution. If an event was found at the maximum depth (just below 3.4 in Figure 114), the peak height versus depth was scanned again to look for a new maximum from the bottom (1.0 cm) to the top (2.0 cm) of the possible 30 mm thick crystal location. For the highest data set (2.65 cm of quartz), the filter was turned on and this had several consequences. The location of the false peak (black in Figure 114) was shifted to a lower depth to where the maximum new peak was searched. As was the goal of the filter, the amplitude did decrease, though the true peak (at 2.9 cm in Figure 114) was broadened and thus the imaging resolution was worsened. As the improvement of events found in the true depth

where the thin crystal was located only improved from 61% without the filter to 65% with the filter, it was decided to not use the filter as this gain taken with the worsened resolution worsened the system performance overall.

Figure 115. The lateral results for each data set (low to high) in the crystal. The colors correspond to the colors on the depth results plot. The broad peaks are due to collimator leakage; it was originally designed for a ^{133}Ba source, and these data were collected with a ^{137}Cs source.

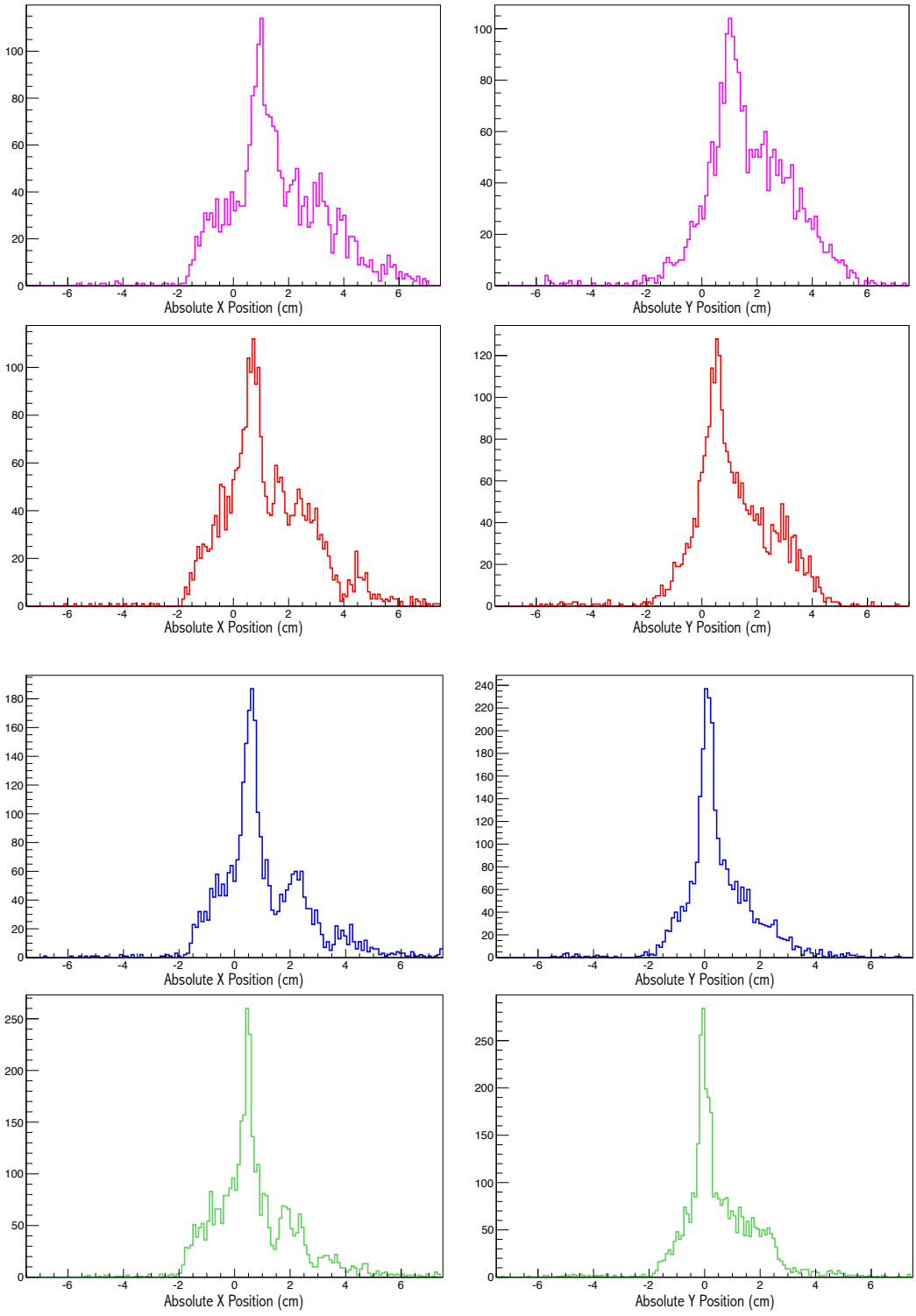

Figure 115. Continued.

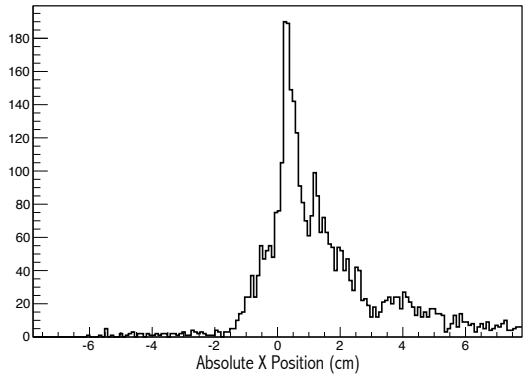

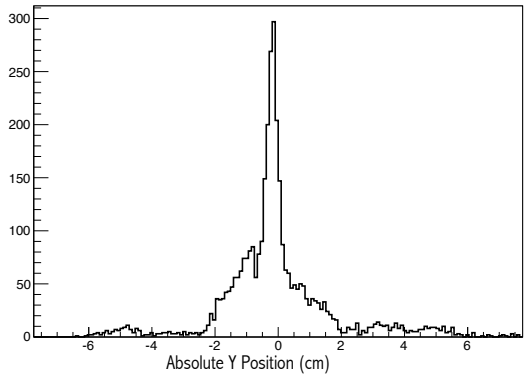

Figure 115. Continued.

Table 10. The lateral results. The X and Y FWHM are the widths of the distributions accounting for the collimator leakage peak baseline seen in Figure 115.

Additional Upper Light Guide (mm)	Equivalent Depth in Crystal (mm)	X FWHM (mm)	X Final (mm)	Y FWHM (mm)	Y Final (mm)	Beam Width
0.0	0.0	5.3	**3.16**	5.0	**2.63**	4.2
3.0	4.76	4.54	**1.94**	4.54	**1.94**	4.10
6.5	10.3	4.19	**1.47**	4.34	**1.86**	3.91
10.0	15.8	3.97	**1.35**	3.87	**1.37**	3.73
16.5	26.1	3.80	**1.71**	3.7	**1.90**	3.39

The lateral results obtained with the thick crystal are shown in Figure 115 and given quantitatively in Table 10. The lateral results are not as "clean" as the depth results due to leakage of the collimator. Originally, the tungsten collimator used was designed for a ^{133}Ba source. When it was used with a ^{137}Cs source, non-interacting events were seen to leak through the collimator outside of the 1-mm diameter collimation hole. These events are seen in all of the lateral distributions.

The events at the bottom of the crystal yield the worst lateral resolution in both dimensions; this is the same trend as with the 2-D system. As with the previous system, this is attributed to the light spot at this depth not fully illuminating a full mask cycle, resulting in a lack of information in the magnified coded-aperture pattern. The results of the entire system (depth and both lateral resolutions) will be compared to simulation results in the next section.

Two additional analyses were used to confirm that the system was behaving as expected. Because the collimator was at a fixed height relative to the outer frame of the system and, in turn, the photomask plane (as quartz was added above this plane), the thin crystal was moved closer to the collimator as the amount of upper light guide was increased. Thus, the width of the reconstructed peak should widen as the amount of light guide decreases. This effect is seen in Figure 115. It is also seen in the X and Y FWHM in Table 10. The second verification was to

check whether the absolute plate scale of the imager was unity in the lateral dimension. Unlike the depth, the index of refraction plays no factor in the lateral reconstruction. Therefore, if the collimator is moved a certain distance, the reconstructed peak must move by the same distance. This was verified for both the x and y dimensions, and the results for 2 cm of movement in the x dimension are shown in Figure 116.

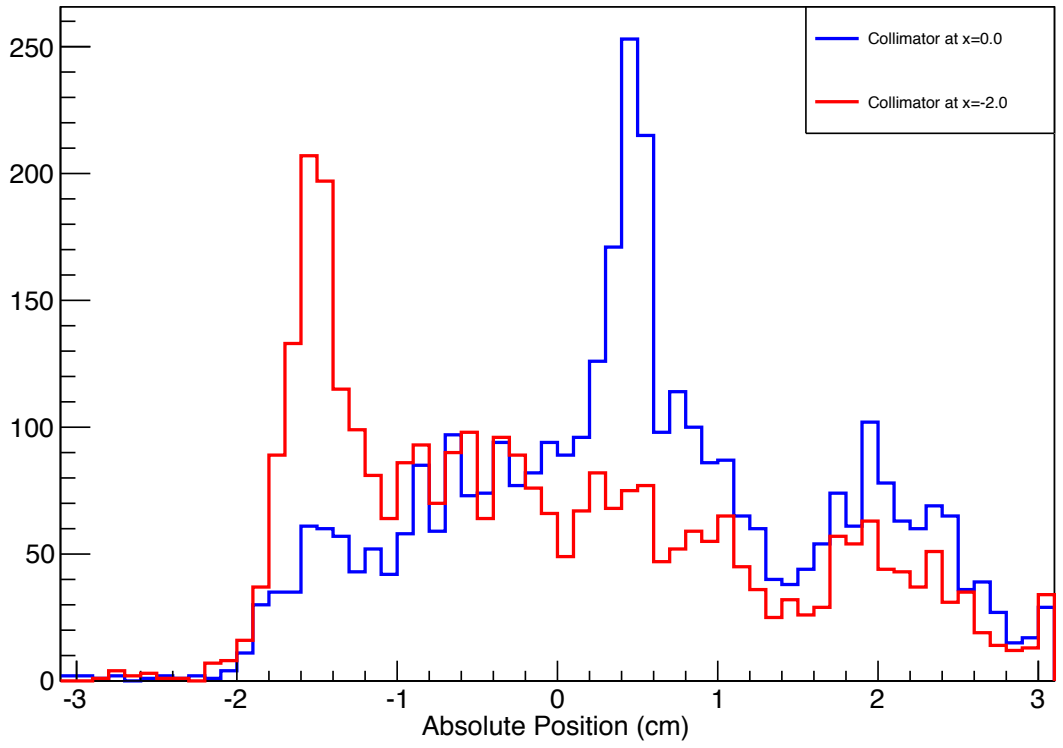

Figure 116. The absolute lateral reconstruction for two data sets with the collimated source moved 2 cm.

As seen in the results, the lateral localization behaved as expected. The asymmetrical background in the red distribution in Figure 116 is due to the collimator movement over the thin crystal while the crystal remains stationary; events are still located uniformly around the peak, but the crystal stops at the boundary just past the peak location (5 cm crystal moved 2 cm from the center).

6.2.G. ENERGY RESOLUTION

The FWHM energy resolution of the system with the mask pattern and a ^{137}Cs source was 23.6%. The spectrum is shown in Figure 117.

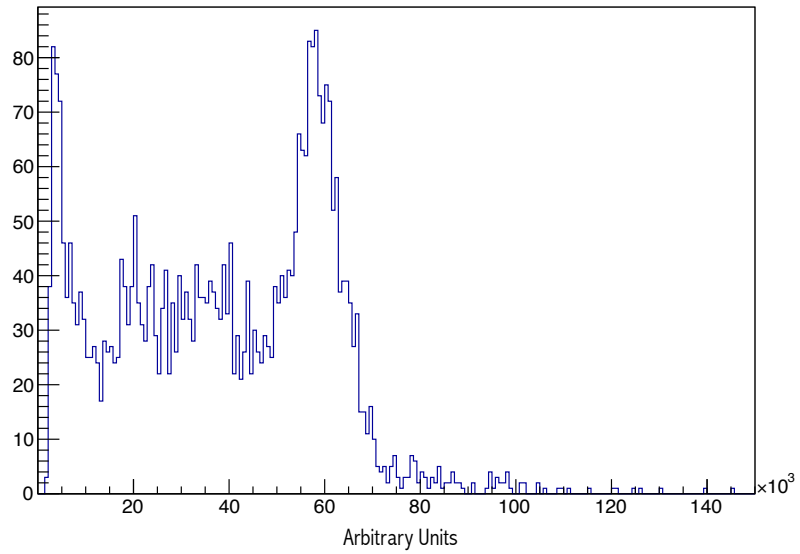

Figure 117. The energy spectrum for the ^{137}Cs source. The 662-keV peak is located at 60 on the horizontal axis.

The poor energy resolution of this system can be attributed to several factors. The system collects a much smaller portion of light than initially deposited by an event. The light in the upward direction is not recorded because the crystal is blackened, the index change accounts for a light loss of about 50%, and the mask pattern blocks 50% of the light. Additionally, the active area of the detector (active anode coverage versus the entire 5 x 5 PMT array) is 80%. The final factor of $\sqrt{1.5}$ is given by this area coverage. Together, these factors decrease the energy resolution by

$$(\sqrt{2})_{Directional\ Losses} \cdot (\sqrt{2})_{Index\ Losses} \cdot (\sqrt{2})_{Mask\ Losses} \cdot (\sqrt{1.5})_{Area\ Losses} = 3.46$$

Eq. 84

The standard FWHM energy resolution of a NaI scintillation detector is about 6-7% for 662 keV [6]. Thus,

$$7\% \cdot 3.46 = 23.8\%$$

Eq. 85

which is what is observed by the system.

6.2.H. COMPARISON TO SIMULATIONS

The full system simulation study was presented in Chapter 4. The original simulations had a focal length of 2.2 cm and were studied for 400-photoelectron events. The experimental setup had a focal length of 2.35 cm and used a ^{137}Cs source, so simulations were also performed using that optical geometry. The comparisons between the lateral results are given in Figure 118 and depth results in Figure 119.

While there are small disagreements between the simulation and experimental results, for similarly located events in the bulk crystal no difference is greater than 1 mm. The general trend for each dimension also is present in both the simulations and experimental results.

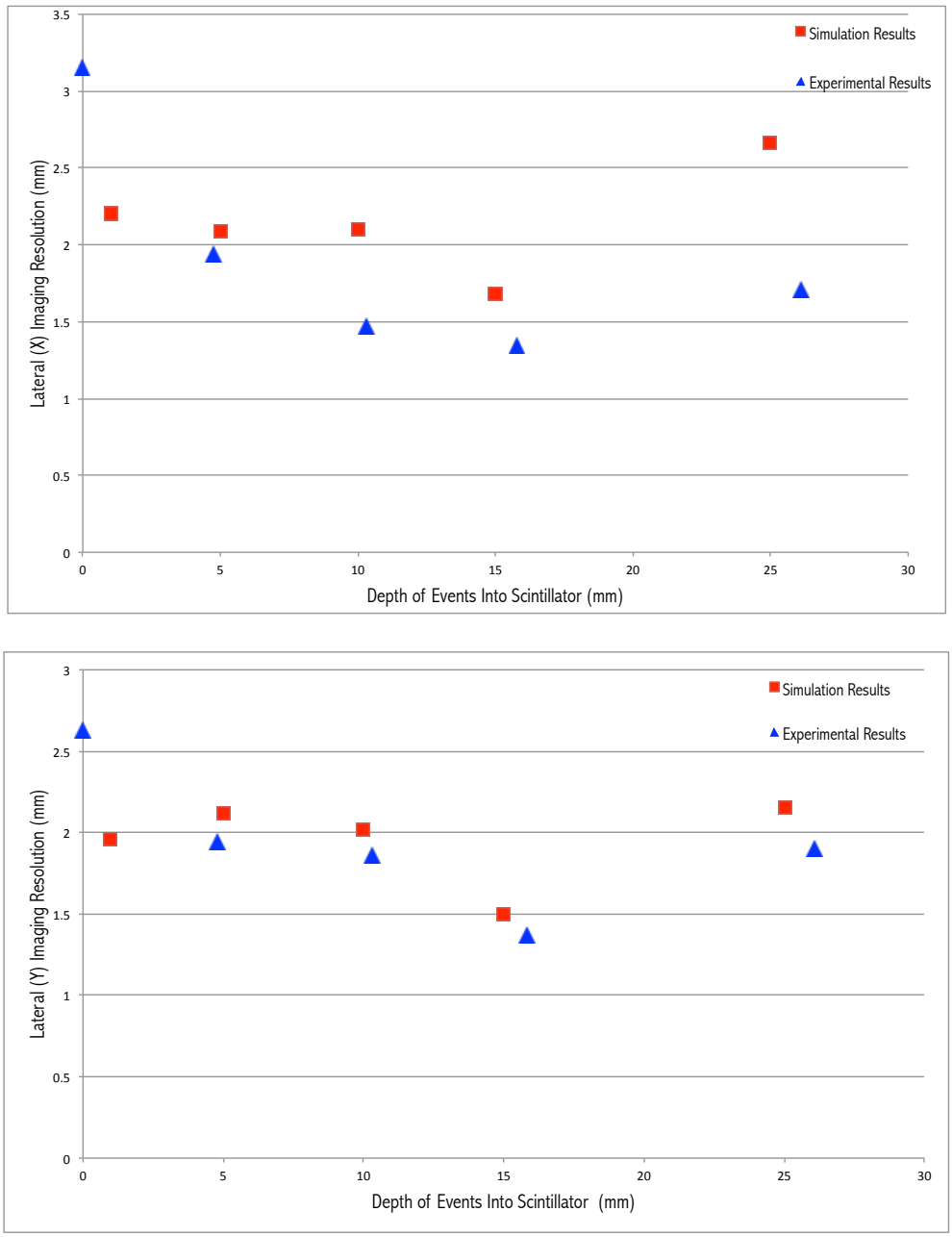

Figure 118. The lateral (X top, Y bottom) results for the 3-D system compared to simulations. The error bars are too small to be visible on the plot ($O(10^{-3}\text{-}10^{-5})$).

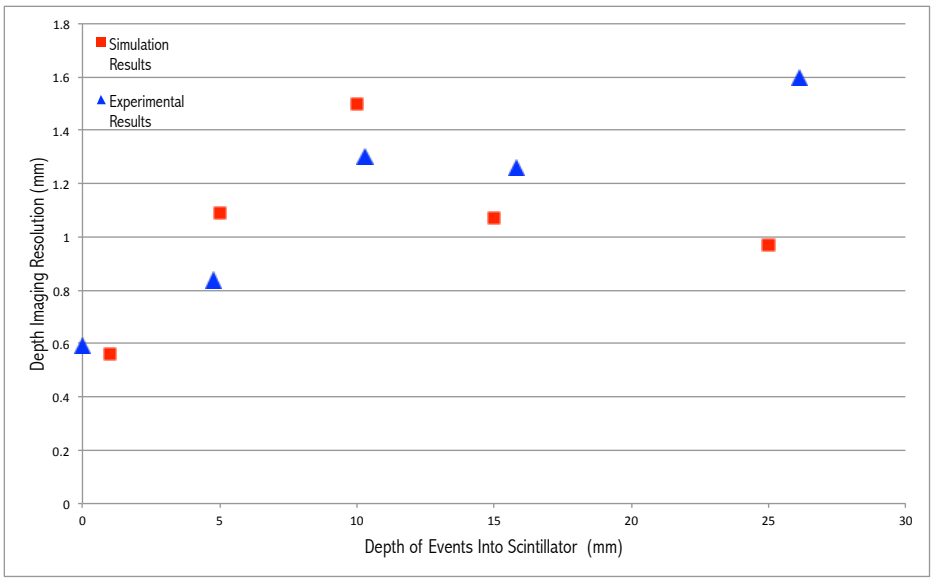

Figure 119. Simulation results versus experimental results for the depth dimension.

6.2.I. ^{133}BARIUM RESULTS

The system was originally designed for 356-keV events. While the system was originally planned for events in this energy range, the results did not behave as well as expected. The depth results are shown in Figure 120.

The data sets were collected with the same thicknesses of upper light guide as were collected for the ^{137}Cs data. The lower energy results are significantly worse in two ways; the width of each distribution is broader and the number of events found in the correct peak is lower. The measurement FWHM and percentage of events found in the correct peaks are given in Table 11.

The ^{133}Ba results are very poor, especially in regard to the percentage of events found in the correct peak. For one, the position resolutions are several millimeters worse than initial simulations indicated. Additionally, the very poor performance in the amount of correctly located events was not present in simulation data. Once the results were processed, several events were viewed by eye to understand why so many events were failing to be correctly localized. A sample event is shown in Figure 121. The event has an energy value within the 356-keV peak.

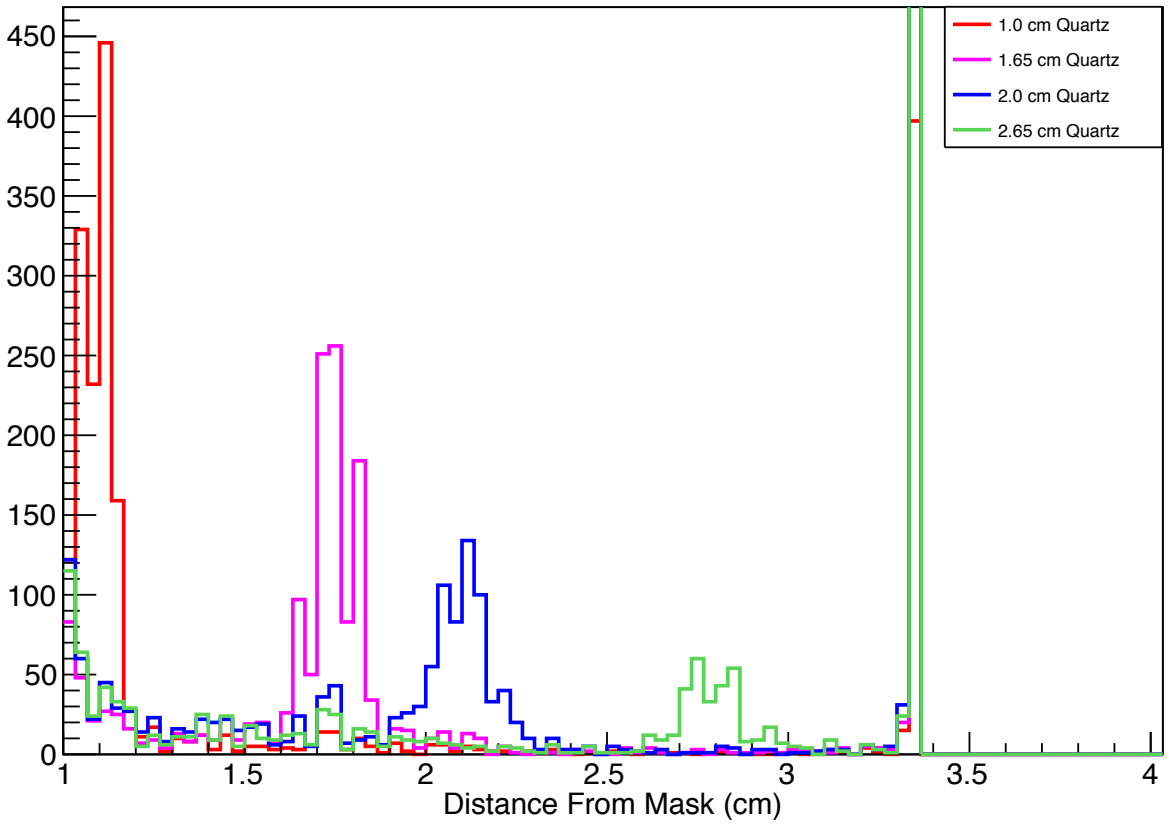

Figure 120. The ^{133}Ba depth results. The FWHM and percentage of events in the peaks are given in Table 11.

Table 11. The ^{133}Ba results.

Additional Upper Light Guide	Equivalent Depth in Crystal (mm)	FWHM (mm)	Percentage of Events Found in Peak
0.0	0.0	1.14	71%
6.5	10.3	1.38	54%
10.0	15.8	2.0	32%
16.5	26.1	1.71	16%

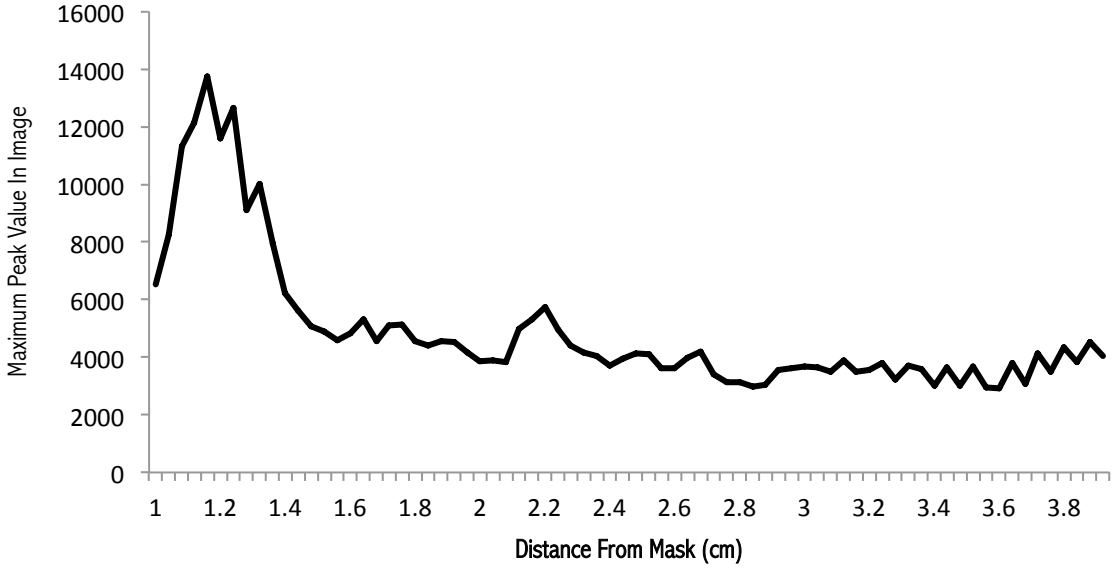

Figure 121. A single event (experimental data) reconstructed over the depth range. The true event exists at 2.1 cm.

As seen in the peak-height-versus-depth-estimate plot, the maximum bin value is dominated by large values at the bottom of the depth reconstruction. Additionally, the far right edge of the image shows an increasing peak height. Other observed events contained this shape closer towards ~3.0 cm (the top of the crystal), resulting in incorrectly localized events. The events tend to be biased towards one of the two ends so the events do not reconstruct properly.

To investigate this result, dead pixels were added to simulation setups that mimicked the dead regions of the experimental PMT array. While the resolution was very slightly worsened, the large percentage of incorrectly found events was not accounted for. Next, slight gain variations were added into the detector response in the simulations and events with 400 and 650 detected photons were simulated from the same points in the crystal. Figure 122 (400 photons) and Figure 123 (650 photons) show the depth results of the events at 5 mm (left) and 20 mm (right) with varying gain adjustments on two PMTs that border the center PMT in the experimental H9500 array. The values in the top right corner of each figure are the amount that the PMT gains are raised with respect to the center. To emphasize, only two of the 20 PMT gains are changed by less than 3%.

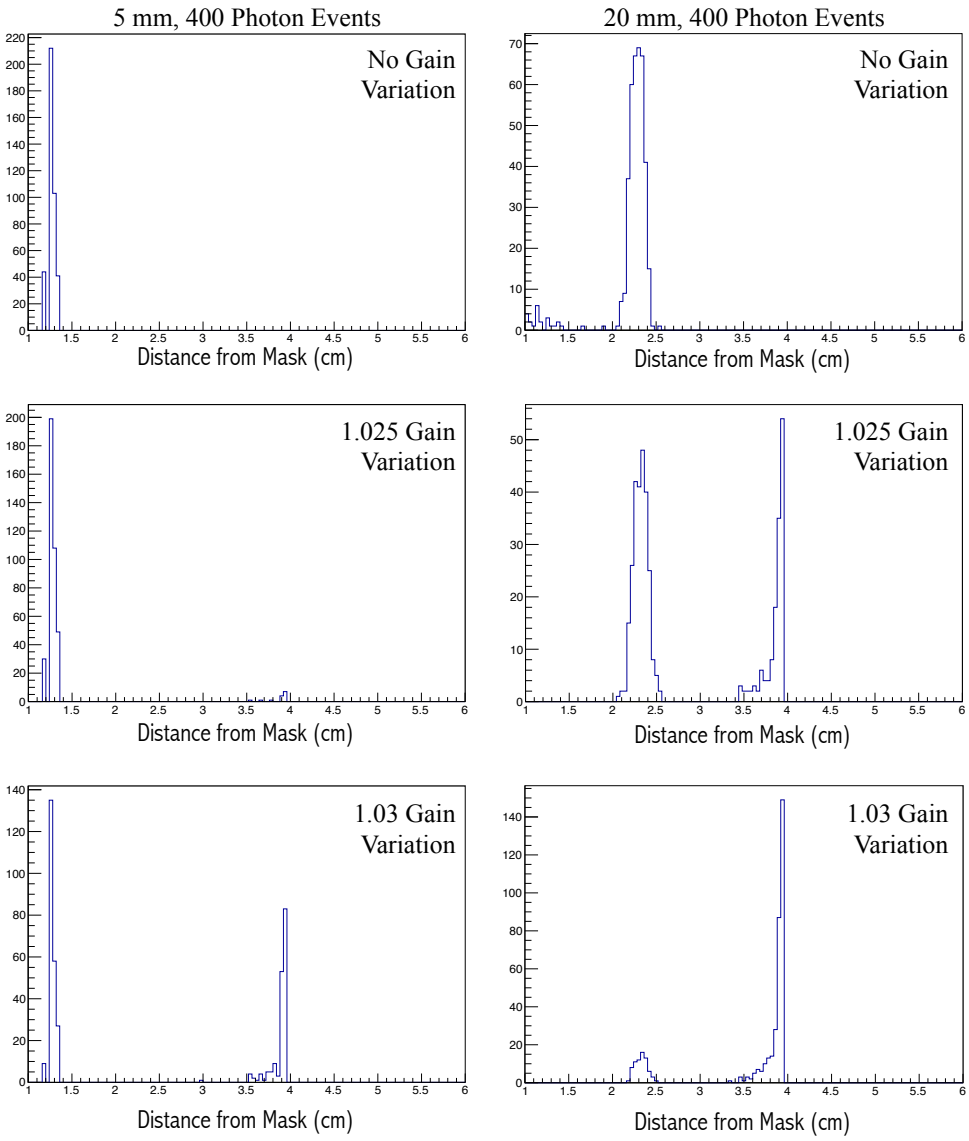

Figure 122. 400, 400-photoelectron events at two depths (5 mm and 20 mm) with varying gain changes to two PMTs that surround the center PMT in the 3-D experimental PMT array.

With no gain variations the system works as expected for both cases (See Figure 123). When a very small gain variation (1.025 to 1.0, or 2.46% difference between) was added to only two of the PMTs in the 20 PMT array, the imaging ability begins to break down. This effect is larger for events at the top of the crystal than the bottom of the crystal, and mimics the behavior seen experimentally. With even a slight increase in the gain from 1.025 to 1.03 on the same two PMTs, the system breaks down even further. Again, this is only a 2.9% difference between the gains in only two of the center 3 x 3 ring of PMTs.

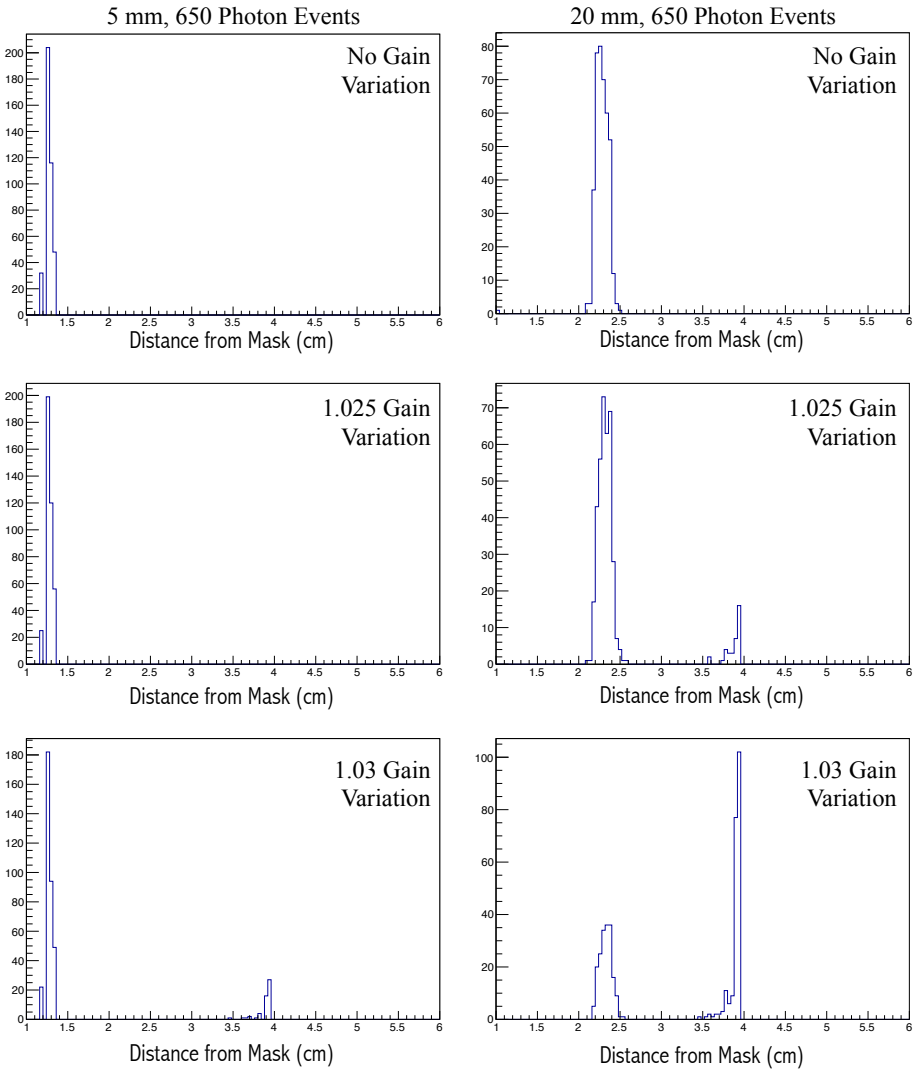

Figure 123. 400, 650-photon events at two depths (5 mm and 20 mm) with varying gain changes to two PMTs that surround the center PMT in the 3-D experimental PMT array.

The effect is present in both cases but is significantly worse for the lower photon case. This explains why the ^{133}Ba results are worse than expected; the gain mapping impacts the number of incorrectly found (depth) events more than the higher photon events. This is because relative to the center PMT, a small change in the gain on an outer PMT will have a larger effect on the overall number of counts used in the reconstruction if the total number of counts is smaller.

Three single events are shown in Figure 124. Each 400-photon simulated event was reconstructed using the experimentally used detector array (i.e. corner PMTs turned off and dead

channels where they existed experimentally). When individual images were examined at the same depths with the gain variations turned on and off, the source of the increasing false peak counts (value of the maximum in each image where the true event does not occur) shown in Figure 124 was found to be due to the random fluctuations of noise artifacts in the images. While the background fluctuations center around zero at all depths, the values of the positive and negative fluctuations are larger for higher depths compared to lower depths. For example, for the event in the top figure in Figure 124, with the gain variations turned on, the fluctuations in the image range from -50 to 50 (arbitrary units) at 1.24 cm from the mask, and -80 to 80 at 3.16 cm from the mask. While each is centered on zero, the larger background at the upper depth results in the upward trends seen in all events in Figure 124. In some events, the true image peak is larger than the upper depth background fluctuation and the image can be correctly localized, but many times (Figure 122) the upper depth fluctuation is larger and the event is incorrectly localized. The large magnitude of increasing fluctuations in both directions was used to try and flatten the maximum peak height response with a peak height of zero by adding the maximum (positive) and minimum (negative) for several events, but this resulted in the events to be incorrectly found as the new maximum was shifted off of the true event location. As the background trend is due to (even a very small) the gain mismatch, the conceptual interpretation can be understood as weighting one section of the mask (reconstruction) more than another section. This breaks the fundamental properties of the mask (Section 2.3) and removes the constant background properties derived earlier. This information has potential to help improve the system and would be extremely useful in developing filtering algorithms that could improve the results. These are discussed in Appendix 2.

While the experimental system was gain-mapped anode by anode and two methods were used to gain map the system by PMT (by eye and using an automated normalization using the total amount of signal collected with the diffusing glass and LED array), a gain matching this finely tuned could not be achieved. In addition to explaining the poor ^{133}Ba results, this also verifies the gain mapping was done reasonably well, as the ^{137}Cs results are better with respect to the percentage of correctly found events experimentally for a higher depth compared to simulations (62% at 25 mm for experimental results, versus 45% for simulation results at 20 mm).

Figure 124. Single events (400-photon simulation events with experimentally used detector array) reconstructed with (green) and without (purple) the gain variations (1.03 difference as discussed) in two PMTs that neighbor the center PMT.

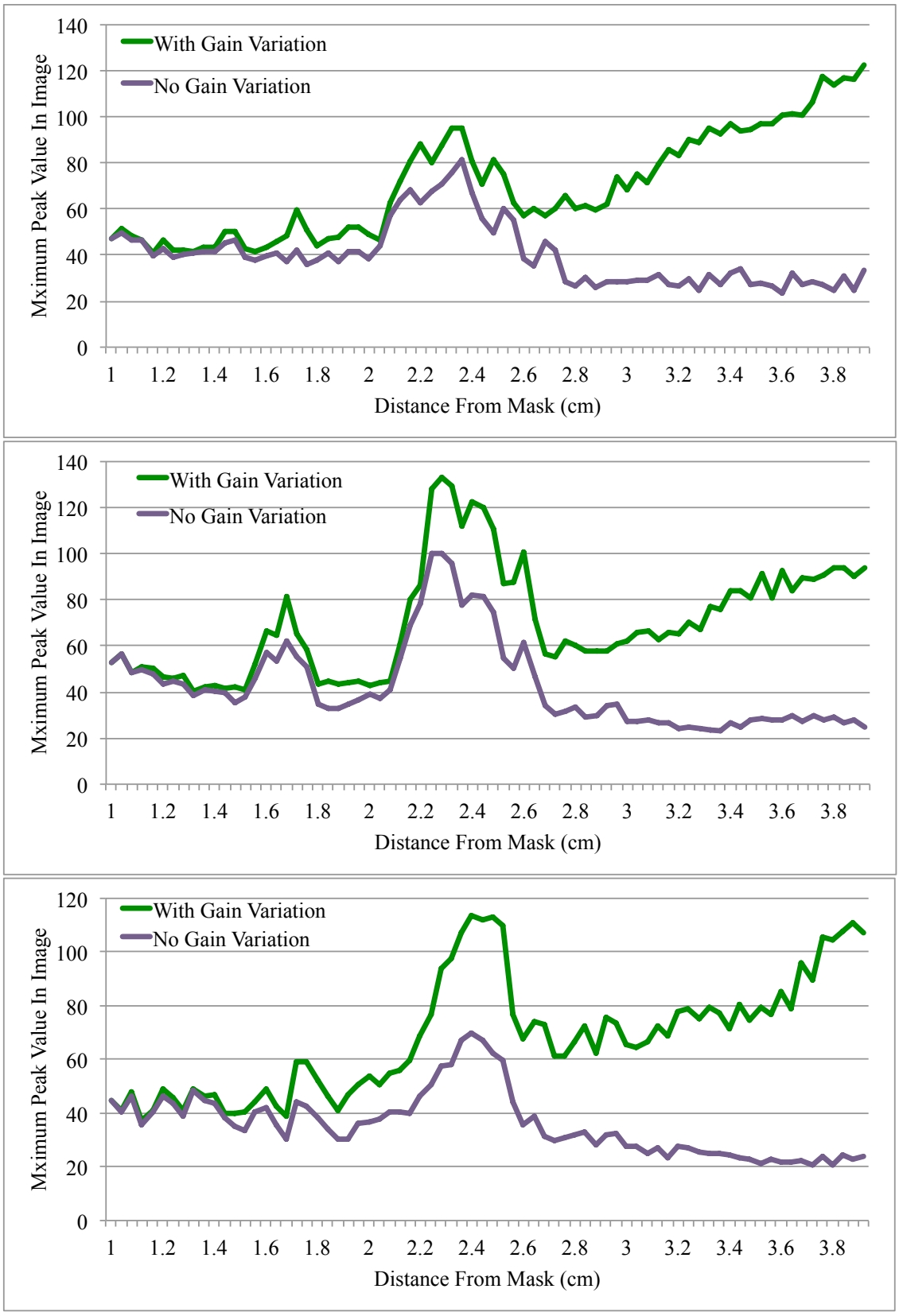

Figure 124. Continued.

6.2.J. THICK CRYSTAL RESULTS

Data were collected with a 30-mm-thick crystal using both a vertical and angled collimated beam. While this method did not allow for events to be deposited at known depths in the crystal, it did allow for us to check general trends to verify the system behaved as expected. Unfortunately, due to the collimator leakage with the ^{137}Cs source, we could not make sense of the imaged data due to the large amount of events leaking through the collimator. The ^{133}Ba source was used instead.

The collimator was placed vertically over the system. As the collimated beam spreads out farther from the collimation hole, the reconstructed lateral results should be broader for lower depths (close to the PT plane) relative to upper depths in the crystal. While the ^{133}Ba position resolution was too poor to measure an imaging resolution, the general expected behavior is seen in Figure 125.

The overall trend is as expected (broader for lower depth and a large cluster at the upper depth of incorrectly found events), but the distributions are skewed for both lateral dimensions versus the depth. The upper depth (>~2.25 cm) is symmetrical around the center of the beams, but the lower depths show more reconstructed events in the positive directions for both dimensions.

This can be explained using 400-photoelectron simulation results. With an ideal 3 mm pixel array, the lateral dimensions both show a small asymmetry around the center, correctly located peak. The percent of events found in the asymmetrical peak is 8%. This is shown in Figure 126. As the detector array is ideal; (i.e. a completely uniform, gapless pixel array), this means that a small number of the events in the skewed section of the distributions are a result of the imaging. When the real detector array, along with the empty PMT position and dead pixels are used in the simulations, the number of events in the asymmetrical peak increased by 12%, to 20% of the total events.

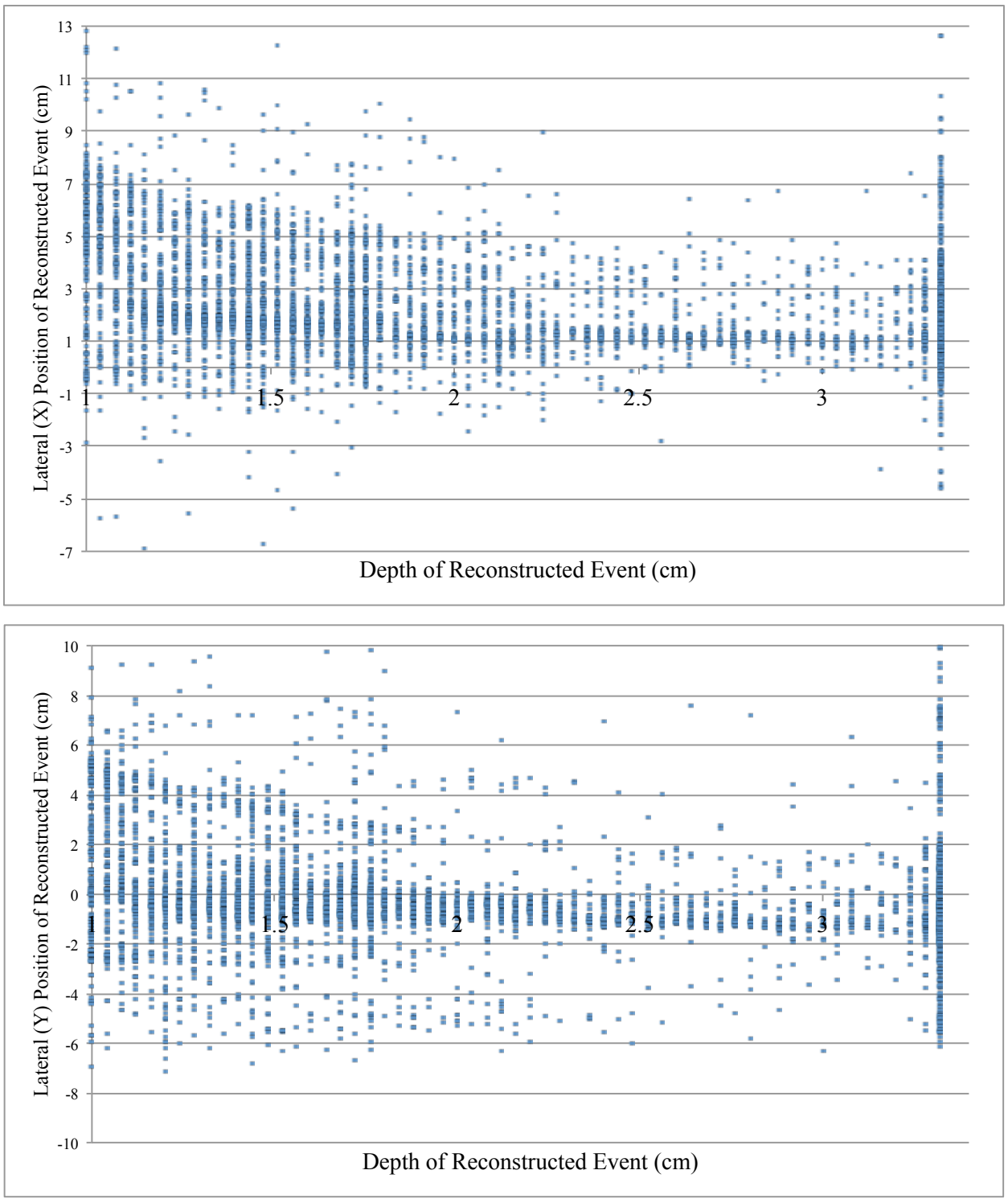

Figure 125. Depth versus X (top image) and Depth versus Y (bottom image) for a vertical beam incident on a thick crystal, using the ^{133}Ba collimated source. The spread of the collimated beam is seen in both distributions along with a skewed behavior.

Thus, the asymmetry seen in Figure 125 is a result of the physical detector array with the missing corner PMTs, missing dead PMT and dead pixel groups. The width of the beam at the bottom of the crystal (1.0 on the plots) is about 1 cm. The beam spreads out 1 cm and the distance from the correct to the asymmetric peak is about 1.5 cm, Additionally, the position resolution of ~2-3 mm contributes to the spread in the distribution. This explains the events several cm away from the center of the distributions. This asymmetry is likely also present to a lessor degree in the ^{137}Cs data in Figure 115, but with the collimator leakage it is difficult to precisely locate it. In addition to the vertical collimator setup, data was also collected with an angled beam. Due to triggering issues it was not useful in verifying the event localization technique. The details of these results are given in Appendix 3.

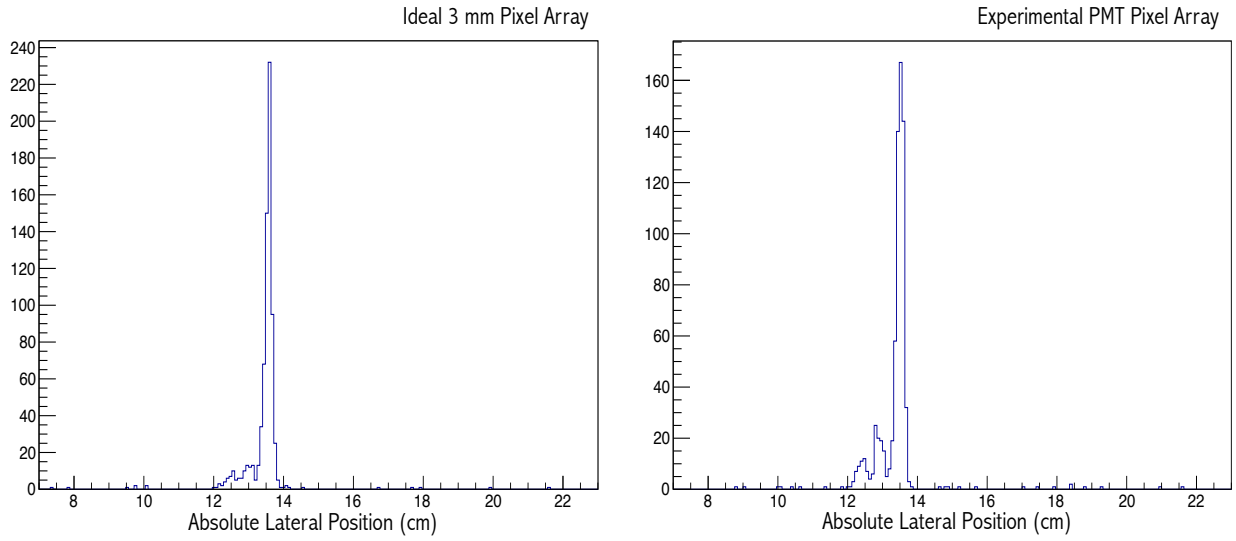

Figure 126. The simulation results (400-photon events) with an ideal PMT array with 3 mm pixels (left) and the array used in the experiment (right).

CHAPTER 7. CONCLUSION

Single event localization in bulk scintillator crystals is important to a wide variety of applications. The work done for this dissertation using optical coded apertures provides an extremely effective technique of encoding the spatial information of radiation interactions without using a segmented crystal or adding another plane of phototransducers. While the coded-aperture technique is a mature concept that has been used successfully over several decades, applying the same principles to visible light was a simple expansion on the method to image radiation in a different energy range (visible light) while using the projection of the shadow pattern to locate events in the initially unknown depth dimension. Although the results of this project were extremely successful in many respects, there are some important limitations in the technique that were discovered experimentally. In addition to summarizing the impact of the project, this chapter discusses the challenges that were overcome to obtain the results shown in Chapter 6, limitations of the technique, and possible approaches to improve the system.

While the original goal of the project was to build a full-volume Compton imager, complications in the experiment led to delays that did not make this a possibility when the funding and timeline were considered. Although Compton imaging was not achieved, the work in this dissertation still provided the framework for the goals of the event localization capabilities, as the goals of the system (~1 mm^3 localization, energy resolution, etc.) came from parameters that were desired in the Compton camera.

For the single event localization, the imager did work quite well; as stated in Chapter 6.1-6.2, the results using our system gave 2-3 times better position resolution in each dimension than previously published work. The work in this dissertation provides the foundation for new applications using the optical coded-aperture technique. Many options exist that could be investigated in future projects, including using methods to collect more light, different types of mask patterns such as pseudo-random [99] arrays, different geometries such as two one-dimensional mask patterns at different sides of the crystal, and using different types of phototransducers.

The main challenges of the project were typical of experimental measurements, including instrumenting both data acquisition systems, detecting real signals, verifying that the system was triggering on the correct signals, and working to physically build and adapt the system as new challenges arose. Specifically, the three-dimensional system presented many more challenges

than the two-dimensional system. The data acquisition system was not delivered as a final product ready to be used in a plug-and-go system and there were several major issues that arose in utilizing it. There were problems instrumenting the full system due to the sparse information provided regarding the fully connected electronic components. However, this did provide a useful understanding of how the electronics behaved when bad connections existed between different sections of the data acquisition system, and if the project is continued or electronic readouts reused, this information will be extremely valuable. Additionally, building the physical experiment (256-channel PMT multiplexer modules, PMT coupling, light-tight cable feeds, etc.) proved to be a complicated challenge that required changing the system as we made progress in assembling each component.

In terms of the system performance, the most obvious limitations involve the poor results using the lower energy 356-keV events. While the system worked very well for higher energy events (1-2 mm^3 throughout almost all of the 30-mm-thick crystal emulation) the initial goal was to instrument the imager for events closer to 400 keV. As seen with the ^{133}Ba results, while some events were correctly localized, many more were found at the wrong locations. The only difference between the two cases (^{133}Ba and ^{137}Cs) is the amount of light that the PT receives. We knew the low light signal would be the largest overall challenge of making this method work, and the differences between the two cases of results prove this to be a dominant feature that determines the success of the technique. The most straightforward approach to improve the system performance would be to gain map the system to give as flat a response as possible. This proved to be a difficult experimental task, as creating a large area and truly uniform flood field is not trivial.

Apart from gain fixes, there are several approaches that could improve the results with lower-light events. First, if a high-index optical coupling compound were manufactured or found, the system could be built using a full stack of high-index material from the high-index crystal to a sapphire light guide to a sapphire PMT entrance window (the two former are commercially available). This could increase the amount of light seen by the PMT by ~2 and for a 356-keV event would result in a light yield at the PT plane about equal to that of the 662-keV events where the system was shown to work successfully. As shown in Section 4.2.D., when this material was sought commercially, no viable option was discovered.

Another change would be to use a photocathode material with a much higher QE than that of the H9500 ordered in 2011. This option is currently not available in the H9500, but Hamamatsu does offer a photocathode material with a QE as high as 43% [84] in other PMTs. Again, this would result in an increase in the number of photons seen by the PT.

An additional idea also involves increasing the amount of light collected; the use of a retro-reflector above the scintillator crystal could increase the light by ~ 40% [96]. A retro-reflector reflects the light in the same direction in which it was emitted, as opposed to a diffuse reflector that spreads the light out. Thus, the retro-reflector would not create a virtual image when reconstructing the event. This was not implemented in this project as the goal was to investigate the initial concept and maximize the chances of a successful conclusion, and while possibly very helpful, the use of a retro reflector would complicate the system.

Another important characteristic of the technique was discovered experimentally. The bimodal structure seen in both the experimentally collected 2-D data and the simulations (both the 2-D and 3-D systems) was not initially seen in the early simulation work [13]. Originally, it was thought that the system (depth localization) broke down when the magnified feature size was equal to about 0.5 of the anode size. In practice, it was shown that this factor varies depending on the rank of the mask used. This provided a quantitative understanding of where the system stopped working in the upper depths of a crystal. In the future, knowing this performance allows for a more precise understanding of what rank must be used to instrument a desired depth range (1.0 ratio of smallest magnified mask features at the PT plane relative to the anode pixel sizes for rank 7 mask, 0.7 for rank 17, 0.66 for rank 19) with a selected anode pixel size.

Another major limitation with the current iteration of the project is the event processing time. To reconstruct events over the respective depth ranges, the event processing times were 0.7 seconds and 7.5 (for 0.2 mm step sizes) seconds for the 2-D and 3-D systems, respectively. For a fieldable system for the national security applications discussed in Chapter 1, and in possible applications in PET imaging, this event processing time is too slow. This would need to be significantly shortened for use in one of these applications. While some of the code was optimized, there is great deal of room for improvement. Some ideas are already in place for the next version of the project; including using rebinned boundaries that are pre-calculated once and used for all events, and using a coarse depth localization to limit the reconstruction range in the 3-D system similar to the method used in the 2-D system. Additionally, improving the

computational methods with multiple threads or using a GPU could significantly improve the processing time.

In regard to the larger impact of this work, the progress made in localizing events in crystals could be useful to a wide variety of applications; some of these were highlighted in Sections 2.10-2.11. The most obvious use of this technology is for a bulk volume Compton camera that was discussed in Chapter 1 and in detail in Sections 3.1-3.2. While the challenges of this work led to complications in realizing the final adaptation of the image localization technology to be used within a full-volume Compton camera, the success in position resolution lays the groundwork for the next step of the project. In the same field of national security applications, this work has been envisioned for use in a full volume neutron scatter camera. The primary difference will be the difference in materials and electronics used for neutron detection instead of gamma-rays. Still, many of the lessons learned in this dissertation work will be important in that application.

In medical imaging, as stated in Section 2.11, the depth of interaction is often the largest uncertainty in the overall resolution in PET imaging. The depth resolution was found to work the best of the three dimensions in the optical coded-aperture technique. The application of this work to PET imaging could significantly improve the overall resolution and allow for the cost to be reduced by decreasing the required number of segmentations in the crystal ring.

Finally, in astrophysical applications, the same principles of the Compton camera bulk volume imager could be very useful by adapting the system to detect cosmic gamma-rays on a larger scale.

The work in this dissertation provides the entire framework of a novel method for gamma-ray event localization in bulk scintillator crystals from the motivation for and theory of the concept, to presenting the final results of two prototype systems, along with all pieces of information for the project to be understood. This technique has the very important benefit of much improved position resolution in all three dimensions compared to other currently published work and is a significant contribution to the field of radiation detection.

BIBLIOGRAPHY

[1] "Against the Spread of Nuclear Weapons," *Against the Spread of Nuclear Weapons*. http://www.iaea.org/Publications/Booklets/Safeguards/pia3810.html.

[2] The Nuclear Threat Initiative and Project on Managing the Atom, Belfer Center, "Nuclear Terrorism FAW," September 2007.

[3] A. C. Raffo-Caiado, J. P. Hayward, S. E. Smith, and K. P. Ziock, "Investigation of Combined Measurements with Three Dimensional Design Information Verification System and Gamma-Ray Imaging Systems for International Safeguards Applications," *Proceedings on the 50th Annual INMM Conference*, July 2009.

[4] K. P. Ziock et al., "A fieldable-Prototype, Large-Area, Gamma-Ray Imager for Orphan Source Search," *IEEE Transactions on Nuclear Science*, vol. 55, pp. 3643-3653, 2008.

[5] K. P. Ziock et al., "Performance of the Roadside Tracker Portalless Moniter," *IEEE TNS*, pp. 2195-2203, October 2011.

[6] Glenn F. Knoll, *Radiation Detection and Measurement*. New York, NY, USA: Wiley, 1979.

[7] F.N. Flakus, "Detecting and Measuring Ionizing Radiation - A Short History," *Radiation Detection*, vol. 23.4, pp. 31-36.

[8] S. E. Boggs and P. Jean, "Performance characteristics of high resolution Compton telescopes," *A & A*, vol. 376, pp. 1126-1134, 2001.

[9] V. Schönfelder, "The Imaging Gamma-Ray Telescope Comptel Aboard GRO," *Advances in Space Research*, vol. 11, no. 8, pp. 313-322, 1991.

[10] Radiation Physics Research | Compton Cameras. Radiation Physics Research. [Online]. http://www.medphys.ucl.ac.uk/research/acadradphys/researchactivities/comptoncameras.htm

[11] National Institute of Standards and Technology. (2014) NIST _ X-Ray Mass Attenuation Coefficients.

[12] K. P. Ziock et al., "Large Area Imaging Detector for Long-range, Passive Detection fo Fissile Material," *IEEE Transations on Nuclear Science*, vol. 51, no. 5, pp. 2238-2244, 2004.

[13] K. P. Ziock, M. A. Blackston, and T. Van Vuure, "3D Millimeter Event Localization in

Bulk Scintillator Crystals," *Nuclear Science Symposium*, pp. 2014-2022, 2011.

[14] Alessandro Curioni. Columbia University (2004): 22.LXeGRIT - A Liquid Xenon Gamma-Ray Imaging Telescope.

[15] J. S. Karp and G. Muehllehner, "Performance of a Position-Sensitive Scintillation Detector," *Physics in Medicine and Biology*, vol. 30, no. 7, pp. 643-655, 1985.

[16] C. J. Hailey, F. Harrison, J. H. Lupton, and K. P. Ziock, "An inexpensive hard x-ray imaging spectrometer for use in x-ray astronomy and atomic physics," *Nuclear Inst. Methods in Physics Research A*, vol. 276, pp. 340-346, 1989.

[17] P. Antich, N. Malakhov, R. Parkey, N. Slavin, and E. Tsyganov, "3D position readout from thick scintillators," *Nucl. Inst. Meth. in Phys. Res. A*, vol. 480, pp. 782-787, 2002.

[18] C. Levin, "Detecor Design Issues for Compact Nuclear Emission Cameras Dedicated to Breast Imaging," *Nuclear Instruments and Methods in Physics Research Section A: Accelerators, Spectrometers, Detectors and Associated Equiptment*, vol. 497, no. 1, pp. 60-74, 2003.

[19] E. E. Fenimore and T. M. Cannon, "Coded aperture imaging with uniformly redundant arrays," *Applied Optics*, vol. 17, pp. 337-347, 1978.

[20] H. O. Anger, "Scintillation Camera," *Review of Scientific Instruments*, vol. 29, no. 1, 1958.

[21] J. G. Rogers et al., "Design of an Efficient Position Sensitive Gamma Ray Detector for Nuclear Medicine," *Physics in Medicine and Biology*, vol. 31, no. 10, pp. 1061-1090, 1986.

[22] R. H. Dicke, "Scatter-Hole Cameras for X-Rays and Gamma Rays," *The Astrophysical Journal*, vol. 29, no. 1, p. 27, 1968.

[23] Roberto Accorsi, "Design of a Near-field Coded Aperture Camera for High-resolution Medical and Industrial Gamma-ray Imaging," *Massachusetts Institute of Technology*, 2001.

[24] Godard Space Flight Center. (1996, March) Coded Aperture Imaging Concept. [Online]. http://astrophysics.gsfc.nasa.gov/cai/coded_intr.html

[25] Wikipedia. Wikipedia. [Online]. http://en.wikipedia.org/wiki/cross-correlation

[26] E. E. Fenimore, "Time-resolved and Energy-resolved Coded Aperture Images with URA

tagging," *Applied Optics*, vol. 26, no. 14, p. 2760, 1987.

[27] B. R. Frieden, "Restoring Maximum Likelihood and Maximum Entropy," *Journal of the Optical Society of America*, vol. 62, no. 4, p. 511, 1972.

[28] R. Willinggale, *MNRAS*, vol. 194, no. 359, 1981.

[29] A. Wouters, M. Simon, and J. G. Hirschberg, "Direct Method of Decoding Multiple Images," *Applied Optics*, vol. 12, no. 8, p. 1871, 1973.

[30] Chris Koolsaet. (1996, December) Cyclic Difference Sets. [Online]. http://www.inference.phy.cam.ac.uk/cds/part3.htm

[31] M. Hall, *Combinational Theory*.: Waltham: Blaisdell, 1976.

[32] D. Calabro and J. K. Wolf, "On the Synthesis of Two-Dimensional Arrays with Desirable Correlation Properties," *Inf. Control*, vol. 11, pp. 537-560, 1968.

[33] F. J. MacWilliams and N. J. A. Sloane, "Pseudo-random Sequences and Arrays," *Proceesings of the IEEE*, vol. 64, no. 12, pp. 1715-1729, 1976.

[34] Stephen R. Gottseman and E. E. Fenimore, "New Family of Binary Arrays for Coded Aperture Imaging," *Applied Optics*, vol. 28, no. 20, p. 4344, 1989.

[35] A. R. Gourlay and J. B. Stephen, "Geometric Coded Aperture Masks," *Applied Optics*, vol. 22, no. 24, p. 4042, 1983.

[36] Walter J. Wild, "Dilute Uniformly Redundant Sequences for Use in Coded-aperture Imaging," *Optics Letters*, vol. 8, no. 5, p. 247, 1983.

[37] Barker R. H., "Group synchronizing of binary digital systems," in *Communication Theory*, W. Jackson, Ed. London: Butterworths, 1953.

[38] E. E. Fenimore, "Coded Aperture Imaging: Predicted Performance of Uniformly Redundant Arrays," *Applied Optics*, vol. 17, no. 22, p. 3562, 1978.

[39] Matthew C. Fleenor, Matthew A. Blackston, and Klaus P. Ziock, "Correlated statistical uncertainties in coded-aperture imaging," *Nuclear Instruments and Methods in Physics Research A*, December 2014.

[40] R. Accorsi and R. C. Lanza, "Near-Field Artifact Reduction in Planar Coded Aperture Imaging," *Applied Optics*, vol. 40, no. 26, p. 4697, 2001.

[41] L. T. Chang, B. Macdonald, V. Perez-Mendez, and L. Shiraishi, "Coded Aperture Imaging of Gamma-Rays Using Multiple Pinhole Arrays and Multiwire Proportional Chamber Detector," *IEEE Transactions of Nuclear Science*, vol. 22, no. 1, pp. 374-378, 1975.

[42] E. Klotz and H. Weiss, "X-ray 3-D Coded Aperture Imaging: Displaying the Heart," *Applied Optics*, vol. 15, no. 8, p. 1913, 1976.

[43] "Coded Aperture Imaging Of The Heart," *Journal of Computer Assisted Tomography*, vol. 4, no. 5, p. 723, 1980.

[44] R. Accorsi, F. Gasparini, and R. C. Lanza, "A Coded Aperture for High-resolution Nuclear Medicine Planar Imaging with a Conventional Anger Camera: Experimental Results," in *IEEE Transactions on Nuclear Science*, vol. 48.6, 2001, pp. 2411-2417.

[45] G. Skinner, "Imaging with Coded-aperture Masks," *Nuclear Instruments and Methods in Physics Research*, vol. 221, no. 1, pp. 33-40, 1984.

[46] G. K. Skinner et al., "Hard X-ray Images of the Galactic Centre," *Nature*, vol. 330, pp. 544-547, 1974.

[47] E. Caroli, J. B. Stephen, G. Cocco, L. Natalucci, and A. Spizzichino, "Coded Aperture Imaging in X-ray and Gamma-ray Astronomy," *Space Science Reviews*, vol. 45, no. 3, 1987.

[48] K. P. Ziock, C. J. Hailey, T. B. Gosnell, J. H. Lupton, and F. A. Harrison, "A Gamma-ray Imager for Arms Control," *IEEE Transactions on Nuclear Science*, vol. 39, no. 4, pp. 1046-1050, 1992.

[49] M. Woodring et al., "Advanced Radiation Imaging of Low Intensity Gamma-Ray Sources," *Nuclear Instruments and Methods in Physics Research A*, vol 442, pp. 709-712, 1999.

[50] M. Woodring et al., "Advanced multi-dimensional imaging of gamma-ray radiation," *Nuclear Instruments and Methods in Physics Research Section A*, vol. 505, pp. 415-419, 2003.

[51] K. P. Ziock et al., "A Fieldable-Prototype, Large-Area, Gamma-Ray Imager for Orphan Source Search," *IEEE Transactions on Nuclear Science*, vol. 55, no. 6, pp. 3643-3653, 2008.

[52] C. E. Ordonez, A. Bolozdynya, and W. Chang, "Dependance of Angular Uncertainties on the Energy Resolution of Compton Camera," *IEEE Nuclear Science Symposium*, vol. 442, pp. 1122-1125, 1997.

[53] Y. Du, Z. He, G. Knoll, D. Wehe, and W. Li, "Evaluation of a Compton Scattering Camera Using 3-D Position Sensitive CdZnTe Detectors," *Nuclear Instruments and Methods in Physics Research Section A: Accelerators, Spectrometers, Detectors and Associated Equiptment*, vol. 457, no. 1, pp. 203-211, 2001.

[54] D. V. Rao, "Importance of Doppler-broadening in Compton scatter imaging techniques," *Proceedings SPIE*, vol. 4508, pp. 157-166, 2001.

[55] M. S. Bandstra et al., "Detection and Imaging Of The Crab Nebula With The Nuclear Compton Telescope," *The Astrophysical Journal*, vol. 783, no. 1, p. 8, 2011.

[56] E. Aprile et al., "The Electronics Read out and Data Aquisition System for a Liquid Xenon TIme Projection Chamber as a Baloon-borne Comptom Telescope," *Nuclear Instruments and Methods in Physics Research Section A: Accelerators, Spectrometers, Detectors and Associated Equiptment*, vol. 412, no. 2, pp. 425-436, 1998.

[57] E. A. Wulf, B. F. Philips, W. N. Johnson, J. D. Kurfess, and E. I. Novikova, "Thick Silicon Strip Detector Compton Imager," *IEEE Transactions on Nuclear Science*, vol. 51, no. 5, pp. 1997-2003, 2004.

[58] S. Watanabe et al., "A SiCdTe Semiconductor Compton Camera," *IEEE Transactions on Nuclear Science*, vol. 52, no. 5, pp. 2045-2051, 2005.

[59] M. Ricard, "Imaging of Gamma Emitters Using Scintillation Cameras," *Nuclear Instruments and Methods in Physics Research Section A: Accelerators, Spectrometers, Detectors and Associated Equiptment*, vol. 527, no. 1, pp. 124-129, 2004.

[60] C-H. Baek, S. J. An, H-I. Kim, Y. Choi, and Y.H. Chung, "Development of a large-angle pinhole gamma camera with depth-of-interaction capability for small animal imaging," *13th International Workshop on Radiation Imaging Detectors*, vol. 7, January 2012.

[61] L. R. Macdonald and M. Dahlbom, "Depth of Interaction for PET Using Segmented Crystals," *IEEE Transactions on Nuclear Science*, vol. 45, no. 4, pp. 2144-2148, 1998.

[62] J. M. Ollinger and J. A. Fessler, "Positron-Emission Tomography," *IEEE Signal*

Processing Magazine, vol. 14, no. 1, pp. 43-55, 1997.

[63] J. Katoak, et al,, "Handy Compton camera using 3D position-sensitive scintillators coupled with large-area monolithic MPPC arrays," *Nucl. Inst. Meth. in Physics. Res. A*, vol. 732, pp. 403-407, 2013.

[64] Stefaan Tavernier, *Radiation Detectors for Medical Applications*. Dordecht: Springer, 2006.

[65] Gopal B. Saha, *Basics of PET Imaging; Physics, Chemistry and Regulations*. New York, NY, USA: Springer, 2010.

[66] W. Moses, S. Derenzo, and T. Budinger, "PET Detector Modules Based on Novel Detector Technologies," *Nuclear Instruments and Methods in Physics Research Section A: Accelerators, Spectrometers, Detectors and Associated Equiptment*, vol. 353, no. 1, pp. 189-194, 1994.

[67] Moses, W., "Trends in PET Imaging," *Nuclear Instruments and Methods in Physics Research Section A: Accelerators, Spectrometers, Detectors and Associated Equiptment*, vol. 471, no. 1-2, pp. 209-214, 2001.

[68] Tom K. Lewellen, "Recent Developments in PET Detector Technology," *Physics in Medicine and Biology*, vol. 53, no. 17, pp. 287-317, 2008.

[69] Robert M. Gray and Albert Macovski, "Maximum a Posteriori Estimation of Position in Scintillation Cameras," *IEEE Transactions on Nuclear Science*, vol. 23, no. 1, pp. 849-852, 1976.

[70] T. Ling, T. K. Lewellen, and R. S. Miyaoka, "Depth of Interaction Decoding a Continuous Crystal Detector Module," *Physics in Medicine and Biology*, vol. 52, no. 8, pp. 2213-2228, 2007.

[71] Y. Shao et al., "Dual APD Array Readout of LSO Crystals: Optimization of Crystal Surface Treatment," *IEEE Transactions on Nuclear Science*, vol. 49, no. 3, pp. 649-654, 2002.

[72] D. P. Mcelroy, Sung-Cheng Huang, and E. J. Hoffman, "The Use of Retro-reflective Tape for Improving Spatial Resolution of Scintillation Detectors," *IEEE Transactions on Nuclear Science*, vol. 49, no. 1, pp. 165-171, 2002.

[73] J. Braverman, M. Harrison, and K. P. Ziock, "An Approximate Analytic Expression for the Flu Density of Scintillation Light at the Photocathode," in *Nuclear Science Symposium 2012 Conference Record*, Anaheim, 2012, pp. N1-155.

[74] T. Woldemichael, "Design of Floating-Boundary Multi-Zone Scintillation Camera With Pileup Prevention and Misplaced Pileup Supression (MPS)," *IEEE Transactions On Nuclear Science*, vol. 55, pp. 2704-2715, 2008.

[75] S. et al. Agostinelli, "GEANT4- a simulation toolkit," *Nucl. Inst. and Meth. in Phys. Res. A*, vol. 506, no. 3, pp. 250-303, 2003.

[76] Saint-Gobain Crystals. http://www.saint-gobain.com/en.

[77] David J. Griffiths, *Introduction to Electrodynamics*. Saddle River, NJ, USA: Prentice Hall, 1999.

[78] Cargille Labs. http://www.cargille.com/.

[79] Physical Chemistry Group, ORNL. http://web.ornl.gov/sci/csd/Research_areas/POC_staff.html.2.

[80] SensL. (2011) http://www.sensl.com/downloads/ds/TN%20-%20Intro%20to%20SPM%20Tech.pdf.

[81] Spectral Instruments Inc. [Online]. http://www.specinst.com/What_Is_A_CCD.html

[82] Andor an Oxford Instruments Company. [Online]. http://www.andor.com/

[83] Hamamatsu. [Online]. www.hamamatsu.com/resources/pdf/etd/PMT_handbook_v3aE-Chapter9.pdf

[84] Hamamatsu. www.hamamatsu.com.

[85] Hamamatsu.com. [Online]. https://www.hamamatsu.com/resources/pdf/etd/H9500_H9500-03_TPMH1309E01.pdf

[86] Strück. Strück Innovative System. [Online]. www.struck.de

[87] Phillips Scientific. www.phillipsscientific.com/phisci1.htm.

[88] ROOT Data Analysis Framework. http://root.cern.ch/drupal/.

[89] Velmex, Inc. Velmex. [Online]. www.velmex.com

[90] Toppan Photomasks. [Online]. http://www.photomask.com/

[91] XIA LLC. XIA. [Online]. www.xia.com

[92] J. T. Harris, P. M. Grudberg, and W. K. Warburton, "Digital Electronics for 256 Anode Hamamtsu H9500 PSPMT Arrays in Full-volume Compton Imagers," *15th International Workshop on Radiation Imaging Detectors*, 2014.

[93] Planacon Photonis. Photonis. [Online]. http://www.photonis.com/en/ism/63-planacon.html

[94] National Instruments. http://www.ni.com/.

[95] Alpha Spectra. Alpha Spectra Scintillation Detectors. [Online]. http://www.alphaspectra.com/

[96] Edmunds Optics. Edmunds Optics Worldwide. [Online]. http://www.edmundoptics.com/

[97] Prism Research Glass. [Online]. www.prismresearchglass.com

[98] Visual Basic. http://msdn.microsoft.com/en-us/library/2x7h1hfk.aspx.

[99] F. J. MacWilliams and N. J. A. Sloane, "Pseudo-Random Sequences and Arrays," *Proceedings of the IEEE*, vol. 64, no. 12, pp. 1715-1729, December 1976.

[100] J. Gunson and Polychronopulos, "Optimum design of a coded mask x-ray telescope for rocket applications," *Mon. Not. R. Astron. Soc.*, vol. 177, 1976.

APPENDICES

APPENDIX 1. FLUX DENSITY EXPRESSION DERIVATION

For a point-like radiation interaction in a scintillator crystal that creates light at a depth y_1 as shown in Figure 127, the light radiates uniformly in all directions. The flux density through the surface S_1 with radius r_1 is given by

$$\frac{\phi_0}{4\pi r_1^2} \text{ [74]}.$$

Eq. 86

Consider an area element dA as shown in Figure 127, and given by

$$dA = du\, ud\alpha$$

Eq. 87

The flux through this region is given by the dot product of flux density and the area where the cosine of the angle between r_1 and y_1 is used to obtain the normal component of the flux

$$\frac{d\phi}{dA} = \frac{\phi_0}{4\pi r_1^2}\frac{ds_1}{du}.$$

Eq. 88

Substituting r_1,

$$\frac{\mathrm{d}\phi}{\mathrm{dA}} = \frac{\phi_0}{4\pi}\frac{\mathrm{y}_1}{\mathrm{r}_1^3}.$$

Eq. 89

Finally, replacing r_1 in terms of u and y_1, one obtains the expression for the flux density [74]

$$\frac{\mathrm{d}\phi}{\mathrm{dA}} = \frac{\phi_0}{4\pi \mathrm{r}_1^2}\frac{\mathrm{ds}_1}{\mathrm{du}} = \frac{\phi_0}{4\pi}\frac{\mathrm{y}_1}{\mathrm{r}_1^3} = \frac{\phi_0}{4\pi}\frac{\mathrm{y}_1}{(\mathrm{u}^2+\mathrm{y}_1^2)^{3/2}}.$$

Eq. 90

In a realistic scintillator detector one must include a light pipe or PT entrance window and these materials generally have a significantly different index of refraction than the scintillator.

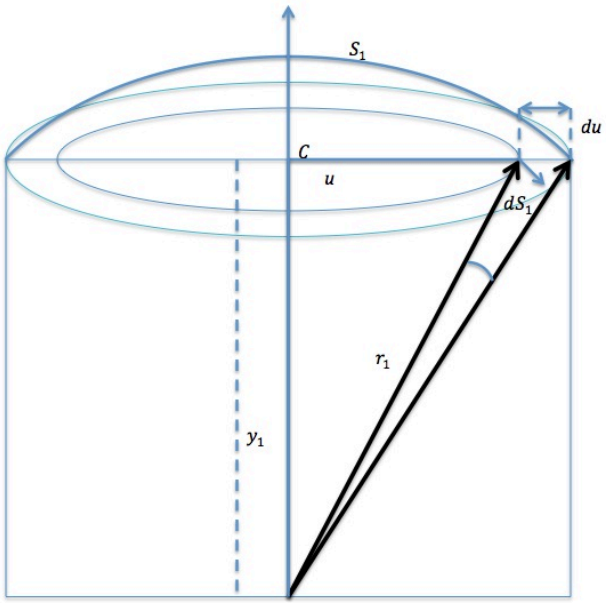

Figure 127. The light spot occurs at a depth y_1 from the face of the PT. The radius from the center of the light spot is given by u.

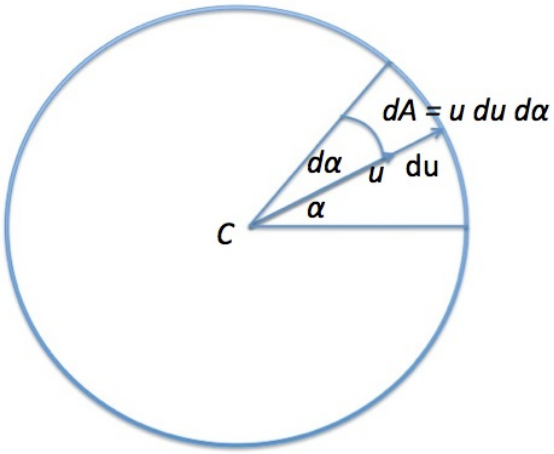

Figure 128. A horizontal view of the face of the PT with C as a reference point. Eq. 90 describes the flux density through the area dA.

Substituting r_1,

$$\frac{d\phi}{dA} = \frac{\phi_0}{4\pi}\frac{y_1}{r_1^3}.$$

Eq. 91

Finally, replacing r_1 in terms of u and y_1, one obtains the expression for the flux density

$$\frac{d\phi}{dA} = \frac{\phi_0}{4\pi r_1^2}\frac{ds_1}{du} = \frac{\phi_0}{4\pi}\frac{y_1}{r_1^3} = \frac{\phi_0}{4\pi}\frac{y_1}{(u^2+y_1^2)^{3/2}}\ [74].$$

Eq. 92

In a realistic scintillator detector one must include a light pipe or PT entrance window and these materials generally have a significantly different index of refraction than the scintillator.

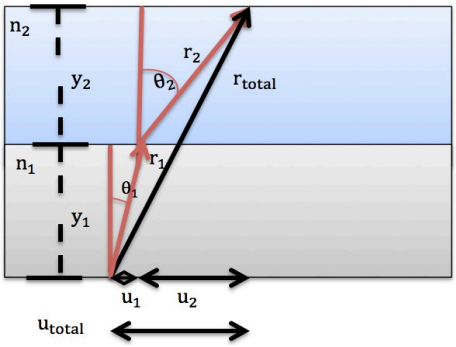

Figure 129. The light spot occurs at the bottom of the crystal, and between the PT face at the top of the figure and the top of the crystal is a light pipe with index of refraction n_2. The crystal has index of refraction $n_1 > n_2$. Generally the light pipe has a lower index than the scintillator crystal in order to provide a better match for a glass face.

To account for the change, a new effective u_{total} was found as shown in Figure 129. From Snell's Law,

$$n_1 \sin(\theta_1) = n_2 \sin(\theta_2).$$

Eq. 93

Each value is indicated in Figure 129. Knowing θ_2 allows one to know u_2 and, in turn, u_{total}. In addition to the new effective radius u, the index change causes reflection losses as shown in Figure 130.

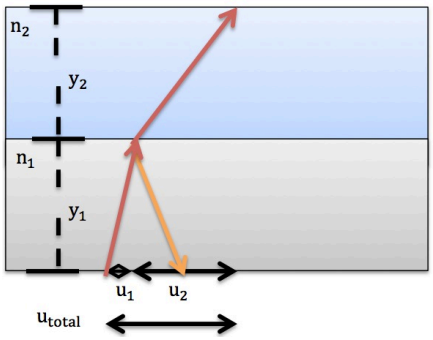

Figure 130. A fraction of the incident ray is reflected due to the index of refraction change.

These are described by the well-known Fresnel's equations. Again, knowing θ_2 gives the fraction of transmitted light at each opening angle,

$$T = 1\text{-}R = 1\text{-}\frac{(R_s+R_p)}{2}$$

Eq. 94

where T is the transmission coefficient and R_s and R_p are the reflection coefficients for each type of polarized light,

$$R_s = \left|\frac{n_1\cos(\theta_1)\text{-}n_2\cos(\theta_2)}{n_1\cos(\theta_1)+n_2\cos(\theta_2)}\right|^2$$

Eq. 95

$$R_p = \left|\frac{n_1\cos(\theta_2)\text{-}n_2\cos(\theta_1)}{n_1\cos(\theta_2)+n_2\cos(\theta_1)}\right|^2.$$

Eq. 96

For scintillators, the light is not polarized, so equal values of both polarizations are used. With the new *u* from Snell's law and transmission coefficient from Fresnel's equations, the expression becomes,

$$\frac{d\phi}{dA} = \frac{\phi_0}{4\pi} \frac{y_1+y_2}{\left(u_{total}^2+(y_1+y_2)^2\right)^{3/2}} T.$$

Eq. 97

In addition to reflection loses, the coordinate system changes from θ_1 to θ_2. This requires a Jacobian equal to

$$\frac{d\theta_1}{d\theta_2} = \frac{\sqrt{1-\left(\frac{n_2}{n_1}\right)^2 \sin(\theta_2)^2}}{\frac{n_2}{n_1}\cos(\theta_2)}.$$

Eq. 98

Adding this term to (10) one obtains the final expression,

$$\frac{d\phi}{dA} = \frac{\phi_0}{4\pi} \frac{y_1+y_2}{\left(u_{total}^2+(y_1+y_2)^2\right)^{3/2}} \frac{d\theta_1}{d\theta_2} TN \text{ [73]}.$$

Eq. 99

ϕ_0 is a normalizing factor.

This expression is not exact, but an approximation. In reality, the shape of the light spot after undergoing an index change is no longer spherical, and continuing the method from [74] does not provide an exact analytic expression. While not exact, this analytic approximation has been verified to work very well for low numbers of photons. Figure 131 shows the expression compared to GEANT4 [75] simulation data. The data simulated is for mono energetic photons launched in a high index material of 1.83 to a low index material of 1.44. As labeled in Figure 129 above, y_1=15 mm and y_2=30 mm [73].

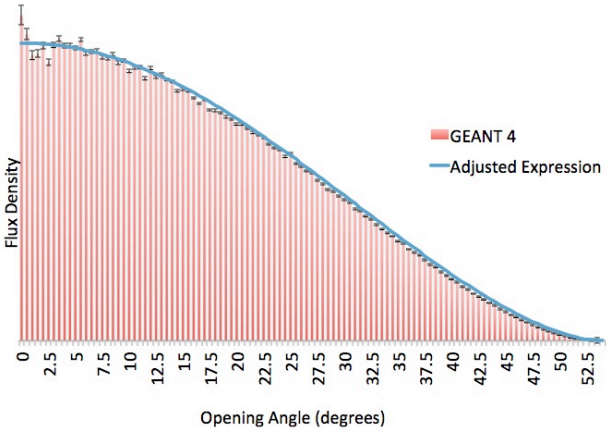

Figure 131. A comparison of the flux density expression to simulation data. The reduced Chi-Squared method was used for the fit routine. Chi-Squared/Degree of Freedom=3.17.

As seen in the figure, the reduced Chi-Square value is 3.17. While this indicates the expression is not an exact fit, the expression works much better for a very low number of photons. In particular, for 1100 photons and when going from high index to low index as in the case of this project, the reduced chi-square value is 1.04 [73].

APPENDIX 2. FILTERING ALGORITHMS

As stated in Section 6.2.I, several features of the gain-mapping-impacted events were examined to see if it was possible to correctly localize the events from other parameters (besides the maximum peak height) of the images. No method was found to work well for resolving events between upper and lower depths. Some of the parameters of the images examined were the RMS, sum of the entire image, and average, as well as ratios of the maximum channel peak heights with each. None were found to work well to disentangle the events.

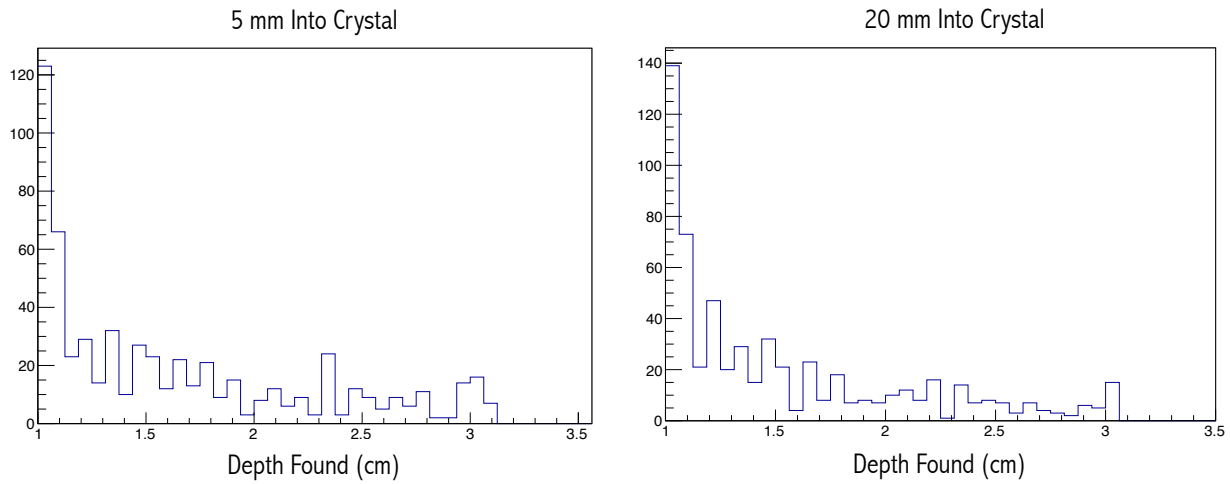

Figure 132. The depth found for 400-photoelectron simulation events for launch points 5 mm and 20 mm into the crystal, using the maximum RMS method.

As seen in Figure 132, the maximum RMS method did not yield a difference in the two data sets, even though the depth of the events was separated by 15 mm. The minimum of the RMS as well as the sum and ratios of the peak height versus each were looked at as well and yielded similar results.

APPENDIX 3. ANGLED BEAM SETUP

In addition to the vertical collimator geometry with the thick (30 mm) scintillator crystal, data were also collected with an angled collimator mount. The goal of this was to see a correlation between the depth of interaction and the distance from the collimator. As seen in Figure 133, this geometry should show a trend of decreasing depth versus increasing X. Additionally, the events in the Y direction (into the page in Figure 133) should be constant.

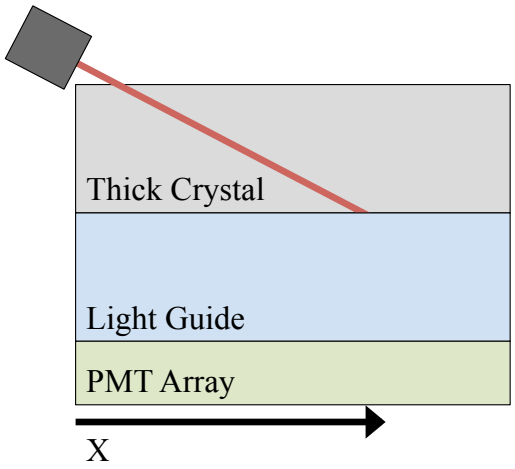

Figure 133. A schematic of the angled beam approach. Events at lower depth should be found at higher X.

No correlation was seen between the depth and X dimensions. To investigate this, the collimator was arranged vertically and moved over the center of each PMT, and the energy spectrum at each point was collected. The position of the vertically collimated beam and corresponding spectra are shown in Figure 134. The spectra at positions 2, 5, 7, 8, and 9 are as expected; the positions of the peaks are known to be the 356-keV peaks, as the 622-kev peak position is known. However, the spectra at 1, 3, 4, and 6 do not show well-behaved energy spectra. As the source does not contain broad spectral lines at the positions observed, these events are badly behaved triggering events. Thus, the angled beam measurement could not be

collected and analyzed correctly, as the events over the problematic PMT modules are not "good" events. As shown above, the outer cycles are required to image events correctly, so the angled beam over the lower row of PMTs would not allow for a proper measurement, as events on the edge of the system would not be able to be imaged with additional outer cycles.

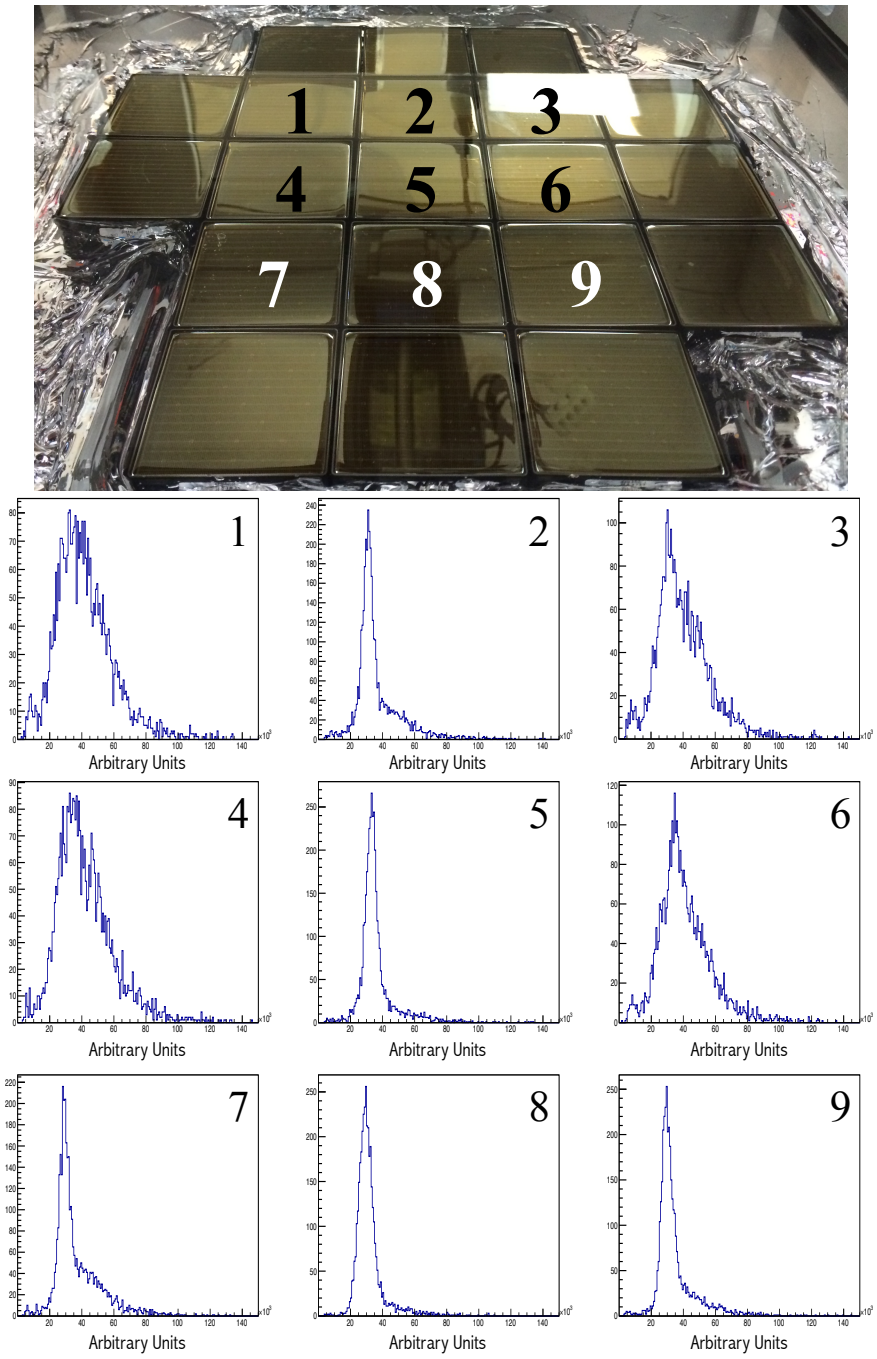

Figure 134. The upper image shows the position of the collimated vertical beam with the corresponding spectra in the bottom image. The data were each collected with the 30-mm-thick crystal and mask pattern coupled to the quartz plane shown.

VITA

Joshua Brian Braverman was born in Los Angeles, California. After completing high school in 2006, he moved to Boulder, Colorado to attend the University of Colorado where he received a Bachelor of Arts in Physics and English Literature in 2010. The following fall he began his graduate work at the University of Tennessee, Knoxville, where he received a Master of Science in Physics in 2012, and worked on an applied nuclear physics detection experiment at Oak Ridge National Laboratory beginning in Fall 2011.